A UNITED STATES DEPARTMENT OF COMMERCE PUBLICATION

SECTION **A**

JOURNAL OF RESEARCH

of the NATIONAL BUREAU OF STANDARDS

Volume 74A, Number 4 July-Aug. 1970

Physics and Chemistry

U.S. DEPARTMENT OF COMMERCE
National Bureau of Standards

UM

Journal of Research

of the

National Bureau of Standards

A. Physics and Chemistry

July–Aug. • 1970

VOLUME • 74A

NUMBER • 4

Editor: C. W. Beckett

Associate Editor: D. D. Wagman

Publication dates:
Feb. 1, Apr. 1, June 1, Aug. 1, Oct. 1, Dec. 1, 1970

J. Res. Nat. Bur. Stand. (U.S.), A
CODEN: JNBAA 74A (4) 461–616 (1970)

JOURNAL OF RESEARCH

The National Bureau of Standards Journal of Research reports research and development in the fields of activity shown at right. Also included from time to time are survey articles on topics closely related to the Bureau's scientific and technical program.

The Journal is published in three separate sections as follows:

A. Physics and Chemistry

Contains papers of interest primarily to scientists working in these fields. Issued six times a year. Annual subscription: domestic, $9.50; foreign, $11.75. Single copy, varies.

B. Mathematical Sciences

Presents studies and compilations designed mainly for the mathematician and the theoretical physicist. Issued quarterly. Annual subscription: domestic, $5.00; foreign, $6.25. Single copy, $1.25.

C. Engineering and Instrumentation

Reports research and development results of interest chiefly to the engineer and the applied scientist. Issued quarterly. Annual subscription: domestic, $5.00 foreign, $6.25. Single copy, $1.25.

U.S. DEPARTMENT OF COMMERCE
Maurice H. Stans, Secretary
NATIONAL BUREAU OF STANDARDS
Lewis M. Branscomb, Director

Order all publications from the Superintendent of Documents
U.S. Government Printing Office, Washington, D.C. 20402
Use of funds for printing this publication approved by the Director of the Bureau of the Budget (June 22, 1966).

JOURNAL OF RESEARCH of the National Bureau of Standards—A. Physics and Chemistry
Vol. 74A, No. 4, July–August, 1970

Solubility of $CaHPO_4 \cdot 2H_2O$ in the System $Ca(OH)_2 - H_3PO_4 - H_2O$ at 5, 15, 25, and 37.5 °C*

Thomas M. Gregory, Edgard C. Moreno,*** and Walter E. Brown******

**Institute for Materials Research,
National Bureau of Standards,
Washington, D.C. 20234**

(January 1, 1970)

Solubility isotherms for $CaHPO_4 \cdot 2H_2O$, dicalcium phosphate dihydrate, DCPD, in the ternary system $Ca(OH)_2 - H_3PO_4 - H_2O$ were determined at 5, 15, 25, and 37.5 °C in the pH range 3.5 – 7; the relative positions of the isotherms indicate that DCPD has a negative thermal coefficient of solubility. The solubility product, K_s, of DCPD and the stability constants K_x and K_y for the ion pairs $[CaHPO_4^0]$ and $[CaH_2PO_4^+]$, respectively, were obtained as functions of temperature by the use of a generalized least squares procedure subject to three condition functions—constancy of the solubility product, electrical neutrality in the solution, and congruent dissolution of the solid. The equations obtained are

$$\ln K_s = -8403.5/T + 41.863 - 0.09678T$$
$$\ln K_x = 51090/T - 341.14 + 0.5880T$$
$$\ln K_y = 19373/T - 122.81 + 0.1994T.$$

The existence of a maximum in K_s in the neighborhood of 25 °C is plausible on the basis of available thermodynamic data for DCPD. Thermodynamic functions are reported for the solution of DCPD and for the association of the ion pairs.

Key words: Calcium phosphate; dicalcium phosphate dihydrate; ion pairs; solubility; solubility isotherms; solubility product.

1. Introduction

In a previous publication [1][1] on the solubility at 37.5 °C of dicalcium phosphate dihydrate (DCPD), $CaHPO_4 \cdot 2H_2O$, in dilute phosphoric acid solutions, we reported that the "apparent" solubility product, K'_{DC}, exhibited a concentration dependence. This dependence could be removed by postulating the presence of the ion pairs $[CaHPO_4^0]$ and $[CaH_2PO_4^+]$, making it possible to calculate a "true" solubility product, as well as the stability constants of these ion pairs.

In view of the importance of DCPD in the areas of biology, agronomy and industry, we have extended to other temperatures our solubility measurements of this compound in the ternary system $Ca(OH)_2 - H_3PO_4 - H_2O$ to obtain standard free energies, enthalpies and entropies for dissolution of DCPD and for formation of the ion pairs.

We report here the consolidated results and calculations on the solubility behavior of DCPD at 5, 15, 25, and 37.5 °C. Although measurements at 25 °C had been reported previously [2], it was decided to repeat the work at this temperature in order to make all the data comparable in terms of analytical techniques. In the light of our continued experience with these systems we have reevaluated the data collected at 37.5 °C [1] by the use of a more general statistical treatment. No measurements formerly reported [1] have been rejected, but additional measurements have been included.

The data were treated by generalized least squares [3, 4] to obtain estimates of the constants of interest, their standard errors and the adjusted values of the data. The major departure from customary [5, 6] least squares applications introduced in this paper is the use of multicomponent observation and condition function vectors: each of N independent systems is associated with a 4-component observation vector and a 3-component function vector. It will be shown that, where applicable, the imposition of more than one

*This investigation was supported in part by research grant DE-02659-02 to the American Dental Association from the National Institute of Dental Research and is part of the dental research program conducted by the National Bureau of Standards, in cooperation with the Council on Dental Research of the American Dental Association; the United States Army Medical Research and Development Command; the Dental Sciences Division of the School of Aerospace Medicine, USAF; the National Institute of Dental Research; and the Veterans Administration.

**Research Associate of the American Dental Association at the National Bureau of Standards.
***Present address: Forsyth Dental Center, 140 Fenway, Boston, Mass. 02115.
****Director, Research Associate Program of the American Dental Association at the National Bureau of Standards.

[1] Figures in brackets indicate the literature references at the end of this paper.

condition function per system materially reduces the computed standard deviation. We have applied multi-function conditions in other solubility studies [7] and in the study of diffusion in ternary systems [8].

2. Methods and Materials

2.1. Preparation of Materials

Dicalcium phosphate dihydrate and the phosphoric acid solutions were prepared and characterized as described in previous publications [1, 2].

2.2. Experimental Method

The DCPD preparations were leached in a thermostatted saturator with a series of dilute phosphoric acid solutions as described previously [1]. The pH of the effluent was measured in situ and a number of samples (4–8) were collected for the determination of total calcium and phosphorus.

2.3. Calcium and Phosphorus Determinations

Phosphorus was determined spectrophotometrically (relative error, 0.01) in a double beam instrument using the vanado-molybdate reagent of Brabson et al. [9], as described for our previous work at 37.5 °C [1]. Calcium was determined by atomic absorption with a relative error of 0.015.

2.4. pH Determinations

The pH measurements were made with glass and calomel electrodes with a commercially available pH meter (claimed relative accuracy ± 0.0037 pH unit). Standardization of the meter was done with certified NBS buffer standards [10]. The error in the pH measurements was taken as 0.015, which includes the estimated error (0.005) in the value of the standard buffer used [10].

3. Calculations

The aim of these calculations was to obtain as a function of temperature, the "true" solubility product, K_s, of DCPD, the stability constants K_x and K_y, of the ion pairs $[CaHPO_4^0]$ and $[CaH_2PO_4^+]$, respectively, and the adjusted values of the experimental data. This was accomplished as described, by minimizing the weighted sum of squares of the residuals in the observations subject to three condition functions: saturation with respect to DCPD, electroneutrality, and congruent dissolution of this salt.

Preliminary calculations were done separately on the data collected at each of the four temperatures and the equilibrium constants, K_m, so obtained were each fitted by subsequent adjustments to equations of the form $\ln K_m = A_{m_1} T^{-1} + A_{m_2} + A_{m_3} T$. Since the results of this procedure showed that the assumed form of temperature dependence was quite reasonable, the calculations reported here were then done on the combined sets of raw data using the above form of temperature dependence ab initio. In this way the nine constants were obtained without the necessity of further adjustment. Throughout this work the temperature was considered as a preset, error-free variable.

In order to formulate the condition functions, it is first necessary to characterize the systems in terms of the measurements and constants. This is done in sections 3.1, 3.2, and 3.3.

3.1. Balance Equations

Using the symbols X^0 and Y^+ for the names and concentrations of the species $[CaHPO_4^0]$ and $[CaH_2PO_4^+]$, respectively, the total molar concentrations of calcium, Ca, and phosphorus, P, are given by

$$\mathrm{Ca} = [\mathrm{Ca}^{++}] + \tau \tag{1}$$

and

$$\mathrm{P} = \sum_{i=0}^{3} [\mathrm{H}_i\mathrm{PO}_4^{i-3}] + \tau \tag{2}$$

in which $\tau = X^0 + Y^+$, and $[Ca^{++}]$ denotes the concentration of free calcium ions. Equation (2) may be written in terms of the activity of the $HPO_4^=$ ion, $(HPO_4^=)$, and the three dissociation constants k_1, k_2, and k_3 of phosphoric acid as

$$\mathrm{P} = (\mathrm{HPO}_4^=) \cdot N + \tau, \tag{3}$$

where

$$N = \sum_{i=0}^{3} N_i g_i = \frac{(\mathrm{H}^+)^2}{k_1 k_2} g_0 + \frac{(\mathrm{H}^+)}{k_2} g_1 + g_2 + \frac{k_3}{(\mathrm{H}^+)} g_3. \tag{4}$$

In eq (4), $(H^+) = 10^{-pH}$ is hydrogen ion activity and g_i is the reciprocal of the activity coefficient f_i of species i. The subscript i takes the value of the charge magnitude of the several free phosphate species.

3.2. Solubility Product and Concentrations of Ion Pairs

The solubility product is defined here as

$$K_{DC} = (\mathrm{Ca}^{++})(\mathrm{HPO}_4^=) = (\mathrm{Ca} - \tau)(\mathrm{P} - \tau)/g_{Ca} N. \tag{5}$$

In eq (5), and in eqs (6, 7) below, the parentheses around quantities with a charge symbol denote activities. The third member of eq (5) follows from eqs (1) and (3). An apparent solubility product, K'_{DC}, was calculated taking τ to be zero. K_{DC}, as defined by eq (5), is distinct from the quantity K_s; the latter is the least squares value of the solubility product constant as

found by the adjustment procedure described in section 3.5. The quantity K_{DC}, on the other hand, is the ionic-activity product computed for each individual system; in the absence of experimental errors, its value should be the same for all systems, and equal to K_s, if the saturation condition is fulfilled and if the model for ion pairs is valid.

The concentrations of the ion pairs can be expressed in terms of the stability constants as follows:

$$K_x = (CaHPO_4^0)/(Ca^{++})(HPO_4^=) = X^0/K_{DC}, \quad (6)$$

$$K_y = (CaH_2PO_4^+)/(Ca^{++})(H_2PO_4^-) = Y^+/K_{DC}g_1N_1. \quad (7)$$

Adding eqs (6) and (7) and using the identity $\tau = X^0 + Y^+$, a quadratic equation in τ is obtained whose pertinent solution is

$$\tau = U - (U^2 - P \cdot Ca)^{1/2}, \quad (8)$$

where $U = \frac{1}{2}\{P + Ca + g_{Ca}N/(K_x + g_1N_1K_y)\}$. Writing $R = (1 + K_x/g_1N_1K_y)^{-1}$, the ion pair concentrations are

$$X^0 = (1-R)\tau, \; Y^+ = R\tau. \quad (9)$$

3.3. Ionic Strength and Activity Coefficients

The ionic strength, μ, is defined in these calculations by

$$2\mu = 4(Ca - \tau) + g_H(H^+) + g_{OH}k_w/(H^+) + Y^+ + \phi_2(P - \tau)/N, \quad (10)$$

where k_w is the dissociation constant of water,

$$\phi_2 = \sum_{i=0}^{3} i^2 N_i g_i,$$

and the N_i are defined by eq (4).

Inasmuch as individual ionic activities are required for the computations, the results are bound to reflect the particular expression arbitrarily chosen for the activity coefficients. For this reason calculations were carried through using two different expressions: the Debye-Hückel limiting law extension (D.-H.) and the expression used by Davies [11]. These expressions are given by eqs (11a) and (11b), respectively.

$$-\log f_i = A(T)z_i^2\sqrt{\mu}/(1 + B(T)a_i\sqrt{\mu}) \quad (11a)$$

$$-\log f_i = A(T)z_i^2\{\sqrt{\mu}/(1 + \sqrt{\mu}) - 0.3\mu\} \quad (11b)$$

where z_i is the valence of the ith ion, a_i is the "distance of closest approach" parameter, and A and B are temperature-dependent constants. Following convention, the activity coefficients of the uncharged species H_3PO_4 and $[CaHPO_4^0]$ were taken as unity. The coefficient of the charged ion pair $[CaH_2PO_4^+]$ was taken to be equal to that of the ion $H_2PO_4^-$.

Values used at the various temperatures for the dissociation constants k_1, k_2, k_3, k_w, and for the parameters $A(T)$ and $B(T)$ are given in table A1, section 6.2. In table A2 are listed the values for the parameters a_i.

Iteration Procedure. Approximate values were first obtained for N in eq (4), and for τ and Y^+ in eqs (8) and (9), using initial guesses for the constants K_x and K_y and assuming all $f_i = 1$. An approximate value of the ionic strength, μ, eq (10), was then obtained which yielded better estimates for the f_i (eq (11)). The calculations were iterated until a constant value of μ was attained (2–3 cycles). New estimates for the parameters A_{mk} were then obtained by the adjustment procedure to be described in 3.5; new values of K_x and K_y computed from eq (16), when inserted into eqs (8) and (9), yielded improved estimates for the ion pair concentrations. A new iteration on μ was started, but using the last values of the f_i, and the whole process was continued until the weighted sum of squared residuals attained a constant value.

3.4. Weights of the Observations

The weights of the observations, defined below by (12), were computed from the estimated variances. The constant s_0 was taken as 1.0×10^{-8}.

$$w = s_0^2/\text{variance} \quad (12)$$

Using the value given in section 2.4 for the error, the variance of pH was calculated as $(0.015)^2$. The variances of phosphorus and of calcium were computed from the relative errors given in section 2.3. At 37.5 °C, the relative error for calcium was 0.025.

3.5. Least Squares Adjustment

This section adheres closely to the notation of section 11.3 of reference [4]. Equation numbers referred to in this text from that source are enclosed in square brackets. The symbols used in this paper are defined in table 1; they differ from those in table [11.3.3] of reference [4] in several respects, as indicated in section 6.1.

TABLE 1. *Matrix symbols*

Name	Symbol	Order	Element
Condition function	f^a	$r \times 1$	$F_q^a(Y_l^a; \beta_v^0)$
Observation	y^a	$n \times 1$	Y_i^a
Residual	v^a	$n \times 1$	V_i^a
Adjusted observation	u^a	$n \times 1$	U_i^a
Weight	W^a	$n \times n$	W_{ii}^a (diagonal)
Parameter	β	$p \times 1$	$\beta_v = \beta_v^0 - \vartheta_v$
Correction	θ	$p \times 1$	ϑ_v
	J^a	$r \times p$	$F_{qv}^{a'} = \partial F_q^a/\partial\beta_v$
	F^a	$r \times n$	$F_{qi}^{a'} = \partial F_q^a/\partial Y_i^a$
	L^a	$r \times r$	$L_{qs}^a = \Sigma_i F_{qi}^{a'} F_{si}^{a'} W_{ii}^{a-1}$
Lagrangian	λ^a	$r \times 1$	λ_q^a
	C	$p \times p$	$C_{\mu\nu}$

The general formulation of reference [4], applied to the combined data (35 points) with 3 condition functions per system and 9 parameters, leads to the matrix [11.3.3, 1a] of order $3\times35+9=114$. In an alternative formulation of the normal equations [11.3.3.1, 5a], the matrix L is of order $3\times35=105$. However, if the condition functions for the αth system depend on the measurements on that system only, as is true here, then, as shown in section 3.5.3, the order of the largest matrix that appears is 9, the maximum number of parameters considered here.

a. Condition Functions

The available conditions to be imposed on each system are:

1. F_1^α: Saturation with respect to DCPD

$$(\mathrm{Ca}-\tau)(\mathrm{P}-\tau)/g_{\mathrm{Ca}}N-K_s=0. \tag{13}$$

2. F_2^α: Electroneutrality

$$2(\mathrm{Ca}-\tau)+g_{\mathrm{H}}(\mathrm{H}^+)+Y^+-g_{\mathrm{OH}}k_w/(\mathrm{H}^+) -\phi_1(\mathrm{P}-\tau)/N=0, \tag{14}$$

where $\phi_i=\sum_{i=1}^{3} iN_ig_i$.

3. F_3^α: Congruent dissolution of DCPD

$$\mathrm{Ca}/(\mathrm{P}-\mathrm{P}_0)-1=0, \tag{15}$$

where P_0 is the molar concentration of initial phosphoric acid.

In eq (13), K_s is the solubility product constant to be estimated. The stability constants to be estimated, K_x and K_y, appear implicitly in τ and Y^+; see eqs (8) and (9).

b. Choice of Parameter and Indices

In these calculations the equilibrium constants were represented by equations of the form

$$\ln K_m=\sum_{k=1}^{\mathrm{L}} A_{mk}T^{k-2}, \qquad \begin{cases} \mathrm{L}=1 \text{ or } 3 \\ m=1, \ldots, \mathrm{C} \end{cases} \tag{16}$$

where $m=1, 2, 3$ corresponds to the subscripts s, x and y, and T is the temperature in kelvins. In the case $\mathrm{L}=1$ (computations at individual temperatures), T^{-1} was replaced by 1. The number of constants, C, was 3 in every case except when ion pairs were assumed absent. In any event, $p=\mathrm{CL}$ is the total number of parameters, A_{mk}, to be found, and $\beta=(A_{11}, \ldots, A_{1\mathrm{L}}, \ldots, A_{\mathrm{CL}})$.

In order to establish the soundness of the data treatment adopted here, i.e., assumption of the presence of ion pairs and use of three condition functions, calculations were made using the following combinations of parameters and functions: (I) Calculations at individual temperatures, assuming ion pairs present; (II) combined data at all temperatures, with temperature dependence for K_s, but ion pairs assumed absent; (III) combined data, ion pairs present, and temperature dependence of the K_m. In each of these cases, separate calculations were made, using as conditions: (A) F_1^α only; (B) F_1^α and F_2^α; (C) F_1^α, F_2^α, and F_3^α. (When F_3^α is omitted, the observable P_0 is not used, i.e., $n=3$). These combinations are tabulated below. The calculated quantities reported here correspond to Case III–C.

Case	C	L	p	r	n
I	3	1	3	3	4
II–A	1	3	3	1	3
–B				2	4
–C				3	4
III–A	3	3	9	1	3
–B				2	4
–C				3	4

c. Reduced Normal Equations and Their Solution

In terms of the analysis of this paper, the reduced or "p normal" [12] eqs [11.3.3.1, 5a], may be written

$$C\theta=z, \tag{17}$$

where

$$C=\sum_\alpha \bar{J}^\alpha L^{\alpha-1}J^\alpha, \quad z=\sum_\alpha \bar{J}^\alpha L^{\alpha-1}f^\alpha. \tag{18}$$

Since J^α is of order $r\times p$ and L^α is of order $r\times r$, the matrix C is of order $p\times p$.

Equation (17) was scaled by the substitution $\theta=D^{-1}\theta^*$ and premultiplication by D^{-1} to give

$$C^*\theta^*=z^*, \tag{19}$$

where $D_{\nu\nu'}=\sqrt{C_{\nu\nu}}\delta_{\nu\nu'}$ ($\delta_{\nu\nu'}$ is the Kronecker delta), $C^*=D^{-1}CD^{-1}$, and $z^*=D^{-1}z$. The solution for the parameter corrections is then

$$\theta=D^{-1}C^{*-1}z^*. \tag{20}$$

The inversion of C^* was accomplished using Gaussian elimination and double precision arithmetic.

New estimates, $\beta=\beta^0-\theta$, were thus obtained and used for a subsequent iteration (sec. 3.3).

The convergence of the process at the nth iteration was followed by computing the sum of squares (q^2) and testing the ratio q_n^2/q_{n-1}^2 against 10^{-7}. For $p=3$, convergence was attained in 3–4 cycles and for $p=9$, about 15 cycles were required. The expression used for q^2 is given in eq (A–15) of section 6.1c. In computations for consecutive values of α during a given cycle, partial sums (denoted by the prime) were accumulated:

$$C'_{(\alpha)} = C'_{(\alpha-1)} + J^{\alpha} L^{\alpha^{-1}} J^{\alpha},$$

$$z'_{(\alpha)} = z'_{(\alpha-1)} + J^{\alpha} L^{\alpha^{-1}} f^{\alpha},$$

and

$$q^{2\prime}_{(\alpha)} = q^{2\prime}_{(\alpha-1)} + f^{\alpha} L^{\alpha^{-1}} f^{\alpha}.$$

The sum $q^{2\prime}_{(N)} = \Sigma_{\alpha} f^{\alpha} L^{\alpha^{-1}} f^{\alpha}$ was then corrected, after obtaining the solution for θ, by subtracting the quantity $\tilde{\theta} C \theta$.

d. Standard Deviation and Errors

The total number of condition functions considered here is Nr, i.e., the number of systems, times the number of functions per system. Hence, [11.3.4.1, 3] for the estimated sum of squares is

$$\mathscr{E}(\Sigma_{\alpha} \tilde{V}^{\alpha} W^{\alpha} V^{\alpha}) = (Nr - p) s^2. \tag{21}$$

The standard deviation of the adjustment is thus

$$s = \sqrt{[q^2/(Nr-p)]}, \tag{22}$$

with dispersion (standard error) given by [13]

$$\sigma\{s\} = s/\sqrt{[2(Nr-p)]}.$$

The covariance matrix of the parameter set β is $s^2 C^{-1}$ by [11.3.4.2c] and (A−1). This may be written as

$$\text{Cov } \beta = s^2[(C^{-1})_{mm'}],\ m, m' = 1, \ldots, \text{C}. \tag{23}$$

Here $s^2(C^{-1})_{mm'}$, one of the C^2 submatrices of $s^2 C^{-1}$, is of order $\text{L} \times \text{L}$ and is the moment matrix of the set $(A_{mk}, A_{m'k'})$. (See eq (16)). Then the elements of the covariance matrix for the pair of equilibrium constants K_m, $K_{m'}$ are given by

$$\text{Cov } (K_m, K_{m'}) = s^2 K_m \tilde{\chi}_t (C^{-1})_{mm'} \chi_{t'} K_{m'}, \tag{24}$$

where the vector $\tilde{\chi}_t = (1)$ for $\text{L} = 1$, and $\tilde{\chi}_t = (T_t^{-1}, 1, T_t)$ for $\text{L} = 3$. When the selected temperatures are identical ($t = t'$), the dispersion of K_m is given by

$$\sigma\{K_m\} = \sqrt{[\text{Cov } (K_m, K_m)]}. \tag{25}$$

For the adjusted observations the dispersions were computed from eq (A−10) by

$$\sigma\{U_i^{\circ}\} = \sqrt{[\text{cov } (U_i^{\circ}, U_i^{\circ})]}. \tag{26}$$

4. Results

4.1. Solubility and Solubility Products

The compositions of saturated DCPD solutions at four temperatures are summarized in tables 2 through 5. Congruent dissolution of the salt is indicated by the values of the Ca : $(\text{P} - \text{P}_0)$ ratio, which do not depart significantly from unity. In columns 6 and 7 are given the apparent solubility products, K'_{DC}, (assuming no ion pairs) of the salt calculated with the use of the activity coefficients of Davies and of Debye-Hückel, respectively. It is apparent that the results exhibit the trend noted in previous work [1]: a minimum value of

Table 2. *Solubility of DCPD at 5 °C*

Unadjusted quantities

Initial acid, P_0 $M \times 10^3$	Composition of equil. solns.			Ca / (P − P_0)	$K'_{pc} \times 10^7$	
	pH	Ca $M \times 10^3$	P $M \times 10^3$		Davies	D.-H.
0.0979	7.64_2	0.755	0.843	1.01	2.96	2.98
.490	6.87_8	1.00	1.49	1.00	2.95	2.97
.987	6.40_0	1.41	2.44	0.969	2.74	2.77
2.94	5.66_8	3.18	6.12	.999	2.81	2.86
4.83	5.25_5	5.13	9.92	1.01	2.60	2.66
9.78	4.73_8	9.95	19.6	1.01	2.53	2.63
10.1	4.71_3	10.3	20.4	1.00	2.56	2.66
19.7	4.27_5	19.6	39.3	0.999	2.75	2.90
49.5	3.72_0	47.2	96.8	0.997	3.33	3.46

TABLE 3. *Solubility of DCPD at 15 ° C*

Unadjusted quantities

Initial acid, P_0 $M \times 10^3$	Composition of equil. solns.			Ca / (P − P_0)	$K'_{pc} \times 10^7$	
	pH	Ca $M \times 10^3$	P $M \times 10^3$		Davies	D.-H.
0.0967	7.62_7	0.736	0.842	0.988	2.93	2.95
.499	6.79_3	1.01	1.51	.998	2.83	2.86
1.01	6.36_6	1.41	2.41	1.01	2.78	2.81
2.95	5.60_6	3.20	6.03	1.04	2.69	2.74
4.83	5.20_9	5.11	9.96	0.996	2.59	2.66
5.04	5.17_5	5.19	10.1	1.02	2.47	2.54
10.0	4.68_0	9.97	19.8	1.02	2.48	2.58
20.1	4.21_5	19.4	39.0	1.02	2.61	2.75
50.0	3.62_8	46.7	96.4	1.01	2.89	3.01

TABLE 4. *Solubility of DCPD at 25 °C*

Unadjusted quantities

Initial acid, P_0 $M \times 10^3$	Composition of equil. solns.			Ca / (P − P_0)	$K'_{pc} \times 10^7$	
	pH	Ca $M \times 10^3$	P $M \times 10^3$		Davies	D.-H.
0.101	7.58_0	0.760	0.847	1.02	2.98	3.00
.503	6.77_5	1.03	1.49	1.05	2.89	2.92
1.02	6.33_0	1.41	2.42	1.00	2.75	2.78
2.98	5.58_3	3.27	6.21	1.01	2.84	2.90
4.91	5.18_4	5.19	10.2	0.978	2.70	2.78
9.70	4.72_8	10.1	19.9	.985	2.98	3.10
19.7	4.22_1	19.7	39.1	1.01	2.84	3.00
49.5	3.65_2	47.2	97.6	.983	3.29	3.44

TABLE 5. *Solubility of DCPD at 37.5 °C*

Unadjusted quantities

Initial acid, P_0 $M \times 10^3$	Composition of equil. solns.			$\frac{Ca}{P-P_0}$	$K'_{DC} \times 10^7$	
	pH	Ca $M \times 10^3$	P $M \times 10^3$		Davies	D.-H.
0.498	6.75_5	1.02	1.50	1.02	2.84	2.86
1.00	6.30_5	1.41	2.40	1.01	2.66	2.69
1.00	6.29_9	1.37	2.43	0.963	2.60	2.63
5.02	5.13_2	5.29	10.1	1.04	2.47	2.55
5.02	5.12_0	5.32	10.2	1.04	2.43	2.50
9.99	4.58_7	10.5	20.3	1.01	2.31	2.42
20.2	4.13_7	19.7	40.3	.980	2.43	2.58
20.2	4.13_0	20.2	40.4	1.00	2.43	2.59
49.8	3.56_0	48.9	97.9	1.02	2.73	2.87

K'_{DC} occurs near a pH of 5. The K'_{DC} values in columns 6 and 7 tend to converge in the more dilute solutions, since both expressions for ionic activity coefficients approach the limiting law in this region.

Tables 6 through 9 summarize the data adjustments for 5, 15, 25, and 37.5 °C, respectively, as obtained under the conditions of Case III–C in section 3.5b

TABLE 6. *Solubility of DCPD at 5 °C*

Adjusted quantities

Initial acid, P_0 $M \times 10^3$	Composition of equil. solns.			$\frac{Ca}{P-P_0}$	$\mu \times 10^3$	$K_{DC} \times 10^7$
	pH	Ca $M \times 10^3$	P $M \times 10^3$			
0.0984	7.66_1	0.753	0.851	1.00	2.49	2.33_8
.482	6.84_4	1.00	1.49	1.00	3.10	2.33_9
.996	6.39_1	1.41	2.40	1.00	4.18	2.33_9
2.91	5.62_7	3.18	6.10	1.00	9.17	2.34_8
4.85	5.25_1	5.07	9.92	1.00	14.5	2.33_9
9.78	4.75_1	9.92	19.7	1.00	27.7	2.33_9
10.1	4.72_6	10.3	20.4	1.00	28.6	2.33_9
19.7	4.27_6	19.6	39.3	1.00	52.8	2.33_8
49.2	3.70_5	47.6	96.8	1.00	119.	2.34_0

TABLE 7. *Solubility of DCPD at 15 °C*

Adjusted quantities

Initial acid, P_0 $M \times 10^3$	Composition of equil. solns.			$\frac{Ca}{P-P_0}$	$\mu \times 10^3$	$K_{DC} \times 10^7$
	pH	Ca $M \times 10^3$	P $M \times 10^3$			
0.0969	7.63_6	0.746	0.843	1.00	2.61	2.53_5
.502	6.79_5	1.01	1.51	1.00	3.25	2.53_5
1.01	6.35_9	1.41	2.42	1.00	4.32	2.53_5
2.93	5.60_0	3.17	6.10	1.00	9.33	2.53_5
4.88	5.22_4	5.07	9.94	1.00	14.7	2.53_5
5.03	5.20_3	5.21	10.2	1.00	15.2	2.54_1
9.98	4.70_9	10.1	20.0	1.00	28.8	2.54_3
19.8	4.23_6	19.7	39.5	1.00	54.8	2.54_0
49.6	3.65_0	47.5	97.1	1.00	126.	2.54_1

TABLE 8. *Solubility of DCPD at 25 °C*

Adjusted quantities

Initial acid, P_0 $M \times 10^3$	Composition of equil. solns.			$\frac{Ca}{P-P_0}$	$\mu \times 10^3$	$K_{DC} \times 10^7$
	pH	Ca $M \times 10^3$	P $M \times 10^3$			
0.101	7.58_4	0.751	0.852	1.00	2.64	2.56_1
.499	6.76_8	1.01	1.51	1.00	3.27	2.56_1
1.01	6.32_5	1.41	2.43	1.00	4.36	2.56_1
2.98	5.55_8	3.22	6.20	1.00	9.52	2.56_7
4.97	5.17_9	5.15	10.1	1.00	15.1	2.56_2
9.79	4.69_0	9.88	19.7	1.00	28.6	2.57_8
19.7	4.20_4	19.5	39.2	1.00	55.2	2.56_4
49.5	3.61_3	47.1	96.6	1.00	128.	2.57_5

TABLE 9. *Solubility of DCPD at 37.5 °C*

Adjusted quantities

Initial acid, P_0 $M \times 10^3$	Composition of equil. solns.			$\frac{Ca}{P-P_0}$	$\mu \times 10^3$	$K_{DC} \times 10^7$
	pH	Ca $M \times 10^3$	P $M \times 10^3$			
0.492	6.73_7	1.01	1.51	1.00	3.18	2.37_5
.995	6.29_7	1.41	2.40	1.00	4.25	2.37_5
1.00	6.29_2	1.42	2.42	1.00	4.26	2.37_4
5.00	5.13_1	5.20	10.2	1.00	15.2	2.37_4
5.02	5.12_8	5.22	10.2	1.00	15.2	2.37_4
10.1	4.62_1	10.2	20.3	1.00	29.6	2.37_8
20.3	4.14_2	20.0	40.3	1.00	56.9	2.37_5
20.3	4.14_0	20.0	40.4	1.00	57.1	2.37_5
50.3	3.56_3	47.2	97.5	1.00	130.	2.37_4

using D.-H. activity coefficients. Comparison with tables 2 through 5 shows that in all systems the magnitudes of the individual residuals are small relative to the values of the corresponding observables. The small size of the relative adjustments, (residual/observed value)$\times$ 100, is crucial, since the linearization of the condition functions, neglecting higher order terms, can be justified only if the above ratios are indeed small.

The relative dispersion of the adjusted values of Ca and P, $\sigma\{U_i^q\}/U_i^q$, where the dispersions are given by eq (26), are not shown in the tables, but were well below the assigned relative errors given in section 2.3; likewise, the dispersion of the adjusted pH values were less than the absolute error given in section 2.4. Thus, the calculated dispersions support the reasonableness of the weights assigned in section 3.4.

The last two columns of tables 6 to 9 give the ionic strength and solubility product, K_{DC}, calculated with the adjusted data and final values of the stability constants. The values of K_{DC} are given with more figures than are significant to indicate the adequacy of the adjustment procedure. Since K_{DC} is defined (sec. 3.2) as the function $(Ca-\tau)(P-\tau)/g_{Ca}N$, its near invariance over the range of concentrations supports the correctness of the model involving two ion pairs.

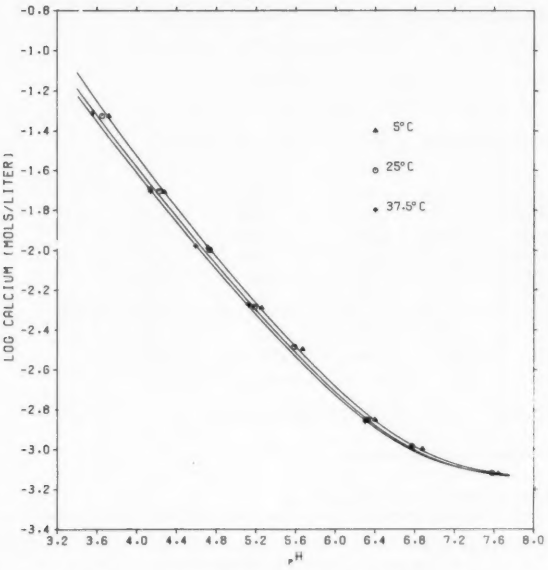

FIGURE 1. *Calculated solubility isotherms of DCPD at 5, 25, and 37.5 °C.*

Points represent experimental data.

In this respect it may be observed that the variations in the listed K_{DC} values are clearly independent of pH, in contrast with those for K'_{DC} in tables 2 to 5. Finally, it may be observed that the K_{DC} values are practically identical to the value of the solubility parameter K_s listed in table 12. This is further evidence as to the soundness of the adjustment and the applicability of the model.

4.2. Solubility Isotherms

In figure 1 are shown the solubility isotherms for DCPD in terms of total concentration of calcium as a function of pH for three temperatures. These curves were computed, as explained in section 5.1, on the basis of the constants derived here. Thus, these curves are the loci of the adjusted data. Experimental points are shown on the same plot. It is apparent that the experimental data at 5 and 37.5 °C are well represented by the calculated isotherms. The reason for the less satisfactory fit for the data at 25 °C will be discussed in section 5.1. The isotherm for 15 °C lies very close to that for 25 °C and, for the sake of clarity, is not shown. The relative positions of the isotherms in figure 1, show that the solubility of DCPD decreases with increase in temperature. This behavior is similar to that displayed [14] by $CaHPO_4$ although the decrease in solubility is more marked in the latter case. Similarly smooth curves are obtained if the concentration of phosphorus is plotted against pH or if the concentration of calcium is plotted against the concentration of phosphorus.

4.3. Ion pairs

The concentration of the ion pair $[CaH_2PO_4^+]$, Y^+, and the percent of bound calcium (100 τ/Ca) for the adjusted data are given for all systems in tables 10 and 11. In table 10 the results for 25 °C are shown for the calculations using the Davies and the D.-H. ionic activity coefficients. Only the results obtained with the latter coefficients are given in table 11 for the other three temperatures, since, as indicated by the values in table 10, the results using the two types of coefficients do not differ markedly. The concentration of the ion pair $[CaHPO_4^0]$, X^0, was nearly invariant in all systems at each temperature, its value being calculated in each cycle from eq (9), involving the quantities R and τ, both of which vary with pH. This constancy was not assumed ab initio but is a consequence of saturation: eq (6) gives $X^0 = K_x \cdot K_{DC}$ and therefore X^0 should be constant under the condition of saturation with respect to DCPD. The values of X^0 and its dispersion, given at the foot of each table, were computed after the final cycle, with K_s replacing K_{DC} in eq (6).

4.4. Equilibrium Constants

In table 12 are assembled the parameters A_{mk} of eq (16) and the sets of values of K_s, K_x, and K_y, and their respective errors at each of the four temperatures. (The standard deviation is discussed in section 5a.) The values obtained using the D.-H. and the Davies activity coefficients are both shown. The differences in the values so obtained persists in a uniform manner from one temperature to another. Values of K_s, K_x, and K_y, given by eq (16), are plotted in figure 2; their standard errors are indicated at the four experimental temperatures. The presence of a minimum in K_x is in agreement with the behavior observed in many other weak electrolytes; usually they exhibit ionization maxima in the region 0 to 60 °C and it has been suggested [15] that this is a property of all weak electrolytes. It is noteworthy that such a maximum (minimum for association) has been reported [16] for the second ionization constant of phosphoric acid. Furthermore, the maximum in K_s can be antici-

TABLE 10. *Concentrations of ion pairs and bound calcium at 25 °C*

Debye-Hückel			Davies		
pH	Y^+, $M \times 10^3$	100 τ/Ca	pH	Y^+, $M \times 10^3$	100 τ/Ca
7.58_4	0.0006	8.76	7.58_3	0.0004	8.96
6.76_8	.0037	6.83	6.76_7	.0025	6.89
6.32_5	.0104	5.35	6.32_4	.0069	5.26
5.55_8	.0631	3.99	5.55_8	.0405	3.47
5.17_9	.154	4.25	5.18_1	.0964	3.41
4.69_0	.496	5.68	4.69_4	.297	4.21
4.20_4	1.59	8.48	4.20_9	.905	6.05
3.61_3	6.70	14.4	3.60_8	4.75	10.2
$X^0 = 0.0652 \pm 0.0080$			$X^0 = 0.0669 \pm 0.0081$		

TABLE 11. *Concentrations of ion pairs and bound calcium calculated with D.-H. activity coefficients* [a]

5 °C			15 °C			37.5 °C		
pH	Y^+, $M \times 10^3$	100 τ/Ca	pH	Y^+, $M \times 10^3$	100 τ/Ca	pH	Y^+, $M \times 10^3$	100 τ/Ca
7.66_1	0.0010	14.0	7.63_6	0.0007	9.34	6.73_7	0.0032	9.72
6.84_4	.0069	11.1	6.79_5	.0049	7.31	6.29_7	.0088	7.39
6.39_1	.0197	8.80	6.35_9	.0134	5.85	6.29_2	.0089	7.36
5.62_7	.118	7.00	5.60_0	.0792	4.67	5.13_1	.137	4.46
5.25_1	.285	7.68	5.22_4	.193	5.16	5.12_8	.138	4.46
4.75_1	.937	10.5	5.20_3	.203	5.22	4.62_1	.462	5.45
4.72_6	.995	10.7	4.70_9	.658	7.22	4.14_2	1.46	7.78
4.27_6	2.92	15.4	4.23_6	2.05	10.8	4.14_0	1.47	7.79
3.70_3	11.7	24.9	3.65_0	8.49	18.0	3.56_3	5.97	12.8
$X^\circ = 0.104 \pm 0.010$			$X^\circ = 0.0690 \pm 0.0079$			$X^\circ = 0.0954 \pm 0.0153$		

[a] The values are not comparable across the table due to differences in initial H_3PO_4 concentrations.

TABLE 12. *Temperature dependence of equilibrium constants*

$$\ln K_m = \sum_{k=1}^{k=3} A_{mk}\, T^{-2+k} \quad \text{[eq (16)]}$$

	Debye-Hückel				Davies			
	A_{mk}				A_{mk}			
m \ k	1	2	3		1	2	3	
1(s)	−8403.5	41.863	−0.096779		−9418.4	48.746	−0.10848	
2(x)	51090	−341.14	.58804		54735	−365.90	.63022	
3(y)	19373	−122.81	.19943		31465	−202.88	.33085	
K_m \ °C	5	15	25	37.5	5	15	25	37.5
$K_s \times 10^7$	$2.33_8 \pm 0.058$	$2.53_5 \pm 0.044$	$2.56_1 \pm 0.048$	$2.37_5 \pm 0.057$	$2.28_9 \pm 0.058$	$2.50_5 \pm 0.044$	$2.53_4 \pm 0.048$	$2.32_8 \pm 0.057$
K_x	446 ± 54	272 ± 35	255 ± 35	401 ± 71	479 ± 57	283 ± 36	264 ± 36	431 ± 74
K_y	10.1 ± 1.7	6.62 ± 1.23	5.10 ± 1.03	4.51 ± 1.44	9.69 ± 1.83	5.23 ± 1.29	3.67 ± 0.98	3.28 ± 1.48

pated, as shown in section 5a, on the basis of the thermodynamic properties of DCPD itself.

4.5. Thermodynamic Quantities

The results of the thermodynamic computations are given in table 13. The values of the thermodynamic functions were calculated from eq (16) and the following equations:

$$\Delta G^0 = -RT \ln K_m = -R(A_{m_1} + A_{m_2}T + A_{m_3}T^2), \quad (27)$$

$$\Delta S^0 = -(\partial \Delta G^0/\partial T) = R(A_{m_2} + 2A_{m_3}T), \quad (28)$$

$$\Delta H^0 = \Delta G^0 + T\Delta S^0 = R(-A_{m_1} + A_{m_3}T^2), \quad (29)$$

where R is the gas constant. For DCPD ($m=1$) the functions refer to the dissolution of 1 mole of $CaHPO_4 \cdot 2H_2O$ according to the reaction

$$CaHPO_4 \cdot 2H_2O = Ca^{++} + HPO_4^{=} + 2H_2O. \quad (30)$$

In the case of the ion pairs, $[CaHPO_4^0]$ ($m=2$) and $[CaH_2PO_4^+]$ ($m=3$), each function applies to the formation of 1 mole of the ion pair from its constituent calcium and ortho-phosphate ions. The errors were computed by use of the appropriate moment matrix of the A_{mk}, eq (23), and the derivatives of eqs (27–29). Whereas the errors for the quantities associated with the dissolution of DCPD, and formation of $[CaHPO_4^0]$ are within acceptable limits, this is not the case for those related to the formation of $[CaH_2PO_4^+]$.

The negative values of ΔS^0 for formation of the ion pairs at the lower temperatures are atypical. It would be desirable to check these values by another experimental method. On the other hand, the value of ΔS^0_{25}, -31.5 ± 0.8 cal/mol.deg, for eq (30) is in satisfactory agreement with the value -32.56 calculated from the S^0 (DCPD) [21] and the entropies [22][2] of the products in that equation.

[2] The revised value of −12.7 cal/mol deg for S^0_{298} (Ca^{++}) was supplied by Dr. V. B. Parker, Thermochemistry Section, NBS.

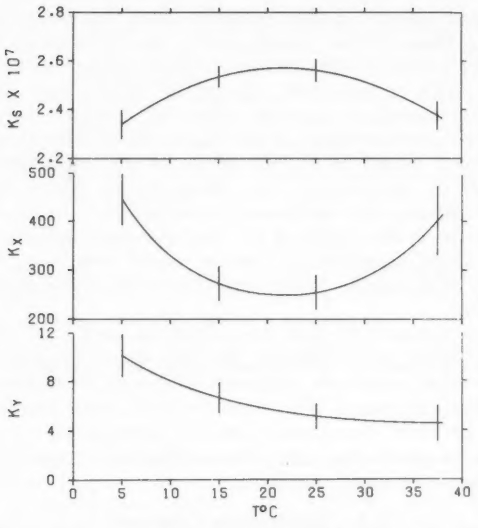

FIGURE 2. *Temperature dependence (eq (16)) of the solubility product of DCPD and the stability constants for ion pairs.*

Length of vertical lines at the four experimental temperatures corresponds to twice the standard errors.

It may be observed that the thermodynamic values appear to be relatively insensitive to the choice of activity-coefficient expression, and that the two sets of values differ by less than their errors. (The errors are approximately the same for the two sets.) By way of contrast, the large temperature dependence of the equilibrium constants produces marked variations in ΔH^0 and ΔS^0; this is so for the values pertaining to the dissolution process even though the temperature coefficient of K_s is relatively small. It is clear that a high degree of confidence in the results can be attained only by measurements made at short temperature intervals and extended over the widest practical temperature range. Thus, measurements on DCPD at other temperatures are highly desirable.

5. Discussion

5.1. Solubility isotherms

The measurements reported in this paper were made on solutions that had reached equilibrium with respect to DCPD from undersaturation; the experimental design was selected on the basis of previous experience [1, 2] to assure attainment of equilibrium conditions. The consistency of the data, the smoothness of the experimental plots, and the success of the adjustment procedure in the calculation of a solubility product constant applicable to all the systems (over a wide range of solution compositions) constitute further evidence that a true equilibrium was attained in the experiments reported here. The adjustment of the data yields points which lie on the calculated isotherms at the several temperatures (fig. 1), and it may be seen from tables 2–9 that the only residuals that exceed 2 percent of the observed value are those of calcium, one at 25 and two at 37.5 °C. Furthermore, the residuals of positive sign constitute approximately half of the total at each temperature.

TABLE 13. *Thermodynamic quantities*

	Dissolution of DCPD			Formation of $[CaHPO_4^0]$			Formation of $[CaH_2PO_4^+]$		
t °C	ΔG° kJ/mol	ΔH° kJ/mol	ΔS° J/mol.K	ΔG° kJ/mol	ΔH° kJ/mol	ΔS° J/mol.K	ΔG° kJ/mol	ΔH° kJ/mol	ΔS° J/mol.K
5	[a]35.3±0.04	7.6±2.5	−99.6±8.8	−14.1±0.3	−46±15	−117±54	−5.4±0.4	−33±22	−100±79
	[b]35.3	8.5	−96.6	−14.3	−50	−125	−5.3	−50	−155
15	36.4±0.04	3.0±1.2	−115±4	−13.4±0.3	−19±7	−19±24	−4.5±0.5	−23±10	−67±34
	36.4	3.4	−115	−13.5	−20	−23	−4.0	−33	−100
25	37.6±0.04	−1.7±1.0	−132±3	−13.7±0.3	10±7	79±23	−4.1±0.5	−14±12	−32±40
	37.7	−1.9	−133	−13.8	11	84	−3.2	−17	−46
37.5	39.4±0.04	−7.8±2.6	−152±9	−15.5±0.5	46±19	201±63	−3.9±0.8	−1±30	9±100
	39.4	−8.7	−155	−15.7	50	213	−3.0	4	23

[a] D.-H. activity coefficients. [b] Davies activity coefficients.

The discrepancy at low pH values between the data at 25 °C and the isotherm computed for that temperature can be attributed to the difference between two estimates of the value of K_y. The adjustment of these data alone (Case I, sec. 3.5b) resulted in values for K_s, K_x, and K_y of 2.59×10^{-7}, 244, and 8.2, respectively. Isotherms computed with these values, and with the values reported for K_s and K_x (table 12) but with 8.2 for K_y, both fitted the data in a satisfactory manner. Nevertheless, we have elected to accept the lower estimate (5.1) of the value of K_y for the sake of increased confidence in the values of K_s and K_x resulting from the adjustment of the combined data.

Thus, the curves in figure 1 constitute solubility isotherms for DCPD at the indicated temperatures; they represent solutions metastable with respect to $CaHPO_4$ [14] over all the experimental range, and with respect to hydroxyapatite [1], β-tricalcium phosphate [17], and octacalcium phosphate [18] in parts of that range. Metastability, however, does not preclude the application of thermodynamic concepts to these systems so long as precipitation of more insoluble calcium phosphates is impossible to detect during the time of the experiment. In this connection, if more basic calcium phosphates had precipitated, the apparent $Ca:(P-P_0)$ ratio for the dissolution reaction would be significantly less than unity; the ratios reported here do not depart significantly from unity. For example, at 25 °C, table 4, the dissolution ratios may be weighted by propagation on the quantity $Ca/(P-P_0)$. The weighted average ratio obtained is 1.0067 with standard error of the mean 0.0087. With 7 degrees of freedom, the excess over unity of the average ratio would have to exceed 0.020 to be significant at the 95 percent confidence level. Similar conclusions can be drawn from the data at other temperatures. Furthermore, with one exception [1], petrographic examination of the solid phase after the saturated solution was obtained failed to show any solid other than DCPD.

Effect of Temperature on the Solubility of DCPD. Examination of the curves in figure 1 leads to the tentative conclusion that the solubility of DCPD varies inversely with temperature. However, since the observed solubility differences are very small, it was considered desirable to ascertain the significance of these differences by the following statistical procedure. The isotherms in figure 1 were generated, using the constants K_x, K_y, and K_s as found by the adjustment procedure (D.-H. activity coefficients), by solving the electroneutrality eq (14) for calcium concentrations corresponding to a selected set of pH values. The value for total phosphorus used in this equation, as well as the derivatives of calcium with respect to the three equilibrium constants, were obtained from the saturation condition, eq (13). The variance of calcium was calculated at each pH by use of the derivatives and the covariance matrix, eq (24), of the constants as given by the adjustment. For two temperatures, $T_1 < T_2$, $Ca(T_1)$ was compared with $Ca(T_2)$ at the 95 percent level by direct computation of critical values [19].

The results indicated, with one exception, that throughout the larger part (4.0–6.4) of the experimental pH range, the solubility of DCPD decreased significantly with increase in temperature. The exception to this statement is that there was no significant difference between the solubility at 15 and at 25 °C. The resulting plateau can be related to the variation of the equilibrium constants with temperature shown in figure 2. Between 5 °C and a temperature near 25 °C, the decrease in K_x should tend to depress the solubility of DCPD, whereas from that temperature up to 37 °C the reverse effect would be expected. The temperature variation of K_s clearly should have the opposite effects on the solubility over the range 5 to 37 °C. Thus, in the region where the extrema in the curves occur, a decreasing rate of change of solubility with temperature should be anticipated. The results, therefore, indicate that the decrease in the relative concentration of ion pairs (tables 10–11) is a dominant factor in the decrease of the solubility of DCPD in the region 5 to about 25 °C. Above this temperature, the dominant factor appears to be the decrease in the value of K_s. The decrease in K_y over the whole temperature range would reinforce the effect of K_x in the lower, and that of K_s in the upper, region.

It is noteworthy that the anhydrous salt [14] does not display any solubility plateau, which possibly is due to the monotonic decrease of K_s with temperature for that compound. The variation of K_s with temperature for both compounds can be anticipated on the basis of their respective thermodynamic properties, as discussed in section 5.2a.

5.2. Equilibrium Constants

a. Dependence Upon Conditions and Hypotheses

The solubility product constant, K_s, obtained by the adjustment procedure is a least-squares estimate and is thus associated with a minimum sum of squares, i.e., eq (A–15). With a given set of data, however, the actual value of q^2 at the minimum, as well as the value of K_s itself, depend upon the condition functions that are satisfied by the systems and upon the hypothesis of ion pairs. This is illustrated in table 14. Because the number of condition functions and parameters vary across the columns of the table, the results are best compared by reference to the sixth line, which gives the standard deviation of the adjustment, eq. (22).

It is clear from the table that the use of three condition functions has definite advantages over the use of only one condition function, whether ion-pairs are considered or not. Furthermore, it is evident that the minimum value of the standard deviation is obtained by the use of three condition functions with the hypothesis of ion pairs present. Thus, the best set of values for K_s, K_x, and K_y are those obtained with the use of three condition functions. The argument for the presence of ion pairs is strengthened by this comparison. In a previous publication [1] we reported a set of values for K_s, K_x, and K_y at 37.5 °C which differ from those reported here. Although the present calculations are based on a larger sample of data, these differences are primarily due to the method of calculation. The criteria used in our earlier work [1] were valid but the procedure to establish an unequivocal minimum in the standard variance was not fully adequate. Treatment of the previously published data [1] by the adjustment procedure of the present paper yielded results in agreement with the values reported in table 12.

b. Temperature Dependence of K_s

The appearance of a maximum in the K_s of DCPD in the neighborhood of 25 °C, as shown in figure 2, de-

TABLE 14. *Effect of the number of condition functions and the ion pair hypothesis on the estimates of the standard deviation and the equilibrium constants*

Function(s) [a]	1		1 + 2		1 + 2 + 3	
Case [b]	II–A	III–A	II–B	III–B	II–C	III–C
Ion pairs	Absent	Present	Absent	Present	Absent	Present
Degrees of freedom	32	26	67	61	102	96
$q^2 \times 10^{16}$, eq (A–15)	139	57.1	182	78.8	322	107
$s \times 10^8$, eq (22)	2.08 ± 0.26	1.48 ± 0.21	1.65 ± 0.14	1.14 ± 0.10	1.78 ± 0.12	1.06 ± 0.08
$K_s \times 10^7$, 25 °C	2.85 ± .05	2.59 ± .09	2.84 ± .04	2.52 ± .07	2.85 ± .04	2.56 ± .05
K_x, 25 °C		237 ± 77		297 ± 60		255 ± 35
K_y, 25 °C		4.8 ± 1.7		6.0 ± 1.4		5.1 ± 1.0

[a] 1-Solubility product, eq (13); 2-Electroneutrality, eq (14); 3-congruent dissolution, eq (15).
[b] Cases as given in the tabulation of sec. 3.5.3.

serves special consideration, particularly since such a maximum does not appear [14] in the solubility product of the closely related compound [3] $CaHPO_4$. It is shown below that this behavior is a possible consequence of the thermodynamic properties of the respective solids.

The van Hoff's equation provides an expression for the temperature coefficient of K_s. If the enthalpy of solution, ΔH_d^0, for reaction (30) can be given explicitly as a function of temperature, then the temperature at which K_s has a maximum, if any, may be obtained as a root of that equation. The enthalpy of solution is given by

$$\Delta H_d^0 = \Delta H_0^0 + \int \Delta C_p dT. \qquad (31)$$

The change in the heat capacity can be obtained as a function of temperature with the aid of some reasonable approximations. Furthermore, since ΔH_d^0 can be calculated at 25 °C from the corresponding value of K_s, the entropy of DCPD [21], and tabulated thermodynamic quantities [22] for the products of reaction (30), the constant ΔH_0^0 in eq (31) can be evaluated. In the present calculations using the value of K_s at 25 °C given in table 12, a value for ΔH_d^0 of −0.73 Kcal mol^{-1} is obtained.

The heat capacity for Ca^{++} (aq) was roughly estimated to be −6 cal mol^{-1}.[4] We assumed that the heat capacity for $HPO_4^=$ (aq) does not differ appreciably from the isoelectronic species $SO_4^=$ [23]. The additional assumption was made that the heat capacities of water and the aqueous ions did not change with temperature over the range considered. The temperature dependence of the heat capacity, Cp, of crystalline DCPD (and that for $CaHPO_4$) was obtained by a least squares fitting of an equation of standard form to the data of Egan and Wakefield [21, 24],[5] with the results (cal mol^{-1})

$$Cp(\text{DCPD}) = 7.582 + 0.1361T - 2.217 \times 10^4 T^{-2}, \quad (50\text{–}310\ \text{K});$$

$$Cp(\text{DCPA}) = 10.590 + 0.05579T - 4.896 \times 10^4 T^{-2}, \quad (80\text{–}310\ \text{K}).$$

In eq (31) for DCPD, ΔCp can thus be replaced by the expression

$$\Delta Cp = -47.58 - 0.136T + 2.217 \times 10^4 T^{-2}$$

and ΔH_0^0 is then found to be 19.58 Kcal mol^{-1}. Then the van Hoff's equation takes the form

$$R \frac{\partial}{\partial T} \ln K_s(\text{DCPD}) = -\frac{22.2}{T^3} + \frac{19.6}{T^2} - \frac{0.0476}{T} - 6.81 \times 10^{-5}.$$

The pertinent root of this equation corresponds to a maximum at 17 °C, which is in satisfactory agreement with the plot in figure 2. A variation of ± 10 percent in the assumed value for the $Cp(HPO_4^=)$ and the use of −9 cal mol^{-1} for $Cp(Ca^{++})$ did not affect this result significantly.

Similar calculations for DCPA indicated a maximum in K_s, far below the experimental range (i.e., ca −22 °C); although this finding is not physically meaningful, it is consistent with the observed [14] monotonic decrease in K_s for this compound in the range 5 to 37 °C.

In view of the approximations and assumptions used in the calculations, only the qualitative aspects of these results are to be emphasized. They show that the presence of a maximum in the K_s of DCPD, which contrasts with the monotonic decrease in that of DCPA, is consistent with the results of calculations based on the known thermodynamic properties of these compounds.

c. Association Constants and Bjerrum's Theory

The relationship of the association constant and the distance, a, between the constituent ions in an ion pair was derived by Bjerrum [25] on the basis of Coulombic forces

[3] It may be pointed out that the salt $CaSO_4 \cdot 2H_2O$, which is isostructural with DCPD, does show a maximum in its solubility near 15 °C [20], although it can not be inferred from this that a maximum exists in its solubility product.

[4] Values of the necessary partial molar heat capacities at infinite dilution (cal mol^{-1}) are (1) for Cl^-, −32.6 [22]; (2) for $CaCl_2$, −71, kindly estimated by Dr. Vivian B. Parker of the National Bureau of Standards, Thermochemistry Section, by a rough extrapolation from the available data. A check on the value of −6 for Ca^{++} derived in this way was obtained by using the value −74.4 for $BaCl_2$ given in table (8–4–3) of reference [26]; a value of −9 was estimated in this way.

[5] Only "normal" points in reference [24] included.

$$K_{\text{assoc.}} = \frac{4\pi N}{1000}\left[\frac{|z_1 z_2|\epsilon^2}{DkT}\right]^3 Q(b), \qquad (32)$$

with

$$b = \frac{|z_1 z_2|\epsilon^2}{aDkT}.$$

Values for the function $Q(b)$ have been calculated by various investigators and summarized by Harned and Owen [26]. The use in eq (32) of the extreme values of the 95 percent confidence interval for K_x(25 °C) and K_y(25 °C) reported here, yielded the ranges 3.8–4.5 Å and 5.9–6.1 Å for the a parameters of $[CaHPO_4^0]$ and $[CaH_2PO_4^+]$, respectively. Larger values of a are expected for $[CaH_2PO_4^+]$ than for $[CaHPO_4^0]$ on the basis of the valences of the constituent ions in the two ion pairs.

Considering the interatomic distances usually found in calcium phosphates [27] and assuming sharing of the PO_4-tetrahedron edge by the calcium, the distance between the phosphorous and calcium atoms would be in the order of 3 Å. The apparent consistency between this result and the a values calculated above should be taken cautiously because if the two ions were indeed that close, polarization effects, not considered in equation (32), would undoubtedly play a role. It is pertinent to point out that in the investigation by Dunsmore and James [28] on the dissociation of $[MgSO_4^0]$ (isoelectronic with $[CaHPO_4^0]$), the results of their conductivity measurements could be explained on the basis of eq (32), and were consistent with a value of 5.1 Å for a.

5.3. Comparison With Reported Data

Greenwald et al. [29] studied the formation of the ion pair $[CaHPO_4^0]$ in mixtures containing H_3PO_4, NaOH, and $CaCl_2$. From their pH measurements with a glass electrode (presumably at 25 °C) and also with a hydrogen electrode at 25 °C they calculated instability constants at various ionic strengths; in their calculations, ionic concentrations were used instead of activities. The equation used by Greenwald et al. [29], to describe the dependence of their values on ionic strength yields a stability constant $K_x = 316$ for infinite dilution, in reasonable agreement with the value K_x(25 °C) = 255 reported here.

Davies and Hoyle [30] reported instability constants at 25 °C for systems containing sodium and potassium phosphate buffers saturated with respect to $CaIO_3$; their pH measurements were made colorimetrically. The range of values obtained by Davies and Hoyle, K_x(25 °C) = 417 to 625 and K_y(25 °C) = 11.5 to 12.5, agree in order of magnitude with those reported here.

Greenwald [31] used the measurements reported by Bjerrum [32] in the dilute range of the homogeneous system $Ca(OH)_2$—H_3PO_4—H_2O at 18 °C to calculate values for the instability constant of $[CaHPO_4^0]$; these varied from 1.01 to 9.55×10^{-3}. The average value, 2.77×10^{-3}, yields a K_x(18 °C) = $1/(2.77 \times 10^{-3})$ = 361, agreeing in order of magnitude with the value reported here at 15 °C. Greenwald [31] also recalculated the value of K_x from the data of Davies and Hoyle [30]; for this purpose, he calculated the pH from the experimental buffer ratios; his values for K_x thus obtained covered the range from 56 to 100. As in previous reports by the same author [29, 33], ionic concentrations instead of activities were used in these calculations. Therefore, only order of magnitude agreement with the values reported here is significant.

Similar rough agreement is found with the result of Gosselin and Coghlan [34], K_x(25 °C) = 72, who also used ionic concentrations instead of activities in their calculations.

Recently, Chughtai et al. [35] have reported stability constants for the species $[CaH_2PO_4^+]$, $[CaHPO_4^0]$, and $[CaPO_4^-]$ calculated from pH measurements in the system KOH—NaOH—H_3PO_4—$CaCl_2$—H_2O. By working in a low pH region (where the concentrations of the neutral and negatively charged species are negligible) those investigators calculated K_y(25 °C) = 25.6; this value was then used in systems at higher pH values to calculate K_x(25 °C) = 548; reported values at 37 °C were K_y(37 °C) = 31.9 and K_x(37 °C) = 681.

In the calculations of Chughtai et al. [35], the equation describing the condition of electrical neutrality was solved algebraically with the measured concentrations and pH values considered exempt of error. Calculations based on perfect compliance of the data to the electroneutrality condition are extremely sensitive to small experimental errors; this was an important factor in the adoption of the statistical procedure reported in this paper. Furthermore, by the procedure of Chughtai et al. [35], the two constants are obtained as ostensibly independent quantities, whereas in fact, a strong correlation should be expected.

The use in eq (32) of the values for K_x and K_y at 25 °C reported by Chughtai et al. yields values of 3.1Å and 2.3Å for the interionic distance parameters for $[CaHPO_4^0]$ and $[CaH_2PO_4^+]$, respectively. This is an unreasonable result in view of the crystallographic radii of the ions involved [27], and, furthermore, contradicts the expectation $a[CaH_2PO_4^+] > a[CaHPO_4^0]$ (sec. 5.2c).

6. Appendix

6.1. Generalized Least Squares for Independent Systems

In this paper attention is focused on individual systems and this is reflected in the notation of table 1 by the use of the superscript α to denote the αth system. Apart from this feature, our notation differs from that of reference [4] in the following respects: (1) n and r designate here the number of components in the αth observation and condition function vector, respectively, with $\alpha = 1, \ldots, N$; in table [11.3.3], n and r refer to the total of such components for N systems. (2) The correction vector θ with components ϑ_ν replaces $-b$. (3) The vector of adjustable constants (parameters) is here denoted by β with initial values β^0. The definitions of reference [4] are inconsistent. The

equation $b_j = b_j^0 + b_j'$, following [11.3, 1], uses b_j and b_j^0 like β_ν and β_ν^0, with $-b_j = \vartheta_\nu$. Elsewhere b^0 is consistently used like β^0, but b appears in table [11.3.3] and subsequent equations as the correction vector. (4) The matrices J^α and F^α are the transposes of submatrices of J and F. Transposed matrices are indicated by the tilde.

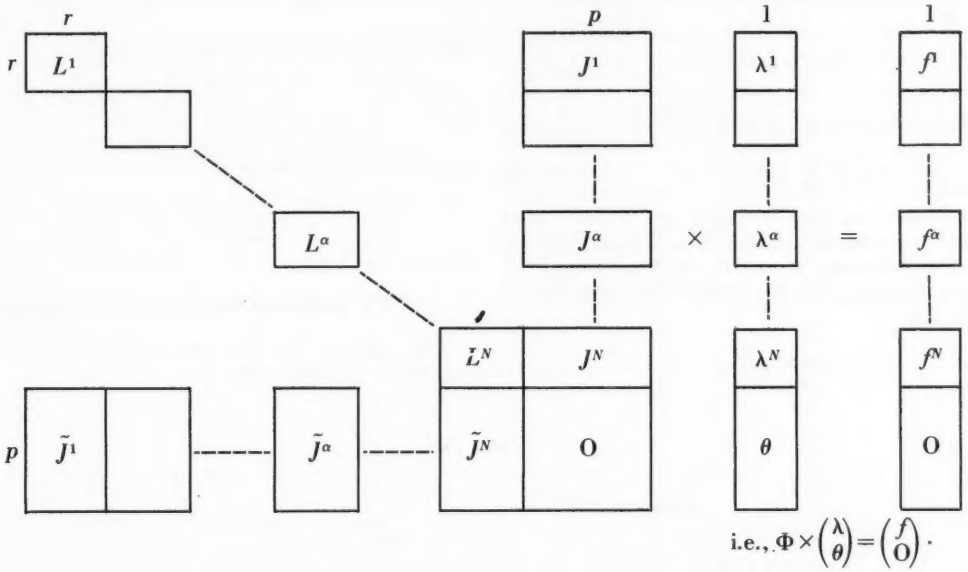

The matrix Φ is readily inverted by the method of submatrices [36] with the result

$$\Phi^{-1} = \chi = \begin{pmatrix} [\chi^{\alpha\beta}] & [\chi^{\alpha p}] \\ [\chi^{p\alpha}] & -C^{-1} \end{pmatrix}, \qquad \text{(A–1)}$$

where

$$\chi^{\alpha\beta} = L^{\alpha^{-1}}\delta_{\alpha\beta} - L^{\alpha^{-1}} J^\alpha C^{-1} \tilde{J}^\beta L^{\beta^{-1}}, \qquad \text{(A–2)}$$

$$\chi^{p\alpha} = C^{-1}\tilde{J}^\alpha L^{\alpha^{-1}}, \qquad \text{(A–3)}$$

and C is defined by eq (18). In eq (A–2) $\delta_{\alpha\beta}$ is the Kronecker delta. Since the submatrices of χ^{rr} and χ^{pr} are $\chi^{\alpha\beta}$ and $\chi^{p\alpha}$, respectively, solutions analogous to [11.3.3.1, 1c] may be written as linear combinations of the multivariate vectors f^α:

$$\lambda^\alpha = \Sigma_\beta \chi^{\alpha\beta} f^\beta, \qquad \text{(A–4)}$$

and

$$\theta = \Sigma_\beta \chi^{p\beta} f^\beta. \qquad \text{(A–5)}$$

The last equation, by virtue of the definition (A–3), is just the solution of the reduced normal equations, eq (17).

a. Solution of the General Normal Equations

In order to determine the specific covariance matrices needed in these calculations it is necessary to identify the submatrices of χ, [11.3.3, 2]. The system of eqs [11.3.3.1, 1a] adapted to the analysis used in this paper can be exhibited in diagrammatic form as follows:

b. Covariance Matrices

Observations. The observations Y_i^α are independent for all α and i, and therefore

$$\mathscr{E}(\delta Y_i^\alpha \delta Y_j^\alpha) = s^2 w_{ii}^{\alpha^{-1}} \delta_{ij},$$

and

$$\text{Cov}\ (y^\alpha, y^\beta) = \mathscr{E}(\delta y^\alpha \tilde{\delta} y^\beta) = s^2 W^{\alpha^{-1}} \delta_{\alpha\beta}. \qquad \text{(A–6)}$$

Conditions functions. The analogue of [11.3.3.1, 5b] for a pair of vectors is

$$\text{Cov}\ (f^\alpha, f^\beta) = s^2 F^\alpha W^{\alpha^{-1}} \tilde{F}^\beta \delta_{\alpha\beta} = s^2 L^\alpha \delta_{\alpha\beta}. \qquad \text{(A–7)}$$

Other covariance matrices. The following are submatrices of the indicated covariance matrices derived in [4]:

(1) Lagrangians [11.3.4, 2a]

$$\text{Cov}(\lambda^\alpha, \lambda^\beta) = s^2 \chi^{\alpha\beta}. \qquad \text{(A–8)}$$

(2) Residuals [11.3.4.1, 2a]

$$\text{Cov}(V^\alpha, V^\beta) = s^2 W^{\alpha^{-1}} \tilde{F}^\alpha \chi^{\alpha\beta} F^\beta W^{\beta^{-1}}. \qquad \text{(A–9)}$$

(3) Adjusted observations [11.3.4.2, 3b]

$$\mathrm{Cov}(U^\alpha, U^\beta) = s^2 W^{\alpha -1}\delta_{\alpha\beta} - \mathrm{Cov}(V^\alpha, V^\beta) = s^2\omega^{\alpha\beta}. \tag{A-10}$$

c. Residuals and Sum of Squares

The individual residuals vectors are subvectors of [11.3.4.1, 1]:

$$V^\alpha = W^{\alpha -1}\tilde{F}^\alpha\lambda^\alpha \tag{A-11}$$

and the weighted sum of squares is

$$q^2 = \sum_\alpha \tilde{V}^\alpha W^\alpha V^\alpha. \tag{A-12}$$

This expression can be converted into a form more convenient for testing for convergence as follows: With the substitution of eq (A-11) for V^α and the subsequent identification $L^\alpha = F^\alpha W^{\alpha -1}\tilde{F}^\alpha$ by eq (A-7), (A-12) becomes

$$q^2 = \sum_\alpha \tilde{\lambda}^\alpha L^\alpha \lambda^\alpha. \tag{A-13}$$

Now, with the aid of (A-2), (A-3) and (A-5), (A-4) for λ^α can be converted into

$$\lambda^\alpha = L^{\alpha -1}(f^\alpha - J^\alpha\theta). \tag{A-14}$$

With the substitution of (A-14) into (A-13) we get

$$q^2 = \sum_\alpha (\tilde{f}^\alpha - \tilde{\theta}\tilde{J}^\alpha)L^{\alpha -1}(f^\alpha - J^\alpha\theta);$$

carrying out the multiplication and using

$$C\theta = \sum_\alpha \tilde{J}^\alpha L^{\alpha -1} f^\alpha,$$

eq (17), the final result is

$$q^2 = \sum_\alpha \tilde{f}^\alpha L^{\alpha -1} f^\alpha - \tilde{\theta}C\theta. \tag{A-15}$$

6.2 Constants Used in the Calculations

The values for the temperature-dependent constants are given in table A1.

TABLE A1

t °C	Phosphoric Acid			Water $10^{14}k_w$[39]	$A(T)$[40]	$B(T)$[40]
	10^2k_1[37]	10^7k_2[16]	$10^{12}k_3^a$			
5	0.845	0.523	0.226	0.1846	0.4952	0.3256
15	.782	.587	.320	0.4505	.5028	.3273
25	.711	.636	.452	1.008	.5115	.3291
37.5	.618	.659	.692	2.485	.5242	.3318

[a] From the equation $pk_3 = 12.45 - (t\,°\mathrm{C} - 18) \times 0.015$ of [38].

The values of the inter-atomic distance parameter a_i used here are listed in table A2.

TABLE A2

	$H_2PO_4^-$	$HPO_4^=$	$PO_4^{\equiv}$	H^+	OH^-	Ca^{++}
10^8a_i[41]	4	4	4	9	3.5	6

7. References

[1] Moreno, E. C., Gregory, T. M., and Brown, W. E., Nat. Bur. Stand. (U.S.), **70A** (Phys. and Chem.), No. 6, 545–552 (Nov.–Dec. 1966).

[2] Moreno, E. C., Brown, W. E., and Osborn, G., Soil Sci. Soc. Amer. Proc. **24**, 94 (1960).

[3] Deming, W. E., Statistical Adjustment of Data, pp. 49–58 (John Wiley & Sons, Inc., New York, N.Y., 1943). (Reprinted by Dover Publications, New York, N.Y., 1964).

[4] Guest, P. G., Numerical Methods of Curve Fitting, pp. 370–381 (Cambridge University Press, Cambridge, England, 1961).

[5] Wentworth, W. E., Hirsch, W., and Chen. E., J. Phys. Chem. **71**, 218 (1967).

[6] Izatt, R. M., Eatough, D., Snow, R. L., and Christensen, J. J., J. Phys. Chem. **72**, 1208 (1968).

[7] Moreno, E. C., Gregory, T. M., and Brown, W. E., Nat. Bur. Stand. (U.S.), **72A**, (Phys. and Chem.), No. 6, 773–782 (Nov.–Dec. 1968).

[8] Patel, P. R., Moreno, E. C., and Gregory, T. M., Nat. Bur. Stand. (U.S.), **73A** (Phys. and Chem.), No. 1, 43–49 (Jan.–Feb. 1969).

[9] Brabson, J. A., Dunn, R. L., Epps, E. A., Jr., Hoffman, W. M., and Jacob, K. D., J.A.O.A.C. **41**, 517 (1958).

[10] Bates, R. G., Nat. Bur. Stand. (U.S.), **66A** (Phys. and Chem.), No. 2, 179–184 (Mar.–Apr. 1962).

[11] Davies, C. W., Ion Association (Butterworth & Co. Ltd., London, England, 1962).

[12] Deming, W. E., Phil. Mag. **11**, 146 (1931).

[13] Arley, N., and Buch, K. R., Introduction to the Theory of Probability and Statistics, Ch. 12 (John Wiley & Sons, Inc., New York, N.Y. 1950).
[14] McDowell, H., Ph. D. Thesis, Howard University, Washington, D.C. (1967).
[15] Harned, H. S. and Embree, N. D., J. Am. Chem. Soc., **56,** 1050 (1934).
[16] Bates, R. G., and Acree, S. F., J. Res. NBS **34,** 373 (1945) RP1648.
[17] Moreno, E. C. and Brown, W. E. (Abstract), Internat. Assoc. Dental Res., 46th General Meeting, San Francisco, Calif. (1968).
[18] Moreno, E. C., Brown, W. E., and Osborn, G., Soil Sci. Soc. Amer. Proc. **24,** 99 (1960).
[19] Aspin, A. A., Biometrika **35,** 88 (1948). See also, Welch, B. L., Ibid **34,** 28 (1947).
[20] Kelley, K. K., Southard, J. C., and Anderson, C. T., U.S. Bureau of Mines, Tech. Paper No. 625, p. 55, (1941).
[21] Egan, E. P., and Wakefield, Z. T., J. Chem. Engin. Data **9,** 544 (1964).
[22] Nat. Bur. Stand. (U.S.), Tech. Note 270–3, 267 pages (Jan. 1968).
[23] Nat. Bur. Stand. (U.S.), Circ. 500 (1952).
[24] Egan, E. P., and Wakefield, Z. T., J. Chem. Engin. Data, **9,** 541 (1964).
[25] Bjerrum, N., Kgl. Danske Vidensk. Selskab. (Mat.-Fys.) **7,** No. 9 (1926).
[26] Harned, H. S., and Owen, B. B., The Physical Chemistry of Electrolytic Solutions, p. 171 (Reinhold Publishing Corp., 3d ed., New York, N.Y., 1958).
[27] Kay, M. I., Young, R. A., and Posner, A. S., Nature **204,** 1050 (1964).
[28] Dunsmore, H. S., and James, J. C., J. Chem. Soc. 2925 (1951).
[29] Greenwald, I., Redish, J., and Kibrick. A. C., J. Biol. Chem. **135,** 65 (1940).
[30] Davies, C. W., and Hoyle, B. E., J. Chem. Soc. 4134 (1953).
[31] Greenwald, I., J. Phys. Chem. **67,** 2853 (1963).
[32] Bjerrum, N., Kgl. Danske Vidensk. Selskab. (Mat.-Fys.) **31,** No. 7 (1958).
[33] Greenwald, I., J. Biol. Chem. **161,** 697 (1945).
[34] Gosselin, R. E., and Coghlan, Arch. Biochem. and Biophys. **45,** 301 (1953).
[35] Chughtai, A., Marshall, R., and Nancollas, G. H., J. Phys. Chem. **72,** 208 (1968).
[36] Frazer, R. A., Duncan, W. J., and Collar, A. R., Elementary Matrices, p. 112 (Macmillan Co., New York, N.Y., 1947).
[37] Bates, R. G., J. Res. NBS **47,** 127 (1951) RP2236.
[38] Bjerrum, N., and Unmack, A., Kgl, Danske Vidensk. Selskab. (Mat.-Fys.) **9,** 5–206 (1929).
[39] Ref. [26], p. 645, equation 15–3–7a.
[40] Bates, Roger G., Determination of pH, Theory and Practice, p. 406 (John Wiley & Sons, Inc., New York, N.Y., 1964).
[41] Kielland, J., J. Am. Chem. Soc. **59,** 1675 (1937).

(Paper 74A4–612)

JOURNAL OF RESEARCH of the National Bureau of Standards—A. Physics and Chemistry
Vol. 74A, No. 4, July–August 1970

Effect of Oxide Additions on the Polymorphism of Tantalum Pentoxide

II. "Stabilization" of the High Temperature Structure Type

R. S. Roth, J. L. Waring, and W. S. Brower

Institute for Materials Research, National Bureau of Standards, Washington, D.C. 20234

(March 12, 1970)

The high temperature, apparently tetragonal, polymorph of tantalum pentoxide can be obtained at room temperature by quenching a specimen containing 2–5 mole percent of the following oxides: SnO_2, Ga_2O_3, Cr_2O_3, Fe_2O_3, Sc_2O_3, or MgO. All the x-ray patterns can be indexed on a body centered tetragonal cell with $a \approx 3.830$ Å, $c \approx 35.68$ Å. However, P_2O_5, V_2O_5, Nb_2O_5, ZrO_2, Lu_2O_3, NiO, or ZnO do not stabilize the tetragonal form at room temperature. Single crystals of scandium "stabilized" Ta_2O_5 have been grown by the Czochralski technique.

Key words: High temperature polymorph; single crystals; stabilization; tantalum oxide.

1. Introduction

Ta_2O_5 is probably the only pure metal oxide stable at high temperature in air (mp ~ 1890 °C) about which little or nothing is known of the crystal structure. The reason for this is that no suitable crystals of pure Ta_2O_5 have been prepared due to the peculiar polymorphic behavior of the material. The polymorphism of Ta_2O_5 has been discussed by several authors [1, 2, 3][1] and fully reviewed by the present authors in a previous publication [4] together with the changes which occurred in the polymorphic behavior with the addition of TiO_2.

The low-temperature form of Ta_2O_5 has an, as yet, unknown structure related to the low-temperature form of Nb_2O_5, as well as to $\alpha-U_3O_8$ and $\alpha-UO_3$. On heating to a temperature of about 1360 °C [2] Ta_2O_5 exhibits an enantiotropic, sluggishly reversible, phase transition to a high-temperature form. This form apparently has a unique structure unlike any other reported compound. When quenched from above the equilibrium phase transition, the apparently tetragonal high-temperature form transforms, through a monoclinic polymorph, to a third metastable polymorph which has an x-ray powder pattern which appears to be triclinic at room temperature [4]. These transformations result in a mechanical disruption of the crystals, making an accurate measurement of the intensities of the x-ray diffraction spots essentially an impossible task. The addition of TiO_2 lowers the equilibrium transition temperature from about 1360 °C to about 1150 to 1200 °C and the metastable tetragonal ⇄ monoclinic transition of the high-temperature form from about 950 °C to as low as 600 °C [4]. However, the quality of the room temperature single crystals is not improved by this addition.

In the present study, oxides other than TiO_2, containing cations of similar size, have been added to Ta_2O_5 in an effort to obtain the high temperature tetragonal modification of Ta_2O_5 at room temperature.

2. Materials

The general quantitative spectrochemical analyses for the Ta_2O_5 used in this study has been previously reported [4]. All other oxides used were of reagent grade or better, as described in previous publications [5, 6, 7, 8, 9]. These other oxides were P_2O_5, V_2O_5, Nb_2O_5, SnO_2, ZrO_2, Ga_2O_3, Cr_2O_3, Fe_2O_3, Sc_2O_3, Lu_2O_3, MgO, NiO, and ZnO.

3. Specimen Preparation and Test Methods

One gram batches of 95 : 5 and 90 : 10 mole ratio compositions of Ta_2O_5 and each of the additional oxides were weighed, mixed in a mechanical shaker for approximately 10 min, and pressed into disks at about 10^4 psi. The disks were placed on Pt setters and calcined in air at appropriate temperatures from 500 to 1200 °C depending on the relative volatility of

[1] Figures in brackets indicate the literature references at the end of this paper.

383-876 O - 70 - 2

the additive, for 6 to 12 hr. Other compositions of interest were prepared in a similar manner. After the preliminary heat treatment portions of the ground specimen were placed in sealed Pt tubes and heated in the quenching furnace at approximately 1325, 1450, and 1600 °C for various periods of time. Some specimens of particular interest were heated at other temperatures.

The sealed tubes containing specimens were quenched into ice water, opened, and examined by x-ray diffraction techniques. A high angle recording Geiger counter-diffractometer and Ni-filtered Cu radiation was used in the study. The Geiger counter traversed the specimen at ¼ deg/min and radiation was recorded on the chart at 1 deg-2θ/in. The unit cell dimensions reported can be considered accurate to about ± 2 in the last decimal place listed.

4. Results and Discussion

The experimental data is shown in table 1 and is interpreted diagramatically as phase equilibria data in figures 1–4. Sufficient data has not been collected to establish the exact nature of the phase equilibria diagrams. Therefore, the system, Ta_2O_5-TiO_2 (redrawn in fig. 1), has been used as a model and the other systems have been drawn in accordance with Ta_2O_5-TiO_2, with the appropriate modifications necessary to fit the limited experimental data. No attempt has been made to delineate the metastable equilibrium relations of the H-Ta_2O_5 solid solution phase transitions as was previously done for Ta_2O_5-TiO_2 [4].

From the results reported for the system Ta_2O_5-TiO_2 [4], it can be concluded that any specimen containing some form of H-Ta_2O_5 solid solution was

TABLE 1. *Experimental data*

System	Composition mol percent	Heat treatment				X-ray diffraction analyses [c]
		Initial [a]		Final [b]		
		Temp. °C	Time hr	Temp. °C	Time hr	
Ta_2O_5-P_2O_5	95 : 5	300	1			
		500	1			
		[d] 1000	10			
				1331	16	$P^{0.5}_{19}O_{25}$(ss) + L-Ta_2O_5 phase(s)
				1457	16	PTa_9O_{25}(ss) + H$_{tri}$-Ta_2O_5
				1585	4.5	PTa_9O_{25}(ss) + H$_{tri}$-Ta_2O_5
	90 : 10	300	1			
		500	1			
		[d] 1000	10			
				1331	16	PTa_9O_{25} + $PTaO_5$ (trace)
				1457	16	PTa_9O_{25} + $PTaO_5$ (trace)
				1585	4	PTa_9O_{25} + $PTaO_5$ (trace)
Ta_2O_5-V_2O_5	95 : 5	1000	10	1333	19	VTa_9O_{25}(ss) + L-Ta_2O_5 phase(s)
				1444	65	VTa_9O_{25}(ss) + H-Ta_2O_5(ss)
				1587	5	H$_{tri}$-Ta_2O_5 + H$_{mon}$-Ta_2O_5
	90 : 10	500	16			
		1000	16			VTa_9O_{25} + unknown phase
				1247	6	VTa_9O_{25}
				1390	16	VTa_9O_{25} + L-Ta_2O_5 phase(s) [e]
				1444	0.667	VTa_9O_{25} + L-Ta_2O_5 phase(s) [e]
				1597	4	H$_{tri}$-Ta_2O_5(ss) + liquid
				1608	3.75	H$_{tri}$-Ta_2O_5(ss) + H$_{mon}$-Ta_2O_5(ss) + liquid
Ta_2O_5-Nb_2O_5	95 : 5	1000	10			
				1333	19	L-Ta_2O_5 phase(s)
				1444	65	H$_{tri}$-Ta_2O_5(ss) + L-Ta_2O_5 phase(s) (trace)
	90 : 10	1000	10	1331	16	L-Ta_2O_5 phase(s)
				1444	65	H$_{tri}$-Ta_2O_5(ss) + L-Ta_2O_5 phase(s) (trace)
Ta_2O_5-SnO_2	99 : 1	1200	10			
				1445	16	H$_{tri}$-Ta_2O_5(ss) + L-Ta_2O_5 phase(s) (trace)
		—		1571	4	H$_{tri}$-Ta_2O_5(ss)
	98 : 2	1200	10			
				1446	16	H$_{tri}$-Ta_2O_5(ss) + H$_{tet}$-Ta_2O_5(ss)
	97 : 3	1200	10			
				1446	16	H$_{tri}$-Ta_2O_5 + H$_{tet}$-Ta_2O_5(ss)
				1571	4	H$_{tri}$-Ta_2O_5 + H$_{tet}$-Ta_2O_5(ss)
	95 : 5	1000	10	1325	16	H$_{tet}$-Ta_2O_5(ss); $a = 3.830$, $c = 35.68$
				1448	16	H$_{tet}$-Ta_2O_5(ss); $a = 3.830$, $c = 35.68$
				1660	2	H$_{tet}$-Ta_2O_5(ss) + H$_{tri}$-Ta_2O_5(ss) [f]
				1769	17	H$_{tet}$-Ta_2O_5(ss) + H$_{tri}$-Ta_2O_5(ss) [f]
		1769	17	1463	65	H$_{tet}$-Ta_2O_5(ss) + H$_{tri}$-Ta_2O_5(ss) [f]

TABLE 1. *Experimental data*—Continued

System	Composition mol percent	Heat treatment				X-ray diffraction analyses [c]
		Initial [a]		Final [b]		
		Temp. °C	Time hr	Temp. °C	Time hr	
	90 : 10	1000	10	1325	16	H_{tet}-Ta_2O_5(ss) + SnO_2(ss)
				1448	16	H_{tet}-Ta_2O_5(ss) + SnO_2(ss)
Ta_2O_5-ZrO_2	95 : 5	1000	10			
				1326	19	L-Ta_2O_5 phase(s)
				1449	19	H_{tri}-Ta_2O_5(ss) + H_{mon}-Ta_2O_5(ss)
				1586	4	H_{tri}-Ta_2O_5(ss) + H_{mon}-Ta_2O_5(ss)
	90 : 10	1000	10			
				1327	19	L-Ta_2O_5 phase(s) + H-Ta_2O_5(ss)
				1449	19	H_{mon}-Ta_2O_5(ss)
				1592	4.5	H_{mon}-Ta_2O_5(ss)
		1225	168			L-Ta_2O_5 phases(s)
	75 : 25	1000	10	1523	16	H_{mon}-Ta_2O_5(ss) + $Ta_2O_5 \cdot 6ZrO_2$
Ta_2O_5-Ga_2O_3	95 : 5	1000	10			
				1300	16	L-Ta_2O_5 phase(s) + H-Ta_2O_5(ss) + $GaTaO_4$-wolframite type [g]
				1444	64	H_{tet}-Ta_2O_5(ss) + $GaTaO_4$-ixiolite type
				1586	4	H_{tet}-Ta_2O_5(ss) + $GaTaO_4$-rutile type
				1602	20	H_{tet}-Ta_2O_5(ss) [f]
	90 : 10	1000	10	1300	16	L-Ta_2O_5 phase(s) + $GaTaO_4$-wolframite type
				1444	64	H_{tet}-Ta_2O_5(ss) + $GaTaO_4$-ixiolite type
				1602	4	H_{tet}-Ta_2O_5(ss) + $GaTaO_4$-rutile type
Ta_2O_5-Cr_2O_3	95 : 5	300	1			
		[d] 1000	10			
				1320	16	H-Ta_2O_5(ss) + L-Ta_2O_5 phase(s) + $CrTaO_4$-rutile type [g]
				1444	16	H_{tet}-Ta_2O_5(ss) + H_{mon}-Ta_2O_5(ss) + $CrTaO_4$-rutile type [g]
				1591	44	H_{tet}-Ta_2O_5(ss) + $CrTaO_4$-rutile type (trace) [f]
				1602	4	H_{tet}-Ta_2O_5(ss) + $CrTaO_4$-rutile type
	90 : 10	300	1			
		[d] 1000	10			
				1320	16	L-Ta_2O_5 phase(s) + H-Ta_2O_5(ss) + $CrTaO_4$-rutile type [g]
				1448	16	H_{tet}-Ta_2O_5(ss) + $CrTaO_4$-rutile type
				1597	4	H_{tet}-Ta_2O_5(ss) + $CrTaO_4$-rutile type
Ta_2O_5-Fe_2O_3	99 : 1	1200	10			
				1457	16	H_{tri}-Ta_2O_5(ss)
				1585	4	H_{tri}-Ta_2O_5(ss)
	98 : 2	1200	10			
				1445	16	H_{tet}-Ta_2O_5(ss)
				1468	65	H_{tet}-Ta_2O_5(ss)
				1650	67	H_{tri}-Ta_2O_5(ss) [f]
				1725	0.5	L-Ta_2O_5 phase(s)
		[d] 1445	16	[h] 1000	1	H_{tet}-Ta_2O_5(ss) + L-Ta_2O_5 phase(s)
				[h] 1000	16	H_{tet}-Ta_2O_5(ss) + L-Ta_2O_5 phase(s)
				[h] 1100	16	L-Ta_2O_5 phase(s)
				[h] 1200	60	L-Ta_2O_5 phase(s)
				[h] 1250	10	L-Ta_2O_5 phase(s)
				[h] 1300	10	L-Ta_2O_5 phase(s)
				1641	2	H_{tet}-Ta_2O_5(ss)
	97 : 3	1200	10			
				1445	16	H_{tet}-Ta_2O_5(ss) + $FeTaO_4$-rutile type
				1581	4	H_{tet}-Ta_2O_5(ss) + $FeTaO_4$-rutile type
	95 : 5	1000	10			
				1327	16	H_{tet}-Ta_2O_5(ss) + L-Ta_2O_5 phase(s) + $FeTaO_4$-rutile type [g]
				1442	16	H_{tet}-Ta_2O_5(ss) + $FeTaO_4$-rutile type
				1619	19	H_{tet}-Ta_2O_5(ss) + $FeTaO_4$-rutile type
	90 : 10	1000	10			
				1327	16	L-Ta_2O_5 phase(s) + H_{tet}-Ta_2O_5(ss) + $FeTaO_4$-rutile type [g]
				1442	16	H_{tet}-Ta_2O_5(ss) + $FeTaO_4$-rutile type
Ta_2O_5-Sc_2O_3	98 : 2	1200	10	1650	72	H_{tet}-Ta_2O_5(ss)
				1734	19	H_{tet}-Ta_2O_5(ss)
				1737	2	H_{tet}-Ta_2O_5(ss)
	97 : 3	1200	10			
				1737	0.5	H_{tet}-Ta_2O_5(ss)
	95 : 5	1000	10			
				1327	16	H_{tet}-Ta_2O_5(ss) + L-Ta_2O_5(ss) + $ScTaO_4$-$AlNbO_4$ type [g]
				1448	16	H_{tet}-Ta_2O_5(ss) + $ScTaO_4$-$AlNbO_4$ type
				1606	4	H_{tet}-Ta_2O_5(ss) + $ScTaO_4$-$AlNbO_4$ type

TABLE 1. *Experimental data*—Continued

System	Composition mol percent	Heat treatment				X-ray diffraction analyses[c]
		Initial[a]		Final[b]		
		Temp. °C	Time hr	Temp. °C	Time hr	
	90 : 10	1000	10			
				1327	16	L-Ta_2O_5 phase(s) + H_{tet}-Ta_2O_5(ss) + $ScTaO_4$-$AlNbO_4$ type[g]
				1448	16	H_{tet}-Ta_2O_5(ss) + $ScTaO_4$-$AlNbO_4$ type
				1608	4.5	H_{tet}-Ta_2O_5(ss) + $ScTaO_4$-$AlNbO_4$ type
Ta_2O_5-Lu_2O_3	95 : 5	1200	10			
				1640	20	H_{trl}-Ta_2O_5(ss) + $LuTaO_4$
	90 : 10	1200	10			
				1640	19	H_{trl}-Ta_2O_5(ss) + $LuTaO_4$
Ta_2O_5-MgO	95 : 5	1000	10			
				1327	16	L-Ta_2O_5 phase(s) + $MgTa_2O_6$-trirutile type
				1445	16	H"30:1" Ta_2O_5(ss) + $MgTa_2O_6$-trirutile type
				1608	4.5	H_{tet}-Ta_2O_5(ss) + $MgTa_2O_6$-trirutile type (trace)
	90 : 10	1000	10			
				1327	16	L-Ta_2O_5 phase(s) + $MgTa_2O_6$-trirutile type
				1445	16	H"30:1"-Ta_2O_5(ss) + $MgTa_2O_6$-trirutile type
				1597	4.5	H_{tet}-Ta_2O_5(ss) + $MgTa_2O_6$-trirutile type
Ta_2O_5-NiO	95 : 5	1000	10			
				1331	65	L-Ta_2O_5 phase(s) + $NiTa_2O_6$-trirutile type
				1445	16	L-Ta_2O_5 phase(s) + H-Ta_2O_5(ss) + $NiTa_2O_6$-trirutile type[g]
				1583	16	H"30:1"-Ta_2O_5(ss) + L-Ta_2O_5 phase(s)[f]
				1597	4.5	H"30:1"-Ta_2O_5(ss) + L-Ta_2O_5 phase(s)
	90 : 10	1000	10	1331	65	L-Ta_2O_5 phase(s) + $NiTa_2O_6$-trirutile type
				1444	16	L-Ta_2O_5 phase(s) + H-Ta_2O_5(ss) + $NiTa_2O_6$-trirutile type[g]
				1559	16	H-Ta_2O_5(ss) + L-Ta_2O_5(ss) + $NiTa_2O_6$-trirutile type[g]
				1570	16	H-Ta_2O_5(ss) + L-Ta_2O_5(ss) + $NiTa_2O_6$-trirutile type[g]
				1590	4	H-Ta_2O_5(ss) + L-Ta_2O_5(ss) + $NiTa_2O_6$-trirutile type[g]
Ta_2O_5-ZnO	95 : 5	1000	10	1331	65	L-Ta_2O_5 phase(s) + $ZnTa_2O_6$-columbite type
				1444	16	L-Ta_2O_5 phase(s) + H-Ta_2O_5(ss) + $ZnTa_2O_6$-columbite type[g]
				1590	4	H"30:1"-Ta_2O_5(ss) + $ZnTa_2O_6$-rutile type
	90 : 10			1333	19	L-Ta_2O_5 phase(s) + $ZnTa_2O_6$-columbite type
				1444	16	L-Ta_2O_5 phase(s) + H-Ta_2O_5(ss) + $ZnTa_2O_6$-columbite type[g]
				1585	4.5	H"30:1"-Ta_2O_5(ss) + $ZnTa_2O_6$-rutile type

[a] (Initial Heat Treatment)—All specimens were calcined as pressed disks on Pt foil at the indicated heat treatment with heating and cooling rates of approximately 4 °C/min unless otherwise specified.

[b] (Final Heat Treatment)—All specimens were quenched in sealed Pt tubes from the indicated temperature, unless otherwise specified.

[c] The phases identified are given in the order of amount present at room temperature (greatest amount first). The phases are not necessarily those present at the temperature to which the specimen was heated.

L-Ta_2O_5 phase(s)—One or more phases with an x-ray powder diffraction pattern similar to the low-temperature form of Ta_2O_5.

H_{trl}-Ta_2O_5 —Triclinic metastable distortion of the high-temperature form.

H_{mon}-Ta_2O_5 —Monoclinic metastable distortion of the high-temperature form related to the triclinic form by $\sim a\sqrt{2}$ and $\sim b\sqrt{2}$.

H_{tet}-Ta_2O_5 —The tetragonal high-temperature form of Ta_2O_5.

H"30:1" Ta_2O_5 —A metastable monoclinic form of Ta_2O_5 solid solution similar to that reported as "30:1" in the Ta_2O_5 : TiO_2 system [4].

H-Ta_2O_5 —The high-temperature form of Ta_2O_5 in such poor crystallinity or insufficient amounts that the exact symmetry could not be determined.

ss —Solid solution.

[d] Specimen was sealed in a large Pt tube to minimize possible loss of more volatile component.

[e] Probably a result of reduction of the addition oxide.

[f] Probably due to change of specimen composition by the addition oxide reacting with Pt tube.

[g] Presence of three phases indicates non-equilibrium.

[h] Specimen powder was prepared for x-ray diffraction on a Pt bar, heated, and subjected to x-ray examination without further disturbance of the specimen. Each succeeding heat treatment had also had the previous treatments.

probably of tetragonal symmetry at the temperature from which the specimen was quenched. Just as in the Ta_2O_5-TiO_2 system, this tetragonal phase could not be quenched to room temperature in the systems involving P_2O_5, V_2O_5, Nb_2O_5, ZrO_2, Lu_2O_3, NiO, or ZnO. However, very good apparently tetragonal x-ray diffraction powder patterns could be obtained from systems involving SnO_2, Ga_2O_3, Cr_2O_3, Fe_2O_3, Sc_2O_3, and MgO added to Ta_2O_5 in amounts less than 5 mol percent

The heat treatment of the single phase apparently tetragonal specimen containing 2 mol percent Fe_2O_3 (table 1) $a = 3.830$, $c = 35.68$Å indicates that this phase is not stable below about 1300 °C where it reverts to the low temperature polymorph. Nevertheless, it was assumed that single crystals of a size sufficient for structure analyses could be made in any of the second group of materials by annealing a specimen at high temperatures for a long period of time in a sealed platinum tube and subsequently quenching to room temperature. As can be seen from table 1 (footnote f) this cannot be done for systems involving SnO_2, Ga_2O_3, Cr_2O_3, or Fe_2O_3, since the latter components apparently react with the Pt container over a period of time. The specimen becomes enriched in Ta_2O_5 and "destabilized."

Therefore only Sc_2O_3 and MgO can be used to synthesize crystals of tetragonal H-Ta_2O_5 solid solu-

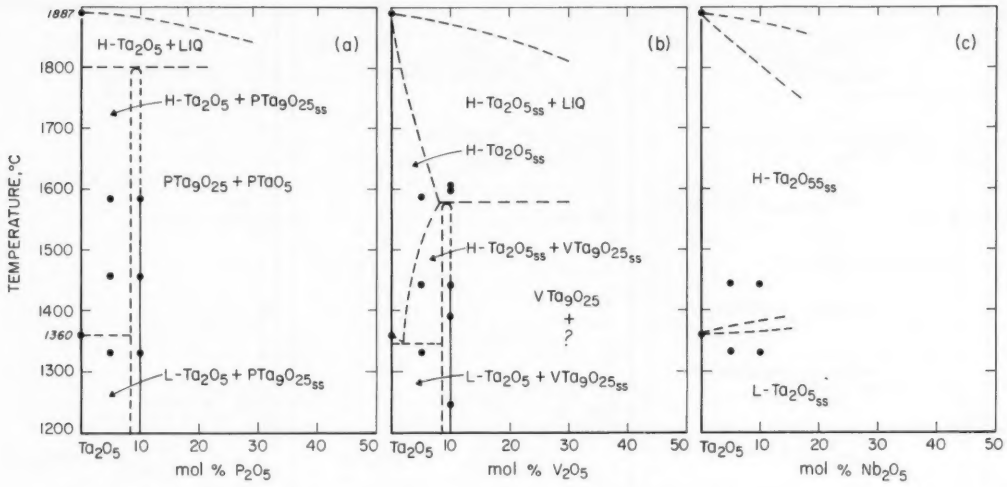

FIGURE 1. Ta_2O_5*-rich region of* Ta_2O_5-Me_2O_5 *systems, as deduced from limited quenching and x-ray diffraction data.*

● – experimental data points
H-Ta_2O_5 – high temperature form of Ta_2O_5
L-Ta_2O_5 – low temperature form of Ta_2O_5
ss – solid solution
(c) See references [13, 14] for more complete phase diagrams of Ta_2O_5-Nb_2O_5 system.

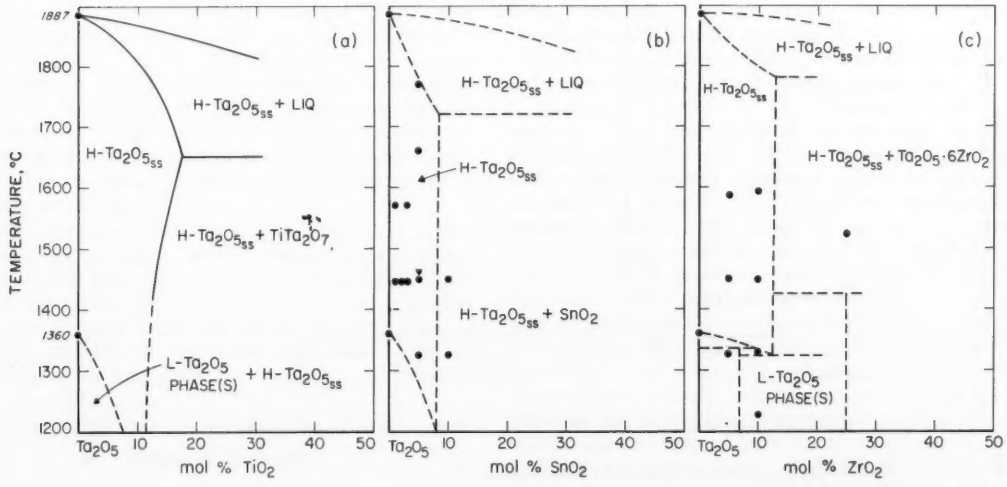

FIGURE 2. Ta_2O_5*-rich regions of* Ta_2O_5-MeO_2 *systems, as deduced from limited quenching and x-ray diffraction data.*

● – experimental data points
▼ – specimen reheated at lower temperature than original heat treatment (see table 1)
H-Ta_2O_5 – high temperature form of Ta_2O_5
L-Ta_2O_5 phase(s) – one or more phases with an x-ray powder diffraction pattern similar to the low temperature form of Ta_2O_5
ss – solid solution
(a) Portion of Ta_2O_5-TiO_2 system redrawn from reference [4].

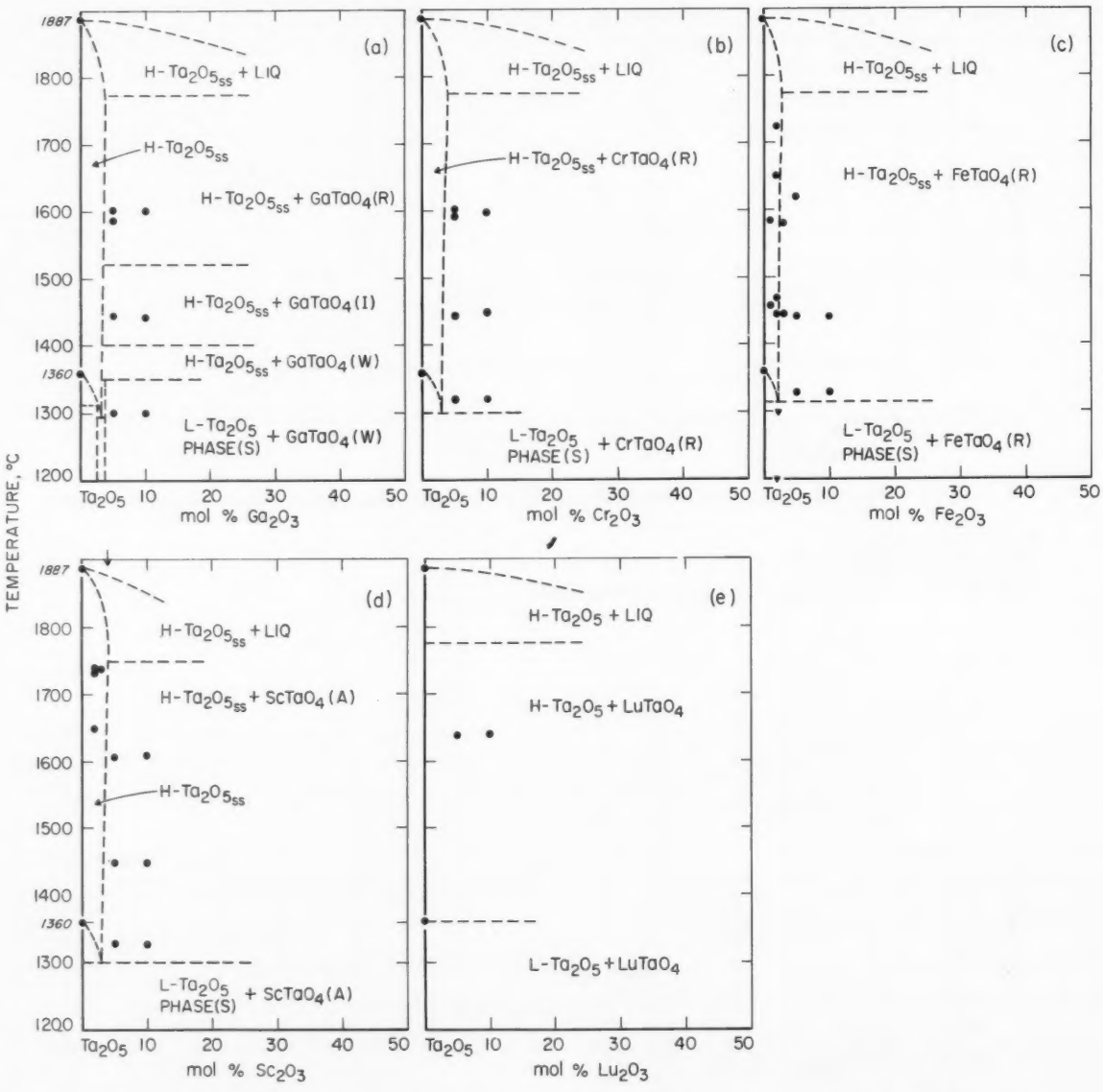

FIGURE 3. *Ta_2O_5-rich regions of Ta_2O_5-Me_2O_3 systems, as deduced from limited quenching and x-ray diffraction data.*

● – experimental data points
▼ – specimens reheated at lower temperatures than original heat treatment (see table 1)
H-Ta_2O_5 – high temperature form of Ta_2O_5
L-Ta_2O_5 phases – one or more phases with an x-ray diffraction powder pattern similar to the low temperature form of Ta_2O_5
ss – solid solution
R – rutile-type structure
I – ixiolite-type structure
W – wolframite-type structure
A – $AlNbO_4$-type structure.

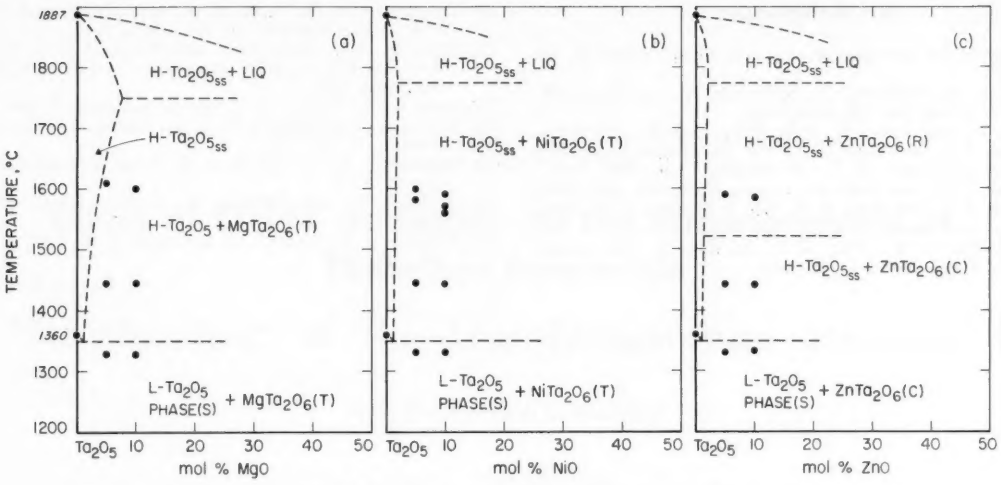

FIGURE 4. Ta_2O_5-*rich regions of* Ta_2O_5-MeO *systems, as deduced from limited quenching and x-ray diffraction data.*

● – experimental data points
H-Ta_2O_5 – high temperature form of Ta_2O_5
L-Ta_2O_5 phase(s) – one or more phases with an x-ray diffraction powder pattern similar to the low temperature form of Ta_2O_5
ss – solid solution
T – trirutile-type structure
R – rutile-type structure
C – columbite-type structure.

tion. Small crystals of $98Ta_2O_5 : 2Sc_2O_3$ were succesfully grown in the solid state using sealed or open Pt tubes at about 1735 °C. Preliminary single crystal x-ray patterns, made with the Burger precession camera and Weissenburg camera, indicated that the crystals were of sufficient size for single crystal structure determination. However, accurate measurement of intensities revealed serious inconsistencies from one crystal to the next.

It should be noted that all of the additional oxides which tend to stabilize the high-temperature form are those with cations generally occurring in octahedral coordination. Another group of oxides containing smaller cations were found to stabilize phases structurally similar to the low-temperature form of Ta_2O_5. These experiments are reported in Part III of this series [10].

5. Crystal Growth

Attempts to grow larger crystals of H_{tet}-Ta_2O_5-Fe_2O_3 solid solution by the Czochralski method were unsuccessful as there was an apparent slow reaction with the iridium container. Therefore efforts were directed toward growing a Sc stabilized crystal. The initial crystal growth attempts were made using 2 mol percent Sc_2O_3 in the melt. At this level the amount of Sc incorporated into the crystal was insufficient to stabilize the high form. The concentration of Sc_2O_3 in the melt was increased to 4 mol percent and this was sufficient for the crystals to be stabilized in the high form in the "as grown condition." The actual amount of Sc incorporated in the crystals is not known.

For all compositions there were some general problems encountered which seem noteworthy and give a general indication of the unusual nature of this material. The first problem encountered was in the preliminary melting or filling of the iridium crucibles with either partially sintered pellets or powder. As the material melted it wet the iridium and the surface tension would pull the unmelted central core up in the container until some of the contents would flow over the sides. This problem was overcome by increasing the size of the container from 3/4 in ID to 1 1/2 in ID. The second problem was encountered when the Ta_2O_5 remaining in the iridium container was solidified at the termination of a growth attempt. Evidently Ta_2O_5 undergoes a volume expansion on freezing and this expands the container after each run, thus drastically shortening the container's useful lifetime. The third problem was one which is common to those materials which are poor thermal conductors, particularly at high temperatures. In such a material, growth across the melt surface occurs, which insulates the top of the melt. "Melt off" occurs and a hollow bowl like crystal is grown. A similar behavior has been noted for the growth of TiO_2 [11]. Due to the difficulties mentioned the largest crystals obtained were of the order of 1×2 mm long and about 1 inch in diameter. A small cleavage fragment of one of these crystals has been used to determine the structure of H-Ta_2O_5 and the results of this structure determination will be reported elsewhere [12].

6. References

[1] Lagergren, S., and Magneli, A., Acta Chem. Scand. **6,** 444 (1952).

[2] Reisman, A., Holtzberg, F., Berkenblit, M., and Berry, M., J. Am. Chem. Soc. **78,** 4514 (1956).

[3] Laves, F., and Peter, W., Helv. Phys. Acta **37,** 617 (1964).

[4] Waring, J. L., and Roth, R. S., Nat. Bur. Stand. (U.S.), **72A** (Phys. and Chem.) No. 2, 175–186 (Mar.–Apr. 1968).

[5] Waring, J. L., and Roth, R. S., Acta Cryst. **17,** 455 (1964).

[6] Waring, J. L., and Roth, R. S., Nat. Bur. Stand. (U.S.), **69A,** (Phys. and Chem.) No. 2, 119–129 (Mar.–Apr. 1965).

[7] Coughanour, L. W., Roth, R. S., Marzullo, S., and Sennett, F. E., J. Res. NBS **54,** 149 (1955).

[8] Coughanour, L. W., Roth, R. S., Marzullo, S., and Sennett, F. E., J. Res. NBS **54,** 191 (1955) RP2576.

[9] Schneider, S. J., Roth, R. S., and Waring, J. L., J. Res. Nat. Bur. Stand. (U.S.), **65A** (Phys. and Chem.) No. 4, 345–374 (July–Aug. 1961).

[10] Roth, R. S., Waring, J. L., (to be published, J. Res. NBS).

[11] Nassau, K., and Boyer, A. M., J. Am. Ceram. Soc. **45,** 474–478 (1962).

[12] Stephenson, N. C., and Roth, R. S. (to be published, Acta Cryst.).

[13] Holtzberg, F., and Reisman. A., J., Phys. Chem. **65,** 1192 (1961).

[14] Mohanty, G. P., Fiegel, L. J., and Healy, J. H., J. Phys. Chem. **68,** 208 (1964).

(Paper 74A4–613)

JOURNAL OF RESEARCH of the National Bureau of Standards—A. Physics and Chemistry
Vol. 74A, No. 4, July–August 1970

Effect of Oxide Additions on the Polymorphism of Tantalum Pentoxide

III. "Stabilization" of the Low Temperature Structure Type

R. S. Roth and J. L. Waring

Institute for Materials Research, National Bureau of Standards, Washington, D.C. 20234

(March 11, 1970)

The "low temperature structure type" of Ta_2O_5 has been found to occur in two distinct forms with the lowest temperature form having a unit cell 14 times the subcell and an intermediate temperature form with a unit cell 11 times the subcell. The two types form intermediate partially ordered mixtures which are apparently in thermal equilibrium at various temperatures between ~ 1000 and 1350 °C. The addition of MoO_3, WO_3, SiO_2, GeO_2, ZrO_2, TiO_2, B_2O_3 and Al_2O_3 each affect the multiplicity of the true unit cell in different ways. WO_3, SiO_2, GeO_2, B_2O_3, and Al_2O_3 form phases structurally similar to "low-Ta_2O_5" which are stable up to the solidus temperatures of the corresponding systems.

Key words: Low temperature polymorph; single crystals; stabilization; tantalum oxide.

1. Introduction

The low-temperature form of Ta_2O_5 has an, as yet, unknown structure related to the low-temperature form of Nb_2O_5 as well as to α-U_3O_8 and α-UO_3. As Ta_2O_5 exhibits a reversible phase transition at about 1360 °C to a structurally dissimilar high-temperature form [1][1] it is not possible to grow single crystals of the room temperature stable form by conventional high-temperature techniques such as the Verneuil and the Czochralski methods. Whereas impurities appear to enter into solid solution in the high-temperature form of Ta_2O_5 [2] they apparently form new discrete phases in the low-temperature form [2]. In a previous publication [2] the present authors suggested that at least two discrete phases related to the low temperature form of Ta_2O_5 (L-Ta_2O_5) were formed at about 2 and 12.5 mol percent TiO_2 in the Ta_2O_5 : TiO_2 system. However, these phases transform at even lower temperatures than does the low-temperature form of pure Ta_2O_5. Jahnberg and Andersson [3] concluded that a series of discrete compounds of a similar type exist in the system Ta_2O_5-TaO_2F. Although they were able to obtain small crystals by heating specimens in sealed Pt tubes between 800 and 1300 °C they did not report any crystallographic or phase equilibria data for these phases.

In the present study, oxides containing cations smaller than Ta^{+5} have been added to Ta_2O_5 in an effort to obtain compounds related to L-Ta_2O_5 which may be stable at the melting point of the compositions.

2. Materials, Specimen Preparation, and Test Methods

The general quantitative spectrochemical analyses for the Ta_2O_5 used in this study has been previously reported [2]. All other oxides used were of reagent grade or better as described in previous publications [4]. These other oxides were MoO_3, WO_3, SiO_2, GeO_2, B_2O_3, and Al_2O_3. Some of the results previously reported for ZrO_2 [5] are duplicated here for discussion. The specimen preparation and test methods were the same as reported in the previous paper [5].

3. Results and Discussion

The experimental data is shown in table 1 and interpreted diagramatically as phase equilibria data in figures 1–3. The table columns need no comment except for the next to last and last columns. The "C-line" represents the position of a characteristic and diagnostic peak in the x-ray powder diffraction patterns, first referred to by Moser [6].

Moser has pointed out that the exact nature of the x-ray diffraction powder pattern of low-Ta_2O_5 is dependent upon the heat treatment of the specimen.

[1] Figures in brackets indicate the literature references at the end of this paper.

On the basis of the position of one characteristic peak (called the "C" line) he divided low-Ta_2O_5 into four different conditions ("Zustanden") with the notation that one grades into the other with no perceptible boundaries. This "C"-line was also found in the present study to be very diagnostic of the amount of impurities added to Ta_2O_5, and its position is listed in table 1 for each specimen in which it could be observed.

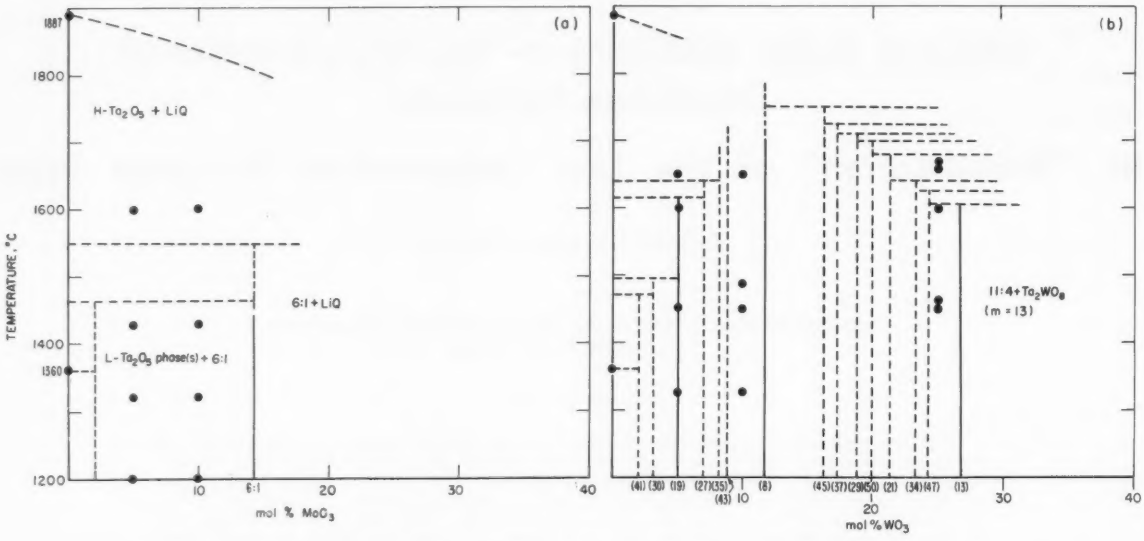

FIGURE 1. Ta_2O_5-*rich regions of* Ta_2O_5-MeO_3 *systems, as deduced from limited quenching and x-ray diffraction data.*

●—experimental data points
H-Ta_2O_5—high temperature form of Ta_2O_5
L-Ta_2O_5 phase(s)—one or more phases with an x-ray powder diffraction pattern similar to the low temperature form of Ta_2O_5
( )—numbers in parentheses indicate postulated multiplicity (m) of the unit cell for the indicated compositions.

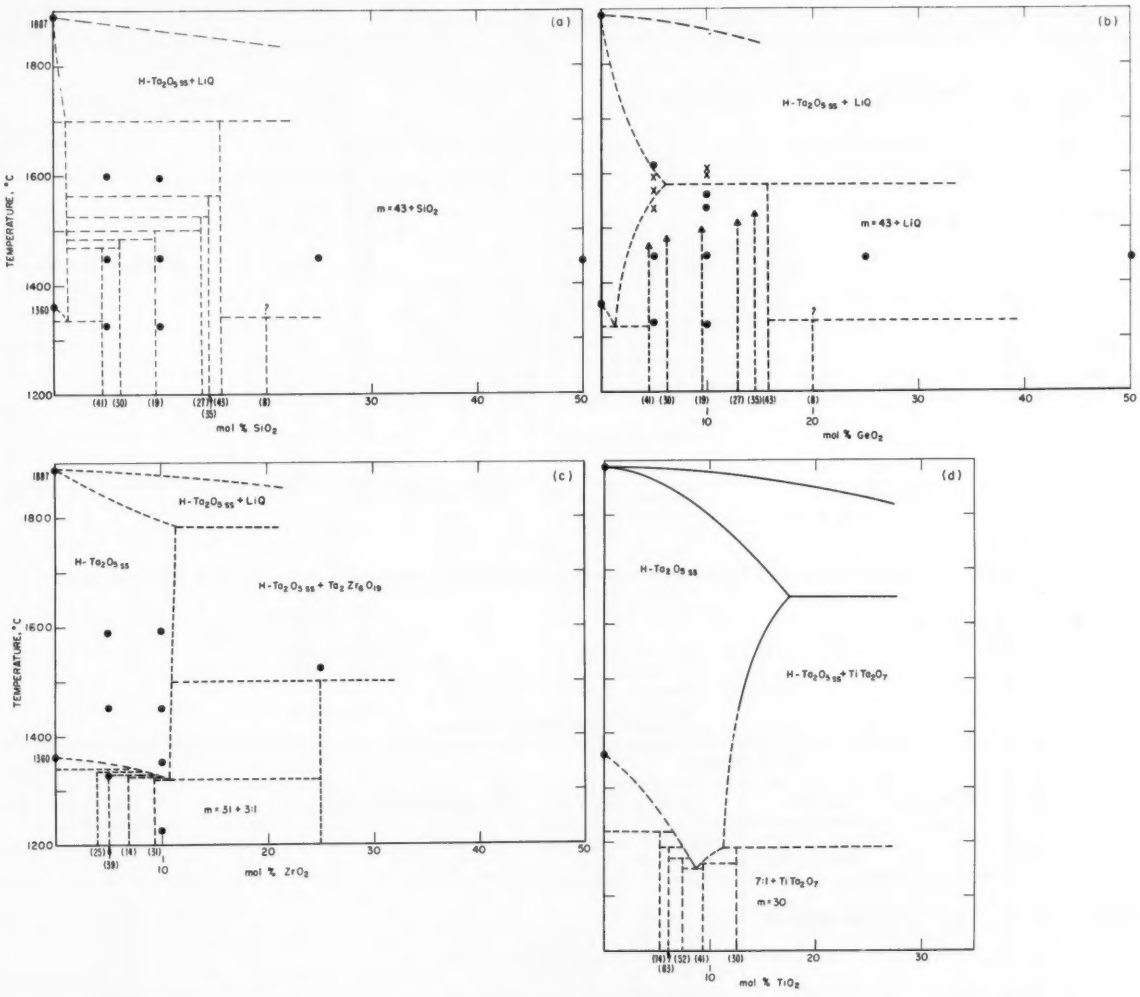

FIGURE 2. Ta_2O_5-*rich regions of* Ta_2O_5-MeO_2 *systems, as deduced from limited quenching and x-ray diffraction data.*

●—experimental data points
X—experimental data point—composition may have changed due to leak or reaction with Pt tube
H-Ta_2O_5—high temperature form of Ta_2O_5
ss—solid solution.

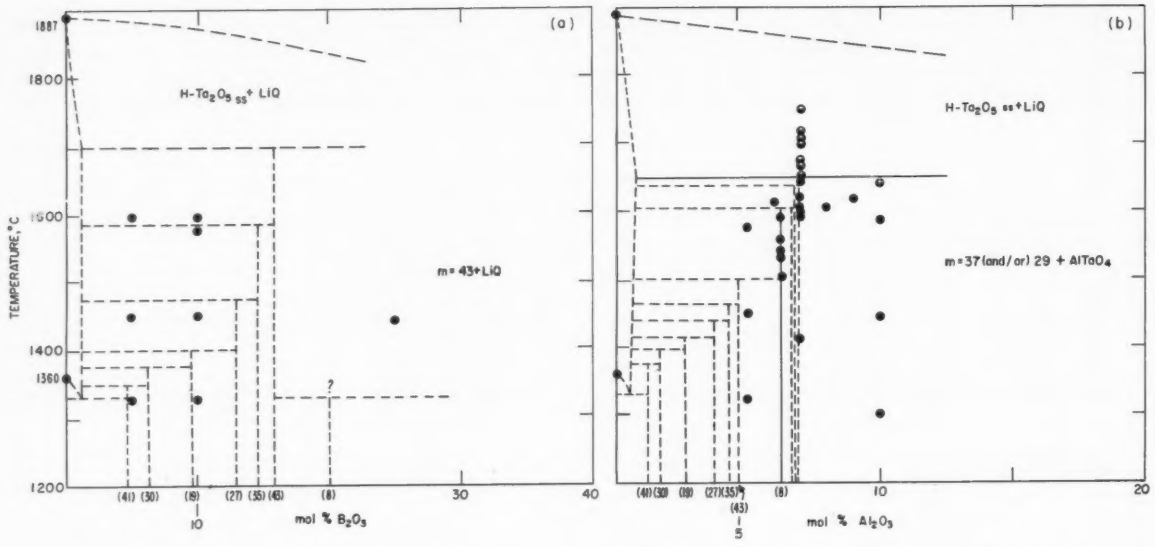

FIGURE 3. Ta_2O_5-*rich regions of* Ta_2O_5-Me_2O_3 *systems, as deduced from limited quenching and x-ray diffraction data.*

●—experimental data points.
H-Ta_2O_5—high temperature form of Ta_2O_5
ss—solid solution.

TABLE 1. *Experimental data*

System	Composition	Heat treatment				X-ray diffraction analyses [c]	"C" line CuKα radiation $2\theta_{obs}$	*m*
		Initial [a]		Final [b]				
		Temp. °C	Time hr	Temp. °C	Time hr			
Ta_2O_5		(as received)					26.75	14
				[d] 995	552	L-Ta_2O_5	26.65	
				1220	264	L-Ta_2O_5	26.44	
				[d] 1326	24	L-Ta_2O_5	26.40	
				[d] 1327	312	L-Ta_2O_5	26.38	11
				[d] 1389	1.0	L-Ta_2O_5	26.35	
				[d] 1402	2.0	L-Ta_2O_5	26.35	
				[d] 1402	17	L-Ta_2O_5 + H-Ta_2O_5 (trace)	26.38	
				[d] 1448	2	H_{trr}-Ta_2O_5 + L-Ta_2O_5 (trace)		
				[d] 1448	1	H_{trr}-Ta_2O_5 + L-Ta_2O_5		
				[d] 1450	0.5	H_{trr}-Ta_2O_5 + L-Ta_2O_5		
				[d] 1450	.25	L-Ta_2O_5	26.38	
				[d] 1498	.08	H_{trr}-Ta_2O_5		
				[d] 1499	.03	L-Ta_2O_5	26.37	
		[e] 1702	20			H_{trr}-Ta_2O_5		
				[d] 1224	425	L-Ta_2O_5	26.40	
				1225	353	L-Ta_2O_5	26.44	
		1350	336			L-Ta_2O_5	26.55	
				[d] 1402	1.0	L-Ta_2O_5	26.45	
				[d] 1404	5.0	L-Ta_2O_5	26.43	
				[d] 1499	0.03	L-Ta_2O_5	26.35	
		[e] 1405	2.5			L-Ta_2O_5	26.38	
				[d] 995	552	L-Ta_2O_5	26.65	
				[d] 1162	168	L-Ta_2O_5	26.58	
Ta_2O_5-MoO_3	95:5	500	10					
		[f] 700	60			L-Ta_2O_5 phase(s)		
				1185	19	L-Ta_2O_5 phase(s) + $MoTa_{12}O_{33}$	26.48	
		[f] 1200	60			L-Ta_2O_5 phase(s) + $MoTa_{12}O_{33}$		
				1323	71	L-Ta_2O_5 phase(s) + $MoTa_{12}O_{33}$	26.40	
				1426	19	L-Ta_2O_5 phase(s) + $MoTa_{12}O_{33}$	26.34	
				1599	4.5	H_{trr}-Ta_2O_5 + Q-Liquid		

TABLE 1. *Experimental data*—Continued

System	Composition	Heat treatment: Initial [a] Temp. °C	Initial Time hr	Final [b] Temp. °C	Final Time hr	X-ray diffraction analyses [c]	"C" line CuKα radiation $2\theta_{obs}$	*m*
	90:10	500	10					
		[f]700	60			L-Ta_2O_5 phase(s)		
				1185	19	$MoTa_{12}O_{33}$ + L-Ta_2O_5 phase(s)		
		[f]1200	60			$MoTa_{12}O_{33}$ + L-Ta_2O_5 phase(s)		
				1323	71	$MoTa_{12}O_{33}$ + L-Ta_2O_5 phase(s)	26.32	
				1426	19	$MoTa_{12}O_{33}$ + L-Ta_2O_5 phase(s)	26.28	
				1599	4.5	H_{tri}-Ta_2O_5 + Q-Liquid		
Ta_2O_5-WO_3	95:5	1000	10	1326	19	L-Ta_2O_5 phase(s)	26.17	
				1453	16	L-Ta_2O_5 phase(s)	26.15	
				1603	100	L-Ta_2O_5 phase(s)	26.08	19
				1652	4	L-Ta_2O_5 phase(s) + H-Ta_2O_5 trace	25.98	
		700	10					
		[f]1450	60			L-Ta_2O_5 phase(s)	26.20	
	90:10	500	64					
		1000	10					
				1327	19	L-Ta_2O_5 phase(s)	25.90	
				1449	19	L-Ta_2O_5 phase(s)	25.89	
				1486	2.5	L-Ta_2O_5 phase(s)	25.86	
				1649	4	L-Ta_2O_5 phase(s)	25.82	
				1651	5	L-Ta_2O_5 phase(s)	25.85	
				1652	4	L-Ta_2O_5 phase(s)	25.85	
		[f]1450	60			L-Ta_2O_5 phase(s)	25.90	
	75:25	700	10					
		[f]1100	672			L-Ta_2O_5 phase(s) + WTa_2O_6	25.55	
		700	10	1463	64	L-Ta_2O_5 phase(s)	25.22	
				1659	4	L-Ta_2O_5 phase(s) + Q-Liquid	25.45	
		[f]1450	60			L-Ta_2O_5 phase(s)	25.24	
				1602	1	L-Ta_2O_5 phase(s) + Q-Liquid	25.25	
				1669	1	L-Ta_2O_5 phase(s) + Q-Liquid	25.30	
Ta_2O_5-SiO_2	95:5	1000	10					
				1325	65	L-Ta_2O_5 phase(s)	26.10	19
				1448	16	L-Ta_2O_5 phase(s)	26.00	
				1597	4	H_{tri}-Ta_2O_{5ss} + L-Ta_2O_5 phase(s) (trace)		
	90:10			1325	65	L-Ta_2O_5 phase(s)	26.10	
				1448	16	L-Ta_2O_5 phase(s) + cristobalite (trace)	25.95	
				1595	4	H_{tri}-Ta_2O_5 + L-Ta_2O_5 phase(s)		
	75:25	1000	10					
				1448	64	L-Ta_2O_5 phases + H-Ta_2O_5 + cristobalite [g]	25.96	
	50:50	1000	10					
				1442	17	L-Ta_2O_5 + H-Ta_2O_{5ss} + cristobalite [g]	25.94	
Ta_2O_5-GeO_2	95:5	1000	10					
				1325	16	L-Ta_2O_5 phase(s)	26.08	
				1448	16	L-Ta_2O_5 phase(s)	25.97	
				1536	5	$H_{^{30.1}}$-Ta_2O_{5ss} + L-Ta_2O_5 phase [h]		
				1568	5	$H_{^{30.1}}$-Ta_2O_{5ss} [h]		
				1592	4.5	H_{tri}-Ta_2O_5 [i]		
				1614	3.5	$H_{^{30.1}}$-Ta_2O_{5ss} + Q-Liquid		
	90:10	1000	10					
				1322	16	L-Ta_2O_5 phase(s)	25.97	
				1448	16	L-Ta_2O_5 phase(s)	25.92	
				1536	4	L-Ta_2O_5 phase + L-Ta_2O_5 phase	25.05, 25.68	
				1560	5	L-Ta_2O_5 phase(s)	25.90	
				1597	4	$H_{^{30.1}}$-Ta_2O_{5ss} + Q-Liquid [h]		
				1607	5	$H_{^{30.1}}$-Ta_2O_{5ss} + Q-Liquid [h]		
	75:25	500	10					
		700	10					
				1445	16	L-Ta_2O_5 phase(s)	25.94	43
	50:50	500	10					
		700	10					
				1443	19	L-Ta_2O_5 phase(s) [j]	25.90	
Ta_2O_5-ZrO_2	95:5	1000	10					
				1326	19	L-Ta_2O_5 phase(s)	26.60	
	90:10	1000	10					
		1225	168			L-Ta_2O_5 phase(s)	26.92	
Ta_2O_5-B_2O_3	95:5	1000	10					
				1325	65	L-Ta_2O_5 phase(s)	26.37	

TABLE 1. *Experimental data*—Continued

System	Composition	Heat treatment				X-ray diffraction analyses [c]	"C" line CuKα radiation $2\theta_{obs}$	m
		Initial [a]		Final [b]				
		Temp. °C	Time hr	Temp. °C	Time hr			
				1449	16	H-Ta_2O_{5ss} + L-Phase(s)		
				1596	4.5	H_{tri}-Ta_2O_{5ss} + L-Ta_2O_5 phases(s)		
	90:10	1000	10	1326	16	L-Ta_2O_5 phase(s)	26.27	
				1449	16	L-Ta_2O_5 phase(s) + H-Ta_2O_{5ss}		
				1576	5.5	H_{tri}-Ta_2O_{5ss} + L-Ta_2O_5 phase(s)		
				1595	4	H_{tri}-Ta_2O_{5ss} + L-Ta_2O_5 phase(s)		
	75:25	500	10					
		700	10					
				1442	20	L-Ta_2O_5 phase(s)	25.85	43
Ta_2O_5-Al_2O_3	95:5	1000	10					
				1322	65	L-Ta_2O_5 phase(s)	25.84	
				1449	16	L-Ta_2O_5 phase(s)	25.76	
				1576	5.5	L-Ta_2O_5 phase(s) + H-Ta_2O_{5ss}	25.63	
	94:6	1200	6					
				1611	4	L-Ta_2O_5 phase(s) + H-Ta_2O_{5ss}	25.63	
	93:7	1250	168					
		1450	60					
				1504	20	L-Ta_2O_5 phase(s)	25.65	
				1534	336	L-Ta_2O_5 phase(s)	25.65	
				1540	20	L-Ta_2O_5 phase(s)	25.65	
				1558	139	L-Ta_2O_5 phase(s) + H-Ta_2O_{5ss}	25.65	
				1592	142	L-Ta_2O_5 phase(s) + H-Ta_2O_{5ss}	25.65	
		1200	6	1594	288	L-Ta_2O_5 phase(s)	25.63	
				1598	4	L-Ta_2O_5 phase(s)	25.60	29
				1668	4	H-Ta_2O_{5ss} + Q-Liquid		
				1674	16	H-Ta_2O_{5ss} + Q-Liquid		
		1560	60					
		1600	12			L-Ta_2O_5 phase(s) + $AlTaO_4$-$AlNbO_4$ type	25.92	
				1411	20	L-Ta_2O_5 phase(s) + $AlTaO_4$-$AlNbO_4$ type	25.60, 25.75	
				1606	3.5	L-Ta_2O_5 phase(s) + $AlTaO_4$-$AlNbO_4$ type	25.60, 25.95	
				1622	4	L-Ta_2O_5 phase	25.60	29
				1645	4	L-Ta_2O_5 phase	25.60	
				1653	4	H-Ta_2O_{5ss} + Q-Liquid		
				1699	1	H-Ta_2O_{5ss} + Q-Liquid		
				1707	1	H-Ta_2O_{5ss} + Q-Liquid		
				1719	1	H-Ta_2O_{5ss} + Q-Liquid		
				1750	1	H-Ta_2O_{5ss} + Q-Liquid		
	92:8	1200	6					
				1605	4	L-Ta_2O_5 phase(s) + $AlTaO_4$-$AlNbO_4$ type	25.60	
	91:9	1200	6					
				1618	4	L-Ta_2O_5 phase(s) + $AlTaO_4$-$AlNbO_4$ type	25.60	
	90:10	1000	10					
				1300	16	L-Ta_2O_5 phase(s) + $AlTaO_4$-$AlNbO_4$ type	25.85	
				1444	64	L-Ta_2O_5 phase(s) + $AlTaO_4$-$AlNbO_4$ type	25.75	
				1586	4	L-Ta_2O_5 phase(s) + $AlTaO_4$-$AlNbO_4$ type	25.60	
				1640	4	L-Ta_2O_5 phase + Q-Liquid (rutile type)	25.60	

[a] Initial Heat Treatment—All specimens were calcined as pressed disks on Pt foil at the indicated heat treatment with heating and cooling rates of approximately 4 °C/min, unless otherwise specified.

[b] Final Heat Treatment—All specimens were quenched in sealed Pt tubes from the indicated temperature (unless otherwise specified).

[c] The phases identified are given in order of amount present at room temperature (greatest amount first). The phases are not necessarily those present at the temperature to which the specimen was heated.

[d] Pt tube not sealed.

[e] Quenched from indicated temperature.

[f] Specimen was sealed in a large Pt tube to minimize possible loss of more volatile component.

[g] Presence of three phases indicates non-equilibrium.

[h] Probably due to change of specimen composition by the addition oxide reacting with Pt tube.

[i] Specimen tube leaked and all or most of addition oxide was lost by volatilization.

[j] Petrographic examination shows considerable amounts of glass.

Examination of single crystals [7] has shown that the "C-line" of the powder pattern is actually a 1k0 diffraction peak and is always the closest spot on the origin side of the 1k0 substructure reflection. The Low-Ta_2O_5 type phases in these systems always have only a b axis superstructure so that the "C-line" can be used directly to calculate the true unit cell. All of the superstructures in these systems are made up of ordered mixtures of phases having multiples of $3n+5$ (multiplicities, m) along the b axis [7]. Thus, if the structure happens to have a multiplicity of 5, 8, 11, 14, etc., the strong substructure line at about 28.3°2θ (CuKα radiation) will have the index (150), (180), (1,11,0), (1,14,0), etc., and the "C-line" will be (140), (170), (1,10,0),

(1,13,0), etc. If, however, the true structure is a mixture of $3n+5$ multiplicities such as

$$5+8=13 \quad \text{or} \quad 5+8+8=21,$$

etc., the substructure line will be (1,13,0), (1,21,0), etc., and the "C-line" will be (1,11,0), (1,18,0), etc. The "C-line," therefore, has a k index equal to $(m-x)$ where m equals the *multiplicity* and x equals *the number of* $(3n+5)$ *phases involved in the ordered mixture.* For $m=5$, 13, 8, 19, 11, 25, and 14 the "C-line" has been observed to equal (24.14°)[2], 25.18°, 25.75°, 26.08°, 26.38°, 26.58° and 26.76°, 2θ (CuKα radiation), respectively. From the above information the real multiplicity and true unit cell (the b axis) can be calculated by trial and error and the powder pattern completely and uniquely indexed on this basis. The calculated multiplicity (m) is listed in table 1 for some of the appropriate specimens.

The Low Temperature Polymorph(s) of Ta_2O_5. The various "conditions" of the low temperature form of Ta_2O_5 reported by Moser [6] can now be explained in terms of the multiplicities of their unit cells, as shown by the C-line (see figs. 15 and 16 and table 14 of ref. [6]). Moser used several different methods of preparing Ta_2O_5 and on the basis of the value of the C-line divided them into four different conditions: α_1, α_2, α_3, and α_4. His α_2 phase corresponds approximately to a multiplicity of 8 times the subcell and grades into α_1 which is about $8+13=21$. These specimens were mostly from transport reactions or heat treatments above the phase transition. It can be concluded from the present work that these materials have been contaminated by the transport medium or during the heat treatment and do not represent *pure* Ta_2O_5. The α_4 phase apparently also is contaminated by impurities either from the transport reaction or from OH^- present in the amorphous or semiamorphous starting materials. The quoted value of the C-line makes α_4 intermediate in composition between the 8 and 11 multiplicities or about $m=19$.

The α_3 phase of Moser therefore is probably the only condition which represents *pure* Ta_2O_5. This condition still is not very satisfactory as the C-line varies with temperature of heat treatment from about 26.75°2θ to 26.35°2θ (table 1). Furthermore, the position of the C-line versus temperature apparently represents an equilibrium condition as it can be made to occur at the same value when approached from higher temperatures as when approached from low temperatures. This condition is *reversible* (table 1).

The as-received materials from several different sources all contain a C-line at about 26.75°2θ and represents the largest value (smallest d value) which can be observed for *pure* Ta_2O_5. This value corresponds approximately to a multiplicity of 14 times the subcell. Upon heating above 1000 °C the C-line changes gradually with temperature to a value of 26.38°2θ at the phase transition temperature ~1360 °C. Unlike Moser's report, heating above this temperature did *not* cause a significant further shift in the value of the C-line. This last position corresponds to a multiplicity of about 11. Small single crystals of pure Ta_2O_5 with $m=11$ can be obtained by inverting the high temperature form and holding the specimen for many weeks just below the phase transition. These crystals have been used to study the crystal structure of low Ta_2O_5 ($m=11$) and the results of this study have been reported elsewhere (Stephenson and Roth [8]).

It may be concluded therefore that pure Ta_2O_5 exists in *two* low temperature polymorphic types: the lowest temperature form (~1000 °C and below) with $m=14$ ($Ta_{28}O_{70}$) and a higher temperature form (~1350 °C) with $m=11$ ($Ta_{22}O_{55}$). At intermediate temperatures ordered (or partially ordered) mixtures of the two phases occur in equilibrium with each other. The crystal structures of the two types must be very similar, and one can grade into the other by a small movement of only a few of the atoms (Stephenson and Roth [8]).

The Effect of other Ions on the Low Temperature Polymorph(s). It can be seen from table 1 and figures 1–3 that WO_3, SiO_2, GeO_2, B_2O_3, and Al_2O_3 when added to Ta_2O_5 all form phases structurally similar to low-Ta_2O_5 which are stable up to the solidus temperatures of the corresponding systems. These oxides all contain small cations which are often found in tetrahedral coordination. It may be inferred that the stabilizing influence of these oxides on the L-Ta_2O_5 structure-type is due to the cations entering into the structure interstitially in tetrahedral coordination, or else lowering the average cation radius by substituting for Ta^{+5} in the lattice. MoO_3, although even more likely than WO_3 to go into tetrahedral coordination does not form these stable phases at high temperatures. Instead a new compound isostructural with $WNb_{12}O_{33}$ is formed with the Mo^{+6} ion in tetrahedral coordination and all the Ta^{+5} ions in octahedral coordination. GeO_2 apparently reacts with the Pt tubes when held at high temperatures for long periods of time (table 1), thus, making determination of the true equilibrium diagram very difficult. The Ta_2O_5-B_2O_3 and Ta_2O_5-SiO_2 systems show some promise in terms of determining the true phase diagrams. However, the Ta_2O_5-Al_2O_3 and Ta_2O_5-WO_3 systems appear to offer the most promise for determining the nature of the low-Ta_2O_5 type phases, as the characteristic "C"-line shows the most displacement for these systems.

The data for the system Ta_2O_5-ZrO_2 is reproduced in table 1 (from ref. [5]) as this is the only system yet found in which the "C"-line is displaced (from pure Ta_2O_5) toward higher 2θ (smaller d). It can be assumed that HfO_2 will also cause this type of displacement. These phases are not stable at high temperatures, since both Zr^{+4} and Hf^{+4} are larger than Ta^{+5} and would increase the average radius of the cations.

The exact compositions at which each multiplicity is postulated to occur in the systems studied is shown in tables 2a and 2b. The addition ion is believed to occur substitutionally in the Ta_2O_5 structure in the systems involving WO_3, TiO_2, ZrO_2, and Al_2O_3 but interstitually, in tetrahedral coordination, for the systems involving MoO_3, SiO_2, GeO_2, and B_2O_3. All values of

[2] Calculated.

TABLE 2a. *Postulated compositions of phases in the systems involving* Ta_2O_5 *and oxides of other small cations*

System and mol ratio	m [a]	x_1 [b] ($m=13$)	x_2 ($m=8$)	x_3 ($m=11$)	Formula per unit cell
Ta_2O_5	11			1	$Ta_{22}O_{55}$
$Ta_2O_5:WO_3$		($Ta_{22}W_4O_{67}$)	($Ta_{15}WO_{40.5}$)	($Ta_{22}O_{55}$)	
81:2	41		1	3	$Ta_{81}WO_{205.5}$
59:2	30		1	2	$Ta_{59}WO_{150.5}$
37:2	19		1	1	$Ta_{37}WO_{95.5}$
13:1	27		2	1	$Ta_{52}W_2O_{136}$
67:6	35		3	1	$Ta_{67}W_3O_{176.5}$
41:4	43		4	1	$Ta_{82}W_4O_{217}$
15:2	8		1		$Ta_{15}WO_{40.5}$
41:8	45	1	4		$Ta_{82}W_8O_{229}$
67:14	37	1	3		$Ta_{67}W_7O_{188.5}$
13:3	29	1	2		$Ta_{52}W_6O_{148}$
89:22	50	2	3		$Ta_{89}W_{11}O_{255.5}$
37:10	21	1	1		$Ta_{37}W_5O_{107.5}$
59:18	34	2	1		$Ta_{59}W_9O_{174.5}$
81:26	47	3	1		$Ta_{81}W_{13}O_{241.5}$
11:4	13	1			$Ta_{22}W_4O_{67}$
$Ta_2O_5:SiO_2$			($Si_2Ta_{16}O_{44}$)	($Ta_{22}O_{55}$)	
41:2	41		1	3	$Si_2Ta_{82}O_{209}$
15:1	30		1	2	$Si_2Ta_{60}O_{154}$
19:2	19		1	1	$Si_2Ta_{38}O_{99}$
27:4	27		2	1	$Si_4Ta_{54}O_{143}$
35:6	35		3	1	$Si_6Ta_{70}O_{187}$
43:8	43		4	1	$Si_8Ta_{86}O_{231}$
4:1	8		1		$Si_2Ta_{16}O_{44}$
$Ta_2O_5:TiO_2$			($Ta_{12}Ti_4O_{38}$)	($Ta_{22}O_{55}$)	
18:1	74		1	6	$Ta_{144}Ti_4O_{368}$
61:4	63		1	5	$Ta_{122}Ti_4O_{313}$
25:2	52		1	4	$Ta_{100}Ti_4O_{258}$
39:4	41		1	3	$Ta_{78}Ti_4O_{203}$
7:1	30		1	2	$Ta_{56}Ti_4O_{148}$
$Ta_2O_5:B_2O_3$			($B_4Ta_{16}O_{46}$)	($Ta_{22}O_{55}$)	
41:2	41		1	3	$B_4Ta_{82}O_{211}$
15:1	30		1	2	$B_4Ta_{60}O_{156}$
19:2	19		1	1	$B_4Ta_{38}O_{101}$
27:4	27		2	1	$B_8Ta_{54}O_{147}$
35:6	35		3	1	$B_{12}Ta_{70}O_{193}$
43:8	43		4	1	$B_{16}Ta_{86}O_{239}$
4:1	8		1		$B_4Ta_{16}O_{46}$
$Ta_2O_5:Al_2O_3$		($Ta_{24}Al_2O_{63}$)	($Ta_{15}AlO_{39}$)	($Ta_{22}O_{55}$)	
81:1	41		1	3	$Ta_{81}AlO_{204}$
59:1	30		1	2	$Ta_{59}AlO_{149}$
37:1	19		1	1	$Ta_{37}AlO_{94}$
26:1	27		2	1	$Ta_{52}Al_2O_{133}$
67:3	35		3	1	$Ta_{67}Al_3O_{172}$
41:2	43		4	1	$Ta_{82}Al_4O_{211}$
15:1	8		1		$Ta_{15}AlO_{39}$
42:3	45	1	4		$Ta_{84}Al_6O_{219}$
69:5	37	1	3		$Ta_{69}Al_5O_{180}$
27:2	29	1	2		$Ta_{54}Al_4O_{141}$

[a] m = Multiplicity of the b axis.
[b] The phase with $m=13$ is really $(m=5)+(m=8)$, therefore $x=2$ so in order to find the real k index of the "C"-line for the Ta_2O_5-WO_3 phases one must add $2x_1+x_2+x_3$ to find the value of x in the equation $k=(m-x)[k=m-(2x_1+x_2+x_3)]$.

TABLE 2b. *Postulated compositions of phases in the systems involving* Ta_2O_5 *and oxides of other small cations*

System and mol ratio	m [a]	x_3 [b] ($m=11$)	x_4 ($m=14$)	x_5 ($m=17$)	Formula per unit cell
$Ta_2O_5ZrO_2$		($Ta_{22}O_{55}$)	($Ta_{27}ZrO_{69.5}$)	($Ta_{32}Zr_2O_{84}$)	
49:2	25	1	1		$Ta_{49}ZrO_{124.5}$
19:1	39	1	2		$Ta_{76}Zr_2O_{194}$
27:2	14		1		$Ta_{27}ZrO_{69.5}$
59:6	31		1	1	$Ta_{59}Zr_3O_{153.5}$

[a] m = Multiplicity of the b axis.
[b] To find the value of x in the equation $k=(m-x)$ expand into $k=m-(x_3+x_4+x_5)$.

multiplicity equal to, or less than, 50 are shown diagrammatically on the postulated diagrams (fig. 1–3). Several larger values are shown in the system Ta_2O_5-TiO_2 for illustrative purposes. It has now been found that the compound 7:1, originally described in the Ta_2O_5-TiO_2 system [2] has a multiplicity of 30. However, the compound originally described as occurring around 2 mol percent Ta_2O_5 has been found to be a manifestation of equilibrium obtained in the Ta_2O_5 by the impurities added. This phase has a multiplicity of exactly 11, which can not be achieved by pure Ta_2O_5 at the same temperatures.

It can be seen from table 2a that compositions having equivalent multiplicities in different systems have different cation/anion ratios. Each system has to be calculated on the basis of a different formula. In table 2a the formula $k=(m-x)$ is expanded into

$$k=m-(2x_1+x_2+x_3)$$

where x_1, x_2, and x_3 are the number of $(3n+5)$ phases in the compositions with multiplicities of 13, 8, and 11 respectively. The only two systems which are alike are SiO_2 and GeO_2. The composition of the end member Ta_2O_5, of course, is the same in each case $11Ta_2O_5$ ($Ta_{22}O_{55}$). Theoretically this structure might possibly accommodate three more oxygen ions [7,8]. For a phase with $m=8$ the ideal composition is $Me_{16}O_{42}$. In the Ta_2O_5-WO_3 system this phase has been found to contain only 40.5 oxygen atoms per 8 subcells and has a composition of $Ta_{15}WO_{40.5}$. The phase with $m=13$ having an ideal composition of $Me_{26}O_{68}$ has been found to have only 67 oxygen atoms and occurs at the composition $Ta_{22}W_4O_{67}$ [7,8]. All other multiplicities in this system can be calculated on the basis of these observations. In the Ta_2O_5-Al_2O_3 system the phase with $m=8$ occurs at the 15:1 ratio and has the composition $Ta_{15}AlO_{39}$. Again, all other multiplicities have been calculated on this basis, also assuming the hypothetical phase with $m=13$ (not actually observed in this system) having only 63 oxygens. In the Ta_2O_5-TiO_2 system however, the $m=30$ phase has been found at the 7:1 ratio and the hypothetical $m=8$ phase (not found) could therefore have only 38 oxygens as compared to 39 in Ta_2O_5-Al_2O_3, 40.5 in Ta_2O_5-WO_3 and 42 in the ideal structure. The larger Zr^{+4} ion causes the Ta_2O_5-ZrO_2 system to exhibit multiplicities in opposite direction from all the other systems. The data seem to indicate that the phase with $m=14$ occurs at $Ta_{27}ZrO_{69.5}$ as compared to the ideal value of $Me_{28}O_{74}$ and compositions of the various phases have been calculated on this basis.

For the other systems, it has been concluded from the limited data that the addition ion enters into tetrahedral interstitual positions with one extra oxygen ion lying above each tetrahedral ion. The SiO_2 and GeO_2 systems have been calculated assuming that the hypothetical phase with $m=8$ (not observed in either system) has the composition $Me_2^{+4}\ O_2Ta_{16}O_{42}$

$$(Me_2Ta_{16}O_{44}=8Ta_2O_5{:}2MeO_2).$$

However, the Ta_2O_5-B_2O_3 system seems to contain

twice as many tetrahedral ions as are found in the SiO_2 and GeO_2 systems. The compositions have, therefore, been calculated on the basis of a formula for the hypothetical $m=8$ phase (not found) of $B_4O_4Ta_{16}O_{42}$ ($B_4Ta_{16}O_{46}=8Ta_2O_5{:}2B_2O_3$). Due to the extreme volatility of MoO_3 at high temperatures as well as its tendency to reduce at these temperatures, no statement can be made as to the phases which might form in these systems on the basis of the reported experiments (table 1).

It should be noticed (table 1) that the "C"-line moves the same way for a W^{+6} cation as it does for an Al^{+3} cation or for any of the small ions regardless of valence. It is apparent that the position of the "C"-line is more dependent upon the amount and size of the cation than it is upon the valance. This leads to the conclusion that the size of the unit cell superstructure is more dependent upon the number of smaller cations which are included in the composition than upon the total number of oxygen ions. Before a final answer can be offered for this problem, single crystal structure determinations must be made for some of these compositions.

The system Ta_2O_5-WO_3 was, therefore, selected for further study in order to determine the number of phases of the low-Ta_2O_5 type which can be formed and to grow small single crystals for structural analyses. The results of this study will be reported elsewhere [9].

4. References

[1] Reisman, A., Holtzberg, F., Berkenblit, M., and Berry, M., J. Am. Chem. Soc. **78**, 4514 (1956).
[2] Waring, J. L., and Roth, R. S., Nat. Bur. Stand. (U.S.), **72A** (Phys. and Chem.) No. 2, 175–186 (Mar.–Apr. 1968).
[3] Jahnberg, L., and Andersson, S., Acta Chem. Scand. **21**, 615 (1967).
[4] Levin, E. M., and Roth, R. S., Nat. Bur. Stand. (U.S.), **68A** (Phys. and Chem.) No. 2, 197–206 (Mar.–Apr. 1964).
[5] Roth, R. S., Waring, J. L., and Brower, W. S., Nat. Bur. Stand. (U.S.), **74A** (Phys. and Chem.) No. 4, (July–Aug. 1970).
[6] Moser, R., Schweiz. Mineral. Petrog. Mitt. **45**, 35 (1965).
[7] Roth, R. S., and Stephenson, N. C., Chemistry of Extended Defects in Non-Metallic Solids, 167–182 (North Holland Publishing Co., Amsterdam 1970).
[8] Stephenson, N. C., and Roth, R. S., Acta Cryst. (in press).
[9] Roth, R. S., Waring, J. L., Parker, H. S. J. Solid State Chem. (to be published).

(Paper 74A4–614)

383-876 O - 70 - 3

JOURNAL OF RESEARCH of the National Bureau of Standards—A. Physics and Chemistry
Vol. 74A, No. 4, July–August 1970

The Dissociation Constant of *m*-Nitroanilinium Ion in Water-Tetrahydrofuran Solvents at 25 °C

R. A. Robinson*

Institute for Materials Research, National Bureau of Standards, Washington, D.C. 20234

(April 6, 1970)

The dissociation constant of *m*-nitroanilinium ion has been determined in water and in six water-tetrahydrofuran mixtures. The results are compared with those for water-methanol mixtures.

Key words: Dissociation constant; ionization constant; mixed solvents; *m*-nitroaniline; tetrahydrofuran.

1. Introduction

For the dissociation of a weak acid of the charge type A^+B^0, $BH^+ \rightleftharpoons H^+ + B$, the Born equation [1][1] predicts that the influence of solvent on the dissociation constant will be governed by the dielectric constant:

$$pK_s - pK_w = \frac{Ne^2}{2RT \ln 10}\left\{\frac{1}{\epsilon_s}-\frac{1}{\epsilon_w}\right\}\left\{\frac{1}{r_{H^+}}-\frac{1}{r_{BH^+}}\right\} \qquad (1)$$

where ϵ is the dielectric constant, w designates the solvent as water and s another solvent which may be a mixed solvent such as water-methanol; r is the radius of the ion specified by the subscript and, in the case of the hydrogen ion, it is, presumably, the radius of the hydrated ion, H_3O^+ or $H_9O_4^+$ [2]. There can be no doubt that this equation describes correctly the electrostatic energy changes for a macroscopic system of spheres in a continuous dielectric medium. However, it may require modification for microscopic systems where the influence of dielectric saturation of solvent molecules around an ion is important [3]. Moreover, the equation is not concerned with energy changes accompanying the transfer of the neutral molecule from one solvent to another and it has been shown that this is by no means negligible in the case of the transfer of tris(hydroxymethyl)aminomethane from water to water-methanol solvents [4].

The medium effect on the dissociation constant of *m*-nitroanilinium ion has been determined [5] in water-methanol mixtures as solvent; this paper is concerned with the dissociation constant of this acid in water-tetrahydrofuran solvents with the object of comparing the medium effect in water-methanol and water-tetrahydrofuran solvents of the same dielectric constant.

2. Method

The dissociation constant of *m*-nitroanilinium ion in a number of water-tetrahydrofuran solvents was determined by the spectrophotmetric method described in several previous publications [5–10]; the notation used in this paper is that used before. The validity of Beer's Law for this system was demonstrated by measurements of optical density of alkaline solutions in 62.5 wt percent tetrahydrofuran with the concentration of *m*-nitroaniline varying from 2×10^{-4} to $8\times10^{-4}m$.

3. Materials

For the purpose of purification, *m*-nitroaniline was recrystallized from methanol. Tetrahydrofuran was refluxed over anhydrous sodium sulphate for three days and then distilled.

4. Results

The experimental results are given in table 1. In this work, *m*-nitroaniline was dissolved in hydrochloric acid solutions. Some of the *m*-nitroaniline reacted with hydrochloric acid to form the nitroanilinium ion, thereby reducing the hydrogen ion concentration; the fraction of the nitroaniline reacting in this way is given by the spectrophotometric data as $(D_2-D)/(D_2-D_1)$. Allowance for this has been made

*Present address: Department of Chemistry, State University of New York at Binghamton, Binghamton, New York 13901.

[1] Figures in brackets indicate the literature reference at the end of this paper.

TABLE 1. *Dissociation constant of* m*-nitroanilinium ion in water-tetrahydrofuran at 25 °C*

$10^3 m_{HCl}$	D	$-\log a_{H^+}$	$\log \frac{D-D_1}{D_2-D}$	pK
Water. Concentration of *m*-nitroaniline: $3.6\times10^{-4}m$; $D_1=0.041$; $D_2=0.508$				
3.961	0.262	2.424	−0.047	2.471
3.260	.288	2.510	+0.050	2.460
2.081	.340	2.710	.250	2.460
1.006	.408	3.032	.565	2.467
			Average pK	2.465
12.5 wt percent Tetrahydrofuran. Concentration of *m*-nitroaniline: $3.6\times10^{-4}m$; $D_1=0.041$; $D_2=0.485$				
9.370	0.238	2.038	−0.098	2.136
7.118	.267	2.159	+0.016	2.143
5.058	.304	2.309	.162	2.147
3.516	.345	2.468	.337	2.131
2.570	.374	2.605	.477	2.128
			Average pK	2.137
25 wt percent Tetrahydrofuran. Concentration of *m*-nitroaniline: $3.7\times10^{-4}m$; $D_1=0.041$; $D_2=0.475$				
37.92	0.204	1.424	−0.221	1.645
31.08	.227	1.510	− .125	1.635
24.06	.256	1.622	− .008	1.630
16.53	.302	1.786	+0.179	1.607
9.735	.350	2.016	.393	1.623
			Average pK	1.628
37.5 wt percent Tetrahydrofuran. Concentration of *m*-nitroaniline: $3.7\times10^{-4}m$; $D_1=0.041$; $D_2=0.491$				
76.50	0.264	1.117	−0.008	1.125
62.30	.294	1.207	+0.109	1.098
52.58	.313	1.280	.184	1.096
41.66	.340	1.382	.297	1.085
			Average pK	1.101
50 wt percent Tetrahydrofuran. Concentration of *m*-nitroaniline: $3.8\times10^{-4}m$; $D_1=0.042$; $D_2=0.510$				
92.86	0.342	1.033	+0.252	0.781
87.77	.348	1.057	.276	.780
83.13	.352	1.081	.293	.788
73.03	.371	1.137	.374	.763
			Average pK	0.778
62.5 wt percent Tetrahydrofuran. Concentration of *m*-nitroaniline: $3.8\times10^{-4}m$; $D_1=0.042$; $D_2=0.526$				
95.12	0.398	1.022	+0.444	0.578
91.20	.400	1.040	.454	.586
83.36	.416	1.079	.532	.547
75.15	.421	1.125	.557	.568
			Average pK	0.570
75 wt percent Tetrahydrofuran. Concentration of *m*-nitroaniline: $3.9\times10^{-4}m$; $D_1=0.042$; $D_2=0.542$				
294.3	0.316	0.532	+0.084	0.448
193.2	.363	.714	.254	.460
112.0	.418	.951	.482	.469
			Average pK	0.459

All measurements were made at a wavelength of 380 nm in 1 cm cells. The concentration of *m*-nitroaniline was 3.6 mol liter^{-1}.

in calculating the values of $-\log m_{H^+}$ given in the third column of table 1.

5. Discussion

The dissociation constant of *m*-nitroanilinium ion is plotted in figure 1 as a function of the reciprocal of the dielectric constant of the medium, using values of the dielectric constant determined by Critchfield, Gibson, and Hall [11]. The figure also contains a plot of the dissociation constant of *m*-nitroanilinium ion as a function of ϵ^{-1}, in water-methanol solvents, using data published previously [5]. This figure emphasizes once again, what has been said several times before in earlier papers from this laboratory, that the Born effect does not give a complete description of solvent effects on acidity, particularly if the *macroscopic* dielectric constant is used. Thus, at $\epsilon=40$, $\epsilon^{-1}=0.025$, interpolation in figure 1 gives $pK=1.39$ for a water-methanol mixture and $pK=0.78$ for a tetrahydrofuran mixture, each of the same dielectric constant, a significant difference, well beyond the limit of experimental error.

It might be argued that the comparison is invalid because there must be considerable ion-pair formation in hydrochloric acid solutions of such comparatively low dielectric constant. It is true that neglect of such ion-pair formation would result in a pK value of *m*-nitroanilinium ion higher than the true one. Thus, we can make the two curves in figure 1 coincide if we invoke ion-pair formation for water-tetrahydrofuran solvents and assume that it is absent in water-methanol solvents of the same dielectric constant. Or, alternatively, that there is some ion-pair formation in a water-methanol solvent and even more in a water-tetrahydrofuran solvent of the same dielectric constant. This, however, only resolves one difficulty at the expense of another; for most, if not all, theories of ion-pair formation demand that it depends upon the dielectric constant of the medium. Consequently, if we adjust

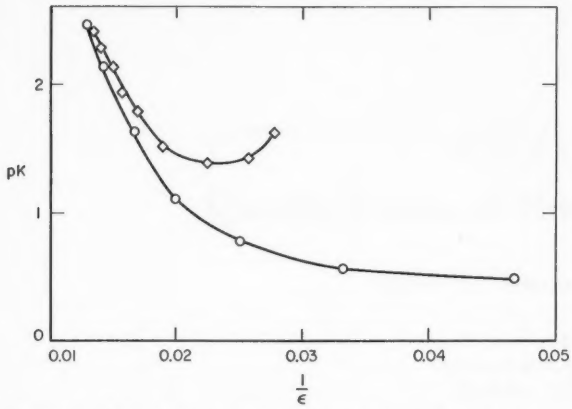

FIGURE 1. *Dissociation constant of* m-*nitroanilinium ion as a function of the dielectric constant of the solvent.*

⊡ Water-methanol solvent.
⊙ Water-tetrahydrofuran solvent.

the extent of ion-pair formation in two solvent mixtures of the same dielectric constant so as to make the dissociation constants of *m*-nitroanilinium ion equal, we negate the theoretical requirement that ion-pair formation between hydrogen and chloride ions should be equal in two solvents of the same dielectric constant.

It is difficult to decide if there is ion-pair formation between H^+ and Cl^- ions in these tetrahydrofuran-rich solvents. The dielectric constant of the 75 percent tetrahydrofuran solvent is $\epsilon = 21.44$ [11], 3.652 times smaller than that of water at the same temperature, 25 °C. The Bjerrum critical distance [12], which is $q = 3.58$ Å for water as solvent, is, therefore, 13.07 Å for 75 percent tetrahydrofuran, a distance within which a considerable amount of ion-pairing is possible.

Roy and Sen [13] have measured the emf of the cell Pt; H_2 (g, 1 atm), HCl (m) in water-tetrahydrofuran, AgCl; Ag. Their conclusion is that there is no appreciable ion association at 8.98 and 18.21 percent tetrahydrofuran, that, at 27.20 percent, there is barely noticeable evidence of ionic association; interaction appears to be considerable at 73.03 percent and hydrochloric acid is a weak electrolyte in 89 percent tetrahydrofuran. Our interpretation of the lower curve of figure 1 is, therefore, correct up to 50 percent tetrahydrofuran ($\epsilon^{-1} = 0.025$); the highest value to which our comparison of pK values of *m*-nitroanilinium ion in water-methanol and water-tetrahydrofuran extends is $\epsilon^{-1} = 0.028$.

However, their contention that there is considerable ionic association of hydrochloric acid in 73.03 percent tetrahydrofuran merits examination. It is consistent with the Bjerrum critical distance, but it does not seem to be consistent with some activity coefficient data they quote (table 1 of ref [13]). The Debye-Hückel equation for the activity coefficient of a 1 : 1 electrolyte is

$$-\log \gamma = \frac{Ad_0^{1/2} m^{1/2}}{1 + Bad_0^{1/2} m^{1/2}}. \qquad (2)$$

Using values of the dielectric constant and density of 73.03 percent tetrahydrofuran solution, interpolated from the data of Critchfield et al. [11], and putting $\mathring{a} = 4.3$Å, the value adopted by Bates and Bower [14] for aqueous solutions, values of the activity coefficient of hydrochloric acid in 73.02 percent tetrahydrofuran have been calculated and compared in table 2 with those observed [13]. The observed activity coefficient is somewhat lower than the calculated values (except at 0.1 m) but the difference is small and cannot correspond to any marked amount of ion-pair formation. Whatever may be the final answer to this question about ion-pair formation in tetrahydrofuran-rich solvents, it will not affect the principal conclusion demonstrated by figure 1, that the macroscopic dielectric constant of the solvent is not the only variable upon which the dissociation constant of a weak acid depends.

TABLE. 2. *Activity coefficient of hydrochloric acid in 73.03 percent tetrahydrofuran at 25 °C*

m	γ obs. (ref. [13])	γ calc.
0.0001	0.929	0.932
.001	.798	.808
.005	.626	.644
.01	.535	.560
.05	.341	.354
.1	.296	.279

The author is indebted to Roland F. Hirsch for assistance in the early phases of the work.

6. References

[1] Born, M., Z. Physik. **1**, 45, 221 (1920).
[2] Bell, R. P., and Bascombe, K. N., Disc. Faraday Soc. **34**, 158 (1957).
[3] Hepler, L. G., Aust. J. Chem. **17**, 587 (1964).
[4] Schindler, P., Robinson, R. A., and Bates, R. G., Nat. Bur. Stand. (U.S.), **72A** (Phys. and Chem.) No. 2, 141–148 (1968).
[5] Sager, E. E., Robinson, R. A., and Bates, R. G., Nat. Bur. Stand. (U.S.), **68A** (Phys. and Chem.) No. 3, 305–312 (1964).
[6] Robinson, R. A., Nat Bur. Stand. (U.S.), **68A** (Phys. and Chem.) No. 2, 159–164 (Mar.–Apr. 1964).
[7] Robinson, R. A., and Bates, R. G., Nat Bur. Stand (U.S.), **70A** (Phys. and Chem.), No. 6, 553–556 (Nov.–Dec. 1966).
[8] Steel, B. J., Robinson, R. A., and Bates, R. G., Nat. Bur. Stand. (U.S.), 71A (Phys. and Chem.) No. 1, 9–12 (1967).
[9] Robinson, R. A., Nat. Bur. Stand. (U.S.), **71A** (Phys. and Chem.), No. 3, 213–218 (May–June 1967).
[10] Robinson, R. A., Nat. Bur. Stand. (U.S.), **71A** (Phys. and Chem.) No. 5, 385–389 (Sept.–Oct. 1967).
[11] Critchfield, F. E., Gibson, J. A., Jr., and Hall, J. L., J. Am. Chem. Soc. **75**, 6044 (1953).
[12] Bjerrum, N., Kgl. Danske Videnskab. Selskab. **7**, No. 9 (1926).
[13] Roy, R. N., and Sen, B., J. Chem. Eng. Data **13**, 79 (1968).
[14] Bates, R. G., and Bower, V. E., J. Res. NBS **53**, 283 (1954) RP 2546.

(Paper 74A4–615)

JOURNAL OF RESEARCH of the National Bureau of Standards—A. Physics and Chemistry
Vol. 74A, No. 4, July–August 1970

Specific Heats of Fluorine at Coexistence*

Robert D. Goodwin and Rolf Prydz

**Institute for Basic Standards,
National Bureau of Standards,
Boulder, Colorado 80302**

(February 28, 1970)

Experimental specific heats of fluorine at constant total volume are reported for the two-phase, liquid-vapor system from triple- to the critical point. Specific heats of liquid along the coexistence path are derived by use of PVT data for the two-phase system, and are represented by a formula to facilitate computations of thermodynamic properties.

Key words: Fluorine; liquid-vapor coexistence; saturated liquid; saturation; specific heats; thermodynamic properties; two-phase.

List of Symbols

A_i	coefficients for various formulas
C_o	gross heat capacity, adjusted for capillary tube
$C_b(T)$	tare heat capacity of empty bomb
$C_v^0(T)$	specific heat at $\rho = 0$
$C_v(\rho, T)$	specific heat of two-phase sample
$C_\sigma(T)$	specific heat of liquid on coexistence path
G	Gibbs free energy per mole
J	the joule
k	conversion factor, 101.325 J/liter atm
ℓ	the liter
N	total g moles of fluid in closed system
N_b	g moles of fluid in the bomb
N_c	g moles of fluid in the capillary tube
P	pressure, 1 MN/m^2 = 9.86923 atm
Q	calorimetric heat input, J
ρ	density (subscripts g and l refer to vapor and liquid)
$\rho_{av} \equiv$	N_b/V_b, overall density
T	temperature, K, on the IPTS (1968)
T_a	average temperature in ΔT
ΔT	calorimetric temperature increment, K
$v \equiv$	$1/\rho$, molal volume
V_b	volume of the calorimeter bomb

1. Introduction

These specific heat measurements are part of a program to determine thermodynamic properties of compressed gaseous and liquid fluorine [1, 2].[1] For computations of the thermodynamic properties of the compressed liquid it may be convenient to use the saturated liquid path from the triple point to near the critical point. Data for specific heats of liquid on this path are derived from experimental observations on the two-phase, liquid-vapor system at constant volume by use of the PVT properties at coexistence.

2. Experimental Procedure

The commercial fluorine very generously was purified for us by G. K. Johnson at the Argonne National Laboratory by fractional distillation. Analyses of samples from our laboratory show a purity of at least 99.99 percent (determined by residual gas analysis after reaction of the fluorine with mercury). Most of the apparatus and procedures are identical with those described for our work on oxygen [3].

The fluorine sample-handling system is shown schematically by figure 1. The small circles represent valves. Numbers 8, 9, and 11 are packless valves, kindly given to us by G. C. Straty [4]. The pure fluorine is stored at 15 atm (1.5 MN/m^2) pressure in the 10-liter, stainless steel tank. It is introduced to the calorimeter by condensing it first in the trap, cooled with liquid nitrogen. Pressures to 200 atm (20 MN/m^2) are obtained in the calorimeter as the trap warms toward room temperature. The null-pressure diaphragm, NPD, isolates the fluorine from the remainder of the precision, dead-weight gage system. At the end of an experiment, fluorine is returned to the 10-liter storage vessel. Sodium fluoride pellets are activated by heating sodium bifluoride. They absorb traces of HF which could arise from organic contaminants in the all-metal system. The activated alumina converts fluorine into oxygen for protection of the rotary pump (containing fluorocarbon oils).

*This work was carried out at the National Bureau of Standards under sponsorship of the U.S. Air Force (MIPR No. FO4611-70-x-0001).

[1] Figures in brackets indicate the literature references at the end of this paper.

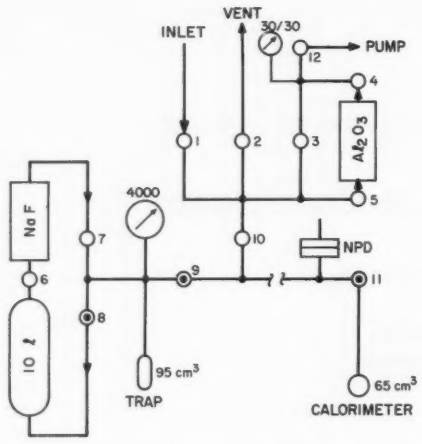

FIGURE 1. *Fluorine sample-handling system.*

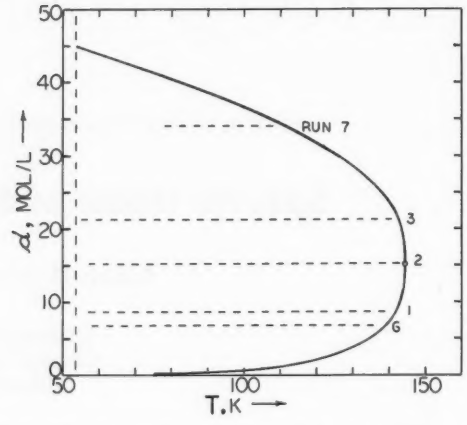

FIGURE 2. *Locus of two-phase specific heat measurements.*

TABLE 1. *Loading conditions for the samples*

Run	T, K	P, Atm	P, MN/m²	V, cm³	D, Mol/ℓ	N, Mol
1.....	174.825	83.142	8.4244	73.014	8.709	0.6360
2.....	166.789	102.908	10.4272	73.008	15.184	1.1087
3.....	175.609	183.593	18.6026	73.114	21.245	1.5535
6.....	195.075	85.469	8.6601	73.079	6.770	0.4948
7.....	116.282	87.461	8.8620	72.850	34.098	2.4843

Temperatures are on the IPTS (1968) via a new calibration table for our platinum resistance thermometer provided by the NBS temperature section [5]. To avoid entering a calibration table in the computer memory for every set of calculations, we have used a formula for computing temperature directly as a function of the observed thermometer resistance, as described in the appendix.

Tare heat capacity of the empty calorimeter bomb was measured in 29 intervals from 58 to 297 K. Data and the formulation are given in the appendix.

The amount of sample for each isochore of specific heat measurements is given in table 1. As in [3], we used an equation of state to find the density corresponding to the observed filling temperature and pressure. For present work the equation is similar to that used in [6], adjusted for forthcoming PVT data on fluorine.

3. Calculations and Results

Calculations in the present work differ from [3] only in modification of the heat of vaporization used for the capillary tube adjustment, as pointed out by R. E. Barieau in section 7 of [3]. With symbols listed above, the gross heat capacity, adjusted for heat effect of vapor forced into the capillary tube, is—

$$C_0 = [Q - T_a \cdot (dP/dT) \cdot \delta N_c/\rho_g]/\Delta T. \quad (1)$$

Specific heat of the two-phase sample, adjusted for heat effect of the bomb expansion, is—

$$\bar{C}_v = [C_0 - C_b - T_a \cdot (dP/dT) \cdot (dV_b/dT)]/N_b. \quad (2)$$

Physical properties needed for these calculations are given in the appendix.

Figure 2 locates the experimental runs by dashed lines inside the coexistence envelope. They represent the overall density of the two-phase system at constant volume. Table 2 gives the experimental conditions and both the direct and derived results for these two-phase specific heat measurements. The pressure and the densities of vapor and of liquid are computed by formulas in the appendix. The first column of table 2 gives the experimental run (sequence) followed by two digits for the individual measurement at this density. Next is the average temperature in the interval and the bomb volume derived from the pressure at this average temperature. The fourth column gives overall density, ρ_{av}. Following columns give the calorimetric temperature increment, ΔT; the experimental gross heat capacity prior to any adjustments, $Q/\Delta T$; the tare heat capacity; the specific heat, $\bar{C}_v$, of the two-phase sample; the derived specific heat, C_σ, of liquid along the coexistence path; and finally the estimated uncertainties (errors) in these specific heats, calculated as described in [3].

Figure 3 shows the two-phase specific heat data for our first three runs, plotted in coordinates $\bar{C}_v/T$ versus T. This plot has been used for interpolation of $\bar{C}_v/T$ onto isotherms, useful to derive values for d^2P/dT^2 via the thermodynamic relation,

$$\bar{C}_v/T = -d^2G/dT^2 + [d^2P/dT^2]/\rho. \quad (3)$$

Results in table 3 are compared with values from the vapor pressure equation of the appendix.

Specific heat of liquid along the coexistence path is derived by the relation [7]

$$C_\sigma = \bar{C}_v - \frac{T_g}{\rho} \cdot \left\{ \frac{1}{\rho} \frac{d\rho}{dT} \frac{dP}{dT} + \left[\frac{\rho \cdot V_b}{N_b} - 1 \right] \cdot \frac{d^2P}{dT^2} \right\}. \quad (4)$$

TABLE 2. *Specific heats of fluorine at coexistence*

ID	Temp. deg. K	V, bmb cm³	D, avr mol/l	ΔT deg. K	$Q/\Delta T$ J/deg.	Tare J/deg.	$\bar{C}_v$ J/M-K	C_σ J/M-K	Errors, percent	
									$\bar{C}_v$	C_σ
101	56.998	72.669	8.752	2.682	58.930	24.237	54.550	54.309	0.48	0.48
102	60.751	72.673	8.751	4.825	62.028	26.340	56.116	55.618	.41	.42
103	66.124	72.679	8.751	5.923	66.399	29.866	57.444	56.279	.41	.43
104	72.184	72.688	8.749	6.208	71.556	33.916	59.183	56.700	.42	.45
105	78.516	72.698	8.748	6.472	77.238	37.960	61.758	57.140	.42	.49
106	85.115	72.710	8.747	6.725	83.556	41.886	65.519	57.820	.43	.54
107	91.892	72.724	8.745	6.849	90.363	45.593	70.388	58.689	.43	.60
108	98.944	72.740	8.743	6.932	97.859	49.108	76.643	60.040	.42	.66
109	105.907	72.757	8.741	7.029	105.644	52.253	83.930	61.940	.42	.73
110	112.955	72.777	8.739	7.093	113.841	55.131	92.244	64.475	.41	.80
111	120.087	72.799	8.736	7.215	122.778	57.759	102.096	68.441	.40	.86
112	126.982	72.823	8.733	6.677	132.505	60.054	113.716	74.905	.40	.91
113	133.380	72.847	8.730	6.167	143.436	61.992	127.764	86.239	.40	.94
114	137.922	72.866	8.728	2.974	152.921	63.267	140.725	102.443	.46	1.04
201	57.538	72.669	15.257	4.551	85.452	24.502	54.975	54.850	.37	.37
202	62.557	72.675	15.255	5.496	89.647	27.492	56.062	55.749	.36	.36
203	68.562	72.683	15.254	6.522	94.650	31.506	56.953	56.211	.36	.37
204	75.531	72.693	15.252	7.428	100.628	36.086	58.214	56.622	.36	.38
205	84.071	72.708	15.248	9.668	108.467	41.285	60.595	57.409	.35	.40
206	93.327	72.727	15.244	8.854	117.344	46.337	64.043	58.563	.36	.45
207	101.874	72.747	15.240	8.260	126.022	50.470	68.137	60.259	.37	.49
208	109.854	72.768	15.236	7.724	134.658	53.901	72.824	62.765	.37	.53
209	117.335	72.790	15.231	7.253	143.307	56.777	78.021	66.354	.37	.57
210	125.182	72.816	15.226	5.493	153.127	59.476	84.391	72.317	.39	.62
211	130.632	72.836	15.221	5.438	161.284	61.181	90.114	79.755	.39	.63
212	135.869	72.857	15.217	5.076	171.190	62.700	97.572	93.541	.39	.64
213	140.687	72.878	15.212	4.653	186.562	64.005	109.849	130.404	.38	.62
214	143.436	72.890	15.210	0.904	204.756	64.712	125.623	256.445	.70	.75
301	55.173	72.667	21.378	2.729	107.984	23.496	54.386	54.343	.39	.40
302	57.860	72.670	21.377	2.654	110.311	24.667	55.130	55.055	.40	.40
303	61.376	72.674	21.376	4.386	113.341	26.733	55.751	55.608	.36	.36
304	66.187	72.679	21.375	5.244	117.404	29.908	56.322	56.025	.35	.35
305	71.829	72.687	21.372	6.047	122.139	33.683	56.940	56.350	.35	.36
306	78.281	72.698	21.369	6.865	127.752	37.815	57.893	56.809	.34	.36
307	84.987	72.710	21.366	6.562	133.702	41.813	59.149	57.394	.35	.38
308	91.937	72.724	21.361	7.356	140.093	45.617	60.813	58.257	.35	.40
309	99.435	72.741	21.356	7.659	147.276	49.341	63.037	59.622	.35	.42
310	107.126	72.761	21.351	7.741	154.930	52.772	65.734	61.643	.35	.44
311	114.649	72.782	21.344	7.325	162.713	55.780	68.799	64.563	.35	.46
312	121.502	72.804	21.338	6.996	170.708	58.249	72.339	68.925	.36	.48
313	128.311	72.827	21.331	6.653	179.334	60.471	76.422	75.868	.36	.49
314	133.951	72.849	21.324	4.659	188.464	62.157	81.180	87.061	.38	.52
315	138.484	72.868	21.319	4.443	198.904	63.419	86.861	107.109	.38	.52
601	57.905	72.670	6.810	7.348	51.665	24.691	54.510	54.116	.41	.41
602	64.890	72.678	6.809	6.635	57.346	29.037	57.209	55.883	.43	.45
603	72.088	72.688	6.808	7.771	63.442	33.854	59.791	56.442	.43	.48
604	79.891	72.701	6.807	7.852	70.512	38.803	64.075	56.976	.44	.55
605	87.709	72.715	6.805	7.802	78.174	43.344	70.382	57.829	.45	.63
606	95.511	72.732	6.804	7.834	86.323	47.440	78.536	59.015	.44	.73
607	103.310	72.751	6.802	7.838	94.932	51.117	88.481	60.760	.44	.83
608	111.099	72.772	6.800	7.774	104.070	54.402	100.274	63.435	.43	.93
609	118.847	72.795	6.798	7.752	113.803	57.321	113.982	67.447	.42	1.02
610	126.540	72.821	6.795	7.669	124.691	59.913	130.613	74.274	.41	1.10
611	133.839	72.849	6.792	6.960	137.309	62.124	151.266	86.946	.40	1.14
701	77.842	72.697	34.173	2.136	179.095	37.542	56.979	56.793	.42	.43
702	80.589	72.702	34.170	3.358	181.333	39.227	57.202	56.992	.37	.38
703	84.641	72.709	34.167	4.745	184.786	41.614	57.631	57.402	.35	.36
704	89.737	72.719	34.162	5.447	189.068	44.450	58.212	58.005	.34	.36
705	95.545	72.732	34.156	6.172	193.931	47.457	58.959	58.882	.34	.36
706	101.200	72.745	34.150	5.147	198.700	50.162	59.788	60.008	.35	.38
707	106.285	72.758	34.144	5.033	203.295	52.415	60.729	61.434	.35	.38

TABLE 3. *Comparisons* d^2P/dT^2 *for fluorine*

$\bar{C}_v/T = -d^2G/dT^2 + (d^2P/dT^2)\cdot v$

T, K	d^2P/dT^2, atm/K^2		
	Expt'l. $\bar{C}_v/T$		V.P. eq. (5.3)
80	0.0080	±0.0008	0.0073
90	.0140	.0008	.0133
100	.0212	.0008	.0203
110	.0289	.0008	.0280
120	.0371	.0008	.0363
130	.0475	.0009	.0464
140	.063	.0035	.0647

Figure 4 shows C_σ for the liquid on this path. On the scale of this plot the data appear to be linear in temperatures below the boiling point (85 K). Figure 5 examines behavior of the data as $T \to T_c$. Upon subtracting C_v^0, we obtain a nearly linear plot in the logarithmic coordinates of figure 5, corresponding to

$$C_\sigma \sim C_v^0 + \text{const} \cdot (1 - T/T_c)^{-\epsilon} \tag{5}$$

where the exponent is roughly $\epsilon = 0.5$.

4. Analytical Representation of C_σ

For thermal computations along the coexistence path we need a description of $C_\sigma(T)$. It is convenient

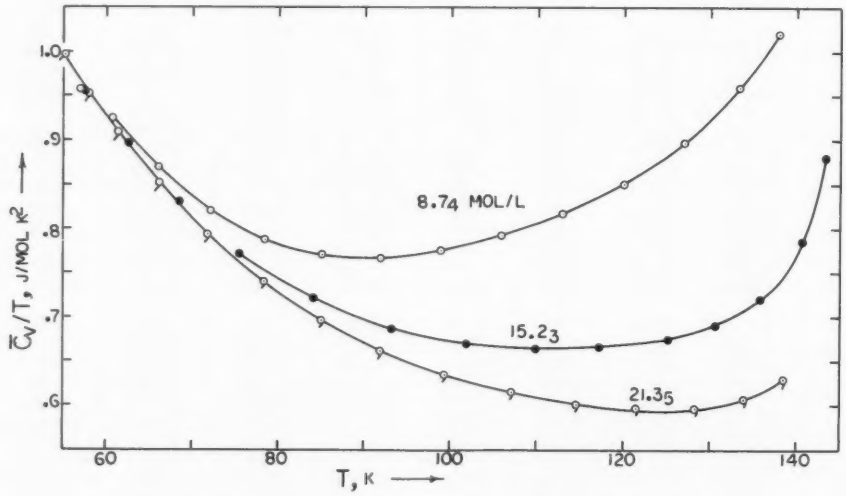

FIGURE 3. *Two-phase specific heats of fluorine at constant volume.*

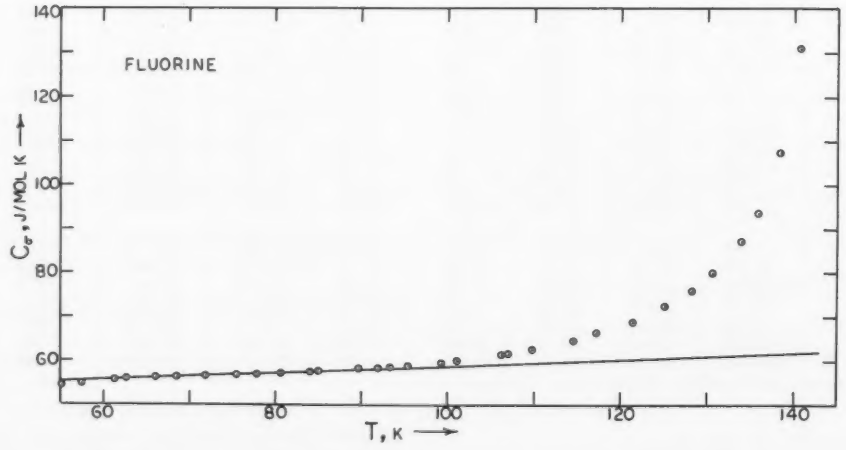

FIGURE 4. *Derived specific heats of liquid fluorine along the coexistence path.*

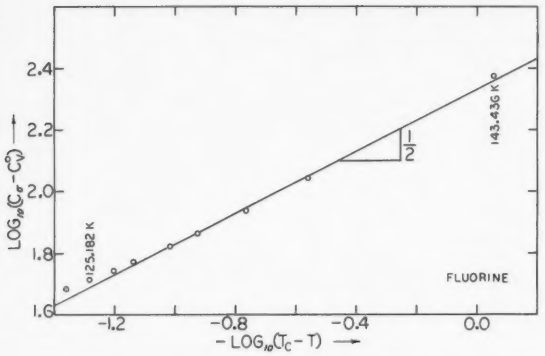

FIGURE 5. *Residual specific heat:* $(C_\sigma - C_v^0)$, *J/mol K, versus* $(T_c - T)$ *in log-log coordinates.*

to define a reduced independent variable which is zero at the critical point, $x \equiv (1 - T/T_c)$. We have sought a simpler form than was used for oxygen. The following expression,

$$C_\sigma = A_1/x^\epsilon + \sum_{i=2}^{N} A_i \cdot x^{i-2}, \qquad (6)$$

is sufficient for oxygen with $N = 3$ terms only, giving an rms relative deviation of 0.33 percent for the 86 data in [3]. For the present fluorine data, however, we must take $N = 6$ terms for optimum representation, $\epsilon = 0.593$,

$A_1 = 10.76\ 214$ $\quad$ $A_4 = -148.92\ 825$

$A_2 = 33.88\ 593$ $\quad$ $A_5 = 341.88\ 386$

$A_3 = 34.85\ 555$ $\quad$ $A_6 = -265.99\ 546$

Table 4 compares the data used for C_σ with values calculated from (6). There is a systematic difference of roughly 0.1 percent between different runs. This increases as the amount of sample (density) decreases. For this reason, runs at densities below critical were omitted in deriving constants for the fitting function. The rms relative deviation of 0.11 percent for (6) with the remaining data is smaller than the uncertainty of individual points. Figure 6 shows low-temperature behavior of the C_σ data relative to the calculated line.

A few specific heats have been reported previously for fluorine in the condensed phase at $T < 85$K, [8,9]. No clear description of the experimental conditions was given. The data in [9] are labeled C_p, and previous reports mention recording the pressure before and after each heating period [10]. The reported values in table 5 are compared with our calculated values from (6) for liquid on the coexistence path.

TABLE 4. *Derived and calculated values of* C_σ, *J/mol K*

ID	T, K	Csat	Calc	Percent
	53.481		54.489	
	54.000		54.578	
301	55.173	54.343	54.766	
	56.000		54.890	
201	57.538	54.850	55.104	
302	57.860	55.055	55.147	−0.17
303	61.376	55.608	55.554	.10
202	62.557	55.749	55.672	.14
304	66.187	56.025	55.991	.06
203	68.562	56.211	56.172	.07
305	71.829	56.350	56.403	−.09
204	75.531	56.622	56.658	−.06
701	77.842	56.793	56.824	−.05
306	78.281	56.809	56.857	−.08
702	80.589	56.992	57.037	−.08
205	84.071	57.409	57.344	.11
703	84.641	57.402	57.399	.01
307	84.987	57.394	57.433	−.07
704	89.737	58.005	57.976	.05
308	91.937	58.257	58.279	−.04
206	93.327	58.563	58.490	.13
705	95.545	58.882	58.861	.04
309	99.435	59.622	59.631	−.01
706	101.200	60.008	60.036	−.05
207	101.874	60.259	60.201	.10
707	106.285	61.434	61.437	−.00
310	107.126	61.643	61.707	−.10
208	109.854	62.765	62.670	.15
311	114.649	64.563	64.754	−.29
209	117.335	66.354	66.200	.23
312	121.502	68.925	68.996	−.10
210	121.182	72.317	72.276	.06
313	128.311	75.868	76.004	−.18
211	130.632	79.755	79.642	.14
314	133.951	87.061	87.059	.00
212	135.869	93.541	93.425	.12
315	138.484	107.109	107.265	−.15
213	140.687	130.404	130.355	.04
214	143.436	256.445	256.446	−.00

NP = 34, RMSPCT = 0.112

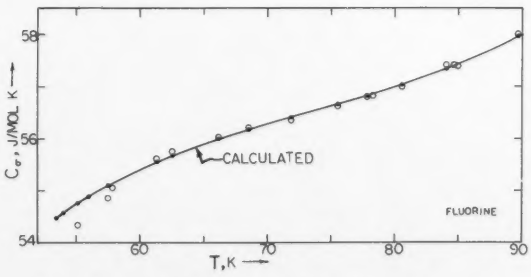

FIGURE 6. *Behavior of* C_σ *data at low temperatures.*

5. Appendixes

5.1. Resistance Thermometer Formula

Coefficients for eq 5.1 were obtained by least squares. Data are from NBS calibration tables on the

TABLE 5. *Other specific heats for the condensed phase, J/mol K*

T, K	C_x, unknown conditions		C_σ Eq (6)
	Kanda [8]	Hu et al. [9]	
57.50	45.4		55.1
58.14		57.3	55.2
62.27		57.3	55.6
62.51	45.7		55.7
67.05		56.7	56.1
67.49	45.9		56.1
71.86		56.8	56.4
76.60		57.4	56.7
77.10	46.5		56.8
81.32		57.7	57.1
83.41	46.9		57.3

IPTS (1968) for platinum thermometer L.N.1,506,157. Maximum deviations are 4 parts per million (0.14 mK) in the range $20 \leq T \leq 100$ K, and 6 parts per million (1.95 mK) in the range $100 \leq T \leq 600$ K. Variables for (5.1) include $x \equiv R/R_1$ where R is thermometer resistance and R_1 is a constant to be found; $T_0 \equiv 273.15$ K; $u \equiv \log_e(1+x)$; and $w \equiv \log_e(1+1/x)$,

$$T/T_0 = A_1 + A_2 \cdot x + A_3 \cdot u + A_4 \cdot x \cdot u + x \cdot \sum_{i=5}^{17} A_i \cdot w^{i-3}. \qquad (5.1)$$

Table 5.1–A gives the constants for (5.1). The number of figures in each is based on the maximum value of each term in (5.1). Table 5.1–B gives a selection of data and calculated values for T and for the first derivative, dT/dR.

TABLE 5.1–A. *Constants for resistance thermometer*

R_1 = 13.0 ohm

$A_1 = -1.0874\ 7037 \ldots \times 10^1$
$A_2 = -2.6699\ 4012 \ldots \times 10^0$
$A_3 = \ 9.2443\ 2475 \ldots \times 10^0$
$A_4 = \ 7.9896\ 2549 \ldots \times 10^{-1}$

$A_5 = \ 2.0807\ 0866 \ldots \times 10^1$
$A_6 = -1.8099\ 5755 \ldots \times 10^1$
$A_7 = \ 2.2519\ 8377\ 2 \ldots \times 10^1$
$A_8 = -1.9086\ 9836\ 9\ 4 \ldots \times 10^1$
$A_9 = \ 1.2724\ 9642\ 9\ 9 \ldots \times 10^1$

$A_{10} = -6.3571\ 7850\ 4\ 7\ 0 \times 10^0$
$A_{11} = \ 2.3872\ 5690\ 3\ 4\ 4 \times 10^0$
$A_{12} = -6.6558\ 6282\ 7\ 2\ 7 \times 10^{-1}$
$A_{13} = \ 1.3550\ 6466\ 3\ 3\ 4 \times 10^{-1}$
$A_{14} = -1.9527\ 0069\ 5\ 7\ 9 \times 10^{-2}$

$A_{15} = \ 1.8847\ 0886\ 4\ 3 \ldots \times 10^{-3}$
$A_{16} = -1.0919\ 0062\ 3\ 0 \ldots \times 10^{-4}$
$A_{17} = \ 2.8697\ 1011\ 5 \ldots \times 10^{-6}$

5.2. Tare Heat Capacity C_b of the Empty Calorimeter

These heat capacities were measured by procedures identical with those used when the calorimeter contained fluid. Results are given here to show the precision attainable in absence of contained fluid. We express C_b in J/K, and describe the data by use of argument $x \equiv 100/T$,

$$\log_e(C_b/50) = \sum_{i=0}^{7} C_i \cdot x^i, \qquad (5.2)$$

$C_0 = \ 0.834\ 3170$ $\quad$ $C_4 = -0.617\ 8472$
$C_1 = -1.254\ 9634$ $\quad$ $C_5 = \ 1.434\ 6722$
$C_2 = \ 1.404\ 5656$ $\quad$ $C_6 = -0.792\ 6938$
$C_3 = -1.167\ 3943$ $\quad$ $C_7 = \ 0.151\ 4253.$

Experimental and calculated values for C_b are compared in table 5.2.

TABLE 5.1–B. *Resistance thermometer comparisons*

R, ohm	Temperature, K		DT/DR, K/ohm	
	Data	Calcd	Data	Calcd
0.10822	20	20.00000	54.450	53.996
.15046	22	22.00001	42.220	41.960
.20387	24	24.00010	33.910	33.744
.26917	26	25.99998	28.140	28.013
.43669	30	29.99999	20.870	20.802
.71483	35	34.99999	15.920	15.886
1.06277	40	39.99994	13.210	13.188
1.92143	50	50.00002	10.610	10.600
2.92121	60	60.00002	9.580	9.576
3.99152	70	69.99999	9.180	9.177
5.09086	80	80.00004	9.040	9.045
6.19807	90	89.99990	9.030	9.032
7.30315	100	100.00003	9.069	9.072
9.49254	120	120.00031	9.199	9.202
11.65079	140	139.99974	9.326	9.328
13.78232	160	159.99946	9.431	9.434
15.89232	180	180.00029	9.519	9.522
17.98437	200	200.00103	9.596	9.597
20.57753	225	225.00024	9.681	9.682
23.14885	250	249.99855	9.760	9.761
25.49666	273	272.99897	9.830	9.832
28.23168	300	300.00079	9.911	9.914
30.74399	325	325.00188	9.988	9.989
33.23712	350	350.00185	10.065	10.066
35.51399	373	373.00105	10.136	10.137
38.16643	400	399.99978	10.220	10.221
43.02058	450	449.99831	10.379	10.380
47.80024	500	499.99964	10.541	10.543
52.50580	550	550.00194	10.708	10.710
57.13738	600	599.99805	10.881	10.880

5.3. The Vapor Pressure of Fluorine

The equation from [11] uses argument $x \equiv (1-T_t/T)/(1-T_t/T_c)$,

$$\log_e(P/P_t) = A_1 \cdot x + A_2 \cdot x^2 + A_3 \cdot x^3 + A_4 \cdot x \cdot (1-x)^\epsilon. \qquad (5.3)$$

Constants are reported in [2],

$P_t = 252.0$ N/m^2 $\quad$ $A_1 = \ 7.8959\ 2346$
$T_t = \ 53.4811$ K $\quad$ $A_2 = \ 3.3876\ 5063$
$T_c = 144.31$ K $\quad$ $A_3 = -1.3459\ 0196$
$\epsilon = \ 1.4327$ $\quad$ $A_4 = \ 2.7313\ 8936.$

TABLE 5.2. *Experimental and calculated* C_b, *J/K*

T_{av}, K	ΔT	C_b, J/K	Calc	Percent
58.263	5.540	24.881	24.882	−0.003
63.565	5.132	28.160	28.154	.021
68.400	4.569	31.382	31.397	−.050
73.178	5.016	34.579	34.567	.035
78.403	5.458	37.895	37.891	.011
84.151	6.067	41.330	41.332	−.003
89.961	5.590	44.566	44.570	−.008
95.780	6.119	47.565	47.573	−.017
102.108	6.573	50.582	50.576	.012
108.805	6.860	53.463	53.473	−.018
115.658	6.896	56.174	56.159	.025
122.840	7.515	58.689	58.703	−.024
130.592	8.055	61.212	61.169	.070
130.114	8.062	61.016	61.024	−.014
138.297	8.378	63.352	63.368	−.026
146.798	8.738	65.541	65.543	−.004
155.637	9.048	67.559	67.564	−.007
164.902	9.637	69.436	69.459	−.033
174.769	10.274	71.283	71.266	.024
185.191	11.128	72.984	72.976	.011
196.516	11.765	74.625	74.643	−.024
208.533	12.559	76.271	76.229	.054
221.291	13.273	77.739	77.745	−.007
234.509	13.536	79.123	79.162	−.050
247.911	13.702	80.442	80.467	−.031
254.509	13.782	81.091	81.068	.029
268.123	13.965	82.256	82.230	.033
282.114	14.621	83.338	83.329	.011
296.823	15.517	84.378	84.395	−.020

NP = 29, RMSPCT = 0.028

5.4. The Vapor Density ρ_g of Fluorine

The equation for saturated vapor [12] uses arguments $x \equiv T/T_c$ and $z \equiv (1-x)$,

$$\log_e(\rho_g/\rho_c) = A_1 \cdot (1-1/x) + A_2 \cdot z^{0.35} + \sum_{i=3}^{7} A_i \cdot z^{i-2}. \tag{5.4}$$

Constants are reported in [2],

ρ_c = 15.10 mol/liter	A_3 = −0.1880 6690
T_c = 144.31 K	A_4 = 6.2116 5939
A_1 = 4.8554 7085	A_5 = −22.9600 8970
A_2 = −1.9601 5519	A_6 = 46.9524 6230
	A_7 = −43.0650 2700

5.5. The Liquid Density ρ_l of Fluorine

The saturated liquid densities are described in [2] with the same arguments as in section 5.4 above,

$$\rho_l/\rho_c = 1 + A_0 \cdot z^{0.35} + \sum_{i=1}^{5} A_i \cdot z^i, \tag{5.5}$$

A_0 = 1.8188 1076	A_3 = 1.3728 4761
A_1 = 0.8752 3649	A_4 = −1.0133 1503
A_2 = −0.8504 5891	A_5 = 0.2738 4013.

6. References

[1] Straty, G. C., and Prydz, R., Fluorine-compatible apparatus for accurate PVT measurements, accepted for publication in The Review of Scientific Instruments.

[1a] Straty, G. C., and Prydz, R., The vapor pressure of liquid fluorine, Advances in Cryogenic Engineering **15**, 36–41 (Plenum Press, New York, N.Y., 1970).

[2] Prydz, R., Straty, G. C., and Timmerhaus, K. D., Properties of fluorine along the vapor-liquid coexistence boundary, submitted to the Journal of Chemical Physics.

[3] Goodwin, R. D., and Weber, L. A., Specific heats of oxygen at coexistence, Nat. Bur. Stand. (U.S.), **73A** (Phys. and Chem.) No. 1, 1–13 (Jan.–Feb. 1969).

[4] Straty, G. C., Bellows-sealed valve for reactive gases at moderately high pressures, Rev. Sci. Instruments **40**, No. 2, 378 (1969).

[5] The International Practical Temperature Scale of 1968, Metrologia **5**, No. 2, 35–49 (1969).

[6] Prydz, R., Timmerhaus, K. D., Stewart, R. B., The thermodynamic properties of deuterium, Advances in Cryogenic Engineering **13**, 384–396 (Plenum Press, New York, N.Y., 1968).

[7] Rowlinson, J. S., Liquids and Liquid Mixtures (Butterworths, London, 1959).

[8] Kanda, E., Determination of molecular heat, heat of fusion of condensed fluorine and the entropy of fluorine, Bull. Chem. Soc. Japan **12**, 511–520 (1937).

[9] Hu, J., White, D., and Johnston, H. L., Heat capacities, latent heats and entropies of fluorine from 13 to 85 °K, J. Am. Chem. Soc. **75**, 5642 (1953).

[10] Gibson, G. E., Giauque, W. F., J. Am. Chem. Soc. **45**, 93 (1923); Giauque, W. F., and Wiebe, R., ibid, **50**, 101 (1928); Giauque, W. F., and Johnston, H. L., ibid, **51**, 2300 (1929); Johnston, H. L., Clarke, J. T., Rifkin, E. B., and Kerr, E. C., ibid, **72**, 3933 (1950).

[11] Goodwin, R. D., Nonanalytic vapor pressure equation with data for nitrogen and oxygen, Nat. Bur. Stand. (U.S.), **73A** (Phys. and Chem.) No. 5, 487–491 (1969).

[12] Goodwin, R. D., Estimation of critical constants T_c, ρ_c from the $\rho(T)$ and $T(\rho)$ relations at coexistence, Nat. Bur. Stand. (U.S.), 74A (Phys. and Chem.), No. 2, 221–227 (1970).

(Paper 74A4–616)

JOURNAL OF RESEARCH of the National Bureau of Standards—A. Physics and Chemistry
Vol. 74A, No. 4, July–August 1970

A Theoretical Investigation of the Configurations $(3d+4s)^6\,4p$ in Neutral Manganese (Mn I)*

C. Roth**

(April 6, 1970)

Experimental levels of the configurations $(3d+4s)^6 4p$ in Mn I were compared with corresponding calculated values. On fitting 228 experimental levels by means of 20 free parameters an rms error of only 170 cm^{-1} was obtained.

It was shown that the correction parameters β and T were not significant.

Key words: Energy levels Mn I; g-factors Mn I; interactions between configurations Mn I; manganese spectrum; Mn I configurations $(3d+4s)^6 4p$.

Introduction

Theoretical investigations of odd configurations for trebly- and doubly-ionized atoms of the iron group have been reported by the author [1–4] [1, 2].

The configurations $(3d+4s)^n 4p$ have also been considered previously for the arc spectra of calcium, scandium, titanium, vanadium, and chromium [5–9].

The configurations $(d+s)^6 p$ comprise 281 terms splitting into 777 levels. In AEL [10], the experimental data include 217 odd levels of which 81 have experimental g-values. Since in the paper of Catalàn, Meggers and Garcia-Riquelme [11], 49 additional odd levels and 83 additional g-values for the odd levels are given, it is used as our source for the experimental data. In this paper, 47 odd terms splitting into 163 levels are assigned to the configurations $3d^6 4p + 3d^5 4s 4p$, 27 odd terms splitting into 72 levels are given without configuration assignments, and an additional 15 odd levels have no term designations.

After examining the final parameters obtained for the first spectra investigated thus far [6–8], it was evident that only for the parameters [3] B, B', C, C' and α is it meaningful to use linear extrapolation in order to obtain the starting values for Mn I. Then, by neglecting the values of C and α for Sc I, we have initially

$$\begin{aligned} B &= 750 \\ B' &= 830 \\ C &= 2{,}850 \\ C' &= 3{,}210 \\ \alpha = \alpha' &= 73 \end{aligned} \qquad (1)$$

For the other interaction parameters the final values obtained [8] for Cr I were used as initial values here.

The initial value for the height of the configuration $3d^5 4s 4p$ was obtained from the ^8P term.

From references [12] and [13] [4]

$$^6S(^3P)\,^8P_{\text{C.G.}} = A' - 35B' - 5G'_{ds} - G'_{ps} = 18572 \qquad (2)$$

Thus, from (1)

$$A' = 61730 \qquad (3)$$

The initial value for the height of $3d^6 4p$ was obtained from the term $(^5D)^6D$. The interaction [13] of this term with the terms:

$^4P(^5P)^6D$ equals $\dfrac{3\sqrt{2}}{10}(K-J)$

$^4D(^5D)^6D$ equals $-\sqrt{70}(H+[K-J]/10)$

$^4F(^5F)^6D$ equals $\dfrac{2\sqrt{7}}{5}(K-J)$

The diagonal matrix element for the electrostatic interaction [12, 13] of $d^6(^5D)p^6D$ is $A-21B-7F_2+6\alpha$.

*An invited paper.

**Present address: Department of Mathematics, McGill University, Montreal 110, Canada.

[1] Figures in brackets indicate literature references at the end of this paper.

[2] The reader is referred to these papers for an explanation of the method used, notation, and significance of the various parameters. The numerical values of all levels and parameters are in cm^{-1}.

[3] Unprimed parameters refer to the configuration $3d^6 4p$, primed parameters to $3d^5 4s 4p$, and doubly primed parameters to $3d^4 4s^2 4p$.

[4] See the appendix of this paper for the theoretical term designations.

However, since the matrices on tape for d^6p were those of Ishidzu and Obi [14] we had, in addition, a contribution of $-10G_1-35G_3$ (see sections 3, 4 [13]). Then, since

$$(^5\mathrm{D})z\,^6\mathrm{D}_{\mathrm{C.G.}}=41950, \qquad ^4\mathrm{P}(^5\mathrm{P})y\,^6\mathrm{D}_{\mathrm{C.G.}}=47750$$

$$^4\mathrm{D}(^5\mathrm{D})x\,^6\mathrm{D}_{\mathrm{C.G.}}=52840, \qquad ^4\mathrm{F}(^5\mathrm{F})w\,^6\mathrm{D}_{\mathrm{C.G.}}=62760$$

we obtain by using second-order perturbation theory

$$A-21B-7F_2-10G_1-35G_3+6\alpha-\frac{9(K-J)^2}{50\times 5{,}800}$$

$$-\frac{70}{10{,}890}\left(H+\frac{[K-J]}{10}\right)^2-\frac{28(K-J)^2}{25\times 20{,}810}=41950 \qquad (4)$$

From the previously determined values of the other parameters we obtain

$$A=61800 \qquad (5)$$

Since in V I and Cr I [7–8], the results were greatly improved by considering the configuration $3d^{n-2}4s^24p$ and its interactions with $3d^{n-1}4s4p$ and $3d^n4p$, a similar investigation was attempted for Mn I. Racah and Shadmi [15] found that the parameter D'', the difference between the weighted averages of the terms $3d^{n-2}4s^2$ and $3d^{n-1}4s$ in the second spectra of the iron group, was a linear function of the atomic number with a quadratic correction. By using the values of D''(Sc), D''(Ti), D''(V), and D''(Cr) [6–8], a parabola was fitted and extrapolated to obtain

$$D''(\mathrm{Mn})=25960. \qquad (6)$$

The expressions (7), (8), and (9) of reference [7] must be modified for the complementary configurations. The matrices of B, C, and α for the configurations d^np, $d^{n-1}sp$, and $d^{n-2}s^2p$ are equal to the corresponding matrices of the complementary configurations $d^{10-n}s^2p$, $d^{11-n}sp$, and $d^{12-n}p$, respectively [13]. Also, the matrices of G'_{ds} and G'_{ps} for $d^{n-1}sp$ are equal to the corresponding matrices of $d^{11-n}sp$. As the weighted average of the terms of d^np is given by $M(d^np)=M(d^9s^2p)=F_0+(G_1+7/2G_3)$, as given in eq (6) of reference [16], we obtain by comparing with eqs (9), (8), and (7) of [7]:

$$M(d^{12-n}p)=A+(7/18)(n-2)(n-3)(C-2B)$$
$$+(2/3)(n-2)(12-n)\alpha+(n-2)(G_1+7/2G_3) \qquad (7)$$

$$M'(d^{11-n}sp)=A'+(7/18)(n-1)(n-2)(C'-2B')$$
$$+(2/3)(n-1)(11-n)\alpha'$$
$$+(n-1)(G'_1+7/2G'_3-G'_{ds}/2-G'_{ps}/2) \qquad (8)$$

$$M''(d^{10-n}s^2p)=A''+(7/18)(n)(n-1)(C''-2B'')$$
$$+2/3(n)(10-n)\alpha''+n(G''_1+7/2G''_3) \qquad (9)$$

For the configuration d^5sp, when d^5 is considered as comprising five electrons, eq (8), [7] should be used to obtain the center of gravity of the configuration, whereas for d^5 consisting of five holes in the d-shell, eq (7) is the appropriate expression. As expected, the two values differ by $-10G_1-35G_3$, [13].

By assuming that the parameters of the three configurations are in arithmetic progression, we obtain from eq (9), [7]

$$M''(d^4s^2p)=A''+8110 \qquad (10)$$

Since in the calculation of the matrices for the configurations $(d+s)^6p$, the configuration d^5sp was considered as five holes in the d-shell we obtain from (8)

$$M'(d^5sp)=69420 \qquad (11)$$

Thus from (6), (10), (11), and (5)

$$A''=87270 \qquad (12)$$

Results and Discussion

Four iterations were required to reach convergence of the diagonalization and the least squares procedures. Finally the parameter values varied by less than their standard deviations.

The effect of β here was even smaller than for Cr I, [8]. When β was allowed to change freely, the rms error was 167 cm^{-1} with

$$\beta=\beta'=\beta''=-56\pm 44 \qquad (13)$$

With β eliminated, the rms error remained at 167 cm^{-1}.

In the least-squares solution of the final iteration in the "uniform treatment"[5] (see ref. [6]), 67 experimental terms splitting into 219 levels and 9 unclassified odd levels were inserted to yield an rms error of only 170 cm^{-1}. The experimental and calculated values of the levels and g-factors obtained from the final least-squares solution of the uniform treatment, are compared in table A of the Appendix. The calculated values, percentage compositions, and g-factors for 469 of the 777 predicted levels are given. All calculated levels up to 81000 cm^{-1} are included. The terms based on B^1S, B^3P, B^1D, B^3F and B^1G of d^6p as well as the terms obtained from $^2S+^1P$, $^2P+^{1,3}P$, $B^2D+^{1,3}P$, $C^2D+^{1,3}P$, B^2F+^1P, A^2G+^1P, $B^2G+^{1,3}P$ and $^2H+^1P$ are not inserted since they are very high and strongly mixed with terms of d^4s^2p. The lowest predicted levels of d^4s^2p based on $d^4s^2\,^5D$ are included, but must be considered only as rough approximations due to the high uncertainty in A''.

The final parameters with their standard errors in the uniform treatment are given in table 1.

Since the value of G'_{ps} is much larger than that of G'_{ds} the $p-s$ interaction is the stronger. Consequently,

[5] The parameters A, A', A'', G'_{ds}, and G'_{ps} are allowed to change freely. The parameters B, C, F_2, and G_1 are in arithmetic progression. The parameters G_3, α, ζ_d, and ζ_p are kept equal, and for the parameters of the interactions between configurations, H' is kept equal to H, J' to J, G to G'_{ds}, and $K'=K+764$ (fixed difference).

the terms of d^5sp are coupled as $d^5(v_1S_1L_1)sp(^{1,3}P)SL$ and not $d^5s(S_2L_1)pSL$ as given in AEL.

TABLE 1. *Parameters for* Mn I $(3d+4s)^6 4p$

Parameter	Initial value	Final value
A	61800	63216 ± 292
A'	61730	63028 ± 318
A''	87270	89176 ± 1433
B	750	800 ± 14
B'	830	861 ± 4
B''	910	922 (Arith. Progress.)
C	2850	2772 ± 17
C'	3210	3140 ± 9
C''	3570	3508 (Arith. Progress.)
$G_{dz} = G$	1590	1532 ± 22
F_2	187	193 ± 7
F_2'	275	314 ± 8
F_2''	363	435 (Arith. Progress.)
G_1	224	227 ± 7
G_1'	236	245 ± 6
G_1''	248	263 (Arith. Progress.)
$G_3 = G_3' = G_3''$	16	18 ± 1
G_{ps}'	6155	6631 ± 60
$\alpha = \alpha' = \alpha''$	73	73 ± 2
$H = H'$	157	70 ± 6
$J = J'$	954	1294 ± 34
K	2311	2599 ± 36
K'	3011	3363 (Fixed Diff.)
$\zeta_d = \zeta_d' = \zeta_d''$	247	321 ± 28
$\zeta_p = \zeta_p' = \zeta_p''$	184	212 ± 60
rms error		169.9

The three high experimental terms $z\,^2$K, $x\,^2$I and $v\,^2$H are above 68500, and were not included in the least-squares solution. It is doubtful to which corresponding theoretical terms they should be assigned, and, in addition, 5 of these 6 levels are given with question marks [11]. Below 68500 the following 16 levels were not included:

1. The three levels of $3d^6(a\,^5\mathrm{D})4p\ x\,^6\mathrm{P}$
2. The three levels of $3d^5 4s(b\,^5\mathrm{D})4p\ w\,^4\mathrm{P}$
3. The two levels of $y\,^2\mathrm{I}$
4. The two levels of $x\,^2\mathrm{H}$
5. The six unclassified odd levels $55924_{2^1/_2}$, $63320_{3^1/_2}$?, $63372_{2^1/_2}$, $66600_{3^1/_2}$, $66655_{2^1/_2}$?, and $66910_{2^1/_2}$?.

The calculated levels of $(^5\mathrm{D})x\,^6\mathrm{P}$ are on the average higher by 750 than the experimental levels of $x\,^6\mathrm{P}$. Most, or all of this difference can be attributed to the interaction between $3d^6(a\,^5\mathrm{D})4p\ x\,^6\mathrm{P}$ and $3d^54s(a\,^7\mathrm{S})5p\ w\,^6\mathrm{P}$, since the difference between the unperturbed terms $x\,^6\mathrm{P}$ and $w\,^6\mathrm{P}$ is very small. Since this interaction was not considered explicitly here, the levels of $x\,^6\mathrm{P}$ have not been inserted.

Below 62000 five ^{4}P terms are predicted while six experimental terms $z\,^4\mathrm{P}$, $y\,^4\mathrm{P}$, $x\,^4\mathrm{P}$, $w\,^4\mathrm{P}$, $v\,^4\mathrm{P}$, and $u\,^4\mathrm{P}$ are given, [11]. The lower terms $z\,^4\mathrm{P}$, $y\,^4\mathrm{P}$, and $x\,^4\mathrm{P}$ corresponded very closely to the theoretical terms with the same designations. The others were not inserted until the least-squares solution of the last iteration. Then, it became apparent that the superfluous term is $w\,^4\mathrm{P}$. Moreover, by noting the experimental values of the terms $3d^54s(a\,^7\mathrm{S})4p\ z\,^8\mathrm{P}$, $3d^54s(a\,^7\mathrm{S})5p\ y\,^8\mathrm{P}$ and $3d^54s(a\,^5\mathrm{S})4p\ z\,^4\mathrm{P}$, by assuming that the values of the parameters for $(3d+4s)^6 5p$ are about half of those for $(3d+4s)^6 4p$, and by performing a calculation similar to that of $w\,^5\mathrm{P}$ of Cr I (see ref. [7]), the term $3d^54s(a\,^5\mathrm{S})5p\,^4\mathrm{P}$ is predicted at the height of 55500, i.e., about the same as $w\,^4\mathrm{P}$. Thus $w\,^4\mathrm{P}$ should be assigned as $3d^5(^6\mathrm{S})4s5p(^3\mathrm{P})\,^4\mathrm{P}$.

The only term to which the levels $y\,^2$I could conceivably be assigned is $^4\mathrm{F}(^3\mathrm{P})^6\mathrm{G}$ with deviations of about $-400cm^{-1}$. However, as the experimental levels $y\,^2$I are based on combinations which include doublets, [11], they were not assigned to ^{6}G.

The level $x\,^2\mathrm{H}_{5^1/_2}$ could conceivably be fitted to the predicted level $^2\mathrm{I}(^3\mathrm{P})\,^2\mathrm{I}_{5^1/_2}$. However, rather than break up the term $x\,^2$H with this doubtful assignment. both levels have been neglected.

None of the 15 miscellaneous odd levels was used in the least-squares calculation until the last iteration. The six levels listed as item 5 above, did not have corresponding experimental levels to which they could be assigned.

The following changes in assignment have been made.

1. $d^5s(b\,^3\mathrm{P})pv\,^4\mathrm{P} \longrightarrow {}^4\mathrm{D}(^3\mathrm{P})\,^4\mathrm{P}$
2. $d^6(a\,^3\mathrm{H})py\,^4\mathrm{G} \longrightarrow {}^4\mathrm{G}(^1\mathrm{P})\,^4\mathrm{G}$
3. $d^6(a\,^3\mathrm{P})pw\,^4\mathrm{D}_{5/2,\,7/2} \longrightarrow (\mathrm{A}^3\mathrm{F})\,^4\mathrm{D}_{5/2,\,7/2}$
4. $d^6(a\,^3\mathrm{P})pz\,^2\mathrm{D}_{3/2,\,5/2} \longrightarrow (\mathrm{A}^3\mathrm{P})^4\mathrm{D}_{3/2,\,5/2}$
5. $d^6(a\,^3\mathrm{P})pw\,^4\mathrm{D}_{3/2} \longrightarrow (\mathrm{A}^3\mathrm{P})^2\mathrm{D}_{3/2}$
6. $d^6(\mathrm{a}\,^3\mathrm{F})pv\,^4\mathrm{D}_{5/2} \longrightarrow (\mathrm{A}^3\mathrm{P})^2\mathrm{D}_{5/2}$
7. $d^6(a\,^3\mathrm{F})pv\,^4\mathrm{D}_{7/2} \longrightarrow (\mathrm{A}^3\mathrm{P})^4\mathrm{D}_{7/2}$
8. $w\,^4\mathrm{G}_{5/2,\,7/2} \longrightarrow (\mathrm{A}^3\mathrm{F})\,^2\mathrm{F}_{5/2,\,7/2}$
9. $w\,^4\mathrm{G}_{9/2} \longrightarrow (\mathrm{A}^3\mathrm{F})\,^2\mathrm{G}_{9/2}$
10. $w\,^4\mathrm{G}_{11/2} \longrightarrow (^3\mathrm{H})^2\mathrm{H}_{11/2}$
11. $z\,^2\mathrm{F}_{5/2,\,7/2} \longrightarrow {}^4\mathrm{G}(^1\mathrm{P})\,^4\mathrm{F}_{5/2,\,7/2}$
12. $y\,^2\mathrm{G}_{9/2} \longrightarrow {}^4\mathrm{G}(^1\mathrm{P})\,^4\mathrm{F}_{9/2}$
13. $y\,^2\mathrm{F}_{5/2,\,7/2} \longrightarrow (^3\mathrm{G})^4\mathrm{G}_{5/2,\,7/2}$
14. $x\,^2\mathrm{F}_{5/2,\,7/2} \longrightarrow \mathrm{A}^2\mathrm{F}(^3\mathrm{P})^4\mathrm{G}_{5/2,\,7/2}$
15. $y\,^2\mathrm{H}_{9/2} \longrightarrow \mathrm{A}^2\mathrm{F}(^3\mathrm{P})\,^4\mathrm{G}_{9/2}$
16. $d^6(a\,^3\mathrm{H})pz\,^2\mathrm{H}_{11/2} \longrightarrow \mathrm{A}^2\mathrm{F}(^3\mathrm{P})^4\mathrm{G}_{11/2}$
17. $d^5s(a\,^5\mathrm{D})pw\,^6\mathrm{D}_{1/2-9/2} \longrightarrow {}^4\mathrm{F}(^3\mathrm{P})^6\mathrm{F}_{1/2-9/2}$
18. $d^6(a\,^3\mathrm{G})pw\,^4\mathrm{H} \longrightarrow {}^4\mathrm{G}(^1\mathrm{P})^4\mathrm{H}$
19. $w\,^2\mathrm{D}_{3/2,\,5/2} \longrightarrow {}^4\mathrm{P}(^1\mathrm{P})\,^4\mathrm{D}_{3/2,\,5/2}$
20. $x\,^2\mathrm{G}_{7/2,\,9/2} \longrightarrow \mathrm{A}^2\mathrm{F}(^3\mathrm{P})^4\mathrm{F}_{7/2,\,9/2}$
21. $u\,^2\mathrm{G}_{7/2,\,9/2} \longrightarrow \mathrm{A}^2\mathrm{G}(^3\mathrm{P})\,^4\mathrm{F}_{7/2,\,9/2}$

In the changes 1, 2, and 18 the theoretical assignments of the core $(d+s)^6$ did not correspond to the experimental assignments. However, in each case the theoretical eigenfunctions contained, also, a considerable mixture (20%–30%) of the experimental term.

The eigenfunctions of the levels of $(\mathrm{A}^3\mathrm{P})^4\mathrm{D}$, $(\mathrm{A}^3\mathrm{F})^4\mathrm{D}$, and $(\mathrm{A}^3\mathrm{P})^2\mathrm{D}$ are mixed quite strongly. When the levels of these three terms were fitted so that the experimental and theoretical designations corresponded, the deviations were very high (600–700). After several variations, taking into consideration the deviations of the levels, the correspondence of the g-factors and the splitting of the terms, it was found that with the

383-876 O - 70 - 4

changes 3, 4, 5, 6, and 7, the most favorable results were obtained.

It is apparent that the levels of $w\,^4G$ could not be assigned to a theoretical term ^4G (see table A of the appendix). After introducing the changes 8, 9, and 10, the theoretical term $(A\,^3F)^2F$ has deviations of 110 and 77, with the experimental g-factor of 1.13 for $w\,^4G_{7/2}$, corresponding closely to the calculated value of 1.057 for $(A\,^3F)^2F_{7/2}$. The theoretical term $(A\,^3F)y\,^2G$ has deviations of 103 and 188; the experimental g-factors of 0.93 and 1.020 correspond to the calculated values of 0.940 and 0.941, respectively. It should be noted that had $y\,^2G_{9/2}$ been assigned to $(A\,^3F)y\,^2G_{9/2}$, the deviations would have been about 103 and 418. Finally, the level $(^3H)^2H_{11/2}$ has a deviation of 128 and the experimental g-factor for $w\,^4G_{11/2}$ corresponds to the calculated value of 1.087 for $(^3H)^2H_{11/2}$.

The changes 11 and 12 were performed in the last iteration. The calculated levels of $^4G(^1P)^4F_{5/2,\,7/2,\,9/2}$ correspond closely to the experimental levels $z\,^2F_{5/2,\,7/2}$ and $y\,^2G_{9/2}$ (see table A of the appendix).

Changes 13 and 14 were performed since the levels of $y\,^2F$ and $x\,^2F$ could not be assigned to theoretical terms ^2F, and furthermore, the theoretical terms $(^3G)^4G$ and $A^2F(^3P)^4G$ had until then no corresponding experimental levels.

By using the changes 15 and 16, not only are the deviations for $A^2F(^3P)^4G$ and $(^3H)^2H$ lower, but also the splitting of the experimental levels correspond well to the intervals between the experimental levels assigned to these two terms.

Originally, the levels of $w\,^6D$ were assigned to the theoretical term with the same designation. However, the average deviation then was over 600, whereas from the change 17, the average deviation for the levels of $^4F(^3P)^6F$ becomes only 101. In addition, the four unclassified odd levels at 63584, 63524, 63546, and 63375 can now be assigned to the theoretical levels $^4F(^3P)^6D_{3/2,\,5/2,\,7/2,\,9/2}$ with an average deviation of only 63.

The theoretical term ^2D nearest to the experimental term $w\,^2D$ is $A^2F(^3P)^2D$ at 67500. Thus, the levels $w\,^2D$ were assigned to $^4P(^1P)^4D_{3/2,\,5/2}$. Although the deviations are 322 for both levels, the experimental g-factor of 1.30 for $w\,^2D_{5/2}$ corresponds closely to the calculated g-factor of 1.366 for $^4P(^1P)^4D_{5/2}$.

The experimental terms $x\,^2G$ and $u\,^2G$ could not be assigned to theoretical ^2G terms (see table A of the appendix). The changes 20 and 21 reduce the deviations for $A^2F(^3P)^4F_{7/2,\,9/2}$ to 76 and 28; the experimental g-factor of 1.307 for $x\,^2G_{9/2}$ corresponds to the calculated value of 1.317 for $A^2F(^3P)^4F_{9/2}$. For $A^2G(^3P)^4F_{7/2,\,9/2}$ the deviations are 154 and 157; the experimental g-factor of 1.320 for $u\,^2G_{9/2}$ corresponds to the calculated value of 1.321 for $A^2G(^3P)^4F_{9/2}$. Table 2 below indicates how the 9 unclassified odd levels inserted were assigned.

It was ascertained that each of the 9 unclassified odd levels is based upon at least 3 combinations with even levels [11]. It should be emphasized that all those levels whose experimental and theoretical assignments did not correspond, as well as the unclassified levels, were not inserted into the least-squares calculation until the parameters were determined by the other levels (whose assignments were not questioned).

TABLE 2. *Unclassified odd levels of* Mn I

Level	Assignment	Deviation	Obs. g-factor	Calc. g-factor
$61744_{11/2}$	$(^3G)^4G_{11/2}$	−20		1.252
$63375_{9/2}$	$^4F(^3P)^6D_{9/2}$	−15		1.547
$63524_{5/2}$	$^4F(^3P)^6D_{5/2}$	54		1.632
$63546_{7/2}$	$^4F(^3P)^6D_{7/2}$	115		1.573
$63584_{3/2}$	$^4F(^3P)^6D_{3/2}$	69		1.789
$65769_{9/2}$	$(^3G)^2G_{9/2}$	2	1.12	1.115
$66504_{3/2}$	$^4P(^1P)^4S_{3/2}$	177		1.975
$66981_{7/2}$	$^4D(^1P)^4D_{7/2}$	−283	1.33	1.421
$67009_{5/2}$	$^4D(^1P)^4P_{5/2}$	−127		1.565

For 25 of the 27 experimental terms given without configuration assignments [11], the theoretical assignments are given in table A in the appendix ($y\,^2I$ and $x\,^2H$ were not inserted).

For the lower-lying levels there was excellent agreement between the experimental and calculated Landé g-factors. The experimental g-factors of 0.826 for $x\,^4D_{3/2}$, 1.770 for $z\,^4S_{3/2}$, 1.94 for $u\,^4P_{1/2}$ and 0.46 for $v\,^2G_{7/2}$ are quite different from the theoretical g-factors. However, as the calculated g-factors for the above 4 levels are very close to the theoretical values, the discrepancies are rather large. The experimental g-factor of 1.043 for $y\,^6F_{7/2}$ seems to be a misprint as the g-factor quoted in AEL for this level is 1.403, and, furthermore, the theoretical and calculated g-factors are 1.397 and 1.411, respectively.

Below 68300 (the limit of the experimental data inserted) there are 326 predicted levels. Thus, excluding $w\,^6P$, there are 95 theoretical levels without corresponding experimental levels to assign to them. The lowest of these are the levels of $^4G(^3P)^3G$ and $^4G(^3P)^6H$ at around 46000. It is hoped that the present theoretical investigation will provide a stimulus for further experimental work on this very complex spectrum.

In table 3 the orders of the submatrices of $(d+s)^6p$ are given.

TABLE 3. *Orders of the submatrices of* $(d+s)^6p$

J	Order
1/2	85
3/2	147
5/2	169
7/2	155
9/2	113
11/2	67
13/2	30
15/2	10
17/2	1

Appendix

The entries in table A of the Appendix may be described as follows: In the column "Name" the calculated designation of the term is given. Whenever the terms of the parent d^n have different seniorities these are denoted by the letters A and B (for $d^5\ ^2$D by A, B, and C), the lower calculated term being designated by A. The terms of d^5sp are denoted by $d^5\nu_1 S_1 L_1(sp\ ^{1,3}\mathrm{P})SL$. The terms of d^6p are differentiated from those of d^4s^2p by using a star for the latter terms.

The entries in the columns "J", "Obs. Level cm^{-1}", "Calc. Level cm^{-1}", "Obs. g" and "Calc. g", are self-evident. In the column "Percentage", for each calculated level either the three highest contributions or all those contributions exceeding six percent are given.

Whenever the experimental and calculated term designations differ, the experimental designation is entered in the column "CMG" (Catalan, Meggers, Garcia-Riquelme, [11]) with the notation of C. E. Moore, [10]. In many instances the exchanges involve complete terms rather than isolated levels. Unless specified otherwise, the entries in the column "CMG" pertain to exchanges in terms.

The column "O–C" gives the difference between the observed and calculated values of the levels.

The entries are in increasing energy of the calculated terms.

TABLE A. *Observed and Calculated Levels of* Mn I $(3d+4s)^6 4p$

Name	J	Percentage	CMG		Obs. Level (cm^{-1})	Calc. Level (cm^{-1})	O–C	Obs. g	Calc. g
			Config.	Desig.					
^{6}S(^{3}P)^{8}P	5/2	100	$3d^54s(a\ ^7\mathrm{S})4p$	$z\ ^8$P	18402	18468	−66	2.284	2.285
	7/2	100			18532	18573	−41	1.938	1.936
	9/2	100			18705	18712	−7	1.779	1.778
^{6}S(^{3}P) ^{6}P	3/2	97	$3d^54s(a\ ^7\mathrm{S})4p$	$z\ ^6$P	24779	24816	−37	2.364	2.400
	5/2	97			24788	24809	−21	1.875	1.886
	7/2	97			24802	24799	3	1.714	1.714
^{6}S(^{3}P) ^{4}P	1/2	98	$3d^54s(a\ ^5\mathrm{S})4p$	$z\ ^4$P	31125	31077	48	2.668	2.666
	3/2	98			31076	31023	53	1.732	1.733
	5/2	98			31001	30940	61	1.600	1.600
^{6}S(^{1}P) ^{6}P	3/2	88+10(^{5}D)^{6}P	$3d^54s(a\ ^5\mathrm{S})4p$	$y\ ^6$P	35690	35742	−52	2.400	2.399
	5/2	88+10(^{5}D)^{6}P			35726	35770	−44	1.886	1.885
	7/2	87+11(^{5}D)^{6}P			35770	35800	−30	1.712	1.714
(^{5}D) ^{6}D	1/2	95+4^{4}D(^{3}P)^{6}D			42199	42334	−135	3.317	3.325
	3/2	95+4^{4}D(^{3}P)^{6}D			42144	42256	−112	1.867	1.862
	5/2	94+4^{4}D(^{3}P)^{6}D			42054	42131	−77	1.653	1.654
	7/2	94+4^{4}D(^{3}P)^{6}D			41933	41966	−33	1.587	1.585
	9/2	95+4^{4}D(^{3}P)^{6}D			41789	41781	8	1.556	1.554
(^{5}D) ^{6}F	1/2	81+17^{4}G(^{3}P)^{6}F			43673	43580	93	−0.602	−0.659
	3/2	80+17^{4}G(^{3}P)^{6}F			43644	43547	97	1.068	1.068
	5/2	80+16^{4}G(^{3}P)^{6}F			43596	43490	106	1.310	1.315
	7/2	80+15^{4}G(^{3}P)^{6}F			43524	43405	119	1.395	1.396
	9/2	80+15^{4}G(^{3}P)^{6}F			43429	43290	139	1.431	1.433
	11/2	83+15^{4}G(^{3}P)^{6}F			43314	43154	160	1.464	1.454
(^{5}D)^{4}F	3/2	90+6^{4}G(^{3}P)^{4}F			44815	45136	−321	0.400	0.408
	5/2	89+6^{4}G(^{3}P)^{4}F			44696	44975	−279	1.030	1.037
	7/2	88+6^{4}G(^{3}P)^{4}F			44523	44746	−223	1.240	1.245
	9/2	89+6^{4}G(^{3}P)^{4}F			44289	44442	−153	1.317	1.336
^{4}G(^{3}P)^{6}G	3/2	98				45613			0.002
	5/2	97				45619			0.848
	7/2	95				45630			1.133
	9/2	94				45647			1.264
	11/2	94				45671			1.336
	13/2	95				45703			1.381
(^{5}D)^{4}D	1/2	93			46170	46070	100	0.000	0.006
	3/2	92			46084	45960	124	1.200	1.202
	5/2	89			45941	45768	173	1.372	1.380
	7/2	82+8(^{5}D)^{6}P			45754	45481	273	1.427	1.458

TABLE A. *Observed and Calculated Levels of* Mn I $(3d+4s)^6 4p$ – Continued

Name	J	Percentage	CMG		Obs. Level (cm^{-1})	Calc. Level (cm^{-1})	O–C	Obs. g	Calc. g
			Config.	Desig.					
$(^5D)^6P$	3/2	$67+21\,^4P(^3P)^6P$			(45259)	46136		(2.399)	2.395
	5/2	$66+20\,^4P(^3P)^6P+5\,^4D(^3P)^6P$			(45156)	45924		(1.885)	1.874
	7/2	$60+17\,^4P(^3P)^6P+11(^5D)^4D$			(44994)	45640		(1.717)	1.680
$^4G(^3P)^6H$	5/2	98				46012			0.296
	7/2	97				46058			0.836
	9/2	96				46111			1.079
	11/2	96				46165			1.209
	13/2	97				46215			1.285
	15/2	100				46255			1.333
$(^5D)^4P$	1/2	91			47299	47288	11	2.666	2.661
	3/2	90			47155	47112	43	1.732	1.729
	5/2	90			46901	46808	93	1.595	1.596
$^4P(^3P)^6D$	1/2	$83+15\,^4D(^3P)^6D$	$3d^54s(a\,^5P)4p$	$y\,^6D$	47452	47648	−196	3.174	3.311
	3/2	$82+14\,^4D(^3P)^6D$			47467	47686	−219		1.852
	5/2	$80+14\,^4D(^3P)^6D$			47754	47754	0	1.820	1.642
	7/2	$77+12\,^4D(^3P)^6D+5\,^4G(^3P)^6F$			47775	47864	−89	1.594	1.570
	9/2	$63+18\,^4G(^3P)^6F+9\,^4D(^3P)^6D$			47904	48020	−116	1.540	1.522
$^4G(^3P)^6F$	1/2	$76+19(^5D)^6F$	$3d^54s(a\,^5G)4p$	$y\,^6F$	48318	48272	46	−0.496	−0.650
	3/2	$76+18(^5D)^6F$			48301	48261	40	1.068	1.078
	5/2	$76+17(^5D)^6F$			48271	48241	30	1.319	1.326
	7/2	$73+16(^5D)^6F+7\,^4P(^3P)^6D$			48226	48212	14	1.403	1.411
	9/2	$60+23\,^4P(^3P)^6D+12(^5D)^6F$			48168	48195	−27	1.432	1.465
	11/2	$80+16(^5D)^6F$			48021	48025	−4	1.460	1.454
$^4P(^3P)^6S$	5/2	99				48210			1.997
$^4P(^3P)^6P$	3/2	$69+20(^5D)^6P$	$3d^54s(a\,^5P)4p$	$v\,^6P$	50099	50084	15	2.398	2.392
	5/2	$65+20(^5D)^6P+8\,^4D(^3P)^6P$			50013	49925	88	1.888	1.879
	7/2	$62+19(^5D)^6P+13\,^4D(^3P)^6P$			49888	49691	197	1.711	1.712
$^4G(^3P)^4H$	7/2	97	$3d^54s(a\,^5G)4p$	$z\,^4H$	50065	50189	−124		0.667
	9/2	96			50073	50199	−126		0.970
	11/2	96			50081	50211	−130		1.133
	13/2	96			50095	50226	−131	1.22	1.231
$^4G(^3P)^4F$	3/2	92	$3d^54s(a\,^5G)4p$	$y\,^4F$	50383	50475	−92		0.401
	5/2	92			50373	50474	−101	1.03	1.029
	7/2	92			50359	50475	−116	1.242	1.238
	9/2	92			50341	50476	−135	1.318	1.333
$^4D(^3P)^6F$	1/2	$92+5\,^4G(^3P)^6F$	$3d^54s(a\,^3D)4p$	$x\,^6F$	50819	50761	58	−0.62	−0.650
	3/2	92			50863	50805	58	1.07	1.073
	5/2	92			50931	50873	58	1.316	1.319
	7/2	92			51015	50952	63		1.400
	9/2	93			51100	51027	73		1.435
	11/2	94			51169	51074	95		1.453
$^4G(^3P)^4G$	5/2	92	$3d^54s(a\,^5G)4p$	$z\,^4G$	51516	51478	38		0.573
	7/2	92			51531	51499	32		0.985
	9/2	92			51546	51524	22		1.172
	11/2	92			51561	51552	9	1.273	1.273
$^4P(^3P)^4P$	1/2	$72+15\,^4D(^3P)^4P$	$3d^54s(a\,^5P)4p$	$x\,^4P$	51553	51647	−94	2.664	2.684
	3/2	$71+16\,^4D(^3P)^4P$			51446	51529	−83	1.728	1.735
	5/2	$70+18\,^4D(^3P)^4P$			51305	51370	−65	1.591	1.600
$^4D(^3P)^6P$	3/2	$86+7\,^4P(^3P)^6P$	$3d^54s(b\,^5D)4p$	$u\,^6P$	52015	52275	−260		2.370
	5/2	$68+19\,^4D(^3P)^6D+7\,^4P(^3P)^6P$			52129	52334	−205		1.832
	7/2	$43+30\,^4D(^3P)^6D+13\,^4P(^3P)^6P$			52253	52320	−67	1.71	1.639
$^4D(^3P)^6D$	1/2	$75+15\,^4P(^3P)^6D$	$3d^54s(a\,^5D)4p$	$x\,^6D$	52883	52681	202		3.240
	3/2	$71+14\,^4P(^3P)^6D$			52884	52651	233		1.860
	5/2	$56+18\,^4D(^3P)^6P+10\,^4P(^3P)^6D$			52884	52656	228		1.693

TABLE A. *Observed and Calculated Levels of* Mn I $(3d+4s)^6 4p$ — Continued

Name	J	Percentage	CMG		Obs. Level (cm^{-1})	Calc. Level (cm^{-1})	O–C	Obs. g	Calc. g
			Config.	Desig.					
	7/2	$47+37\,^4D(^3P)^6P+8\,^4P(^3P)^6D$			52870	52705	165	1.57	1.649
	9/2	$82+13\,^4P(^3P)^6D$			52748	52318	440	1.552	1.555
$^4P(^3P)^4D$	1/2	86	$3d^54s(a\,^5P)4p$	$y\,^4D$	53101	52995	106		0.058
	3/2	85			53103	53032	71		1.224
	5/2	84			53109	53078	31		1.384
	7/2	86			53124	53136	−12	1.423	1.437
$^4G(^3P)^2H$	9/2	97				53637			0.910
	11/2	97				53579			1.091
$^4G(^3P)^2F$	5/2	93				53803			0.858
	7/2	93				53850			1.144
$^4P(^3P)^4S$	3/2	$76+19(A^3P)^4S$	$3d^54s(a\,^5P)4p$	$z\,^4S$	54219	54099	120	1.770	1.966
$^4P(^3P)^2P$	1/2	$46+33\,^4D(^3P)^4D+10\,^4D(^3P)^2D$				54729			0.404
	3/2	$57+14\,^4D(^3P)^2P+14\,^4D(^3P)^4D$				54603			1.336
$^4D(^3P)^4D$	1/2	$50+31\,^4P(^3P)^2P$				53377			0.275
	3/2	$67+13\,^4P(^3P)^2P$	$3d^54s(b\,^5D)4p$	$x\,^4D$	55280	55172	108	0.826	1.202
	5/2	84			55186	55002	184	1.365	1.371
	7/2	$86+7\,^4F(^3P)^4D$			55108	54894	214	1.407	1.427
$^4D(^3P)^4F$	3/2	84				55403			0.450
	5/2	88				55469			1.040
	7/2	$48+41\,^4G(^3P)^2G$				55446			1.076
	9/2	$67+24\,^4G(^3P)^2G$				55456			1.273
$^4G(^3P)^2G$	7/2	$47+42\,^4D(^3P)^4F$				55493			1.054
	9/2	$65+25\,^4D(^3P)^4F$				55490			1.171
$^4P(^3P)^2D$	3/2	$82+6(A^3P)^2D+6(A^3F)^2D$				56660			0.783
	5/2	$81+7(A^3P)^2D$				56507			1.190
$^4D(^3P)^4P$	1/2	$63+21\,^4P(^3P)^4P$	$3d^54s(b\,^3P)4p$	$v\,^4P$	57228	57402	−174	2.671	2.639
	3/2	$48+20(A^3P)^4S+14\,^4P(^3P)^4P$			57361	57607	−246	1.736	1.819
	5/2	$56+26\,^4P(^3P)^4P$			57487	57717	−230	1.590	1.596
$(A^3P)^4S$	3/2	$32+32\,^4P(^3P)^4S+15\,^4D(^3P)^4P$	$3d^54s(b\,^3P)4p$	$y\,^4S$	57512	57520	−8	2.000	1.900
$^4G(^1P)^4G$	5/2	$57+30(^3H)^4G$	$3d^6(a\,^3H)4p$	$y\,^4G$	58160	58039	121	0.578	0.575
	7/2	$56+31(^3H)^4G$			58137	58016	121	0.980	0.984
	9/2	$55+32(^3H)^4G$			58110	57990	120	1.168	1.170
	11/2	$54+35(^3H)^4G$			58075	57955	120	1.269	1.271
$^4D(^3P)^2D$	3/2	$78+8(A^3P)^2D+5\,^4F(^3P)^2D$				58359			0.807
	5/2	$64+23(A^3P)^2D$				58057			1.202
$^4P(^3P)^2S$	1/2	$84+10(A^3P)^2S$				58450			2.001
$(^3H)^4H$	7/2	$60+24\,^4G(^3P)^4H+11\,^2I(^3P)^4H$			58520	58563	−43	0.665	0.674
	9/2	$59+23\,^4G(^3P)^4H+11\,^2I(^3P)^4H$			58486	58534	−48	0.968	0.970
	11/2	$60+24\,^4G(^3P)^4H+11\,^2I(^3P)^4H$			58427	58481	−54	1.133	1.130
	13/2	$62+24\,^4G(^3P)^4H+12\,^2I(^3P)^4H$			58339	58404	−65	1.228	1.228
$(^3H)^4I$	9/2	$49+47\,^2I(^3P)^4I$			58867	58902	−35	0.73	0.736
	11/2	$49+45\,^2I(^3P)^4I$			58851	58901	−50		0.970
	13/2	$50+43\,^2I(^3P)^4I$			58843	58903	−60	1.09	1.109
	15/2	$55+44\,^2I(^3P)^4I$			58853	58918	−65		1.199
$^4D(^3P)^2F$	5/2	$59+15(A^3P)^2D+7\,^4D(^3P)^2D$				59033			0.973
	7/2	$77+8(^3G)^2F+8(A^3F)^2F$				58930			1.147
$(A^3P)^4P$	1/2	$55+15\,^4D(^3P)^4P+11A^2D(^3P)^4P$			59568	59341	227	1.94	2.240
	3/2	$46+14\,^4D(^3P)^4P+10A^2D(^3P)^4P$			59384	59140	244	1.608	1.600
	5/2	$52+21\,^4D(^3P)^4P+10A^2D(^3P)^4P$			59117	58852	265	1.558	1.566

TABLE A. *Observed and Calculated Levels of* Mn I $(3d+4s)^6 4p$ – Continued

Name	J	Percentage	CMG		Obs. Level (cm^{-1})	Calc. Level (cm^{-1})	O – C	Obs. g	Calc. g
			Config.	Desig.					
$(A^3F)^4D$	1/2	$44+23^4P(^3P)^4D+9(A^3P)^4D$			59527	59562	−35		0.374
	3/2	$39+20^4P(^3P)^4D+8(A^3P)^4D$			59528	59515	13		1.261
	5/2	$34+16^4P(^3P)^4D+16(A^3P)^2D$	$3d^6(a\,^3P)4p$	$w\,^4D$	59600	59501	99	1.277	1.306
	7/2	$33+38(A^3P)^4D+13^4P(^3P)^4D$	$3d^6(a\,^3P)4p$	$w\,^4D$	59340	59089	251	1.362	1.413
$^2I(^3P)^4K$	11/2	98				59599			0.776
	13/2	98				59673			0.967
	15/2	99				59759			1.092
	17/2	100				59861			1.176
$(A^3F)^4F$	3/2	$44+17^4G(^1P)^4F+15(A^3P)^2D$			59416	59754	−338	0.39	0.519
	5/2	$44+15^4G(^1P)^4F+11(A^3F)^4G$			59361	59697	−336	1.11	0.957
	7/2	$43+16^4G(^1P)^4F+12(A^3F)^4G$			59290	59590	−300	1.325	1.193
	9/2	$41+17(A^3F)^4G+14^4G(^1P)^4F$			59257	59512	−255	1.327	1.275
$(A^3F)^4G$	5/2	$52+18(^3H)^4G+9(A^3F)^4F$			59818	59783	35	0.584	0.671
	7/2	$46+16(^3H)^4G+10(A^3F)^4F$			59784	59731	53	0.990	1.081
	9/2	$43+16(A^3F)^4F+14(^3H)^4G$			59732	59726	6	1.169	1.218
	11/2	$57+22(^3H)^4G$			59653	59574	79	1.239	1.255
$(A^3P)^2D$	3/2	$49+11(A^3F)^4F+7(A^3F)^4D$	$3d^6(a\,^3P)4p$	$w\,^4D$	59990	59909	81	1.194	0.780
	5/2	$24+23^4D(^3P)^2F+11^4D(^3P)^2D$	$3d^6(a\,^3F)4p$	$v\,^4D$	59481	59169	312	1.281	1.152
$(^3H)^2I$	11/2	$87+6^2I(^3P)^2I$			59828	60024	−196	0.93	0.935
	13/2	$89+6^2I(^3P)^2I$			59617	59785	−168	1.074	1.079
$(A^3P)^4D$	1/2	$65+11A^2F(^3P)^4D+7(A^3F)^4D$			60142	60507	−365	0.17	0.052
	3/2	$59+12A^2F(^3P)^4D+8(A^3F)^4D$	$3d^6(a\,^3P)4p$	$z\,^2D$	60396	60510	−114	0.91	1.186
	5/2	$56+10(A^3F)^4D+8A^2F(^3P)^4D$			60102	60332	−230	1.31	1.367
	7/2	$30+24(A^3F)^4D+9(A^3F)^4F$	$3d^6(a\,^3F)4p$	$v\,^4D$	59470	59953	−483	1.386	1.366
$(^3H)^2G$	7/2	$42+14(A^3F)^2F+12(^3G)^2G$			60739	60675	64		0.943
	9/2	$49+17(^3G)^2G+7^4G(^3P)^2G$			60668	60633	35	1.112	1.098
$^2I(^3P)^4H$	7/2	$58+15^4G(^1P)^4H+14(^3G)^4H$	$3d^54s(^3I)4p$	$x\,^4H$	60957	60804	153		0.702
	9/2	$55+16^4G(^1P)^4H+13(^3G)^4H$			60956	60816	140		0.986
	11/2	$58+19^4G(^1P)^4H+15(^3G)^4H$			60934	60794	140	1.134	1.131
	13/2	$59+20^4G(^1P)^4H+16(^3G)^4H$			60891	60752	139	1.228	1.227
$A^2D(^3P)^4F$	3/2	$58+23A^2F(^3P)^4F+7^4G(^1P)^4F$		$w\,^4F$	60761	60853	−92		0.405
	5/2	$58+20A^2F(^3P)^4F+7^4G(^1P)^4F$			60820	60944	−124		1.024
	7/2	$58+21A^2F(^3P)^4F+8^4G(^1P)^4F$			60903	61075	−172		1.228
	9/2	$57+18A^2F(^3P)^4F+12^4G(^1P)^4F$			60939	61226	−287		1.321
$^2I(^3P)^4I$	9/2	$34+29(^3H)^4I+11(^3H)^2H$	$3d^54s(^3I)4p$	$y\,^4I$	61211	61071	140	0.75	0.820
	11/2	$42+40(^3H)^4I+7(^3H)^2H$			61226	61136	90		0.984
	13/2	$49+46(^3H)^4I$			61226	61182	44		1.109
	15/2	$54+43(^3H)^4I$			61204	61178	26	1.20	1.199
$^4D(^3P)^2P$	1/2	$49+23(A^3P)^2P+20^4P(^3P)^2P$				61235			0.686
	3/2	$41+28(A^3P)^2P+21^4P(^3P)^2P$				61476			1.319
$(A^3F)^2F$	5/2	$64+8^4D(^3P)^2F$		$w\,^4G$	61471	61361	110		0.863
	7/2	$35+16(A^3F)^2G+13(^3H)^2G$		$w\,^4G$	61481	61404	77	1.13	1.057
$(A^3F)^2G$	7/2	$63+5(^3H)^2G$		$y\,^2G$	61786	61683	103	0.93	0.940
	9/2	$30+18(^3H)^4I+15(^3H)^2H$		$w\,^4G$	61485	61297	188	1.020	0.941
$^4G(^1P)^4F$	3/2	$25+14(A^3F)^4F+12A^2F(^3P)^4F$				61859			0.547
	5/2	$21+15A^2D(^3P)^4D+11A^2F(^3P)^4F$		$z\,^2F$	61727	61817	−90		1.094
	7/2	$17+12A^2D(^3P)^4D+10A^2F(^3P)^4F$		$z\,^2F$	61711	61833	−122		1.225
	9/2	$13+14(^3G)^4F+11^4D(^1P)^4F$		$y\,^2G$	61715	61760	−45		1.235
$(^3H)^2H$	9/2	$31+25(A^3F)^2G+7^2I(^3P)^2H$				61826			1.082
	11/2	$55+13^2I(^3P)^2H+9(^3G)^2H$		$w\,^4G$	61469	61341	128	1.164	1.087

TABLE A. *Observed and Calculated Levels of* Mn I $(3d+4s)^6 4p$ – Continued

Name	J	Percentage	CMG		Obs. Level (cm^{-1})	Calc. Level (cm^{-1})	O–C	Obs. g	Calc. g
			Config.	Desig.					
$A^2D(^3P)^4D$	1/2	$53+15{}^4P(^1P)^4D+8{}^4F(^3P)^6F$				62109			0.034
	3/2	$27+10{}^4P(^1P)^4P+8{}^4P(^1P)^4D$				62178			1.184
	5/2	$26+11A^2D(^3P)^4P+7{}^4F(^3P)^6G$				62166			1.217
	7/2	$32+13{}^4P(^1P)^4D+10(^3G)^4G$				62165			1.269
$^4P(^1P)^4P$	1/2	$37+25(^5D)^4P^*+11(^3D)^4P$				61994			2.627
	3/2	$20+15(^5D)^4P^*+12{}^4D(^1P)^4P$				62162			1.451
	5/2	$45+22(^5D)^4P^*+9{}^4D(^1P)^4P$				62505			1.528
$^2I(^3P)^2K$	13/2	96				62182			0.934
	15/2	96				62285			1.068
$^4F(^3P)^6G$	3/2	$84+7A^2F(^3P)^4F$				62267			0.141
	5/2	$79+12A^2D(^3P)^4P$				62278			0.972
	7/2	87				62302			1.135
	9/2	96				62330			1.272
	11/2	97				62368			1.341
	13/2	98				62416			1.383
$(^3G)^4G$	5/2	$28+12(A^3F)^4G+10(^3H)^4G$		$y\,^2F$	62075	62283	−208	0.58	0.781
	7/2	$31+10(A^3F)^4G+9(^3H)^4G$		$y\,^2F$	62034	62256	−222		1.102
	9/2	$39+12(A^3F)^4G+11(^3H)^4G$				62060			1.174
	11/2	$44+16(A^3F)^4G+11(^3H)^4G$	Unclassified		61744	61764	−20		1.252
$(A^3P)^2P$	1/2	$42+29{}^4D(^3P)^2P$			62391	62328	63	0.81	0.760
	3/2	$33+28{}^4D(^3P)^2P$			62355	62370	−15	1.24	1.386
$A^2D(^3P)^4P$	1/2	$53+18{}^4P(^1P)^4P+12{}^4F(^3P)^6D$				62619			2.607
	3/2	$51+20{}^4P(^1P)^4P+7{}^4F(^3P)^6D$				62547			1.688
	5/2	$45+7{}^4P(^1P)^4P+7A^2D(^3P)^4D$				62239			1.350
$(^3G)^4F$	3/2	$25+14A^2F(^3P)^4F+14(A^3F)^2D$			62390	62561	−171		0.494
	5/2	$24+19A^2F(^3P)^4F+10{}^4D(^1P)^4F$			62487	62621	−134		1.050
	7/2	$27+28A^2F(^3P)^4F+11{}^4D(^1P)^4F$			62505	62668	−163		1.240
	9/2	$29+37A^2F(^3P)^4F+10{}^4G(^1P)^4F$			62393	62566	−173	1.35	1.330
$^2I(^3P)^2H$	9/2	$76+6(A^1G)^2H$				62620			0.924
	11/2	$75+6(A^1G)^2H$				62541			1.102
$A^2F(^3P)^4G$	5/2	$56+13(^3G)^4G+11(A^3F)^2D$		$x\,^2F$	63140	62815	325		0.723
	7/2	$68+8(^3G)^4G$		$x\,^2F$	63289	62980	309		0.998
	9/2	$61+10{}^4G(^1P)^4H+7(^3G)^4H$		$y\,^2H$	63348	63072	276		1.135
	11/2	$63+10{}^4G(^1P)^4H+7(^3G)^4H$	$3d^6(^3H)4p$	$z\,^2H$	63289	63045	244	1.127	1.245
$^4F(^3P)^6F$	1/2	82	$3d^54s(a\,^5F)4p$	$w\,^6D$	62768	62916	−148		0.563
	3/2	82			62788	62887	−99		1.093
	5/2	81			62761	62852	−91		1.332
	7/2	83			62851	62820	31		1.405
	9/2	85			62671	62809	−138		1.427
	11/2	88				62855			1.442
$(A^3F)^2D$	3/2	$65+7(^3G)^4F$		$y\,^2D$	63114	63053	61	0.758	0.740
	5/2	$53+8A^2F(^3P)^4G+7(^3G)^4F$			63081	62988	93	1.24	1.132
$^4G(^1P)^4H$	7/2	$42+26(^3G)^4H+12(^3H)^4H$	$3d^6(a\,^3G)4p$	$w\,^4H$	63395	63218	177	0.70	0.693
	9/2	$35+21(^3G)^4H+19A^2F(^3P)^4G$			63445	63242	203		1.020
	11/2	$31+21(^3G)^4H+20A^2F(^3P)^4G$			63458	63223	235	1.14	1.245
	13/2	$44+30(^3G)^4H+11(^3H)^4H$			63364	63184	180	1.231	1.225
$^4F(^3P)^6D$	1/2	$78+8A^2D(^3P)^4P$				63537			3.131
	3/2	$81+6A^2D(^3P)^4P$	Unclassified		63584	63513	69		1.789
	5/2	86	Unclassified		63524	63470	54		1.632
	7/2	87	Unclassified		63546	63431	115		1.573
	9/2	89	Unclassified		63375	63390	−15		1.547
$(^3G)^2H$	9/2	$72+10(^3H)^2H$			63548	63611	−63	0.92	0.915
	11/2	$65+13(^3H)^2H$		$y\,^2H$	63449	63459	−10		1.091

TABLE A. *Observed and Calculated Levels of* Mn I $(3d+4s)^6 4p$ – Continued

Name	J	Percentage	CMG		Obs. Level (cm^{-1})	Calc. Level (cm^{-1})	O–C	Obs. g	Calc. g
			Config.	Desig.					
$A^2D(^3P)^2D$	3/2	$50+27A^2F(^3P)^2D$		$x\,^2D$	63845	63588	257		0.781
	5/2	$57+16A^2F(^3P)^2D$			63765	63665	100		1.198
$(A^3P)^2S$	1/2	$79+9^4P(^3P)^2S$				63778			2.034
$^2I(^3P)^2I$	11/2	$86+9(^1I)^2I$				63836			0.931
	13/2	$84+9(^1I)^2I$				63835			1.086
$A^2F(^3P)^4D$	1/2	$59+16A^2D(^3P)^2P+10(A^3P)^4D$		$u\,^4D$	64639	64555	84	0.22	0.151
	3/2	$61+13A^2D(^3P)^2P+10(A^3P)^4D$			64684	64634	50	1.22	1.234
	5/2	$59+8A^2D(^3P)^2F$			64713	64769	−56		1.281
	7/2	$70+7(A^3P)^4D+7A^2D(^3P)^2F$			64410	64508	−98	1.42	1.386
$A^2F(^3P)^4F$	3/2	$34+20A^2D(^3P)^4F+8^4D(^1P)^4F$				64769			0.441
	5/2	$27+19A^2D(^3P)^4F+7^4D(^1P)^4F$				64694			1.036
	7/2	$21+14A^2D(^3P)^4F+10A^2F(^3P)^4D$		$x\,^2G$	64649	64573	76		1.215
	9/2	$30+17A^2D(^3P)^4F+9^4D(^1P)^4F$		$x\,^2G$	64585	64557	28	1.307	1.317
$A^2D(^3P)^2F$	5/2	$56+8A^2F(^3P)^4D$		$w\,^2F$	64823	64936	−113		0.925
	7/2	$45+15(^3G)^4H+9A^2F(^3P)^4F$			64988	64858	130		1.022
$(^3G)^4H$	7/2	$38+12^2I(^3P)^4H+9(^3H)^4H$		$v\,^4H$	64920	64867	53		0.817
	9/2	$52+18^2I(^3P)^4H+13(^3H)^4H$			64888	64802	86	0.974	0.974
	11/2	$51+19^2I(^3P)^4H+14(^3H)^4H$			64820	64760	60	1.137	1.133
	13/2	$48+21^2I(^3P)^4H+16(^3H)^4H$			64732	64693	39	1.236	1.229
$A^2F(^3P)^2G$	7/2	$58+15(^3G)^2G$		$w\,^2G$	65305	65319	−14		0.929
	9/2	$52+27(^3G)^2G$			65262	65388	−126	1.13	1.120
$^4P(^1P)^4D$	1/2	$20+26A^2D(^3P)^2P+18(^3D)^4D$				65451			0.252
	3/2	$21+19(^3D)^4D+17A^2D(^3P)^4D$		$w\,^2D$	65962	65640	322		1.224
	5/2	$20+27(^3D)^4D+23A^2D(^3P)^4D$		$w\,^2D$	65947	65625	322	1.30	1.366
	7/2	$18+27(^3D)^4D+21A^2D(^3P)^4D$				65638			1.395
$A^2D(^3P)^2P$	1/2	$29+19A^2F(^3P)^4D+10(^3D)^4D$				65688			0.296
	3/2	$48+9(^3D)^4D$				65365			1.281
$(^3G)^2F$	5/2	$55+11A^2F(^3P)^2F+9(A^3F)^2F$		$v\,^2F$	65649	65806	−157		0.838
	7/2	$33+19(^3G)^2G+14A^2F(^3P)^2G$			65617	65451	166	1.015	1.045
$(^3G)^2G$	7/2	$29+20(^3G)^2F+9A^2F(^3P)^2F$				66040			1.005
	9/2	$43+32A^2F(^3P)^2G+12(^3H)^2G$	Unclassified		65769	65767	2	1.12	1.115
$(^3H)^4G$	5/2	$10+15A^2G(^3P)^4G+14^4F(^3P)^4G$		$v\,^4G$	65873	66039	−166		0.604
	7/2	$10+14A^2G(^3P)^4G+12^4G(^1P)^4G$			65876	65993	−117		0.974
	9/2	$12+15A^2G(^3P)^4G+13^4G(^1P)^4G$			65909	66002	−93	1.160	1.160
	11/2	$13+15A^2G(^3P)^4G+13^4G(^1P)^4G$			65887	65985	−98	1.259	1.263
$A^2F(^3P)^2F$	5/2	$25+18^4F(^3P)^4G+15(A^1G)^2F$		$u\,^2F$	66021	66316	−295		0.756
	7/2	$34+21(A^1G)^2F+12(^3G)^2F$			66149	66269	−120	1.14	1.096
$^4P(^1P)^4S$	3/2	$62+27(A^3P)^4S$	Unclassified		66504	66327	177		1.975
$A^2G(^3P)^4H$	7/2	$31+23^2H(^3P)^4H+8(^3H)^4H$		$u\,^4H$	66334	66337	−3	0.764	0.776
	9/2	$28+19^2H(^3P)^4H+7(^3H)^4H$			66356	66357	−1	1.022	1.033
	11/2	$39+27^2H(^3P)^4H+7(^3H)^4H$			66419	66448	−29		1.137
	13/2	$46+32^2H(^3P)^4H+7^2H(^3P)^4I$			66569	66538	31	1.23	1.221
$(A^1G)^2G$	7/2	$23+16^4F(^3P)^4G+8^2H(^3P)^4G$		$v\,^2G$	66738	66630	108	0.46	0.999
	9/2	$22+11A^2G(^3P)^4H+8(^3D)^4F$			66631	66452	179	1.13	1.143
$(^3D)^4F$	3/2	$27+25^4D(^1P)^4F+12(^3G)^4F$		$u\,^4F$	66844	66559	285	0.46	0.411
	5/2	$15+12^4F(^3P)^4G+9^4D(^1P)^4F$			66838	66555	283		0.909
	7/2	$14+17^4F(^3P)^4G+15^4D(^1P)^4F$			66783	66576	207	1.21	1.114
	9/2	$8+11(A^1G)^2G+10^4F(^3P)^4G$			66855	66572	283	1.33	1.209
$^4F(^3P)^4G$	5/2	$19+10(^3D)^4F+9^2H(^3P)^4G$		$u\,^4G$	66395	66662	−267	0.611	0.810
	7/2	$12+15(A^1G)^2G+7(^3D)^4F$			66454	66630	−176	0.932	0.999

TABLE A. *Observed and Calculated Levels of* Mn I $(3d+4s)^6 4p$ – Continued

Name	J	Percentage	CMG		Obs. Level (cm^{-1})	Calc. Level (cm^{-1})	O–C	Obs. g	Calc. g
			Config.	Desig.					
	9/2	$34+13^2H(^3P)^4G+7A^2F(^3P)^4G$			66523	66760	−237	1.13	1.195
	11/2	$54+17^2H(^3P)^4G+8A^2F(^3P)^4G$			66574	66819	−245	1.24	1.256
$^2H(^3P)^4I$	9/2	90				67045			0.745
	11/2	88				67144			0.981
	13/2	89				67229			1.116
	15/2	96				67280			1.198
$(^1I)^2H$	9/2	$34+42(A^1G)^2H+9^2H(^3P)^2H$		$w\,^2H$	67577	67394	183	0.90	0.912
	11/2	$39+35(A^1G)^2H+9^2H(^3P)^2H$			67505	67371	134	1.09	1.094
$^4D(^1P)^4P$	1/2	$25+18^4D(^1P)^4D+13^4P(^1P)^4P$				67627			1.411
	3/2	$22+16^4D(^1P)^4D+12^4P(^1P)^4P$				67685			1.472
	5/2	$42+18^4P(^1P)^4P+5^4D(^1P)^4D$	Unclassified		67009	67136	−127		1.565
$A^2F(^3P)^2D$	3/2	$51+29A^2D(^3P)^2D$				67555			0.769
	5/2	$54+25A^2D(^3P)^2D$				67443			1.197
$^4D(^1P)^4D$	1/2	$19+22^4D(^1P)^4P+15^4P(^1P)^4D$				67726			1.257
	3/2	$20+21^4D(^1P)^4P+16^4P(^1P)^4D$				67533			1.466
	5/2	$33+27^4P(^1P)^4D$				67572			1.392
	7/2	$40+30^4P(^1P)^4D$	Unclassified		66981	67264	−283	1.33	1.421
$(^1I)^2K$	13/2	$92+7^2I(^1P)^2K$				67903			0.935
	15/2	$91+8^2I(^1P)^2K$				68137			1.068
$A^2G(^3P)^4F$	3/2	$31+28^4F(^3P)^4D+8^4F(^3P)^4F$				68151			0.747
	5/2	$36+30^4F(^3P)^4D$				68204			1.138
	7/2	$45+21^4F(^3P)^4D$		$u\,^2G$	68339	68185	154		1.276
	9/2	$58+13^4F(^3P)^4F$		$u\,^2G$	68286	68129	157	1.320	1.321
$^4F(^3P)^4D$	1/2	$76+7^4D(^1P)^4D$				68240			0.019
	3/2	$47+24A^2G(^3P)^4F$				68239			0.877
	5/2	$42+22A^2G(^3P)^4F$				68073			1.230
	7/2	$55+18A^2G(^3P)^4F$				67992			1.371
$^2H(^3P)^4G$	5/2	$17+13A^2G(^3P)^4G+13(^3D)^2F$		$t\,^4G$	67965	68294	−329		0.736
	7/2	$18+16A^2G(^3P)^4G+14(^3G)^4G$			67891	68251	−360		1.057
	9/2	$16+14A^2G(^3P)^4G+13(^3G)^4G$			67819	68184	−365		1.222
	11/2	$23+22A^2G(^3P)^4G+18(^3G)^4G$			67753	68175	−422	1.266	1.260
$(^1I)^2I$	11/2	$53+19^2I(^1P)^2I+18^2H(^3P)^2I$				68363			0.938
	13/2	$55+19^2I(^1P)^2I+19^2H(^3P)^2I$				68364			1.082
$(^3D)^2F$	5/2	$37+8A^2G(^3P)^4G$				68455			0.792
	7/2	$44+14A^2F(^3P)^2F+10A^2D(^3P)^2F$				68668			1.156
$^4F(^3P)^4F$	3/2	$51+25(^3D)^4F+7A^2F(^3P)^4F$				68583			0.432
	5/2	$44+22(^3D)^4F+7A^2F(^3P)^4F$				68589			0.970
	7/2	$36+16(^3D)^4F+7A^2F(^3P)^4F$				68559			1.164
	9/2	$36+20(^3D)^4F+9A^2F(^3P)^4F$				68484			1.284
$(^5D)^6F^*$	1/2	95				68426			−0.662
	3/2	95				68514			1.068
	5/2	95				68656			1.314
	7/2	96				68852			1.396
	9/2	96				69100			1.433
	11/2	96				69396			1.454
$(^3D)^2P$	1/2	$70+13A^2D(^3P)^2P+7(^3D)^4P$				68851			0.852
	3/2	$44+22(^3D)^2D+7(^3D)^4P$				68698			1.204
$(^3D)^2D$	3/2	$48+23(^3D)^2P+7A^2F(^3P)^2D$				68833			0.968
	5/2	$52+23(^3D)^4P$				68799			1.318
$(A^1G)^2H$	9/2	$39+30(^1I)^2H+12A^2G(^3P)^2H$				68864			0.915
	11/2	$43+25(^1I)^2H+10A^2G(^3P)^2H$				68862			1.090

TABLE A. *Observed and Calculated Levels of* Mn I $(3d+4s)^6 4p$ – Continued

Name	J	Percentage	CMG		Obs. Level (cm^{-1})	Calc. Level (cm^{-1})	O–C	Obs. g	Calc. g
			Config.	Desig.					
$(^3D)^4P$	1/2	$63+16(^5D)^4P^*+8(^3D)^2P$				68927			2.455
	3/2	$62+15(^5D)^4P^*+9(^3D)^2P$				68960			1.678
	5/2	$45+23(^3D)^2D+12(^5D)^4P^*$				69107			1.438
$(A^1G)^2F$	5/2	$31+29A^2F(^3P)^2F+14(^3D)^2F$				69282			0.896
	7/2	$32+26(^3D)^2F+24A^2F(^3P)^2F$				69279			1.142
$^2H(^3P)^4H$	7/2	$50+42A^2G(^3P)^4H$				69396			0.680
	9/2	$48+42A^2G(^3P)^4H$				69409			0.982
	11/2	$46+42A^2G(^3P)^4H$				69440			1.133
	13/2	$47+37A^2G(^3P)^4H$				69514			1.211
$(^5D)^6P^*$	3/2	97				69615			2.397
	5/2	96				69805			1.883
	7/2	97				70051			1.713
$(^3D)^4D$	1/2	$47+16^4D(^1P)^4D+12(^5D)^4D^*$				69722			0.008
	3/2	$47+16^4D(^1P)^4D+12(^5D)^4D^*$				69757			1.200
	5/2	$47+17^4D(^1P)^4D+12(^5D)^4D^*$				69822			1.369
	7/2	$40+15^4D(^1P)^4D+10^4F(^3P)^2G$				69958			1.349
$^2H(^3P)^2I$	11/2	$76+13^2I(^1P)^2I$				69909			0.932
	13/2	$75+11^2I(^1P)^2I$				70049			1.091
$^4F(^3P)^2G$	7/2	$55+8A^2G(^3P)^4G+7(^3D)^4D$				70044			0.982
	9/2	$55+16A^2G(^3P)^4G$				70088			1.118
$A^2G(^3P)^4G$	5/2	$46+15^4F(^3P)^4G+15^2H(^3P)^4G$				70225			0.603
	7/2	$37+13^4F(^3P)^2G+12^2H(^3P)^4G$				70305			0.972
	9/2	$35+30^4F(^3P)^2G+10^2H(^3P)^4G$				70312			1.145
	11/2	$45+17^4F(^3P)^4G+12^2H(^3P)^4G$				70090			1.259
$A^2G(^3P)^2G$	7/2	$32+30(A^1G)^2G+15^2H(^3P)^2G$				70594			0.913
	9/2	$30+31(A^1G)^2G+16^2H(^3P)^2G$				70664			1.111
$A^2G(^3P)^2F$	5/2	$37+16^4F(^3P)^2F+15(A^1D)^2F$				70747			0.865
	7/2	$41+22(A^1D)^2F+9^4F(^3P)^2F$				70809			1.118
$(A^1S)^2P$	1/2	$60\ \ 17A^2D(^1P)^2P+12(A^3P)^2P$				70991			0.667
	3/2	$61+16A^2D(^1P)^2P+8(A^3P)^2P$				70707			1.330
$^4D(^1P)^4F$	3/2	$18+37B^2F(^3P)^4F+22A^2G(^3P)^4F$				71171			0.408
	5/2	$20+32B^2F(^3P)^4F+22A^2G(^3P)^4F$				71161			1.028
	7/2	$21+27B^2F(^3P)^4F+22A^2G(^3P)^4F$				71136			1.235
	9/2	$23+22A^2G(^3P)^4F+21B^2F(^3P)^4F$				71090			1.326
$B^2F(^3P)^4F$	3/2	$45+23(^3D)^4F+11(^3G)^4F$				71355			0.409
	5/2	$49+22(^3D)^4F+9(^3G)^4F$				71384			1.025
	7/2	$52+22(^3D)^4F+7(^3G)^4F$				71423			1.232
	9/2	$60+21(^3D)^4F+5(^3G)^4F$				71505			1.325
$A^2G(^3P)^2H$	9/2	$67+9^2I(^1P)^2H$				71548			0.933
	11/2	$74+10^2I(^1P)^2H$				71578			1.094
$^4F(^3P)^2D$	3/2	$81+6^4D(^3P)^2D$				71743			0.802
	5/2	$62+19A^2F(^1P)^2D$				71653			1.169
$^2H(^3P)^2H$	9/2	$41+32A^2F(^1P)^2G$				71865			1.018
	11/2	$75+10B^2F(^3P)^4G$				71937			1.094
$^4F(^3P)^2F$	5/2	$67+12A^2G(^1P)^2F+7(^3D)^2F$				71993			0.871
	7/2	$55+9^2H(^3P)^2G+8A^2G(^1P)^2F$				71770			1.085
$(A^1D)^2P$	1/2	$70+22A^2D(^1P)^2P$				71896			0.655
	3/2	$62+24A^2D(^1P)^2P$				71948			1.324
$B^2F(^3P)^4G$	5/2	$71+22^2H(^3P)^4G$				72034			0.582
	7/2	$70+21^2H(^3P)^4G$				72070			0.995

TABLE A. *Observed and Calculated Levels of* Mn I $(3d+4s)^6 4p$ — Continued

Name	J	Percentage	CMG		Obs. Level (cm^{-1})	Calc. Level (cm^{-1})	O−C	Obs. g	Calc. g
			Config.	Desig.					
	9/2	$66+22\,^2H(^3P)\,^4G$				72150			1.162
	11/2	$63+23\,^2H(^3P)\,^4G+7\,^2H(^3P)\,^2H$				72207			1.258
$A\,^2F(^1P)\,^2G$	7/2	$48+13\,^4F(^3P)\,^2F$				72059			0.940
	9/2	$39+38\,^2H(^3P)\,^2H$				71830			1.015
$(A\,^1D)\,^2D$	3/2	$24+30(^5D)\,^6D^*+13B\,^2F(^3P)\,^2D$				72405			1.163
	5/2	$26+28B\,^2F(^3P)\,^4D+6\,^4F(^3P)\,^2D$				72462			1.279
$(^5D)\,^6D^*$	1/2	91				72218			3.257
	3/2	$59+13B\,^2F(^3P)\,^4D+8(A\,^1D)\,^2D$				72340			1.537
	5/2	81				72502			1.588
	7/2	$59+28B\,^2F(^3P)\,^4D$				72759			1.525
	9/2	93				72940			1.548
$B\,^2F(^3P)\,^4D$	1/2	$74+8\,^4F(^1P)\,^4D+7(^5D)\,^4D^*$				72541			0.070
	3/2	$60+9\,^4F(^1P)\,^4D+6(^5D)\,^4D^*$				72619			1.162
	5/2	$50+13(A\,^1D)\,^2D+8(^5D)\,^6D^*$				72742			1.341
	7/2	$49+36(^5D)\,^6D^*+12\,^4F(^1P)\,^4D$				72675			1.486
$A\,^2F(^1P)\,^2D$	3/2	$62+19(A\,^1D)\,^2D$				73191			0.807
	5/2	$63+13(A\,^1D)\,^2D$				73138			1.199
$(A\,^1D)\,^2F$	5/2	$34+29A\,^2G(^1P)\,^2F+9(^1F)\,^2F$				73327			0.883
	7/2	$39+33A\,^2G(^1P)\,^2F$				73226			1.150
$(^5D)\,^4F^*$	3/2	$55+19\,^4F(^1P)\,^4F$				73302			0.409
	5/2	$51+20\,^4F(^1P)\,^4F$				73371			1.021
	7/2	$53+21\,^4F(^1P)\,^4F$				73454			1.241
	9/2	$52+24\,^4F(^1P)\,^4F$				73553			1.340
$(^5D)\,^4D^*$	1/2	$33+30\,^4F(^1P)\,^4D+8(^5D)\,^4P^*$				73654			0.081
	3/2	$23+20\,^4F(^1P)\,^4D+13(^5D)\,^4P^*$				73634			1.398
	5/2	$33+31\,^4F(^1P)\,^4D$				73690			1.373
	7/2	$32+33\,^4F(^1P)\,^4D$				73756			1.421
$(^5D)\,^4P^*$	1/2	$37+25\,^2S(^3P)\,^4P+13\,^4D(^1P)\,^4P$				73503			2.610
	3/2	$24+17\,^2S(^3P)\,^4P+11(^5D)\,^4D^*$				73738			1.527
	5/2	$35+31\,^2S(^3P)\,^4P+11\,^4D(^1P)\,^4P$				74013			1.586
$^2I(^1P)\,^2K$	13/2	95				74054			0.934
	15/2	96				74121			1.067
$B\,^2F(^3P)\,^2G$	7/2	$48+33\,^2H(^3P)\,^2G$				75010			0.891
	9/2	$50+32\,^2H(^3P)\,^2G$				75004			1.112
$^2S(^3P)\,^4P$	1/2	$57+9(^5D)\,^4P+8(^5D)\,^4P^*$				75173			2.665
	3/2	$54+10(^5D)\,^4P^*+9(^3D)\,^4P$				75301			1.732
	5/2	$49+13(^5D)\,^4P^*+9(^3D)\,^4P$				75522			1.599
$B\,^2F(^3P)\,^2F$	5/2	$79+9(A\,^1D)\,^2F$				75729			0.858
	7/2	$81+10(A\,^1D)\,^2F$				75908			1.141
$^2I(^1P)\,^2I$	11/2	$62+25(^1I)\,^2I$				76017			0.928
	13/2	$64+25(^1I)\,^2I$				76095			1.077
$A\,^2D(^1P)\,^2D$	3/2	$35+36(^1F)\,^2D+11(A\,^1D)\,^2D$				76204			0.803
	5/2	$36+32(^1F)\,^2D+8(A\,^1D)\,^2D$				76213			1.169
$^2I(^1P)\,^2H$	9/2	$59+8(^3G)\,^2H$				76332			0.915
	11/2	$60+7(^1I)\,^2H$				76379			1.087
$A\,^2D(^1P)\,^2F$	5/2	$27+25A\,^2F(^1P)\,^2F+10(^1F)\,^2F$				76798			0.883
	7/2	$29+22B\,^2F(^3P)\,^2G+20A\,^2F(^1P)\,^2F$				76568			1.065
$(^1F)\,^2G$	7/2	$28+15A\,^2F(^1P)\,^2F+10(^1F)\,^2F$				77082			0.982
	9/2	$40+26B\,^2F(^3P)\,^2G+12\,^2H(^3P)\,^4G$				77606			1.110

TABLE A. *Observed and Calculated Levels of* Mn I $(3d+4s)^6 4p$ – Continued

Name	J	Percentage	CMG		Obs. Level (cm^{-1})	Calc. Level (cm^{-1})	O–C	Obs. g	Calc. g
			Config.	Desig.					
$A^2D(^1P)^2P$	1/2	$36+36^2S(^3P)^2P$				77273			0.666
	3/2	$30+21^2S(^3P)^2P+12(A^1S)^2P$				77281			1.192
$(^1F)^2F$	5/2	$13+21^4F(^1P)^4G+16A^2D(^1P)^2F$				77726			0.858
	7/2	$23+23(^1F)^2G+10A^2F(^1P)^2G$				77129			1.001
$B^2F(^3P)^2D$	3/2	$33+19^2S(^3P)^2P+13A^2D(^1P)^2D$				78098			0.950
	5/2	$42+10(^1F)^2F$				77553			1.106
$^4F(^1P)^4G$	5/2	$60+18A^2D(^1P)^2F$				78360			0.666
	7/2	$50+19A^2F(^1P)^2G+14A^2D(^1P)^2P$				78111			0.982
	9/2	86				78231			1.169
	11/2	88				78232			1.270
$^4F(^1P)^4F$	3/2	$58+15(^5D)^4F^*$				78678			0.412
	5/2	$56+16(^5D)^4F^*$				78723			1.026
	7/2	$55+17(^5D)^4F^*$				78754			1.235
	9/2	$55+19(^5D)^4F^*$				78805			1.331
$^2S(^3P)^2P$	1/2	$48+25A^2D(^1P)^2P$				79255			0.668
	3/2	$43+26A^2D(^1P)^2P+16(A^1D)^2P$				79392			1.297
$A^2F(^1P)^2F$	5/2	$35+21(^1F)^2F$				79499			0.875
	7/2	$28+35^4F(^1P)^4G$				79523			1.139
$^2H(^3P)^2G$	7/2	$44+25(^1F)^2G$				80349			0.900
	9/2	$40+23(^1F)^2G$				80309			1.092
$(^1F)^2D$	3/2	$34+22A^2F(^1P)^2D+11(A^1D)^2D$				80306			0.823
	5/2	$28+22A^2F(^1P)^2D+13(A^1D)^2D$				80348			1.195
$^4F(^1P)^4D$	1/2	$30+41(B^3P)^4D+21(^5D)^4D^*$				80728			0.006
	3/2	$30+39(B^3P)^4D+21(^5D)^4D^*$				80897			1.195
	5/2	$33+38(B^3P)^4D+20(^5D)^4D^*$				81133			1.361
	7/2	$25+23(B^3P)^4D+23B^2D(^3P)^4D$				81627			1.386

The approximate time for the diagonalization routine on the I.B.M. 7040 computer was 7 hrs.

The work described in this paper was supported in part by the National Bureau of Standards, Washington, D.C.

References

[1] Roth, C., J. Res. Nat. Bur. Stand. (U.S.), **72A** (Phys. and Chem.), No. 5, 505–520 (Sept.–Oct. 1968).
[2] Roth, C., J. Res. Nat. Bur. Stand. (U.S.), **73A** (Phys. and Chem.), No. 2, 125–157 (Mar.–Apr. 1969).
[3] Roth, C., J. Res. Nat. Bur. Stand. (U.S.), **73A** (Phys. and Chem.), No. 2, 159–171 (Mar.–Apr. 1969).
[4] Roth, C., J. Res. Nat. Bur. Stand. (U.S.), **73A** (Phys. and Chem.), No. 6, 599–609 (Nov.–Dec. 1969).
[5] Rohrlich, F., Phys. Rev. **74,** 1381 (1948).
[6] Roth, C., J. Res. Nat. Bur. Stand. (U.S.), **73A** (Phys. and Chem.), No. 5, 497–510 (Sept.–Oct. 1969).
[7] Roth, C., J. Res. Nat. Bur. Stand. (U.S.), **74A** (Phys. and Chem.), No. 2, 141–156 (Mar.–Apr. 1970).
[8] Roth, C., J. Res. Nat. Bur. Stand. (U.S.), **74A** (Phys. and Chem.), No. 2, 157–179 (Mar.–Apr. 1970).
[9] Smith, G., and Siddall, J., J. Opt. Soc. Am. **59,** 419 (1969).
[10] Moore, C. E., Atomic Energy Levels, Nat. Bur. Stand. (U.S.), Circ. 467, Vol. II, 260 pages (1952).
[11] Catalàn, M. A., Meggers, W. F., and Garcia-Riquelme, O., J. Res. Nat. Bur. Stand. (U.S.), **68A** (Phys. and Chem.) No. 1, 9–73 (Jan.–Feb. 1964).
[12] Roth, C., J. Math. Phys., **9,** No. 4, 686 (1968).
[13] Roth, C., J. Math. Phys., **10,** No. 6, 1038 (1969).
[14] Ishidzu, T., and Obi, S., J. Phys. Soc. of Japan **5,** No. 3, 124 (1950).
[15] Racah, G., and Shadmi, Y., Bull. Res. Counc. Israel, **8F,** No. 1, 15 (1959).
[16] Condon, E. U., and Shortley, G. H., The Theory of Atomic Spectra, p. 299 (Cambridge University Press, London, England, 1935).

(Paper 74A4–617)

JOURNAL OF RESEARCH of the National Bureau of Standards—A. Physics and Chemistry
Vol. 74A, No. 4, July–August 1970

A Literature Survey of the Chemistry of Flame Inhibition

E. C. Creitz

Institute for Applied Technology, National Bureau of Standards, Washington, D.C. 20234

(April 6, 1970)

Evidence is beginning to accumulate indicating that catalytic recombination of oxygen atoms may be the mechanism of extinction of flames by halogenated extinguishing agents. The literature of flame inhibition and of oxygen atom chemistry has been examined to ascertain whether the available data would support such a mechanism. Considerable sustentative evidence was found.

Kinetic rate-constant data are not available covering all reactions of interest, but those that are reported indicate that catalytic recombination of oxygen atoms can probably compete successfully with normal flame processes which require them.

Key words: Flame chemistry; flame extinction; flame inhibition.

1. Introduction

The study of the chemistry of fires is usually viewed as an exercise in fuel chemistry. This viewpoint is somewhat surprising since the oxidant, rather than the fuel, is the feature common to nearly all such fires. Likewise, in the study of the extinction of unwanted fires, the fuel appears to have received nearly all the attention. An examination of literature on the chemistry of atomic oxygen revealed a single reference [1],[1] in which it was suggested that the effects of halogen atoms in recombining oxygen atoms "might have applicability in flame inhibition." The statement was made specifically with respect to I-atoms at 1000 K, which were reported [2] to remove O-atoms from a system some 200 times faster than could NO molecules; and NO had been used in the same system to titrate O-atoms.

A simultaneous study of the literature on O-atom chemistry and the literature on the chemical inhibition of flames gives considerable support to Kaufman's [1] suggestion. The results of such a study are reported herein.

2. The Point of Attack by the Inhibitor

The first question to be asked has to do with the way an inhibitor modifies flame characteristics. Kydd and Foss [3] found that, with hydrogen, the rate of heat released in normal flames was independent of the oxygen concentration, $[O_2]$, if the oxygen was present in excess of stoichiometric proportions. Phillips and Sugden [4] reported that 2 percent Cl_2 raised the flame temperature 20 to 30° in premixed H_2-O_2 flames, while bromine and iodine had much smaller effects. Bulewicz, Phillips and Sugden [5] and Rosser, Inami and Wise [6, 7] report that the addition of inhibitors to flames produced no significant change in flame temperatures. The latter authors observed quite significant changes in quenching distance, however. Lask and Wagner [8], Halpern [9] and Miller, Evers and Skinner [10] related changes in flame speed to the amount of inhibitor and its efficiency. It appears, then that the inhibitor operates primarily by altering reaction rates, rather than the overall flame thermodynamics, i.e., it appears to alter the reaction path without much alteration in the total heat release. However, the rate of fuel consumption in diffusion flames is controlled by rates of diffusion, rather than by reaction rates. The same inhibitors that extinguish premixed flames are effective against diffusion flames and at about the same concentrations, if applied to the air side of diffusion flames [11]. If the same inhibition mechanism is to be proposed for both premixed and diffusion flames, one is forced to consider the near-equilibirum conditions obtaining in diffusion flames.

Diffusion flames may be considered to consist of a series of shells of constant composition, each shell differing in composition from that on each side of it. Reactions in each such shell are thought to be close to equilibrium because of the speed of chemical reactions compared to the rates at which reactants can be supplied to the shell. Within the shell, it appears that the logical point of attack is the equilibrium itself. Most such equilibria in flames are attained as the

[1] Figures in brackets indicate the references at the end of the paper.

result of chain reactions. A reduction of the concentration of a single species, if it is involved in a chain reaction, is a necessary and sufficient condition for the upsetting of any of the equilibria so attained. Diversion of a reactant species to form a product not useful in chain propagation would produce such a disturbance. For example, robbing a hydrogen-oxygen chain of H-atoms by CF_3 to form CF_3H, or of O-atoms to form COF_2 [12] would effectively break the chain.

The same result could be accomplished by the introduction of additional steps in the chain. For example in the hydrogen-oxygen chain, if the recombination of O-atoms could be speeded up so that it was competitive with other reactions removing O-atoms, the equilibrium would be shifted. The recombination and splitting of oxygen effectively only adds additional steps to the normal chain reaction. Since the reaction would eventually go to completion, as species migrate from shell to shell, one would not expect any great change in the overall flame thermodynamics.

Species derived by pyrolysis of the fuel must migrate outward to reach the reaction zone. Thus, reduction of their concentrations or interference with their diffusion would result in a smaller diameter, longer diffusion flame. This effect is usually observed when the inhibitor is added to the fuel. Species migrating inward toward the reaction zone include O_2, and O, as well as some OH and HO_2. Reduction of their concentrations should produce an increase in the diameter of a diffusion flame. This effect is usually observed when the inhibitor is added to the oxygen side of a diffusion flame. Thus, an increase in diameter tends to implicate oxygenated species while a decrease points toward involvement of fuel fragments in the inhibition mechanism.

Experimental results obtained by Rosser, Inami, and Wise [6, 7] indicate that inhibition, in their system, is associated with the use of oxygen as an oxidizer. Some observations by the author indicate that there may be an additional limitation in that the oxygen must be gas phase oxygen. Solid compounds, like perchlorates, appear not to be subject to inhibition by halogen compounds. It appears, also, that inhibition by halogenated compounds may affect only the branching steps of the hydrogen-oxygen chain reactions

$$H_2 + O \rightarrow OH + H, \quad (1)$$

$$O_2 + H \rightarrow OH + O. \quad (2)$$

The oxidation of CO to CO_2 is strongly inhibited [13], while the oxidation of C to CO appears to be unaffected [14, 15] by halogens or their compounds. The oxidation of CO to CO_2 depends in a secondary way on the hydrogen-oxygen chain reaction, since it requires OH and/or HO_2, according to the reactions

$$CO + OH \rightarrow CO_2 + H \quad [16, 17] \quad (3)$$

$$CO + HO_2 \rightarrow CO_2 + OH \quad [18, 19]. \quad (4)$$

Evidence for the involvement of the hydrogen-oxygen chain reaction in the mechanism of inhibition is relatively plentiful. The negative evidence, lack of inhibition when the chain reaction is not present, is harder to document, probably because of the paucity of oxidizing gases which will support flames. Available data appear to be limited to the nitrogen oxides.

The involvement of O-atoms in the inhibition mechanism is supported by the observation [20] that the flame speed, in several fuel-oxygen systems, was linearly related to the [O]. However, the involvement of O-atoms exclusively cannot be supported on this evidence alone, since O, H, and OH are expected to be present in near equilibrium concentrations because of the rapid rates, both forward and backward, of reactions 1 and 2 relative to rates of diffusion. The linear relationships between [O] and flame speed provides rather strong support for the involvement of the hydrogen-oxygen chain reaction in the inhibition mechanism, however.

3. The Nature of the Inhibiting Species

Skinner and Ringrose [12] came to the conclusion that the intact inhibitor molecule is involved in extinguishment. It is generally believed, however, that the actual inhibition is accomplished by one or more fragments of the inhibitor molecule or their recombination products. In the case of halogenated organic inhibitors the most active fragment is believed to be the halogen (Cl, Br, or I) atom. Some support for this belief is given by the observation [11] of emission bands associated with the recombination of bromine atoms on the air side of diffusion flames inhibited by CH_3Br. When Br_2 was substituted for the CH_3Br, no Br_2 emission was seen, but inhibition was still evident. The same system of emission bands was reported [21] in oxygen-rich premixed flames. Fuel rich flames produced emission associated with the excited halogen acid. Much stronger support for the importance of atomic halogen comes from the composition profiles of premixed flames which show [22] that CH_3Br decomposes at an earlier point in the reaction zone than does the fuel (CH_4). Preliminary observations of the author indicate that decomposition of CF_3Br is complete well outside of the reaction zone of a diffusion flame when it is added to the air side. The CF_3 radical produced by removal of the bromine atom from CF_3Br may play a part in inhibition since COF_2 and CF_3H were found [12] in shocked mixtures of H_2, O_2, and CF_3Br.

There are several reasons why the halogen acids are not serious contenders for the position of the primary inhibiting species. In diffusion flames, the region outside the reaction zone, where inhibition appears to take place, is an oxygen-rich, recombination region. If the inhibitor molecule contains no hydrogen (such as CF_3Br) the only source of hydrogen would be the H-atom, the OH radical and HO_2 radical produced by the flame. The most likely reaction for formation of the halogen acid would be

$$H + X + M \rightarrow HX + M. \quad (5)$$

This reaction is third order and would be slow compared to the second order flame reactions. It would introduce an extra step in the generation of the inhibiting species so that CF_3Br would be expected to be less efficient than HBr itself. The reverse is observed, although part of the effect may be due to the CF_3 radical. When the inhibitor is added to the fuel, one would expect that HX would be a common reaction product which would be formed from the inhibitor molecule whether or not it originally contained hydrogen. Emission spectra [21] indicate that this product is actually formed. But the inhibitor (HX), when added to the fuel, is little more effective than the equivalent amount of nitrogen [13]. It would appear that the halogen acids cannot survive the oxidizing conditions in the reaction zone and the region immediately outside it. This would be particularly the case for HI and HBr, while HCl would undoubtedly be somewhat more stable under these conditions. In the oxygen-rich recombination region, recombination of H, OH and HO_2 are to be expected as a normal part of the flame processes. Recombination of oxygen atoms in this region would rob the reaction zone of one of its primary reactants. Reactions such as

$$HX + OH \rightarrow X + H_2O \tag{6}$$

are second order recombination reactions for H and OH, replacing the slower, third order recombination of H and OH to form water, and could be important only in that atomic halogen is formed.

It is of interest to speculate on the mechanism of decomposition of inhibitors. Some of them are thermally quite stable. For example, CF_3Br is prepared commercially by bromination of fluoroform at temperatures of 673 to 873 K, and by brominolysis of perfluoropropane at temperatures of 973 to 1273 K [23]. Thermal stability, with retention of chemical activity may even be an advantage in an inhibitor. It would permit the inhibitor to approach the reaction zone closely enough to be decomposed by active species in the flame front. Both the decomposition reaction and the decomposition products would, thus, be effective at the most appropriate region of the flame. The most probable species present in this region of a diffusion flame would include such stable compounds as O_2, CO_2, H_2O, and CO, as well as such active species as O, H, OH, and HO_2. Reactions of inhibitor molecules with the active species appear not to have been extensively studied. The reaction between O-atoms and CCl_4 appears to be too slow to compete successfully with flame reactions. The overall reaction rate constant[2] was found to be $\log k = -13.48 - \frac{983}{T}$ by Ung and Schiff [24] over a temperature range of 273 to 373 K.

[2] Reaction rates in this paper are quoted in the form $\log_{10} k = A - C/T$ or $\log_{10} k = A + B \log T - C/T$ and are for concentrations in particles cm^{-3}, seconds and degrees Kelvin. The activation energy $E^* = 2.303\,RC$, where R is the gas constant. $R = 8.314$ J mol^{-1} K^{-1}; $= 1.987$ cal mol^{-1} K^{-1}. Many of these rate constants are of lower reliability than indicated by the number of significant figures shown for k, A, B, and C. Assume $\log_{10} k \pm 0.5$ unless otherwise stated.

Enthalpies of reaction were calculated from $\Delta Hf°$ (298.15 K) data in NBS Technical Note 270-3 (1968). No temperature correction was made. Values are given in kJ mol^{-1} and kcal mol^{-1} (1 cal = 4.184J). An "exothermic reaction" has $\Delta H < 0$, and an "endothermic reaction" has $\Delta H > 0$.

4. Halogen Atom Reactions With Flame Species

Reduction of chain branching would have a powerful effect on flame speed. The intermediates H, O, OH, and HO_2 in the branching hydrogen-oxygen chain reaction are of most interest in the inhibition process. Of these, OH is probably the most reactive. The emission of the (O, O) band of OH has been variously reported to decrease [6, 11, 25] with addition of inhibitor or to show no effect up to 2 percent Cl_2 addition [24]. For fuel side injection of methyl bromide and $POCl_3$, the decrease in OH emission was more marked than for air side injection [25]. However, air side injection is expected to produce greater amounts of inhibition [11, 13]. Unexpectedly, CCl_4 enhanced, rather than reduced the OH emission with air side injection [25]. Emission studies are not considered to be definitive, however, since the reduced emission can be attributed equally well to a decreased total [OH] or to simply deactivation of excited OH without change in the [OH] concentration. Wilson [22] has shown, on the basis of calculations from thermodynamics and reaction rates, that the [OH] would be expected to increase with the addition of inhibitor. Direct reaction of halogen atoms with OH via reactions 7, 8, and 9 can be eliminated on several counts.

$$Cl + OH \rightarrow HCl + O \tag{7}$$

$$Br + OH \rightarrow HBr + O \tag{8}$$

$$I + OH \rightarrow HI + O. \tag{9}$$

The production of OH is limited by reaction 2, above, [26] which has a rate constant given by $\log k = -9.3 - \frac{3665}{T}$ over the temperature range 300 to 2500 K. ($k = 9.1 \times 10^{-14}$ cm^3 particle^{-1} s^{-1} at 1000 K) [27].

The rate of reaction 7 is given by $\log k = -12.48 + 0.67 \log T - \frac{22}{T}$ ($k = 3.2 \times 10^{-11}$ cm^3 particle^{-1} s^{-1} at 1000 K), [28] that for reaction 8 by $\log k = -12.02 + 0.5 \log T - \frac{3250}{T}$ ($k = 1.6 \times 10^{-14}$ cm^3 particle^{-1} s^{-1}, at 1000 K), [28] and for reaction 9 by $\log k = -11.96 + 0.5 \log T - \frac{6775}{T}$ ($k = 5.8 \times 10^{-18}$ cm^3 particle^{-1} s^{-1} at 1000 K) [28]. The rate of reaction 7 is faster than reaction 2, reaction 8 about equally fast and reaction 9 is much slower. This order, Cl > Br > I, is the reverse of the observed order of efficiencies as inhibitors for the three halogens. Similarly, the enthalpies of the reactions are -0.90, $+14.80$, and $+31.03$ kcal mol^{-1} (-3.8, $+61.9$, and $+129.8$ kJ mol^{-1}); also in the opposite order to that found for the efficiencies. Additionally, reactions 7, 8, and 9 would produce O-atoms which should lead to increased flame speed, according to the data of Fenimore and Jones [20]. Direct reaction between halogen atoms and hydroxyl, therefore, appears to be an improbable mechanism of inhibition.

Inhibition of the H_2-O_2 chain by ethylene [29, 30], apparently does not involve OH radicals or $[H_2]$, but is linearly dependent on the $[O_2]$. This view is reasonable, since OH is a product, not a reactant, in the H_2-O_2 chain reaction. At least part of the oxidation of CO depends on the presence of OH (reaction 3). The inhibition of the CO oxidation would appear to depend, at least partially, on the reduction of the [OH] by some means other than by reactions 7, 8, and 9, since these reactions do not appear to be involved in inhibition.

Abstraction of hydrogen atoms from the fuel, to form the halogen acid, was proposed by Rosser, Wise, and Miller [31] as the first stage in an inhibition mechanism. The second stage suggested was the removal of O, H, OH, CH_3, etc., by the halogen acid with regeneration of the halogen atom. Thus, in terms of the hydrogen-oxygen chain reaction, the actual inhibitor would be the halogen acid. Some objections to the halogen acid as the primary inhibitor have been listed above. This mechanism, in effect, substituted a halogen atom for an atom of one of the active flame species. It also required a molecule of fuel for the production of the halogen acid. No such fuel species would be expected in the region where inhibition appears to occur. Fish [32] studied the proposal and concluded that it could be successful only if the active flame species removed was "identically equal to OH." Removal of hydroxyl by the halogen acid has also been suggested by Ibiricu and Gaydon [25]. Their work was based on measurements of the intensity of emission of both excited OH and excited CuOH. Only one reaction rate has been found for reaction 6, an order-of-magnitude estimate, $\log k = -12.8 + 0.5 \log T - \frac{1303}{T}$ [33], for X=Cl ($k = 2.5 \times 10^{-13}$ cm^3 particle^{-1} s^{-1} at 1000 K). Fish [32] states that $k(OH + HBr)/k(OH + CH_4) = 160$ at 785 K and that E^* $(OH + HBr) = 0$. By using the value $k = 4.4 \times 10^{-11} \exp(-5000/RT)$ for $OH + CH_4$, i.e., $k = 3.6 \times 10^{-12}$ at 1000 K, one obtains $k(OH + HBr) = 5.8 \times 10^{-10}$ cm^3 particle^{-1} s^{-1} at 1000 K. This makes Tunders estimate [33] doubtful. That work assumed $E^*(OH + HCl) = 6$ kcal/mol. The enthalpies of reaction, however, are in the correct order, and the reactions are exothermic. $\Delta H_{298} = -11.96$, -31.66, and -47.90 kcal mol^{-1} (-50.03, -132.5, and -200.4 kJ mol^{-1}) for X=Cl, Br, and I respectively. The principal objection to the abstraction of OH as a mechanism of inhibition is that it would shift the equilibria of both reactions 1 and 2 to the right, tending to favor their going to completion.

Removal of H-atoms by the third order reaction with halogen atoms, reaction 5, is slow as discussed above. Removal of H-atoms by

$$HX + H \rightarrow H_2 + X \qquad (10)$$

implies that the halogen acids should be more efficient inhibitors than compounds which liberate only halogen atoms. In the latter case an additional step would be needed to convert the halogen atom to the corresponding acid. Additionally, the equilibrium for reaction 10 lies far to the left, at least for X = Cl [34].

With the hydroperoxyl radical two types of reaction may be postulated.

$$X + HO_2 \rightarrow XO + OH \qquad (11)$$

and

$$X + HO_2 \rightarrow HX + O_2 \qquad (12)$$

For reaction 11, the enthalpy of reaction, when X = Cl, is -1 kcal (-4 kJ) mol^{-1}. For X = Br and I, the reaction becomes more endothermic, $\Delta H = +7$ and $+20$ kcal mol^{-1} ($+29$ and $+84$ kJ mol^{-1}) respectively so that this reaction may be discounted as important in inhibition. Reaction 12 is exothermic in all three cases; however. Values calculated for X = Cl, Br, I are $\Delta H = -56$, -40, -24 kcal mol^{-1} (-234, -167, and -100 kJ mol^{-1}), respectively. Little information could be found on the rate constants for either reaction. Jensen [35] gives an estimated rate constant for reaction 12 of $k = 2 \times 10^{-11}$ cm^3 particle^{-1} s^{-1} over the range 1000 to 3500 K, which indicates a relatively fast reaction. The enthalpies of reaction for both reactions 11 and 12 go in the order Cl > Br > I.

In spite of this order, Blackmore, O'Donnell, and Simmons [36] found that HBr was some 400 times more effective than HCl as an inhibitor for the second limit of the H_2-O_2 reaction. They suggested that the quadratic process, reaction 12, is a chain terminating reaction for a chain involving recombination of H-atoms by reaction 10, along with some other reaction converting X-atoms into HX. If reaction 12 is chain terminating for a chain that is essentially inhibiting in nature, it cannot itself be an inhibiting reaction.

The hydroperoxyl radical is credited with being the species chiefly responsible for recombination of O, H, and OH in the recombination region outside the reaction zone [37]. As such, it is difficult to see how its destruction could result in inhibition. A reduction of its concentration in this region should have the effect of extending the recombination region leaving the reaction zone relatively unaffected. Recombination reactions in the H_2-O_2 reaction which do not involve HO_2 are third order [38] and slow.

A mechanism of flame inhibition based on O-atom abstraction seems to offer some advantage over abstraction of H, OH or HO_2. It can explain the lack of inhibition of CH_4-NO flames by CF_3Br and CH_3Br, where hydrogen is present but the hydrogen-oxygen chain reaction is not required for the oxidation.

Inhibition of diffusion flames appears to occur in a location where O-atoms would be expected to be abundant. Such a mechanism would offer an explanation for the apparent lack of inhibition observed when the inhibitor is added to the fuel. This mechanism is bolstered somewhat by the reported emission spectra of the halogen monoxides in inhibited flames. The emission occurs at locations in diffusion flames where O-atoms would be expected to be plentiful, and links the probable inhibiting species to a species important in the hydrogen-oxygen chain reaction. The dependence of inhibitor concentration on $[O_2]$ agrees with such a mechanism, as does the relationship of flame

speed and [O] [20]. The IO emission intensity has been found to vary smoothly with [O] and [OH] in O-atom titration experiments in flames [39].

When halogen compounds are added to the air supplied to diffusion flames, the presence of halogen oxides seems to be indisputible. The first emission spectrum of such compounds was reported in 1929 [40], and a tentative identification of the emitter was made. The identification was confirmed in a series of papers [41–46], but the in-depth study of their kinetics occurred only after the advent of the flash photolysis technique [47]. An excellent review was presented by Porter [48].

Considering the very short lifetimes of the halogen monoxides, a surprising amount of information on them is available. A very thorough study of their absorption spectra was made by Durie and Ramsey [49]. Absorption bands associated with FO were not observed, although a search was made for them by these authors. Electron resonance spectra of ClO and BrO have been measured [50]. The first matrix isolation technique applied to ClO was reported by Norman and Porter [51, 52, 48]. Recently, microwave spectra have been obtained for ClO [53] and BrO [54].

Oxygen atoms may take part in both the formation of halogen monoxides and in their subsequent reactions. Reactions of the type

$$O + X + M \rightarrow OX + M \qquad (13)$$

are thermodynamically probable, since the enthalpies of reaction are exothermic, $\Delta H = -64.29$, -56.23 and -43.25 kcal mol^{-1} (-268.9, -235.3 and -181.0 kJ mol^{-1}) for X = Cl, Br, and I, respectively. The reactions are third order, and could be fast, depending on the number of collisions required for deactivation of the newly formed XO. No information on the rates of these reactions has been found. Reactions of the type

$$O + X_2 \rightarrow XO + X \qquad (14)$$

are more nearly thermoneutral. The enthalpies of reaction are $\Delta H = -6.13$, -10.14 and -7.09 kcal mol^{-1} (-25.6, -42.4 and -29.7 kJ mol^{-1}) for X = Cl, Br and I, respectively. Clyne and Coxon [55] determined a rate constant, $\log k = -11.02 - \frac{677}{T}$ cm^3 particle^{-1} s^{-1} over a temperature range of 174 to 396 K, for $X_2 = Cl_2$. This value appears to have been obtained in the absence of molecular oxygen by measurement of the rate of variation of the [O] in a flow system. No measurements were made of the rate of variation of the [ClO], however. Niki and Weinstock [56] remedied these deficiencies. With the [Cl_2] larger than the [O], and in the presence of O_2, the latter authors found a rate constant of $\log k = -12.85$ (k in cm^3 particle^{-1} s^{-1}) for reaction 14 with $X_2 = Cl_2$, at 300 K. Reaction 14, along with reaction 15,

$$O + OX \rightarrow X + O_2 \qquad (15)$$

was considered sufficient to explain the homogeneous reaction between atomic oxygen and molecular chlorine, provided reaction 15 was considerably faster than reaction 14. The same conclusion was also reached by Clyne and Coxon [57]. The mixing of O-atoms and Cl_2 in a microwave spectrometer failed to produce measurable quantities of ClO [58], indicating that reaction 15 probably is much faster than reaction 14, while a similar experiment with Br_2 produced quantities of BrO ample for measurement. These observations appear to indicate that, when X = Br, the rate of reaction 14 is comparable to that of reaction 15. The proposal of Porter and Wright [59] that a peroxy radical, XOO, is part of the reaction chain, thus appears unnecessary to explain reaction 14.

The existence of BrOO is doubtful, in any event, because of the weakness of the bromine-oxygen bond in such a compound [60]. The mechanism of formation of XO by way of XOO is, additionally, unlikely because the overall reaction is endothermic for X = Br and I. It has been found possible [58] to excite oxygen by collision with electrically excited argon. This excited oxygen has been found to react with Br_2 to produce BrO. It is not known with certainty what the state of excited oxygen is, but it is believed to be a low level state of molecular oxygen, possibly singlet sigma. It appears to be quite long lived, and very reactive. Such a mechanism for the formation of BrO in flames needs further investigation. Kaufman's [1] "catalytic" recombination of O-atoms by Cl-atoms has been interpreted by Niki and Weinstock [56] as a wall recombination of Cl-atoms followed by reaction 14. In the case of iodine at 1000° [2], there can be no doubt that I-atoms were present, since the equilibrium constant for the dissociation

$$1/2\, I_2(g) = I(g)$$

has a value of 0.56 [61]. Molecular iodine was also present, however. Norrish and Thrush [62] found that ClO was formed 46 times faster than Cl-atoms disappeared by recombination (with N_2 as the third body). While there is general agreement that reaction 15 is very fast, the source of the XO has not been clearly explained.

The possibility of the formation of XO by the reaction

$$X + OH \rightarrow XO + H \qquad (16)$$

was considered and rejected by Phillips and Sugden [21]. The reactions are extremely endothermic, $\Delta H = +38.05$, $+46.11$ and $+59.09$ kcal mol^{-1} ($+159.2$, $+192.9$ and $+247.2$ kJ mol^{-1}) for X = Cl, Br, and I.

The arguments presented earlier, implicating atomic, rather than molecular halogen as the active inhibiting species, indicate that reaction 13 may actually be faster than reaction 14 as a producer of XO radicals. The reverse of reaction 15 as a source of XO radicals is improbable for two reasons; the reactions are highly endothermic, $\Delta H = +54.81$, $+62.87$ and $+75.85$ kcal mol^{-1} ($+229.3$, $+263.0$ and $+317.3$ kJ mol^{-1}) for X = Cl, Br, and I. Secondly, reaction 15 would produce

383-876 O - 70 - 5

O-atoms, which would be expected to increase, rather than decrease, the flame speed.

The proposal that reaction 15 may play a major role in inhibition implies that it is fast compared to other reactions by which XO might be consumed. The equilibrium should lie far to the right. Broida, Schiff and Sugden [63] suggested that ClO might be a useful titrant for O-atoms. IO and BrO have been used for this purpose [39]. Accurate reaction rate constants are apparently not available in the open literature. However, a value of log $k = -10.10$ (k in cm^3 particle^{-1}s^{-1}) at 298 K, was given by Clyne and Coxon [55] for X = Cl. Their results also confirm that reaction 15 is fast and stoichiometric, and show that concentrations of ClO radicals may be measured by a titration with atomic oxygen.

In order that the halogen oxides be effective in removing oxygen atoms, their reactions with other species must be slower than the reactions with O-atoms.

The reaction

$$ClO + ClO \rightarrow \text{Products}, \tag{17}$$

where the products are eventually Cl_2 and O_2, is bimolecular in [ClO] and has a reported rate constant [64] of log $k = -11.96 - \frac{546}{T}$ (k in cm^3 particle^{-1} s^{-1}) over the temperature range 294 to 495 K. This reaction is at least one order of magnitude slower than reaction 15, for which $k = 3.9 \times 10^{-12}$ cm^3 particle^{-1} s^{-1} at 1000 K [35].

The bimolecular reaction between ClO and H_2 to form OH + HCl is slow, log $k = -15.3$ (k in cm^3 particle^{-1} s^{-1}) at 298 K, [64] and is exothermic to the extent of $\Delta H = -37.09$ kcal mol^{-1} (-155.2 kJ mol^{-1}). If H_2O + Cl are the products, $\Delta H = -52$ kcal (-218 kJ) mol^{-1}. The decay rate of ClO appeared to be independent of the presence of H_2 [64].

Reactions of XO with atomic hydrogen could yield either O or OH by reactions

$$XO + H \rightarrow HX + O \tag{18}$$

$$XO + H \rightarrow X + OH, \tag{19}$$

and could produce inhibition effects by the interpolation of an additional step in the reaction chain. Both reactions are exothermic. For reaction 18, with X = Cl, Br, or I, the enthalpies are $\Delta H = -38.95$, -31.31 and -28.06 kcal mol^{-1} (-163.0, -131.0 and -117.4 kJ mol^{-1}). No information on their rates have been found. However, the presence of IO* in fuel rich flames [21] indicates that its rate of formation must be as fast or faster than its rate of removal in an H-atom-rich environment.

Abstraction of OH, as a mechanism of inhibition, appears to be somewhat questionable, as discussed earlier. The hydroxyl radical is a product, rather than a reactant, in both reactions 1 and 2. Its removal should increase the yield of both reactions at near-equilibrium conditions. If reactions 1 and 2 lost no H- or O-atoms to diffusion, recombination, etc., they could continue to the depletion of H_2 and O_2. However, H- and O-atoms will be lost in a nonideal system and the chief function of the hydroxyl radical is to replace them by reactions such as

$$OH + OH \rightarrow H_2O + O \tag{20}$$

and

$$OH + H_2 \rightarrow H_2O + H. \tag{21}$$

Thus, the hydroxyl radical has a role as a reactant, and its removal could deplete the [H] and [O] to the point where reactions 1 and 2 would succumb to such losses. The importance of the OH radical, therefore, hinges on the factors governing the losses of H- and O-atoms from reactions 1 and 2. Additionally, the hydroxyl radical, rather than the O-atom, is thought [65, 66] to be the species responsible for the primary attack on the fuel molecule. Removal, of the OH radical could, thus, cause a depletion of the H_2 required in reaction 1.

Bimolecular reactions between the halogen monoxides with OH may be postulated to yield two different sets of products.

$$XO + OH \rightarrow HX + O_2 \tag{22}$$

$$XO + OH \rightarrow X + HO_2. \tag{23}$$

For reaction 22, the enthalpies are exothermic, $\Delta H = -55.71$, -48.07 and -44.82 kcal mol^{-1} (-233.0, -201.1 and -187.5 kJ mol^{-1}), while for reaction 23 they are $\Delta H = +1$, -7 and -20 kcal mol^{-1} ($+4.2$, -29 and -84 kJ mol^{-1}) for X = Cl, Br and I, respectively. All are thermodynamically probably except for X = Cl in reaction 23. No rate constant data have been found for any of these reactions.

The poor inhibitor sensitivity observed when the inhibitor is added to the fuel of a diffusion flame seems to be evidence that there is little competition between the inhibitor and the fuel for OH radicals. However, under these conditions the inhibitor is probably HX rather than XO, because the [O] $\ll$ [H] in this part of the flame. IO emission has been observed in fuel rich premixed flames [21]. It is not clear whether the IO observed under these conditions is attributable to an increased population of excited IO over unexcited IO caused by the particular conditions of the experiment. The absence of ClO and BrO emission does not preclude the presence of the unexcited radicals. The hydroperoxyl radical probably has no very active role in the inhibition process, except as a possible reactant liberating halogen from the inhibitor molecule. Its reactions with XO are not thermodynamically probable.

$$XO + HO_2 \rightarrow HX + O + O_2 \tag{24}$$

$$XO + HO_2 \rightarrow X + OH + O_2. \tag{25}$$

Reaction 24 is endothermic by $\Delta H = +9$, $+16$ and $+19$ kcal mol^{-1} ($+38$, $+67$ and $+79$ kJ mol^{-1}) for X = Cl, Br, and I, respectively. In reaction 25, only X = I is exothermic. The enthalpies are $\Delta H = +9$, $+3$

and -9 kcal mol^{-1} ($+38$, $+13$ and -38 kJ mol^{-1}) for X = Cl, Br, and I. No reaction rate constants appear to have been determined for these reactions.

5. Competition for Oxygen Atoms

Any inhibition mechanism taking place at near-equilibrium conditions by abstraction of an active species is in direct competition with flame reactions which depend on the same species. Therefore, it is necessary to compare the rates of the supposed abstraction reactions in normal flames. O-atom consumption by reaction 1 is relatively fast. Its rate constant is given [27] by $\log k = -10.68 - \frac{2054}{T}$, for k in cm^3 particle^{-1} s^{-1}. The reaction is endothermic by $\Delta H = +1.86$ kcal mol^{-1} (7.78 kJ mol^{-1}). The rate limiting reaction is reaction 2, which produces the O-atoms required in reaction 1. Its rate constant is given [27] by $\log k = -9.378 - \frac{3665}{T}$ for k in the same units, for a temperature range of 300 to 2500 K. The reaction is slow (9.1×10^{-14} cm^3 particle^{-1} s^{-1} at 1000 K) and endothermic by $\Delta H = +16.76$ kcal mol^{-1} ($+70.1$ kJ mol^{-1}). The backward reaction

$$O + OH \rightarrow H + O_2 \qquad (26)$$

is the fastest reaction in the hydrogen-oxygen chain. Its rate constant is given [6] by $\log k = -10.57 - \frac{43.43}{T}$ in cm^3 particle^{-1} s^{-1} for the temperature range 300 to 3000 K. The reaction occurs at 1/10 to 1/20 the gas kinetic collision frequency. The removal of O-atoms by water molecules is slow relative to reaction 26.

$$O + H_2O \rightarrow OH + OH. \qquad (27)$$

The rate is not known with certainty. Bascomb [67] gives $\log k = -10.15 - \frac{3952}{T}$ ($k = 7.9 \times 10^{-15}$ at 1000 K). The reaction is endothermic, $\Delta H = +16.87$ kcal mol^{-1} (70.6 kJ mol^{-1}). The reaction of an O-atom and water to produce an H-atom and a hydroperoxyl radical is very slow and very endothermic, and need not be considered further ($\log k = -12.8 - 0.5 \log T - \frac{12{,}440}{T}$ [68], $\Delta H_{298} = +55$ kcal mol^{-1}, $+230$ kJ mol^{-1}).

The reaction

$$O + CO_2 \rightarrow CO + O_2 \qquad (28)$$

is slow except at high temperatures, with $\log k = -10.50 - \frac{11{,}800}{T}$ [69], $\Delta H_{298} = +8.082$ kcal mol^{-1} (33.814 kJ mol^{-1}). At 1000 K it is twelve orders of magnitude slower than reaction 26.

A very fast reaction, consuming O-atoms in the region of a diffusion flame where inhibition takes place, is the reaction

$$O + HO_2 \rightarrow HO + O_2. \qquad (29)$$

The rate constant has been estimated to be greater than 10^{-11} cm^3 particle^{-1} s^{-1} [70], presumably at room temperature. The reaction is exothermic by $\Delta H = -56$ kcal mol^{-1} (-234 kJ mol^{-1}).

Other bimolecular reactions consuming O-atoms in normal flames appear either to be too slow or the reactants (such as H_2O_2) not too probable in the region of concern in diffusion flames.

Third order reactions consuming oxygen atoms appear to be generally too slow to compete successfully with second order reactions.

$$O + O + M \rightarrow O_2 + M \qquad (30)$$

is extremely exothermic ($\Delta H_{298} = -119.106$ kcal mol^{-1}, (-498.34 kJ mol^{-1})) but slow, $\log k = -29.42 - \log T - \frac{75}{T}$ for M = O_2 [71]. With regard to reaction 30, Kaufman [72] remarked that "Ternary gas phase recombination of O-atoms with Cl_2 as the third body can be ruled out. They would have to be efficient beyond all reasonable magnitudes and their rate law is in disagreement with the observed bimolecular reaction." The reaction

$$O + OH + M \rightarrow HO_2 + M \qquad (31)$$

probably has a rate comparable to that of reaction 30. The rate given by Bahn [68], $\log k = -30.57$ at 300 K, is probably high by a factor of 10, based on an alternate path from reaction 26. This reaction is also probably in the region just outside the reaction zone.

Removal of O-atoms by an inhibitor should produce an increase of [OH] by shifting the equilibrium to the left. However, such an increase has not been conclusively demonstrated. The third order reaction of O- and H-atoms is slow even though it is exothermic.

$$O + H + M \rightarrow OH + M, \qquad (32)$$

$\log k = -29.3 - \log T$ [73], $H_{298} = -102.34$ kcal mol^{-1} (-428.19 kJ mol^{-1}). The direct reaction of O-atoms and CO is not spin conserved [16, discussion].

$$O + CO + M \rightarrow CO_2 + M \qquad (33)$$

$\log k = -31.6 - \frac{764}{T}$ [73], $H_{298} = -128.192$ kcal mol^{-1}, (-536.35 kJ mol^{-1}). The reaction is too slow appreciably to affect the consumption of O-atoms.

6. Recombination of Halogen Atoms

Halogen atoms, if they are to be effective inhibitors, must not disappear by ineffective reactions at rates comparable to the rates of effective inhibition reactions. The third order recombination of halogen atoms is, therefore, of interest. Bromine and iodine atom recombination is about as fast as O-atom recombination at 1000 K. Kaufman [1] reports that "direct recombination (of O-atoms) is so slow that O-atoms react faster with other species in flames."

On the basis of this estimate it appears that Br- and I-atoms also have ample opportunity to react with other flame species. For the reaction

$$X + X + M \rightarrow X_2 + M \qquad (34)$$

the rate constants may be calculated from log $k = -31.26 - 2.7$ log $(T/300)$ [74] for X = Cl, M = Cl_2; log $k = -30.67 - 3.01$ log $(T/300)$ [75] for X = Br, M = Br_2; log $k = -35.54 +$ log $T + 1150/T$ [76] for X = I, M = I_2. All three reactions are exothermic. For X = Cl, Br and I, respectively ΔH_{298} = −58.164, −46.095 and −36.147 kcal mol^{-1} (−243.36, −192.86 and −151.24 kJ mol^{-1}).

The structure of inhibited diffusion flames gives clues to the chemical processes going on in them. The "auxiliary reaction zone," which forms outside the main reaction zone of some inhibited flames when the inhibitor is added to the air side, has been identified as due to the recombination of halogen atoms [11]. It is not present when molecular halogen is used as the inhibiting agent. Presumably, there is a paucity of halogen atoms inside the extra reaction zone compared to the region outside it. Thus, there is an implication that, if inhibition takes place inside the extra reaction zone, reactions of molecular halogen must be responsible for most of the action, especially with X = Cl.

If atomic halogen is responsible for inhibition, the action must take place at about the position of the extra reaction zone.

Since the extra reaction zone occurs some little distance outside the main reaction zone, inhibiting reactions of atomic halogen must occur at somewhat larger distances from the main reaction zone. However, the addition of small quantities of NO to the air supplied to a diffusion flame in this laboratory provided evidence, through the yellow-green emission of excited NO_2, that O-atoms also exist at large distances from the main reaction zone. The extra reaction zone may be taken as evidence that halogen atoms are present in this region in amounts larger than equilibrium concentrations. It is further evidence of the decomposition of the inhibitor, since the extra reaction zone is absent when the inhibitor is molecular halogen. In the latter case, the equilibrium is approached from the opposite direction. It may be argued that the increased effectiveness of CF_3Br over Br_2 (on the basis of equivalent amounts of Br) is attributable to the CF_3 radical. It may be argued equally well that the effect is caused by the above-equilibrium Br-atom concentrations occurring when CF_3Br is used. In practice, it may even be both.

It may be noted in passing, that, at a given temperature, equilibrium concentrations of I-atoms would be greater than Cl-atoms, with Br-atom concentrations between the two [61]. Neglecting any chemical differences, this characteristic of the halogens is sufficient to establish the observed order of efficiencies, I > Br > Cl.

Only at high temperatures, where all three halogens are very nearly completely dissociated, and the differences in degree of dissociation become negligible, would chemical differences outweigh the differences in equilibrium atom concentration.

7. Nonhalogenated Inhibitors

The suggested attack on oxygen atoms may possibly explain the inhibiting effect of such compounds as $Fe(CO)_5$, $Pb(C_2H_5)_4$ and the alkali metal carbonates. In the case of iron pentacarbonyl, the evidence for recombination of O-atoms is fairly direct. Kaufman [72] reported that, in the presence of O-atoms, $Fe(CO)_5$ produced finely divided oxide which deposited on the walls of the reaction tube causing it to be heated to incandescence by the vigorous recombination reaction. The deposited iron oxide caused recombination of O-atoms in the absence of further addition of $Fe(CO)_5$. One would expect the suspended oxide to perform similarly. The addition of $Fe(CO)_5$ to the fuel and oxygen sides of diffusion flames appears not to have been tried, but its effect on flame speed in premixed flames is well documented [7, 8]. The addition of the alkali carbonates to the fuel and oxygen sides of diffusion flames also appears not to have been tried. In either case, the positive nature of the metal would prevent the formation of stable compounds with fuel fragments, (with the possible exception of OH), so that such experiments would tend to be less definitive than when halogenated compounds are used.

It may be noted that the ease of formation and the stabilities of peroxides of the alkali metals increases with molecular weight, as does the extinguishing efficiency of the carbonates. McEwan and Phillips [77] have observed the superoxides of Na, K, and Cs but not of Li in oxygen-rich premixed flames. They interpreted their results in terms of the reaction

$$(Na, K, Cs) + O_2 + M \rightarrow (NaO_2, KO_2, CsO_2) + M. \qquad (35)$$

In the sense that it contains no chlorine, bromine or iodine, hexafluoroacetone will be considered with the nonhalogen containing inhibitors. This compound is known to produce large quantities of thermal CF_3 free radicals. While no analyses of combustion products were made (see however [12]), it was found [78] that hexafluoroacetone was a quite acceptable inhibitor. Its efficiency was found to be a function of the $[O_2]$ when added to the oxidant and it was ineffective when added to the fuel (H_2). It is probable that it operates by abstraction of both H- and O-atoms, by a nonchain process, to form CF_3H and COF_2. Thus, the efficiency of CF_3Br must be divided between the CF_3 and the Br fragments of the molecule.

8. Some Other Implications of Diffusion Flame Structure

The concentration of H_2 would be expected to increase toward the fuel side of the reaction zone, while the [O] would be expected to decrease. Thus, reaction 1

$$H_2 + O \rightarrow OH + H \qquad (1)$$

would be expected to go through a maximum somewhere fairly close to the fuel. This maximum defines a "reaction zone" for reaction 1. Because H-atoms can diffuse considerably faster than O-atoms, one would expect that the "reaction zone" for reaction 2

$$O_2 + H \rightarrow OH + O \qquad (2)$$

would be somewhat outside that for reaction 1. A chain composed of reactions 2 and 21 has been suggested [79]. Reaction 21,

$$OH + H_2 \rightarrow H_2O + H \qquad (21)$$

is fast, its rate being given [80] by $\log k = -11.17 - \frac{878}{T}$. At 1000 K

$$k_1 = 1.9 \times 10^{-13}$$

$$k_2 = 9.1 \times 10^{-14}$$

$$k_{21} = 8.9 \times 10^{-13}.$$

At 2000 K the rates are nearly equal,

$$k_1 = 2 \times 10^{-12}$$

$$k_2 = 6 \times 10^{-12}$$

$$k_{21} = 2.5 \times 10^{-12}.$$

In the chain involving reactions 2 and 21, O-atoms are an unused product species. Any theory of inhibition based on oxygen atoms could not apply to this chain. However, reaction 21, like reaction 1, must occur toward the fuel side of the overall reaction zone. Its position, with respect to reaction 1, will be determined by the availability of reactants and the relative rates of the two reactions (i.e., the local temperature). In any event the reaction zone applicable to reaction 21 will be well inside that for reaction 2, and the arguments for the effectiveness of the inhibitor when applied to the two sides of the overall reaction zone still apply. In fact, the presence of two reactions, each requiring H_2 as a reactant might even increase the separation between the zones for reaction 2 and reactions 1 + 21, because both 1 and 21 produce hydrogen atoms which would increase the concentration gradient responsible for diffusion of H-atoms.

It is obvious that a great deal remains to be learned about the structure of diffusion flames. It has been calculated [81] that the rate of propagation of the flame front in diffusion flames is directly related to the rate of diffusion of H-atoms. Since the transport of H-atoms is affected by many parameters, it would seem probable that there should be available many direct approaches to flame extinguishment. Recombination of oxygen atoms appears to be a somewhat roundabout way of accomplishing the desired result.

9. References

[1] Kaufman, F., Progress in reaction kinetics **1,** 3–39 (1961).

[2] Kaufman, F., Gerri, N. J., and Bowman, R. E., J. Chem. Phys. **25,** 106–15 (1956).

[3] Kydd, H. P., and Foss, W. I., Tenth Symposium (International) on Combustion pp. 101–110 (1965). The Combustion Institute, Pittsburgh.

[4] Phillips, L. F., and Sugden, T. M., Canadian J. Chem. **38,** 1804–8 (1960).

[5] Bulewicz, E. M., Phillips, L. F., and Sugden, T. M., Trans. Faraday Soc. **57,** 921–31 (1961).

[6] Rosser, W. F., Jr., Inami, S. H., and Wise, H., Wright Air Development Center Tech Report 59–206 (April 1965).

[7] Rosser, W. A. Jr., Inami, S. H., and Wise, H. Comb. and Flame **10,** 287–94 (1966).

[8] Lask, G., and Wagner, H. Gg., Eighth Symposium (International) on Combustion, p. 432 (Williams & Wilkins, Baltimore, 1962).

[9] Halpern, C. J., Nat Bur. Stand. (U.S.), **67A,** (Phys. and Chem.), No. 1, 71–77 (Jan.–Feb. 1963).

[10] Miller, D. R., Evers, R. L., and Skinner, G. B., Comb. and Flame **7,** 137–42 (1963).

[11] Simmons, R. F., and Wolfhard, H. G., Trans. Faraday Soc. **52.** 53–9 (1956).

[12] Skinner, G. B., and Ringrose, G. H., J. Chem. Phys. **43,** 4129–33 (1965).

[13] Cretiz, E. C., Nat. Bur. Stand. (U.S.), **65A** (Phys. and Chem.) No. 4, 389–396 (July–Aug. 1961).

[14] Arthur, J. R., and Bowring, J. R., J. Chem. Soc. (London) (Proc.) (1949) S1–S12.

[15] Bridger, G. W., and Appleton, H. J., Soc. Chem. Ind. **67,** 445–9 (1948).

[16] Brabbs, T. A., and Belles, F. E., Eleventh Symposium (International) on Combustion pp. 125–35 (1967). The Combustion Institute, Pittsburgh.

[17] Brokaw, R. S., Eleventh Symposium on Combustion pp. 1063–73 (1967). The Combustion Institute, Pittsburgh.

[18] Hoare, D. E., and Milne, G. S., Trans. Faraday Soc. **63,** 101–110 (1967).

[19] Baldwin, R. R., Jackson, D., Walker, R. W., and Webster, S. J., Tenth Symposium (International) on Combustion pp. 423–32 (1965). The Combustion Institute, Pittsburgh.

[20] Fenimore, C. P., and Jones, G. W., J. Phys. Chem. **62,** 178–83 (1958).

[21] Phillips, L. F., and Sugden, T. M., Trans. Faraday Soc. **57,** 914–20 (1961).

[22] Wilson, W. E., Tenth Symposium (International) on Combustion pp. 47–54 (1965). The Combustion Institute, Pittsburgh.

[23] The Matheson Gas Data Book, 4th ed. (The Matheson Co. Inc., E. Rutherford, N.J.).

[24] Ung, A. Y-M, and Schiff, H. I., Canadian J. Chem. **40,** 486–94 (1962).

[25] Ibiricu, M. M., and Gaydon, A. G., Comb. and Flame **8,** 51–62 (1964).

[26] Miyama, H., and Takeyama, T. J., Chem. Phys. **41,** 2287–90 (1964).

[27] Schofield, K., Planet. Space Sci. **15,** 643 (1967).

[28] Mayer, S. W., and Schieler, L., J. Phys. Chem. **72,** 236 (1968).

[29] Baldwin, R. R., Simmons, R. F., and Walker, R. W., Trans. Faraday Soc. **62,** 2476–85 (1966).

[30] Baldwin, R. R., Simmons, R. F., and Walker, R. W., Trans. Faraday Soc. **62,** 2486–98 (1966).

[31] Rosser, W. A. Jr., Wise, H., and Miller, J., Seventh Symposium (International) on Combustion pp. 175–82 (Butterworths, London, 1959).

[32] Fish, A., Comb. and Flame **8,** 84–5 (1964).

[33] Tunder, R., Mayer, S., Cook, E., and Schieler, L., Aerospace Corp., Thermochemistry Res. Dept., Aerospace Report TR–1001 (9210–02)–1 (1967).

[34] Clyne, M. A. A., and Stedman, D. H., Trans. Faraday Soc. **62,** 2164–74 (1966).

[35] Jensen, D. C., and Kurzius, S. C., AeroChem Res. Lab., Princeton, N.J., March 1967. Report TP–149.

[36] Blackmore, D. R., O'Donnell, G., and Simmons, R. F. Tenth Symposium (Internat'l) on Combustion pp. 303–10 (1965). The Combustion Inst., Pittsburgh.

[37] Fenimore, C. P., and Jones, G. W., Tenth Symposium (International) on Combustion, pp. 489–93 (1965), The Combustion Institute, Pittsburgh.

[38] Getzinger, R. W., Eleventh Symposium (International) on Combustion, pp. 117–24 (1967), The Combustion Institute, Pittsburgh.
[39] McEwan, M. J., and Phillips, L. F., Comb. and Flame **11,** 63–70 (1967).
[40] Urey, H. C., and Bates, J. R., Phys. Rev. **34,** 1541 (1929).
[41] Vaidya, W. M., Proc. Indian Acad. Sci. **6A,** 122–8 (1937).
[42] Vaidya, W. M., Proc. Indian Acad. Sci. **7A,** 321 (1938).
[43] Coleman, E. H., and Gaydon, A. G., Disc. Faraday Soc. **2,** 166–9 (1947).
[44] Coleman, E. H., Gaydon, A. G., and Vaidya, W. M., Nature **162,** 108–9 (1948).
[45] Pannetier, G., and Gaydon, A. G., Nature **61,** 242–3 (1948).
[46] Zeelenberg, A. P., Nature **181,** 42 (1958).
[47] Porter, G., Proc. Roy Soc. (London) **A200,** 284–300 (1949–50).
[48] Porter, G., Science **160,** 1299–1307 (1968).
[49] Durie, R. A., and Ramsay, D. A., Canadian J. Phys. **36,** 35–53 (1958).
[50] Carrington, A., and Levy, D. H., J. Chem. Phys. **44,** 1298–9 (1966).
[51] Norman, I., and Porter, G., Nature **174,** 508–9 (1954).
[52] Norman, I., and Porter, G., Proc. Roy Soc. (London) **A230,** 399–414 (1955).
[53] Amano, T., Saito, S., Hiroto, E., Morino, Y., Johnson, D. R., and Powell, F. X., J. Mol. Spectr. **30,** 275 (1969).
[54] Powell, F. X., and Johnson, D. R., J. Chem. Phys. **50,** 4596 (1969).
[55] Clyne, M. A. A., and Coxon, J. A., Trans. Faraday Soc. **62,** 1175–89 (1966).
[56] Niki, H., and Weinstock, B. J., Chem. Phys. **47,** 3249–52 (1967).
[57] Clyne, M. A. A., and Coxon, J. A., Trans. Faraday Soc. **62,** 2175–82 (1966).
[58] Johnson, D. R., and Powell, F. X., private communication.
[59] Porter, G., and Wright, F. J., Disc. Faraday Soc. **14,** 23 (1953).
[60] Burns, G., and Norrish, R. G. W., Proc. Roy Soc. (London) **A271** 289–95 (1963).
[61] Evans, W. H., Munson, T. R., and Wagman, D. D. J. Research NBS **55,** 147–64 (1955) RP 2614.
[62] Norrish, R. G. W., and Thrush, B. A., Quarterly Review **10.** 149–168 (1956).
[63] Broida, H. P., Schiff, H. I., and Sugden, T. M., Nature **185,** 759–60 (1960).
[64] Clyne, M. A. A., and Coxon, J. A., Proc. Roy Soc. (London) **A303,** 207–31 (1968).
[65] Westenberg, A. A., and Fristrom, R. M., J. Phys. Chem. **65,** 591–601 (1961).
[66] Westenberg, A. A., and Fristrom, R. M., Tenth Symposium (International) on Combustion, pp. 473–83 (1964). The Combustion Institute, Pittsburgh.
[67] Bascombe, K. N., Reaction Rate Data. The Hydrogen/Oxygen System, Ministry of Aviation, Explosives Research and Development Establishment, Waltham Abbey, Essex, England, E.R.D.E. 1/S/65.
[68] Bahn, G. S., Pyrodynamics **5,** 221–72 (1967).
[69] Baulch, D. L., Drysdale, D. C., and Lloyd, A. C., High Temperature Reaction Rate Data, Report No. 1 (May 1968), Dept. of Phys. Chem., The University, Leeds, England.
[70] Kaufman, F. Ann. Geophys. **20,** 106–114 (1964).
[71] Johnston, H. S., Nat. Stand. Ref. Data Ser., Nat. Bur. Stand. (U.S.), **20,** 54 pages (Sept. 1968).
[72] Kaufman, F. Proc. Roy Soc. (London) **A247,** 123–39 (1958).
[73] Cherry, S. S., Gold, P. I., and Van Nice, L. J., TRW Systems, Redondo Beach, California, Report 08832–6001–T0000.
[74] Clyne, M. A. A., and Stedman, D. H., Trans. Faraday Soc. **64,** 2698 (1968).
[75] Ip, J. K. K., and Burns, G., J. Chem. Phys. **51,** 3414–24 (1969).
[76] Porter, G., and Smith, J. A., Nature **184,** 446–7 (1959).
[77] McEwan, M. J., and Phillips, L. F., Trans. Faraday Soc. **62,** 1717–20 (1966).
[78] Unpublished results, E. C., Creitz, Fire Research Section, National Bureau of Standards.
[79] Lloyd, A. C., and Garvin, D., National Bureau of Standards, private communication.
[80] Greiner, N. R., J. Chem. Phys. **51,** 5049–51 (1969).
[81] Tanford, C., and Pease, R. M., J. Chem. Phys. **15,** 431 (1947).

(Paper 74A4–618)

JOURNAL OF RESEARCH of the National Bureau of Standards—A. Physics and Chemistry
Vol. 74A, No. 4, July–August 1970

The NBS Alloy Data Center: Description of Index to the Literature*

G. C. Carter, D. J. Kahan, L. H. Bennett, J. R. Cuthill, and R. C. Dobbyn

**Institute for Materials Research,
National Bureau of Standards,
Washington, D.C. 20234**

(December 11, 1969)

Computerized listings of 10,000 research papers, indexed at the Alloy Data Center, are now being made available in two forms. In the first, the Permuted Materials Index, all records are arranged alphabetically by chemical symbol. Records referring to alloys or compounds are listed under each of the constituent elements. In the second, the Author Index, all papers are listed alphabetically by first author in three groupings: the first, the NMR papers; the second, the soft x-ray papers; and the third, a broad group of papers that have been of general interest to the Alloy Physics Section. The magnetic tape on which the indexed file is stored will be made available at a future date.

Key words: Alloy data; bibliography; index; information; Knight shifts; NMR; soft x ray.

1. General Discussion

The Alloy Data Center (a part of the National Standard Reference Data System) has developed an automated system for retrieving papers indexed for its internal use. In its first years, the Center has concentrated on nuclear magnetic resonance (NMR) and soft x-ray (SXS) data. There are other topics for which we have entered several papers. These are electronic transport properties, magnetic properties, mechanical properties (density, elastic constants; no engineering properties), resonance properties (such as EPR, Mössbauer effect), quantum description of solids (Fermi surface work, band structures, density of states, etc.), radiation (optical and other), superconductivity, and some thermodynamic properties (e.g., specific heats). The NMR and SXS papers and some papers in these other categories have been deep-indexed and the codes entered in structured format onto magnetic tape.

The following information is available on the tape; the first author and journal citation; main experimental technique; physical properties, usually in order of importance in the paper; materials studied (metals, and alloys, up to quaternary); material composition (in atomic percent); and temperature (absolute scale) at which the work was performed. An example of a page of one of our indices is shown in figure 1.

The magnetic tape, the "Biblio-Master-File," can be manipulated in a number of fashions with various available computer programs. The details of format, tape maintenance, and computer programs, and the various capabilities as well as limitations have been described earlier [1].[1]

The indices are now being made available in hard copy in two forms [2]. The magnetic tape containing the "Biblio-Master-File" will be available in the future. The first printed form is the "Permuted Materials Index" (e.g., a CuNi alloy is listed under both Cu and under Ni) and the second, the "Author Index," lists the papers alphabetically by first author. This latter index has been separated into three parts, according to the specific topics with which the Alloy Data Center has been primarily concerned.

The first part deals with NMR, and is now thought to be complete for Knight shifts (property code 4K, see fig. 1, PROPERTIES column). The total number of such papers is approximately 800. These cover the years 1949 (the discovery of the Knight shift) through 1969. Some papers of the year 1970 are also included. The second part deals with soft x-ray spectra, SXS, and now contains ~500 emission papers; some

*This work was partially supported by the National Standard Reference Data System.

[1] Figures in brackets indicate the literature references at the end of this paper.

RUN DATE 01-09-70 NATIONAL BUREAU OF STANDARDS PAGE NO. 238
ALLOY DATA BIBLIOGRAPHY
**** PERMUTED ALPHABETICAL MATERIAL INDEX ****

FIRST AUTHOR	NO OF AUTHORS	JOURNAL NAME	VOL.	PAGE	YEAR	REFER. NUMBER	SUBJECT	PROPERTIES	CARD NO.	ALLOY	ELE STY	COMP. LO	COMP. HI	TEMP. LO	TEMP. HI	CHAN CODE
LAWSON W	2	PHYS LET	28A	203	1968	680480	FER F		2	CD CR SE AG			28	04	180	
LAWSON G	2	PHYS LET	28A	203	1968	680480	FER F		3	CD CR SE AG			58	04	180	
BACKLUND N	1	PHYS CHEM SOL	7	94	1958	580020	ETP F	1B		CD CU			00	01	04	
BLATT F	1	PHYS REV	108	285	1957	570007	ETP T	1D		CD CU			01		00	
HENRY W	2	CAN J PHYS	38	911	1960	600248	MAG F	2X		CD CU		0	01		300	
HUND C	2	J PHYS CHEM SOL	29	2205	1968	680598	QDS T	5N 5W 1D 4N 1T 1H		CD CU		0	05			
HUND C	2	J PHYS CHEM SOL	29	2205	1968	680598	QDS T	8C 2X	1	CD CU		0	05			
KOHN W	2	PHYS REV	119	912	1960	600095	NMR T	4E 3U 5N		CD CU	2			00	300	
ROWLAND T	1	PHYS REV	119	900	1960	600068	NMR F	4B		CD CU	2	0	05			
ROWLAND T	2	PHYS REV	134A	743	1964	640055	NMR F	4K 4H		CD CU	1	0	01			
SAGALYN P	3	PHYS REV	124	428	1961	610077	NMR T	4E 4B 4A 3N 3G		CD CU	2	0	02			
TEMPLETON I	3	ABSTRACT OF LT	11C	47	1968	680765	QDS F	5H 5F		CD CU			00			
SATO H	2	PHYS REV	124	1833	1961	610029	XRA F	3O 8F 3N 5F 5U 5O		CD CU AU				500	700	
SATO H	2	PHYS REV	124	1833	1961	610029	XRA F	8L	1	CD CU AU				500	700	
SATO H	2	PHYS REV	124	1833	1961	610029	XRA F		2	CD CU AU				500	700	
FRANKEL R	6	PHYS LET	15	163	1965	650429	PAC F	4C	*	CD FE			00			
GAIM S	1	PROC PHYS SOC	90	1065	1967	670151	MOS F	4N		CD FE	2		100		300	
GAIM S	3	PROC PHYS SOC	2C	1388	1968	680554	MOS F	4A		CD FE	2		100		300	
SEGNAN R	2	REVSMODERN PHYS	36	408	1964	640504	MOS F	4N 4L		CD FE	2		100		300	
SRIVASTAV P	3	ACTA MET	16	1199	1968	680602	CON F	8F 0M 3O		CD GA		40	85			
SEKIZAWA K	2	J PHYS SOC JAP	21	684	1966	660987	MAG F	2I 2T 2B 3O		CD GD			50	04	300	
PETER M	6	PHYS REV	126	1395	1962	620166	EPR F	4G 3O 4A 2J 2L 2X		CD GD AG			67	01	500	
PETER M	6	PHYS REV	126	1395	1962	620166	EPR F		1	CD GD AG			30	01	500	
PETER M	6	PHYS REV	126	1395	1962	620166	EPR F		2	CD GD AG			03	01	500	
PETER M	1	PROC COL AMPERE	12	1	1963	630128	EPR F	4G 2X 8C 4A 2B		CD GD AG		0	97	20	178	

FIGURE 1. *A typical page of the Permuted Materials Index.*

emission papers published from 1929 to 1940 are included and all papers since 1940 are in the system. Several SXS absorption papers are also in the system but completeness for this group has not been attempted for this listing. The third part contains those papers not dealing specifically with the above named topics, but which are related to them. Examples here are: magnetic susceptibility, density of states, and more generally, Quantum Description of Solids (QDS, see fig. 1, SUBJECT column). In this case there is some overlap, as some of these papers have been included in the soft x-ray files. The topics in the third part of the Author Index are biased somewhat to other research carried out in the Alloy Physics Section, such as Mössbauer effect (MOS, see fig. 1, SUBJECT column), specific heats (electronic and other), and magnetic susceptibility. However, the literature has not been searched specifically for such topics. That is, only a fraction of the total number of papers on these other solid state properties are included. Consequently this third section of the Author Index is useful only in the sense of "some additional information" but does not serve the user as a substitute for a full literature search in these related topics. This is because these additional papers were primarily entered for our own internal use, with no immediate aim toward a compilation of the corresponding properties. On the other hand this Index may be of special interest in that it does include some papers published in the more obscure sources.

We have compiled a list of physical properties pertinent to the general topic of electronic structures of metals. We specifically do not search the literature for several of the properties indicated in this list, as other Data Centers are handling these. Such properties are indexed and therefore retrieved primarily because of our deep indexing scheme: upon fully reading a paper for indexing, such properties are at times described and therefore indexed. These papers can then be brought to the attention of the appropriate Data Centers. Examples of these properties are: phase diagrams [3], structures and lattice constants [4], and diffusion [5]. A compilation of currently existing Data Centers dealing with several of the properties indicated in our List is available in Appendix A of ref. [1]. Another compilation of this kind, for Data Centers covering a much wider scope, has recently become available [6].

We thank R. W. Mebs, A. J. McAlister, I. D. Weisman, and other members of the Alloy Physics Section for their indexing contributions.

2. References

[1] NBS Technical Note 464 (August 1969) by Carter, G., Bennett, L. H., Cuthill, J. R., and Kahan, D. J., available from the Superintendent of Documents, U.S. Government Printing Office, Washington, D.C. 20402, $1.25.

[2] Copies of the Indices are available under separate cover from the Clearinghouse for Federal Scientific and Technical Information, 5285 Port Royal, Springfield, Va. 22151 as:

a. The NBS Alloy Data Center: Permuted Materials Index, NBS Special Publication 324. This publication is also available from the Superintendent of Documents, U.S. Government Printing Office, Washington, D.C. 20402.

b. The NBS Alloy Data Center: Author Index, Office of Standard Reference Data Bibliography Series, OSRD–B–70–2.

[3] Binary Metals and Metalloid Constitution Data Center, Illinois Institute of Technology Research Institute, Chicago, Ill. 60616. The purpose of this center is to keep the compilation "Constitution of Binary Alloys," originally compiled by M. Hansen (McGraw-Hill Book Co., 1958), current.

[4] Pearson, W. P., complete and current compilations are prepared for metals and alloys. See "A Handbook of Lattice Spacings and Structures of Metals and Alloys" (Pergamon, Vol. I, 1958; Vol. II, 1967).

[5] Diffusion in Metals and Alloys Data Center, Institute of Materials Research, National Bureau of Standards, mailing address: Washington, D.C. 20234.

[6] International Compendium of Numerical Data Projects—A Survey and Analysis, produced by CODATA, The Committee on Data for Science and Technology of the International Council of Scientific Unions (Springer Verlag, N.Y., 1969).

(Paper 74A4–619)

Symposium on Electronic Density of States

Electronic Density of States was the subject of the 3d Materials Research Symposium, sponsored by, and held at the National Bureau of Standards, Gaithersburg, Md. on November 3–6, 1969. Attention was focussed on the correlation of various experimental and theoretical techniques such as optical methods; photoelectron, soft x-ray, and ion neutralization spectroscopy; specific heat; Knight shift; and magnetic susceptibility. Band theory and many-body effects, as they relate to the electronic density of states, were included.

Approximately 100 papers were presented at these sessions, including 16 invited presentations. Six of these invited papers were published in the March–April 1970 issue of the Journal, five were published in the May–June 1970 issue, and five appear in this issue. All of the papers presented at the symposium will be published by the National Bureau of Standards as Special Publication 323 which will appear later this year.

JOURNAL OF RESEARCH of the National Bureau of Standards—A. Physics and Chemistry
Vol. 74A, No. 4, July-August 1970

What is a Quasi-Particle?*[1]

J. R. Schrieffer

Department of Physics, University of Pennsylvania, Philadelphia, Pennsylvania

(October 10, 1969)

The concept of a quasi-particle excitation in an interacting many-body system will be discussed from both the physical and the mathematical points of view. The physical origin of mass enhancement, wave function renormalization, interactions between quasi-particles, *etc.* will be presented. Landau's Fermi liquid theory, including the quasi-particle kinetic equation, will be reviewed. Finally, the domain of validity of the quasi-particle approximation will be discussed.

Key words: Density of states; Green's function; mass enhancement; quasi-particle; superconductors.

1. Introduction

Since the early work of Drude and of Sommerfeld [1], it has been clear that an independent-particle picture represents in a qualitatively correct manner the electronic properties of a metal. The electronic specific heat, the transport properties, the magnetic susceptibility, *etc.* are all roughly accounted for by elementary band theory, without recourse to explicit many-body effects. Exceptions to the rule are the plasma modes observed in the energy loss of fast charged particles, as well as cooperative phenomena such as superconductivity ferromagnetism, antiferromagnetism, *etc.*

The success of the independent-particle approximation (IPA) is particularly striking in view of the large ratio of interelectronic Coulomb energy to kinetic energy experienced by electrons in metals. A measure of this ratio is the electron density parameter r_s defined essentially as the mean spacing between electrons, measured in units of the Bohr radius. For $r_s \ll 1$, the Coulomb interactions between electrons are weak compared to the kinetic energy effects, while if $r_s \gg 1$ the potential effects dominate the kinetic effects. For simple metals, r_s is typically between two and six. Thus, one might expect qualitative changes in the properties of metals relative to the IPA since this approximation includes only the *average* Coulomb interaction between electrons. The "correlation energy" neglected by the IPA is of order 1 to 2 eV per electron and is by no means trivial.

The qualitative reason that the IPA works so well is that typical measurements made on metals at normal temperatures ($T \ll T_F \sim 10^5$ K, where T_F is the Fermi temperature) involve only the low lying excited states of the metal. There is good theoretical (and experimental) evidence that these many-body states are well characterized in terms of a set of elementary excitations, called quasi-particles, which for the interacting system play the same role as the excited electrons (above the Fermi surface) and the excited holes (below the Fermi surface) in the IPA. As for electrons and holes, these quasi-particles are labelled by a wave vector $\mathbf{k}$ and a spin orientation $s = \pm 1/2$. It is assumed that there is a sharp Fermi surface in the actual system as $T \to 0$, although its shape may depend on the many-body interactions. By convention, one measures the quasi-particle energies $\epsilon_{\mathbf{k}}$ relative to their (common) value on the Fermi surface so that $\epsilon_{\mathbf{k}_F} = 0$, where $\mathbf{k}_F$ is a wave vector on the Fermi surface.

At sufficiently low temperature, few quasi-particles are excited and therefore this dilute quasi-particle gas is nearly a "perfect" gas, in the sense that the quasi-particles rarely collide. Furthermore, at low temperature only low energy quasi-particles are excited. Since their intrinsic decay rate varies as $\epsilon_{\mathbf{k}}^2$, they constitute long lived, weakly interacting excitations, thereby justi-

*An invited paper presented at the 3d Materials Research Symposium, *Electronic Density of States*, November 3–6, 1969, Gaithersburg, Md.

[1] This work was supported in part by the National Science Foundation.

fying their use as the building blocks for the low lying excitation spectrum.

There is no need in principle for the effective mass of the quasi-particles (q.p.) to be simply related to the free electron (or band structure) mass. For simple metals, it turns out that the q.p. mass m^* is of the order of the free electron mass m_e, differing from it in most cases by a factor of less than two. The main source of the deviation of m^* from m_e (aside from band structure) is the electron-phonon interaction, which in general leads to an increase of m^*.

Unfortunately, there is at present no truly first principles proof of the above statements, *i.e.* the 1:1 correspondence of the low lying excited states of the noninteracting and interacting systems, a simple effective mass spectrum, long lifetimes of the quasi-particles, *etc.*, although one has a proof that these statements are true to *all* orders in perturbation theory starting from the noninteracting states [2]. This lack of a rigorous foundation for the theory is not merely a mathematical nicety, since we know of many systems (*e.g.* the superconducting phase) which are not connected perturbatively with the noninteracting system; nevertheless, quasi-particles are still of use even in this case. One assumes that in normal systems (absence of cooperative effects) perturbation theory (or alternatively, adiabatic switching on of the interactions) gives the correct physics of the interacting system despite subtle nonanalytic effects which are likely present even in normal systems.

Thus far we have discussed only the excitation spectrum and not the many-body wave functions. Response functions (*e.g.* transport phenomena) require information about both quantities. The remarkable fact is that a suitably defined kinetic (or Boltzmann-like) equation for the *quasi-particle* distribution function gives an accurate account of the response of the system to long wavelength, low frequency perturbations such as electric and magnetic fields. This second property of quasi-particles is the heart of why the Drude-Sommerfeld scheme works well for nonequilibrium as well as equilibrium phenomena.

There is not time here to go into the details of the Landau theory of Fermi liquids, upon which the present theory of quasi-particles in metals is based. The excellent books of Pines and Nozieres [3] and of Nozieres [4] deal in depth with this topic. We would like, however, to give a brief sketch of the theory and to make a few comments about it.

2. The Landau Picture of Fermi Liquids

In the Landau picture one assumes that the low energy excited states of the interacting system have energies well approximated by the form

$$E(\delta n_{\mathbf{k}s}) = \sum_{\mathbf{k}s} \epsilon_{\mathbf{k}s} \delta n_{\mathbf{k}s} + \frac{1}{2} \sum_{\mathbf{k}s\mathbf{k}'s'} f^{ss'}_{\mathbf{k}\mathbf{k}'} \delta n_{\mathbf{k}s} \delta n_{\mathbf{k}'s'}. \quad (2.1)$$

Here $\delta n_{\mathbf{k}s}$ is a measure of the quasi-particle (q.p.) occupation numbers. Assuming there is a well defined Fermi surface S_F at zero temperature described by the wave vectors $\mathbf{k}_F$, one has

$$\delta n_{\mathbf{k}s} = \begin{cases} +1, & \mathbf{k}s \text{ outside } S_F \text{ and occupied by a quasi-electron} \\ -1, & \mathbf{k}s \text{ inside } S_F \text{ and occupied by a quasi-hole} \\ 0, & \text{otherwise.} \end{cases}$$

The zero-order q.p. energy $\epsilon_{\mathbf{k}s}$ is measured relative to the chemical potential μ so that $\epsilon_{\mathbf{k}_F s} = 0$. One assumes that $\epsilon_{\mathbf{k}s}$ and its derivatives are continuous across S_F and one makes the effective mass approximation

$$\mathbf{v}_{\mathbf{k}s} = \frac{1}{\hbar} \nabla \epsilon_{\mathbf{k}s} = \frac{\hbar \mathbf{k}}{m^*}, \quad (2.2)$$

The approximation (2.2) often suffices, since one is usually interested in q.p. states $\mathbf{k}s$ in the immediate vicinity of S_F (since $T \ll T_F$). The term involving $f^{ss'}_{\mathbf{k}\mathbf{k}'}$ represents the energy of interaction between quasi-particles. This function and m^* are considered to be parameters to be determined from experiment or to be *roughly* estimated from a more fundamental theory.

Landau argued that if one views the quasi-particles as being described by wave packets whose extent is large compared to the wavelength of a q.p. at the Fermi surface ($\lambda_F \sim 2\pi/k_F \sim 10^{-8}$ cm in metals) then one can define a distribution function $\delta n_{\mathbf{k}s}(\mathbf{r}, t)$ for q.p.'s which plays the role of the single particle distribution function $f(\mathbf{r},\mathbf{p},t)$ in kinetic theory. This concept is reasonable as long as $\delta n_{\mathbf{k}s}(\mathbf{r},t)$ varies slowly in space (compared to λ_F) and in time (compared to $\hbar/\mu$). By the usual arguments of kinetic theory one can write down a kinetic (Landau-Boltzmann) equation for δn.

$$\frac{\partial \delta n_{\mathbf{k}s}(\mathbf{r},t)}{\partial t} + \mathbf{v}_{\mathbf{k}} \cdot \nabla_{\mathbf{r}} \delta \bar{n}_{\mathbf{k}s}(\mathbf{r}, t) - \mathscr{F}_{\mathbf{k}} \cdot \mathbf{v}_{\mathbf{k}} \delta(\epsilon_{\mathbf{k}s}) = I(\delta n_{\mathbf{k}s}). \quad (2.3)$$

$\mathscr{F}_{\mathbf{k}}$ and $I(\delta n_{\mathbf{k}s})$ are the external force acting on the q.p. and the collision integral respectively, while $\nabla_{\mathbf{r}} \delta \bar{n}_{\mathbf{k}s}$ is defined by

$$\nabla_{\mathbf{r}} \delta \bar{n}_{\mathbf{k}s}(\mathbf{r}, t) = \nabla_{\mathbf{r}} \delta n_{\mathbf{k}s}(\mathbf{r}, t) + \delta(\epsilon_{\mathbf{k}s}) \sum_{\mathbf{k}'s'} f^{ss'}_{\mathbf{k}\mathbf{k}'} \nabla_{\mathbf{r}} \delta n_{\mathbf{k}'s'}(\mathbf{r}, t). \quad (2.4)$$

The term $\nabla_r \delta n_{\mathbf{k}s}$ in (2.4) describes the conventional streaming flow of q.p.'s familiar from kinetic theory. The other term, arising from the interactions, may be viewed as a dragging along of the ground state particles by the inhomogeneous distribution of quasi-particles, each q.p. dragging along its own cloud.

Naively, one might guess that the particle current density $\mathbf{J}(\mathbf{r},t)$ at point $\mathbf{r}$ may be expressed as $\sum_{\mathbf{k}s} \mathbf{v}_{\mathbf{k}s} \delta n_{\mathbf{k}s}(\mathbf{r},t)$. This is *not* true, but rather

$$\mathbf{J}(\mathbf{r},t) = \sum_{\mathbf{k}s} \mathbf{v}_{\mathbf{k}s} \delta \bar{n}_{\mathbf{k}s}(\mathbf{r},t)$$
$$= \sum_{\mathbf{k}s} \left[\mathbf{v}_{\mathbf{k}s} + \sum_{\mathbf{k}'s'} f^{ss'}_{\mathbf{k}\mathbf{k}'} \mathbf{v}_{\mathbf{k}'s'} \delta(\epsilon_{\mathbf{k}'s'}) \right] \delta n_{\mathbf{k}s}(\mathbf{r},t). \quad (2.5)$$

The $\mathbf{v}\delta n$ term represents the current of the quasi-particle, while the term involving f represents the current of the ground state particles being "dragged along" with the q.p. It is clear from the kinetic equation (2.3) that this definition is correct since the continuity equation

$$\frac{\partial \rho}{\partial t} + \nabla \cdot \mathbf{J} = 0 \quad (2.6)$$

is satisfied by $\mathbf{J}$ if we use the fact that

$$\rho = \rho_0 + \sum_{\mathbf{k}s} \delta n_{\mathbf{k}s}(\mathbf{r},t). \quad (2.7)$$

Roughly speaking $f^{ss'}_{\mathbf{k}\mathbf{k}'}$ behaves like a velocity dependent potential acting on particles in $\mathbf{k}$ and $\mathbf{k}'$. A change in $\delta n_{\mathbf{k}s}$ acts on the particle in $\mathbf{k}'s'$ like a vector potential would, and induces a current even though the $\mathbf{k}'$ *wavefunction* does not change, like the Meissner effect in a superconductor.

3. Quasi-Particles in Metals

The above picture is suitable for a system like He^3 which is translationally invariant in its ground state and has only the Fermion degrees of freedom. Metals are clearly different: they are invariant only under the translation group of the crystal lattice and have lattice vibrations as well as electronic degrees of freedom. How much of the Landau picture survives? The "non-interacting system" is presumably now the IPA in which the Coulomb interactions between electrons are treated in the mean field approximation. In this case the one particle states are labelled by a wave vector $\mathbf{k}$ (restricted to the first Brillouin zone), a band index n and the spin s. We lump n and $\mathbf{k}$ together for now. There is a sharp Fermi surface at $T = 0$ and excited states are given by the usual electron and hole excitations. Since the Coulomb interaction has full translation invariance, $\mathbf{k}$ remains a good quantum number to describe the quasi-particles, although the ground state of the actual system may be the transform of some excited state of the IPA system, due to changes in shape of the Fermi surface. Luttinger and Nozieres [2] have shown to all orders in perturbation theory that the *volume* of $\mathbf{k}$ space inside S_F remains fixed, as it must for the Landau picture to make sense. The energy expression (2.1) still holds but $f^{ss'}_{\mathbf{k}\mathbf{k}'}$ is in general a function having only the symmetry of the crystal, rather than full the rotational symmetry present for say He^3. The effective mass expression for $\mathbf{v}_{\mathbf{k}}$ still holds except $1/m^*$ is in general a second rank tensor having only the symmetry of the crystal. If the crystalline anisotropy of m^* and f are very weak (as for Na) then the identity

$$\frac{m^*}{m} = \frac{1 + F_1^s}{3} \quad (3.1)$$

relating the effective mass ratio and the spin symmetric $l = 1$ term F_1^s in a Legendre polynomial expansion of $f^{ss'}_{\mathbf{k}\mathbf{k}'}$ for a true Fermi liquid is valid. Here, if $N(0)$ is the density of single particle states of one spin orientation at the Fermi surface, then

$$F_1^s = N(0)[f_1^{\uparrow\uparrow} + f_1^{\uparrow\downarrow}] \quad (3.2)$$

and

$$f^{ss'}_{\mathbf{k}\mathbf{k}'} = \sum_{l=0}^{\infty} f_l^{ss'} P_l(\cos \hat{\mathbf{k}}\mathbf{k}'). \quad (3.3)$$

Thus, for nearly free electron metals the low temperature electronic specific heat, *i.e.* m^*/m, determines F_1. Other pieces of information about $f^{ss'}_{\mathbf{k}\mathbf{k}'}$ can be extracted from other experiments such as the anomalous skin effect, Azbel-Kaner cyclotron resonance, de Haas van Alphen effect, dynamic magnetic susceptibility, *etc.* Presumably the f_l drop off rapidly with increasing l so only $l = 0$, 1 and perhaps 2 need be retained. For non-free electron metals, it appears that the anisotropy of f is so large that unravelling this function will be quite involved. However, we know that the transport and the *dHvA* measurements have already given us a great deal of information about $1/m^*$ in complex metals. When combined with band structure calculations these measurements give information on the many-body effects in these systems. As we mentioned earlier, most of the m^*/m effect is due to the phonons, for which a reasonably good first principles calculation is becoming possible, in many metals. A careful comparison here would provide an important check on the approximation of band theory and of the approximate methods presently used in many-body theory.

Another problem is that the phonons complicate the kinetic equation and the current density expression, since the phonons carry momentum and energy. The necessary generalizations of the Landau theory have been worked by Prange and Kadanoff [5], although we do not have time to discuss these questions here.

4. Green's Function Picture of Quasi-Particle

An alternative way of viewing quasi-particles, which is more general than the Landau theory, is through the Green's function scheme of many-body theory [3,4,6,7]. Suppose that an interacting system of N electrons is initially prepared to be in its exact ground state, $|0, N\rangle$. If $c^+_{\mathbf{k}s}$ creates a (bare) Bloch electron in state $\mathbf{k}s$, then we desire the probability distribution $P_{\mathbf{k}s}(E)$ of the energy for the $N+1$ particle state $\Phi^{N+1}_{\mathbf{k}s}+1$ defined by

$$|\Phi^{N+1}_{\mathbf{k}s}\rangle = c^+_{\mathbf{k}s}|0, N\rangle. \tag{4.1}$$

In general, Φ is not an eigenstate of the full Hamiltonian so that Φ does not have a sharply defined energy, *i.e.* $P_{\mathbf{k}s}(E)$ is not a delta function. The rules of quantum mechanics tell us that if the states $|n, N+1\rangle$ are the exact energy eigenstates of the $N+1$ particle problem then

$$P_{\mathbf{k}s}(E) = \sum_n |\langle n, N+1 | c^+_{\mathbf{k}s} | 0, N\rangle|^2 \delta(E - [E^{N+1}_n - E^N_0] + \mu) \tag{4.2}$$

$$= \sum_n |\langle n, N+1 | \Phi^{N+1}_{\mathbf{k}s}\rangle|^2 \delta(E - [E^{N+1}_n - E^N_0] + \mu),$$

where the E^{N+1}_n are the energy eigenvalues of the many-body system. Within the IPA, $P_{\mathbf{k}s}(E)$ is a delta function, since $c^+_{\mathbf{k}s}$ creates a Bloch state electron, which by definition is an exact single particle eigenstate of energy $\epsilon_{\mathbf{k}s}$. Thus, for the independent particle approximation (IPA)

$$P^{\mathrm{IPA}}_{\mathbf{k}s}(E) = \begin{cases} \delta(E-\epsilon_{\mathbf{k}s}) & \epsilon_{\mathbf{k}s} > 0 \\ 0 & \epsilon_{\mathbf{k}s} < 0. \end{cases} \tag{4.3}$$

Clearly, according to the Pauli Principle P is zero if one tries to add a particle to an already filled state, $\epsilon_{\mathbf{k}s} < 0$. For the interacting system, P will be a complicated (positive) function of E in general, whose shape depends on the value of $\mathbf{k}s$. The essential point is that if $\mathbf{k}$ is slightly above the Fermi surface, $P_{\mathbf{k}s}(E)$ will consist of a narrow high peak centered about a "quasi-particle energy,"

$$E = \tilde{\epsilon}_{\mathbf{k}s}, \frac{1}{\hbar}\nabla_{\mathbf{k}}\tilde{\epsilon}_{\mathbf{k}s} \cong \frac{\hbar\mathbf{k}}{m^*}, \tag{4.4}$$

plus a background continuum which in general has a rather smooth behavior, as sketched in figure 1 for $\mathbf{k}$ just above the Fermi surface. The half-width of the peak $\Gamma_{\mathbf{k}s}$, gives the intrinsic decay rate of the quasi-particle according to $1/\tau_{\mathbf{k}s} = 2\Gamma_{\mathbf{k}s}/\hbar$. Perturbation theoretic arguments show that Γ goes to zero as $\epsilon_{\mathbf{k}s}{}^2$ for $\epsilon_{\mathbf{k}s} \ll \mu$ so that the fractional width (or the reciprocal "Q" of the particle) varies as $\tilde{\epsilon}_{\mathbf{k}s}$, showing the quasi-particle to be a well defined excitation near the Fermi surface. To complete the story, one considers hole states defined by

$$|\bar{\Phi}^{N-1}_{\mathbf{k}s}\rangle = C_{\mathbf{k}s}|0, N\rangle, \tag{4.5}$$

Like $\Phi^{N+1}_{\mathbf{k}s}$, $\Phi^{N-1}_{\mathbf{k}s}$ is not an eigenstate of energy for the interacting system. Thus, the probability distribution of E for the hole state, which is defined by

$$\bar{P}_{\mathbf{k}s}(E) = \sum_n |\langle n, N-1 | \bar{\Phi}^{N-1}_{\mathbf{k}s}\rangle|^2 \delta(E + [E^{N-1}_n - E^N_0] + \mu)$$

$$= \sum_n |\langle n, N-1 | c_{\mathbf{k}s} | 0, N\rangle|^2 \delta(E + [E^{N-1}_n - E^N_0] + \mu) \tag{4.6}$$

is not a delta function in general. Note the change of sign of the excitation energy term in the delta functions appearing in (4.2) and (4.6). This ensures that at zero temperature the holes have negative energy and electrons have positive energy. Within the IPA, $\bar{\Phi}^{N-1}_{\mathbf{k}s}$ is an eigenstate of H and $\bar{P}^{IPA}_{\mathbf{k}s}(E)$ given by

$$\bar{P}^{\mathrm{IPA}}_{\mathbf{k}s}(E) = \begin{cases} 0 & \epsilon_{ks} > 0 \\ \delta(E-\epsilon_{\mathbf{k}s}) & \epsilon_{\mathbf{k}s} < 0. \end{cases} \tag{4.7}$$

For the interacting system, if $\mathbf{k}s$ is just below the Fermi surface, a narrow, high "quasi-hole" peak centered about $\tilde{\epsilon}_{\mathbf{k}s}$ appears in $\bar{P}_{\mathbf{k}s}(E)$, with a continuum background again occurring as sketched in figure 2. The quasi-hole and quasi-electron energies presumably

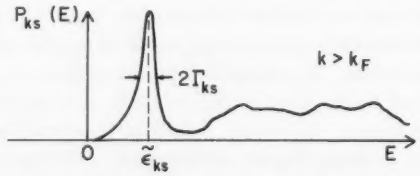

FIGURE 1. *Probability distribution* $P_{ks}(E)$ *for a "quasi-particle" corresponding to a bare Bloch state* $\mathbf{k}s$ *for* $k > k_F$.

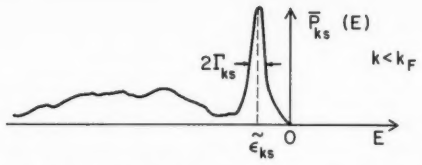

FIGURE 2. *Probability distribution* $P_{ks}(E)$ *for a "quasi-hole" state with* $k < k_F$.

join on smoothly at the Fermi surface so that m^* is continuous across S_F.

At nonzero temperature, one makes a statistically weighted average over initial states, rather than considering only the ground state $|0, N\rangle$. In this case the electron and hole probability distributions overlap, in that they are both nonzero for $E > 0$ and for $E < 0$. The overlapping corresponds to creating or destroying thermally excited quasi-particles, amongst other things. From the Fermi statistics of electrons, there follows the rigorous sum rule

$$\int_{-\infty}^{\infty} [P_{\mathbf{k}s}(E) + \bar{P}_{\mathbf{k}s}(E)]\,dE = 1. \tag{4.8}$$

One advantage of the Green's function description is that it allows the concept of quasi-particles to be usefully extended to systems which are not related by an adiabatic transform or by perturbation theory to the noninteracting states. For example, in a superconductor, $P_{\mathbf{k}s}(E)$ shows at low temperature a sharp peak at the "quasi-particle" energy

$$E = E_{\mathbf{k}s} \equiv \sqrt{\epsilon_{\mathbf{k}s}^2 + \Delta_{\mathbf{k}}^2}, \tag{4.9}$$

while $\bar{P}_{\mathbf{k}s}(E)$ shows a sharp peak at $E = -E_{\mathbf{k}s}$ as sketched in figure 3. In addition, P and $\bar{P}$ show background continua like in the normal metal. Note however that as $\mathbf{k}$ approaches the Fermi surface there is an energy gap between the quasi-hole and quasi-electron peaks, the gap being $2\Delta_{\mathbf{k}_F}$, as is well known from the pairing theory. Thus a minimum energy $2\Delta_{\mathbf{k}_F}$ is required to make a single-particle excitation in a superconductor (*i.e.* creation of a quasi electron-hole pair).

We should mention that the "background continuum" mentioned above corresponds physically to the creation of more complicated excitations, such as a quasi-particle plus electron-hole pairs, phonons, plasmons, *etc.* Generally these extra excitations are not strongly coupled together and therefore an incoherent (smooth) continuum appears. In special cases, however, resonant scatterings states of the excitations can appear, an example being the quasi-bound state of a hole and a plasmon, as Hedin *et al.* [8] have discussed.

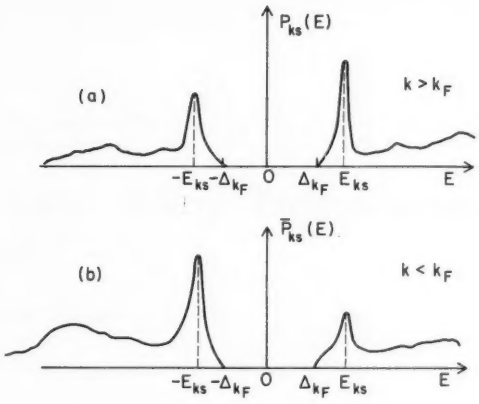

FIGURE 3. $P_{ks}(E)$ *and* $\bar{P}_{ks}(E)$ *for a superconductor showing (a) sharp peak at* $E = E_{ks}$ *in* $P_{ks}(E)$ *and (b) peak in* $\bar{P}_{ks}(E)$ *at* $E = -E_{ks}$.

There is a great deal more one should say about quasi-particles. The interested reader can follow the story further in the books mentioned above and the references contained therein. It is the present author's view that a clearer physical picture of such questions as "drag currents," "back flow," "screening," quasi-particle interactions (both forward and nonforward scattering amplitudes), particularly in real metals, deserve careful attention in the future.

5. References

[1] See C. Kittel, Introduction to Solid State Physics, Chapter 10, J. Wiley & Sons, Inc., New York, and J. Ziman, Principles of the Theory of Solids, Cambridge U. Press (1964).

[2] Luttinger, J. M., and Nozieres, P., Phys. Rev. **127,** 1423, 1431 (1962).

[3] Pines, D., and Nozieres, P., The Theory of Quantum Liquids, **Vol. I,** W. A. Benjamin, Inc., New York (1966).

[4] Nozieres, P., Interacting Fermi Systems, W. A. Benjamin, Inc., New York (1964).

[5] Prange, R. E., and Kadanoff, L. P., Phys. Rev. **134,** A566 (1964).

[6] Abrikosov, A. A., Gorkov, L. P., and Dzysloshinskii, I. E., Methods of Quantum Field Theory in Statistical Physics, Prentice-Hall, Inc. (1963).

[7] Schrieffer, J. R., Theory of Superconductivity, W. A. Benjamin, Inc., New York (1964).

[8] Hedin, L., Lundqvist, B. I., and Lundqvist, S., this Symposium.

(Paper 74A4–620)

383-876 O - 70 - 6

JOURNAL OF RESEARCH of the National Bureau of Standards — A. Physics and Chemistry
Vol. 74A, No. 4, July-August 1970

Electronic Densities of States from X-Ray Photoelectron Spectroscopy *[1]

C. S. Fadley and D. A. Shirley

Lawrence Radiation Laboratory, University of California, Berkeley, California 94720

(October 10, 1969)

In x-ray photoelectron spectroscopy (XPS), a sample is exposed to low energy x rays (approximately 1 keV), and the resultant photoelectrons are analyzed with high precision for kinetic energy. After correction for inelastic scattering, the measured photoelectron spectrum should reflect the valence band density of states, as well as the binding energies of several core electronic levels. All features in this spectrum will be modulated by appropriate photoelectric cross sections, and there are several types of final-state effects which could complicate the interpretation further.

In comparison with ultraviolet photoelectron spectroscopy (UPS), XPS has the following advantages: (1) the effects of inelastic scattering are less pronounced and can be corrected for by using a core reference level, (2) core levels can also be used to monitor the chemical state of the sample, (3) the free electron states in the photoemission process do not introduce significant distortion of the photoelectron spectrum, and (4) the surface condition of the sample does not appear to be as critical as in UPS. XPS seems to be capable of giving a very good description of the general shape of the density-of-states function. A decided advantage of UPS at the present time, however, is approximately a fourfold higher resolution.

We have used XPS to study the densities of states of the metals Fe, Co, Ni, Cu, Ru, Rh, Pd, Ag, Os, Ir, Pt, and Au, and also the compounds ZnS, $CdCl_2$, and HgO. The *d* bands of these solids are observed to have systematic behavior with changes in atomic number, and to agree qualitatively with the results of theory and other experiments. A rigid band model is found to work reasonably well for Ir, Pt and Au. The *d* bands of Ag, Ir, Pt, Au and HgO are found to have a similar two-component shape.

Key words: $CdCl_2$; density of states; HgO; noble metals; rigid band model; transition metals; x-ray photoemission; ZnS.

1. Introduction

The energy distribution of electronic states in the valence bands [1] of a solid is given by the density of states function, $\rho(E)$. There are several techniques for determining $\rho(E)$ at energies within $\sim kT$ of the Fermi energy, E_f, where relatively small perturbations can excite electrons to nearby unoccupied states. However, because of the nature of Fermi statistics, an electron at energy E, well below E_f (in the sense that $E_f - E \gg kT$), can respond only to excitations of energy $E_f - E$ or greater. Because the valence bands are typically several eV wide, a versatile, higher energy probe is required to study the full $\rho(E)$. The principal techniques presently being applied to metals are soft x-ray spectroscopy (SXS) [2,3] ion-neutralization spectroscopy (INS) [4], and photoelectron spectroscopy (by means of ultraviolet [5] or x-ray [6,7] excitation).

In each of these methods, either the initial or the final state involves a hole in the bands under study. Thus the measuring process is inherently disruptive. The actual initial and final states may not be simply related to the undisturbed ground state [8], and only for this ground state does $\rho(E)$ have precise meaning. Even if the deviations from a ground state description can be neglected, there are complications for each of the above techniques in relating measured quantities to $\rho(E)$ [2,3,4,5]. Nevertheless, all four have been applied with some success, and, where possible, experimental

* An invited paper presented at the 3d Materials Research Symposium, *Electronic Density of States*, November 3–6, 1969, Gaithersburg, Md.

[1] Work performed under the auspices of the U.S. Atomic Energy Commission.

results have been compared to the theoretical predictions of one-electron band theory.

In this paper, we outline the most recently developed of these techniques, x-ray photoelectron spectroscopy (XPS) [6,7], and apply it to several metallic and nonmetallic solids. In section 2, the principles of the technique are discussed from the point of view of relating measured quantities to a one-electron $\rho(E)$. In section 3, we present results for the twelve $3d$, $4d$, and $5d$ transition metals Fe, Co, Ni, Cu, Ru, Rh, Pd, Ag, Os, Ir, Pt, and Au, making comparisons with the results of other experimental techniques and theory where appropriate. In addition, results for nonmetallic solids containing the elements Zn, Cd and Hg are presented, to clarify certain trends observed as each d shell is filled. In section 4, we summarize our findings.

2. The XPS Method

The fundamental measurements in both ultraviolet photoelectron spectroscopy (UPS) and x-ray photoelectron spectroscopy (XPS) are identical and very simple. Photons of known energy impinge on a sample, expelling photoelectrons which are analyzed for kinetic energy in a spectrometer. In UPS [5], photon energies range from threshold to ~20 eV, whereas XPS utilizes primarily the $K\alpha$ x rays of Mg (1.25 keV) and Al (1.49 keV). For a given absolute energy resolution, an XPS spectrometer must thus be ~100 times higher in resolving power. We have used a double-focussing air-cored magnetic spectrometer [9], with an energy resolution of $\Delta\epsilon/\epsilon = 0.06$ percent. $\Delta\epsilon$ is defined to be the full width at half maximum intensity (FWHM) of the peak due to a flux of monoenergetic electrons of energy ϵ.

Conservation of energy requires that

$$h\nu = E^h - E^g + \epsilon + \phi_c, \tag{1}$$

where $h\nu$ is the photon energy, E^g the total energy of the initial ground state, E^h the total energy of the final hole state *as seen by the ejected photoelectron*, ϵ the electron kinetic energy, and ϕ_c the contact potential between the sample surface and the spectrometer. If E^h corresponds simply to a hole in some electronic level j, then the binding energy of an electron in level j is by definition $E_b{}^v = E^h - E^g$, where the superscript v denotes the vacuum level as a reference. The Fermi level can also be used as a reference and a simple transformation yields

$$h\nu = E_b^f + \epsilon + \phi_{sp} \equiv -E + \epsilon + \phi_{sp}, \tag{2}$$

where $E_b{}^f \equiv -E$ is the Fermi-referenced binding energy, and ϕ_{sp} is the work function of the spectrometer (a known constant). This transformation makes use of the relations $E_b{}^v = E_b{}^f +$ sample work function and $\phi_c = \phi_{sp}$ − sample work function. Positive charging of the sample due to electron emission can shift the kinetic energy spectrum to lower energies by as much as 1 eV for insulating samples but relative peak positions should remain the same. This effect is negligible for metals.

Returning to eq (1), we see that the fundamental XPS (or UPS) experiment measures the kinetic energy spectrum from which we attempt to deduce the final-state spectrum. This spectrum must then be related to $\rho(E)$, as discussed below.

In addition to $\rho(E)$ modulated by an appropriate transition probability, there will be six major contributors to lineshape in an XPS spectrum. Together with their approximate shapes and widths for the conditions of our experiments, these are:

1. Linewidth of exciting radiation—Lorentzian, ~0.8 eV FWHM for the unresolved Mg$K\alpha_{1,2}$ doublet used as "monochromatic" radiation in this study. The use of a bent-crystal monochromatic might permit narrowing this in future work [7].
2. Spectrometer resolution—slightly skew, with higher intensity on the low-kinetic-energy side, ~0.6 eV FWHM for 1 keV electrons analyzed with 0.06 percent resolution.
3. Hole lifetime in the sample—Lorentzian, ~0.1 to 1.0 eV for the cases studied here.
4. Thermal broadening of the ground state—roughly Gaussian, ~0.1 eV.
5. Inelastic scattering of escaping photoelectrons—all peaks have an inelastic "tail" on the low kinetic-energy side, which usually extends for 10 eV or more.
6. Various effects due to deviations of the final state from a simple one-electron-transition model.

Contributions analogous to (3), (4), and (6) will be common to all techniques used for studying $\rho(E)$. A UPS spectrum will exhibit analogous effects from all six causes. In XPS, there is thus a present lower limit of ~ 1.0 eV FWHM. Core levels with this width are well described by Lorentzian peaks with smoothly joining constant tails [10] (see fig. 1), verifying that the major contribution to linewidth is the exciting x ray. The corresponding lower limit for UPS appears to be 0.2 to 0.3 eV, so that XPS cannot at present be expected to give the same fine structure details as UPS.

The effects of scattering of escaping photoelectrons [(5) above] can be corrected for in both UPS [5] and

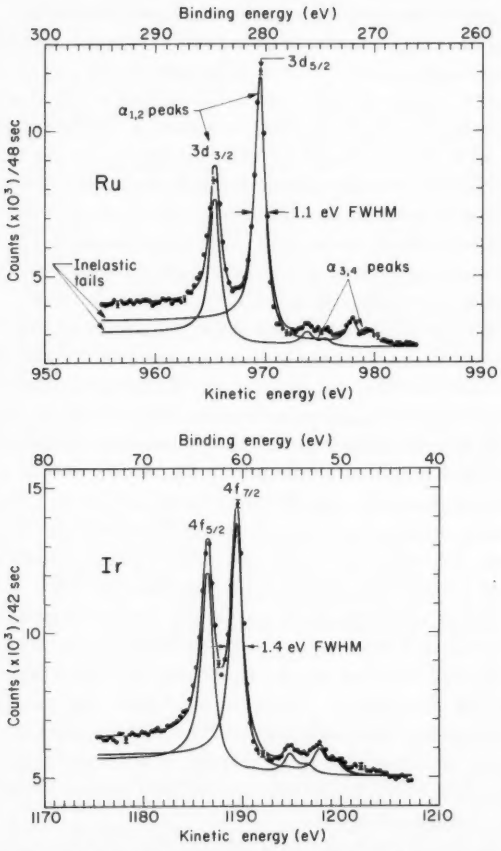

FIGURE 1. *Core level photoelectron spectra produced by exposure of Ru and Ir to Mg x-rays. The levels are Ru $3d_{3/2}-3d_{5/2}$ and Ir $4f_{5/2}-4f_{7/2}$. The peaks due to the Mg$K\alpha_{1,2}$ and Mg$K\alpha_{3,4}$ x rays are noted, as well as the tail observed on each peak due to inelastic scattering. The analysis of these spectra into pairs of Lorentzian-based shapes is described in the text and reference 10.*

XPS [6]. This correction is particularly simple for XPS, however, because narrow core levels can be used to study the scattering mechanisms. As the kinetic energies of electrons expelled from core levels ~100 eV below the valence bands are very near to those of electrons expelled from the valence bands (*i.e*, 1150 eV versus 1250 eV), it is very probable that the scattering mechanisms for both cases are nearly identical.

Subject to this assumption [11], we can correct an observed valence band spectrum, $I_v(\epsilon)$, by using an appropriate core level spectrum, $I_c(\epsilon)$, as a reference [6,10]. If we construct a core level spectrum in the absence of scattering, $I_c'(\epsilon')$, from pure Lorentzian peak shapes, then $I_c(\epsilon)$ and $I_c'(\epsilon')$ can be connected by a response function, $R(\epsilon,\epsilon')$. Since XPS data is accumulated in discrete channels, $I_c(\epsilon)$ and $I_c'(\epsilon')$ can be treated as vectors with typically 100 elements and $R(\epsilon,\epsilon')$ as a 100×100 matrix, these quantities being related by

$$I_c(\epsilon) = R(\epsilon,\epsilon')\, I_c'(\epsilon'). \tag{3}$$

If we now make certain physically reasonable assumptions about the form of $R(\epsilon,\epsilon')$, the effective number of matrix elements to be computed can be reduced to ≤ 100. This permits a direct calculation of $R(\epsilon,\epsilon')$. The next step is to apply $R^{-1}(\epsilon,\epsilon')$ to the observed valence band spectrum, $I_v(\epsilon)$, to yield the corrected spectrum, $I_v'(\epsilon')$. The Lorentzian widths in $I_c'(\epsilon')$ are selected to be 0.6 to 0.8 times the observed widths so that no appreciable resolution enhancement is accomplished by this correction. In addition to inelastic scattering, we can also easily allow for the extra peaks present in any XPS spectrum due to the satellite x-rays of the anode, the most intense of which are $K\alpha_{3,4}$. In XPS spectra produced by bombardment with magnesium x rays, these satellites produce a doublet approximately 10 eV above the main ($K\alpha_{1,2}$) peak and with about 10 percent of the intensity of the main peak (see fig. 1). The details of this correction procedure are discussed elsewhere [10].

The application of this procedure to data on the valence bands of copper is illustrated in figure 2. The strong similarity between corrected and observed spectra indicates the subtle nature of this correction: the essential shape and position of the *d*-band peak is obvious in the uncorrected spectrum. By comparison, this relatively high information content in raw data is not found in UPS [5] or ion-neutralization spectroscopy [4].

An additional advantage of XPS is that the chemical state of the sample can be monitored via observation of core level photoelectron peaks from the sample and possible contaminants [6]. In this way it is possible to detect chemical reactions occurring in the thin surface

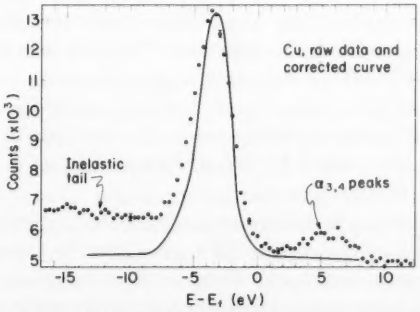

FIGURE 2. *Valence band photoelectron spectrum produced by exposure of Cu to Mg x-rays, together with the corrected spectrum obtained after allowance for the effects of inelastic scattering and Mg$K\alpha_{3,4}$ x-rays in the raw data. A peak due to the 3d bands of Cu is the dominant feature of these spectra.*

layer (~100 Å) responsible for the unscattered photoelectrons of primary interest. Furthermore, experimental results for Fe, Co, and Ni indicate that UPS is more sensitive to surface conditions [6,12].

The relationship of corrected XPS spectra to $\rho(E)$ can be considered in two steps: (1) a one-electron-transition model, in which the appropriate transition probability is expressed in terms of the photoelectric cross section, and (2) deviations from the one-electron-transition model.

The cross section for photoemission from a one-electron state j at energy E will be proportional to the square of the dipole matrix element between that state and the final continuum state,

$$\sigma_j(E) \propto |\langle \psi_j | \bar{r} | \psi(h\nu+E) \rangle|^2, \qquad (4)$$

where $\sigma_j(E)$ is the cross section and $\psi(h\nu + E)$ is the wave function of a continuum electron with energy $h\nu + E$. If there are no appreciable deviations of the final state from a one-electron transition model, the corrected kinetic energy spectrum will be related to $\rho(E)$ by

$$I'(h\nu+E-\phi_{sp}) \propto \int_{-\infty}^{\infty} \bar{\sigma}(E')\rho(E')\rho'(h\nu + E')F(E')L(E-E')dE', \qquad (5)$$

where $\bar{\sigma}(E')$ is an average cross section for all states j at E', $\rho'(h\nu + E')$ is the density of final continuum states, $F(E')$ is the Fermi function describing thermal excitation of electrons near the Fermi surface and $L(E - E')$ is the lineshape due to contributions (1), (2), (3), and (4) discussed above (essentially a Lorentzian).

The factor $\rho'(h\nu + E')$ can be considered constant over the energy range pertinent to the valence bands, as the final state electrons are ~1250 eV into the continuum and the lattice potential affects them very little [6,13]. Therefore, the appropriate final state density will be proportional simply to $\epsilon^{1/2}$. This function is only negligibly smaller for electrons ejected from the bottom of the valence bands ($\epsilon \cong 1240$ eV) than for those emitted from the top of these bands ($\epsilon \cong 1250$ eV). This constancy of $\rho'(h\nu+E')$ cannot be assumed in the analysis of UPS data, however [5].

Any changes in $\bar{\sigma}(E)$ from the top to the bottom of the bands will modulate the XPS spectrum in a way not simply connected to $\rho(E)$. From eq (4) it is apparent that these changes can be introduced by variations in either ψ_j or $\psi(h\nu + E)$ across the bands. The differences in ψ_j from the top to the bottom of the 3*d* band in transition metals have been discussed previously [2,14], but no accurate quantitative estimates of this effect on the appropriate dipole matrix elements have been made to date. It is thus possible that in both XPS and UPS, $\bar{\sigma}(E)$ varies substantially from the bottom to the top of the valence bands because of variation in the initial-state wave functions. This question deserves further study. In XPS, there should be little difference in the final-state wave function, $\psi(h\nu + E)$, between the top and bottom of a band, as a 1240 eV continuum state should look very much like a 1250 eV continuum state. The effects of changes in final state wave function on $\bar{\sigma}(E)$ need not be negligible in a UPS spectrum, however.

Our discussion up to this point has assumed that the photoemission process is strictly one-electron; *i.e.*, that we can describe the process by changing the occupation of only a single one-electron orbital with all other orbitals remaining frozen. This assumption permits the use of Koopmans' Theorem [15], which states that binding energies can be equated to the energy eigenvalues arising from a solution of Hartree-Fock equations. Or, with some admitted errors [16], the one-electron energies obtained from non-Hartree-Fock band structure calculations in which simplifying approximations have been made can be compared directly to a measured binding energy spectrum. We illustrate the use of Koopmans' Theorem in figure 3a, using a hypothetical level distribution for a 3*d* transition metal. There are, however, several types of potentially significant deviations from this one-electron model. We shall discuss these briefly.

The final-state effects leading to these deviations can be separated into several categories, although we note that there is considerable overlap. In a more rigorous treatment some of these separations might not be meaningful, but we retain them here for heuristic purposes. The effects are:

(1) Electrons in the sample may be polarized around a localized positive hole, thereby increasing the kinetic energy of the outgoing electron [8]. In this way, the entire $I(\epsilon)$ spectrum would be shifted toward higher kinetic energy. Polarization might also occur to a different extent for different core levels, for different energies within the valence bands, and for levels at the same energy in the valence bands, but with different wave vector. The latter two effects could act to broaden $I(\epsilon)$ relative to $\rho(E)$. These polarization effects are schematically illustrated in figure 3b. Polarizations will only affect $I(\epsilon)$ to the extent that the kinetic energy of the outgoing electron is altered, however (cf. eq (1)). Since both polarization and photoemission occur on a time scale

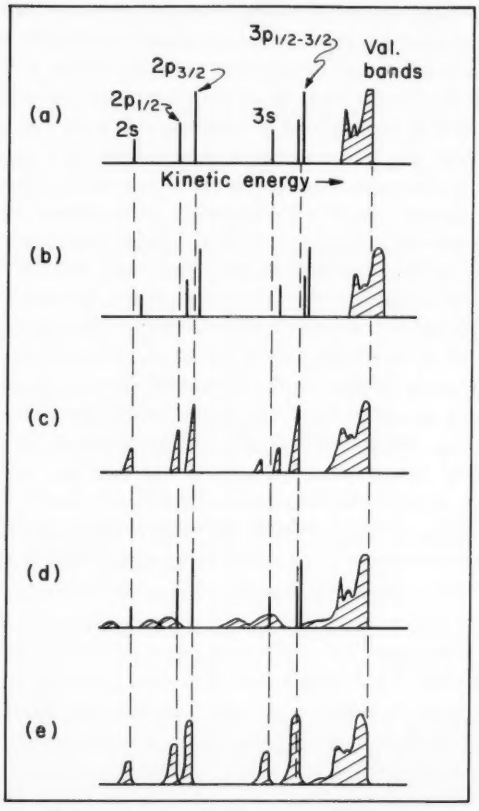

FIGURE 3. *Schematic illustration of various final-state effects on the photoelectron spectrum of a hypothetical 3d transition metal: (a) the Koopmans' Theorem spectrum, in which levels are positioned according to one-electron energies, with relative intensities determined by appropriate photoelectric cross sections; (b) the effect on spectrum (a) of polarization around a localized-hole final state; (c) the effect on spectrum (a) of strong coupling between a localized hole and the valence electrons (note the splitting of the 3s level); (d) the effect on spectrum (a) of two-electron excitation during photoemission; and (e) the effect on spectrum (a) of phonon excitation during photoemission.*

of $\sim 10^{-16}$ s, it is difficult to assess the importance of this effect. As the velocity of an XPS photoelectron is ~10 times that of a UPS photoelectron, the influence of polarization should be somewhat less on an XPS spectrum, however.

(2) In addition to a simple polarization, a localized hole can couple strongly with localized valence electrons [17] or with nonlocalized valence electrons [18]. In iron metal, for example, a 3*s* hole is found to couple in several ways with the localized *d* electron moment, giving rise to an approximately 4 eV "multiplet splitting" in the 3*s* photoelectron peak [17]. Also, it has been predicted that nonlocalized conduction electrons should couple with a localized core or valence hole yielding asymmetric line shapes in electron and x-ray emission [18]. Both of the above effects would act to broaden $I(\epsilon)$ spectra, with the former being more important for systems with a *d* or *f* shell approximately half-filled. These effects are indicated in figure 3c. It has also been predicted that the removal of a core or valence electron will be accompanied by strong coupling to plasma oscillations [19]. This coupling would lead to broad sidebands separated from the one-electron spectrum by as much as 20 eV [19].

(3) It is also possible that not just one electron is fundamentally affected in the photoemission process, but that other electrons or phonons are simultaneously excited [20]. Electrons may be excited to unoccupied bound states or they may be ejected from the sample, and this effect is indicated in figure 3d. The only direct observations of such electronic excitations during photoemission have been on monatomic gases, where two-electron processes are found with as high as 20 percent probability [21]. Vibrational excitations have a marked effect on the UPS spectra of light gaseous molecules [22], but it is difficult to estimate their importance in solids. A classical calculation indicates that for such heavy atoms as transition metals, the recoil energy available for such excitations in XPS is $\leq 10^{-2}$ eV [7]. Also, the observation of core reference levels with linewidths very close to the lower limit of the technique (see fig. 1) seems to indicate that vibrational excitation does not account for more than a few tenths eV broadening and shifting to lower kinetic energy of features observed in the valence-band region. This effect is schematically indicated in figure 3e.

For several reasons, then, XPS seems to be capable of giving more reliable information about the overall shape of $\rho(E)$ than does UPS. However, the present XPS linewidth limit of 1.0 eV precludes determination of anything beyond fairly gross structural features. With these observations in mind, we now turn to a detailed study of the XPS spectra for several solids. We note also that the XPS method is applied to $\rho(E)$ studies in two other papers of these proceedings [23,24].

3. Density-of-States Results for Several 3*d*, 4*d*, and 5*d* Series Metals

3.1. Introduction

Figure 4 shows the portion of the Periodic Table relevant to this work. The twelve elements Fe, Co, Ni, Cu, Ru, Rh, Pd, Ag, Os, Ir, Pt, and Au were studied as metals, while the three elements Zn, Cd, and Hg were studied in the compounds ZnS, $CdCl_2$, and HgO to illustrate the positions, widths, and shapes of filled core-like 3*d*, 4*d*, and 5*d* shells.

Ultra-high vacuum conditions were not attainable during our XPS measurements, as the base pressure in our spectrometer is approximately 10^{-5} torr. Surface contamination of samples is a potential problem, because the layer of the sample that is active in producing essentially inelastic photoelectrons extends only about 100 Å in from the surface [6,7]. This depth is not accurately known, however. Because the contamination consists of oxide formation as well as certain adsorption processes with lower bonding energy for the contaminant, all the metal samples were heated to high temperature (700 to 900 °C) in a hydrogen atmosphere (10^{-3} to 10^{-2} torr) *during* the XPS measurements [6]. These conditions were found to desorb weakly bound species, and to reduce any metal oxides present.

As mentioned previously, it is possible to do *in situ* chemical analyses of the sample by observing core-level photoelectron peaks from the metal and from all suspected contaminants [6]. For all metals, the most important contaminant was oxygen, which we monitored via the oxygen 1*s* peak. Because core electron binding energies are known to be sensitive to the chemical state of the atom [7,25], the observation of core peaks for metal and oxygen should indicate something about the surface chemistry of the sample. The intensities of contaminant peaks should also be a good indicator of the amounts present. Figure 5 shows such results for iron. At room temperature, the oxygen 1*s* peak is strong, and it possesses at least two components. The iron 3*p* peak is also complex and appears as a doublet due to oxidation of a thin surface layer of the sample. As the temperature is increased in the presence of hydrogen, the oxygen peak disappears (the right component disappearing first) and the left component of the iron peak also disappears, leaving a narrow peak characteristic of iron metal. Our interpretation of the disappearing components is that the left oxygen peak (higher electron binding energy) represents oxygen as oxide, the right oxygen peak (lower electron binding energy) represents oxygen present as more loosely bound adsorbed gases, and that the left iron peak (higher electron binding energy) represents oxidized iron [6,25]. Thus at the highest temperatures indicated in figure 5, we could be confident that we were studying iron metal. Similar checks were made on all the other metal samples and oxygen can be ruled out as a contaminant for every case except Pd. (We discuss Pd below.) For example, the core level peaks for Ru and Ir shown in figure 1 do not indicate any significant splitting or broadening due to chemical reaction. The results presented in table 1 indicate similar behavior for all metals studied. The carbon 1*s* peak was also observed and found to disappear for all cases at the temperature of our measurements.

26 $3d^6 4s^2$	27 $3d^7 4s^2$	28 $3d^8 4s^2$	29 $3d^{10} 4s^1$	30 $3d^{10} 4s^2$
Fe	Co	Ni	Cu	Zn
bcc	fcc	fcc	fcc	--
44 $4d^7 5s^1$	45 $4d^8 5s^1$	46 $4d^{10}$	47 $4d^{10} 5s^1$	48 $4d^{10} 5s^2$
Ru	Rh	Pd	Ag	Cd
hcp	fcc	fcc	fcc	--
76 $5d^6 6s^2$	77 $5d^9$	78 $5d^{10}$	79 $5d^{10} 6s^1$	80 $5d^{10} 6s^2$
Os	Ir	Pt	Au	Hg
hcp	fcc	fcc	fcc	--

FIGURE 4. *The portion of the periodic table studied in this work. The atomic number, free-atom electronic configuration, and metal crystal structures are given. Zn, Cd, and Hg were studied as compounds. The crystal structures are those appropriate at the temperatures of our metal experiments (700-900 °C).*

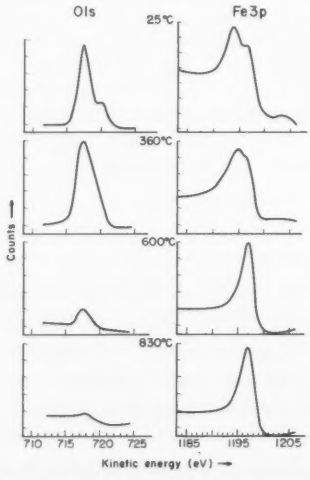

FIGURE 5. *Oxygen 1s and 3p photoelectron peaks from metallic iron at various temperatures in a hydrogen atmosphere. Note that the Fe 3p component at lower kinetic energy (an "oxide" peak) disappears at high temperature along with the O1s peaks. MgKα radiation was used for excitation throughout the work reported here.*

TABLE 1. *Summary of pertinent results for the fifteen solids studied.*

The reference core levels used for inelastic scattering correction are listed, along with their binding energies and widths. The widths of the *d*-band peaks are also given, along with the spacing of the two components in these peaks (if observed).

Solid	Reference core levels	Ref. core level binding energy [a] (eV)	FWHM of core levels [b] (eV)	FWHM of *d*-band peak (eV)	Separation of 2 components in *d*-band peak (eV)
Fe	$3p_{1/2-3/2}$ (unresolved) [c]	52	2.3	4.2	.....
Co	$3p_{1/2-3/2}$ (unresolved) [c]	57	2.5	4.0	.....
Ni	$3p_{1/2-3/2}$ (unresolved) [c]	66	3.4	3.0	.....
Cu	$3p_{1/2-3/2}$ (unresolved) [c]	75	4.2	3.0	.....
ZnS	$3p_{1/2-3/2}$ (unresolved) [c]	90	5.4	1.7	.....
Ru	$3d_{3/2-5/2}$	280	1.1	4.9	.....
Rh	$3d_{3/2-5/2}$	307	1.3	4.4	.....
Pd	$3d_{3/2-5/2}$	335	1.3	4.1	.....
Ag	$3d_{3/2-5/2}$	368	1.0	3.5	1.5–1.8
$CdCl_2$	$3d_{3/2-5/2}$	408	1.2	2.0	.....
Os	$4f_{5/2-7/2}$	50	1.3	6.5	.....
Ir	$4f_{5/2-7/2}$	60	1.4	6.3	3.3
Pt	$4f_{5/2-7/2}$	71	1.5	5.8	3.3
Au	$4f_{5/2-7/2}$	84	1.2	5.7	3.1
HgO	$4f_{5/2-7/2}$	103	1.5	3.8	1.8

[a] Binding energy of the $l + 1/2$ component, relative to the Fermi energy.
[b] Equal widths assumed for both components in the least-squares fits for 3*d* and 4*f* levels.
[c] The theoretical spin-orbit splitting for the 3*p* levels in this series range from 1.6 eV for Fe to 3.1 eV for Zn (Ref. 36). The partially resolved doublet in ZnS is found to have a separation of 2.8 eV, in good agreement.

All metals were studied as high purity polycrystalline foils, except for Ru and Os, which were studied as powders [10].

The nonmetallic samples (ZnS, $CdCl_2$, and HgO) were studied as powders at room temperature. Both considerations of chemical stability and observations of core levels indicated no significant surface contamination, although high purity for these cases was not of paramount importance.

The results reported here were obtained with 1.25 keV Mg$K\alpha$ radiation for excitation. However, no significant changes are introduced with Al$K\alpha$ radiation of 1.49 keV energy.

We present below our experimental results for these *d* group metals, as well as the results of other experiments and theory. Statistical error limits are shown on all XPS results. Throughout our discussion, we shall speak of "$\rho(E)$" as determined by a certain technique, bearing in mind that no experimental technique directly measures $\rho(E)$, but rather some distribution peculiar to the experiment (*e.g.*, the UPS "optical density of states" [5], or the INS "transition density function" [4]), which is related to $\rho(E)$ in some way (*e.g.*, by our eq (5)).

The location of the Fermi energy was determined by using eq (2). This determination was checked against photoelectron peaks from a Pt standard [10]. Our estimated overall accuracy in determining E_f is ± 0.5 eV, so that precise comparison of features in XPS spectra with features present in the results of other experiments (all of which have roughly the same E_f accuracy) is not always possible.

Finally, we note that the dominant feature in our results for all cases is a peak due to the bands derived from *d* atomic orbitals. The XPS method is not particularly sensitive to the very broad, flat, *s*- or *p*-like bands in metals, and such bands are seen with enhanced sensitivity only in studies using ion-neutralization spectroscopy [4].

3.2. The 3*d* Series: Fe, Co, Ni, Cu and Zn

Our results for Fe, Co, Ni, and Cu have been published elsewhere [6], but it is of interest to compare them with more recent results from theory and other experiments [3,12]. There are now enough data available that it is worthwhile to discuss and compare results for these iron group metals individually, as Eastman [12] has done.

a. Iron (bcc)

Hanzely and Liefeld [3] have studied Fe, Co, Ni, Cu, and Zn using soft x-ray spectroscopy (SXS). Their results for Fe, together with Eastman's UPS results [12] and our own, are plotted in figure 6a. In comparing the three $\rho(E)$ curves we note that their relative heights and areas have no significance: we have adjusted the heights to be roughly equal, in order to facilitate comparison. Also the UPS curve is terminated at E_f and is less reliable in the dashed portion, for $E < E_f - 4$ eV [12]. With these qualifications, the overall agreement

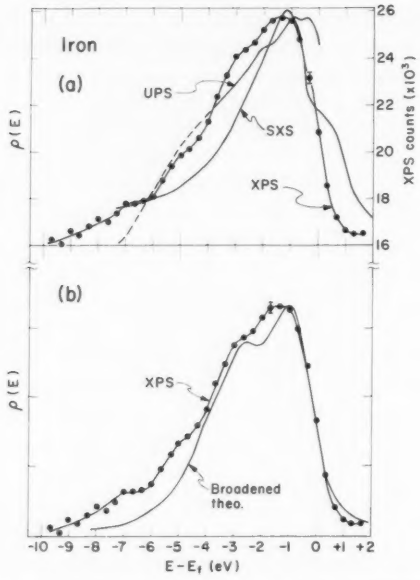

FIGURE 6. *Results for iron metal. The XPS data were obtained at 780 °C and have been corrected for the effects of inelastic scattering and MgK$\alpha_{3,4}$ x-rays. In (a) the XPS data are compared with UPS (ref. 12) and SXS (ref. 3) curves. In (b) the XPS data are shown together with a theoretical curve obtained by broadening the ferromagnetic density-of-states function of reference 26. Right ordinate is thousands of counts in the XPS data*

among these results from three different experimental methods is really quite good. The function $\rho(E)$ appears to be essentially triangular, peaking just below E_f and dropping more or less linearly to zero at $E \sim E_f - 8$ eV.

Upon closer inspection however, the agreement is less impressive. The SXS results are somewhat narrower, but with more intensity *above* E_f, probably due to spurious effects [3]. There is little coincidence of structure, although the maxima for XPS and SXS coincide fairly well. A shift of ~1 eV of the XPS curve toward E_f or the UPS curve in the opposite direction would improve their agreement, but it is unlikely that the combined errors in the location of E_f location are that great.

In figure 6b, the XPS results are compared to the one-electron theoretical $\rho(E)$ calculated by Connolly [26] for ferromagnetic iron. The theoretical $\rho(E)$ has been smeared at the Fermi surface with a Fermi function corresponding to the temperature of our experiment (780 °C) and then broadened with a Lorentzian lineshape of 1.0 eV FWHM. It should thus represent a hypothetical "best-possible" XPS experiment in a one-electron model (*i.e.*, eq (5) with $\bar{\sigma}(E')$ and $\rho'(h\nu + E')$ constant). The agreement between theory and experiment is good, particularly above $E_f - 5$ eV. The XPS (or SXS) results give somewhat higher intensity below $E_f - 5$ eV than theory. We note that hybridization of the d bands can lead to significant broadening of the theoretical $\rho(E)$ of Ni [14]. A similar sensitivity of the iron $\rho(E)$ to the amount of hybridization could account for the discrepancy in width between XPS and theory.

Our reason for comparing experimental results to *ferro*magnetic instead of *para*magnetic theoretical predictions is as follows: In experiments on ferromagnetic metals, no significant differences are observed between XPS [6, 17] and INS [4] results obtained above and below the Curie temperature (T_c, where long-range ferromagnetic order should disappear). Furthermore, exchange-induced splittings of core electronic levels in iron are the same above and below T_c [17]. It thus appears that localized moments persist above T_c for times at least as long as the duration of the photoemission process. Local moments might be expected to affect the kinetic energy distributions of electrons ejected from valence bands and core levels [17] in much the same way, independent of the presence of long range order. Thus a comparison of experiment with a paramagnetic $\rho(E)$ may be *a priori* irrelevant, inasmuch as a ferromagnetic $\rho(E)$ takes these effects into account in an approximate way. Eastman [12] has also noted that UPS results for Fe, Co, and Ni *below* T_c are in general in better agreement with ferromagnetic theoretical $\rho(E)$'s than with similar paramagnetic theoretical results. Accordingly, we shall compare our results only with ferromagnetic theoretical curves for Ni and Co in the next sections.

b. Cobalt (fcc)

The experimental situation is illustrated by the three density-of-states curves in figure 7a. The comparison is quite similar to that for iron. Good overall agreement is apparent, with less agreement in detail. Eastman's UPS curves [12] in both cases show structure near the Fermi energy that is missing from the SXS [3] and XPS results, and at lower energies the UPS curve tends to be higher than the others, especially in the dashed portion where it is less reliable [12]. In this region the XPS curve lies between the other two for Co as well as for Fe. One index of agreement among the three curves in the full width at half-maximum height, which is about 3, 4, and 5 eV for SXS, XPS, and UPS, respectively.

In figure 7b, we compare our XPS results to a ferromagnetic theoretical curve of Wong, Wohlfarth, and Hum [27] for *hcp* Co (our experiments were done on *fcc* Co, for which no detailed theoretical results are available). The theoretical curve has been broadened in an analogous fashion to that for iron. The agreement

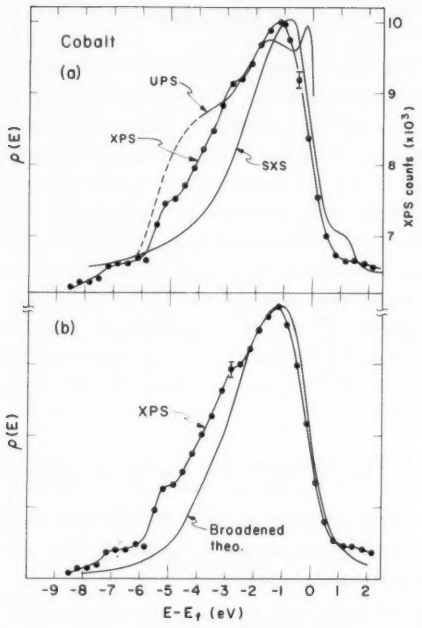

FIGURE 7. *Results for cobalt metal. The XPS data were taken at 925 °C and have been corrected for inelastic scattering and* $MgK\alpha_{3,4}$ *x-rays. In (a) these data are compared with UPS (ref. 12) and SXS (ref. 3) results. In (b) the comparison is with an appropriately broadened ferromagnetic theoretical curve from reference 27.*

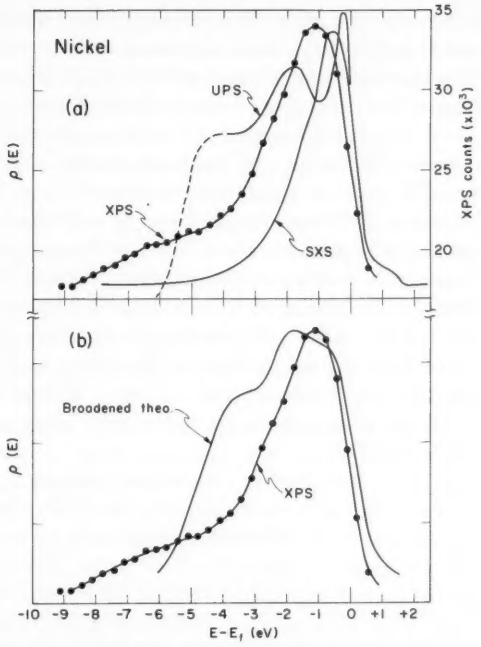

FIGURE 8. *Results for nickel metal. The corrected XPS data are based on measurements at 870 °C. In (a) they are compared with UPS (ref. 12) and SXS (ref. 3) curves. In (b) they are compared to the ferromagnetic theoretical density-of-states function from reference 14, which has been broadened.*

is good for $E > E_f - 3$ eV, but the XPS results are somewhat high below that point. In fact, the overall agreement is probably best between theory and SXS (cf. fig. 7a).

c. Nickel (fcc)

Experimental results for Ni are presented in figure 8a [3,12]. We note a slight decrease in the XPS results in the region $E < E_f - 4$ eV relative to our earlier work [6]. This decrease is due to a more accurate allowance for a weak inelastic loss peak appearing at ~5 eV below the primary photoelectron peaks. The three sets of data show poor agreement, with the widths of the main peak decreasing in the order UPS, XPS, SXS. The SXS results are considerably narrower than the other two (FWHM ≈2 eV, 3 eV, and 5 eV for SXS, XPS, and UPS, respectively), but agree in overall shape with XPS. The SXS results in figure 8a were obtained from measurements of L x rays [3]. Similar work on M x rays (for which transition probability modulation may be a smaller effect [2]) shows somewhat more fine structure and a FWHM of ~3 eV [2], agreeing rather well with XPS. Nickel has also been investigated by INS [4] and a smooth peak of roughly the same position and width as the XPS peak is observed. Even with an allowance for the poorer resolution of XPS, the two peaks appearing in the UPS results are not consistent with the XPS curve.

The various theoretical $\rho(E)$ estimates for Ni have been discussed previously [2,12]. The FWHM of these estimates vary from ~3 to 4.5 eV, with the smallest width coming from an unhybridized calculation [14]. In figure 8b, we compare our XPS results to a hybridized, ferromagnetic $\rho(E)$ for Ni [14] which has been broadened in the same manner as those for Fe and Co. It is clear that the XPS results are too narrow (though they would agree in width with the unhybridized $\rho(E)$ [14]), and that, allowing for our broadening, the UPS results are in best agreement with theory. In view of the considerable discrepancies between UPS and XPS, SXS, or INS, however, we conclude that Ni does not represent a particularly well-understood case, in contrast with Eastman's conclusions [12].

d. Copper (fcc)

The experimental curves from UPS [12,28], SXS [3], and XPS are shown in figure 9a. There is agreement in that all curves show a peak between 2.3 and 3.3

eV below E_f, but with UPS showing more detailed structure and a somewhat uncertain overall width [12,28]. The widths and shapes of XPS and SXS are in good agreement though shifted relative to one another by ~1 eV. (A more accurate E_f location has shifted our XPS curve relative to our previous results [6].) In recent UPS work at higher photon energy ($h\nu = 21.2$ eV), Eastman [29] has obtained results with more intensity in the region 2.5 to 4.0 eV below E_f and which agree very well in shape and width with XPS and SXS. For this case it appears that even a slight increase in photon energy in the UPS measurement causes the results to look a great deal more like those of XPS. Copper has also been studied in INS [4] and the results for the d-band peak are in essential agreement with XPS and SXS.

In figure 9b, we compare a broadened version of the theoretical $\rho(E)$ due to Snow [30] with our XPS results. The agreement is excellent, and would also be so for SXS if we permit a shift of ~1 eV in E_f. The coincidence in energy of structure in the UPS curve with structure in the unbroadened theoretical $\rho(E)$ has been discussed previously [28], but we note that the relative intensities of the various features noted do not in fact coincide with theory.

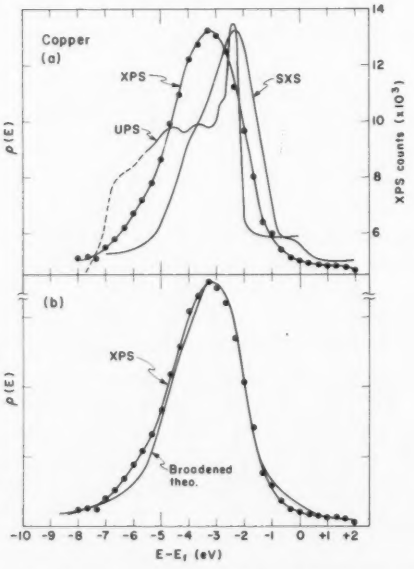

FIGURE 9. *Results for copper metal. The XPS data were obtained at 720 °C and have been corrected for inelastic scattering and MgK$\alpha_{3,4}$ x-rays. Curves from UPS (refs. 12 and 28) and SXS (ref. 3) are compared to the XPS results in (a). In (b) the XPS results are compared to a broadened theoretical curve based on reference 30.*

e. Zinc (as ZnS)

Zinc has been studied by XPS only in compounds, because of the difficulty of obtaining a clean metallic surface. We present results for ZnS in figure 10. The 3d electronic states show up as a narrow intense peak with a FWHM of 1.7 eV and located ~13 eV below E_f. (The separation of this peak from E_f may be too large, because of charging of the sample [25].) The valence bands are just above the d peak. The d states of metallic zinc have been studied also by SXS [3], and a peak of FWHM = 1.45 eV, at 8 eV below E_f, was obtained. Thus XPS and SXS are in good agreement on the width of these core-like 3d states, which are only about 10 eV below E_f.

3.3. The 4d Series: Ru, Rh, Pd, Ag and Cd

The corrected XPS spectra for the four metals Ru, Rh, Pd, and Ag are shown in figure 11. The metals are discussed separately below.

a. Ruthenium (hcp)

Our results for Ru are characterized by a single peak of ~4.9 eV FWHM. The high energy edge is quite sharp, reaching a maximum value at about $E_f - 1.7$ eV. The peak is rather flat, and there is some evidence for a shoulder at $E_f - 4.5$ eV. The peak falls off more slowly with energy on the low energy side than near E_f. The reference core level widths in Ru were quite narrow, as indicated in table 1, and spurious effects due to surface contamination are unlikely. There are no other experi-

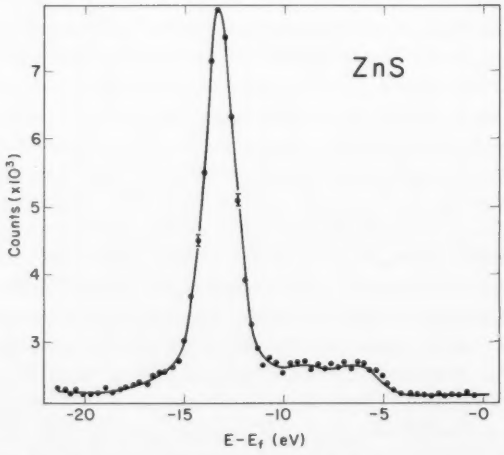

FIGURE 10. *Corrected XPS spectrum for ZnS, showing a narrow intense peak from the 3d levels, as well as the broad, flat valence bands.*

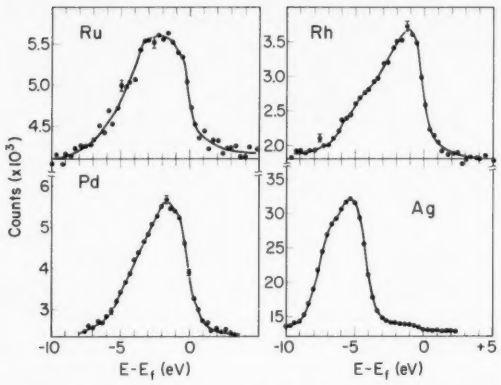

FIGURE 11. *Corrected XPS spectra for the 4d metals Ru, Rh, Pd, and Ag.*

mental or theoretical results on Ru presently available for comparison with our data.

b. Rhodium (fcc)

The XPS-derived $\rho(E)$ can be described by a single triangular peak, very steep on the high energy side, and reaching a maximum at $E_f - 1.3$ eV. There is little evidence for structure on the low energy side, which falls off monotonically. The peak FWHM of ~4.4 eV is slightly smaller than that for Ru. No other experimental or theoretical results on Rh are available for comparison.

c. Palladium (fcc)

Our corrected results for Pd have much the same appearance as those for Rh, but the Pd peak is slightly narrower with a FWHM of ~4.1 eV and the maximum occurs at $E_f - 1.7$ eV. The high-energy edge of the Pd peak is very steep, and most of the slope must be instrumental. Therefore, as expected, the true $\rho(E)$ for Pd is apparently very sharp at E_f.

The results presented in figure 11 have been corrected for a weak inelastic loss peak at 6 eV, and also for the presence of a small peak at $E_f - 10$ eV, arising from oxygen present as a surface contaminant. Samples of Pd were heated in hydrogen to approximately 700 °C and then studied at this temperature with either a hydrogen or argon atmosphere. It was not possible under these conditions (or even by heating to as high as 900 °C) to get rid of the oxygen 1*s* peak completely. Fortunately, the only effect of a slight oxygen contamination on the valence band XPS spectrum of certain metals appears to be a sharp peak at $E_f - 10$ eV (probably caused by photoemission from 2*p*-like oxygen levels). We have also observed this effect for slightly oxidized Cu. Thus we were able to correct our Pd results for this peak (which does not affect the region shown in fig. 11). A recently obtained uncorrected XPS spectrum for Pd is in good agreement with our results [31].

Palladium has also been studied by UPS [32,33], and the agreement with XPS is good in general outline. However, the precise shape of the UPS results below approximately $E_f - 3.5$ eV is uncertain [32,33].

In figure 12, we compare our results with the theoretical predictions of Freeman, Dimmock, and Furdyna [34]. The upper portion of the figure shows the fine structure of their $\rho(E)$ histogram and in the lower portion we compare our results to the broadened theoretical curve. The agreement between XPS and theory is good, although the shape of the peak is somewhat different.

d. Silver (fcc)

Our results for Ag also appear in figure 11. They differ in several respects from the Pd curve. The *d* bands are filled and below E_f, giving rise to a narrow peak (FWHM = 3.5 eV) with its most intense component at $E_f - 5.3$ eV. The edges of this peak are quite sharp, in view of the instrumental contributions of XPS.

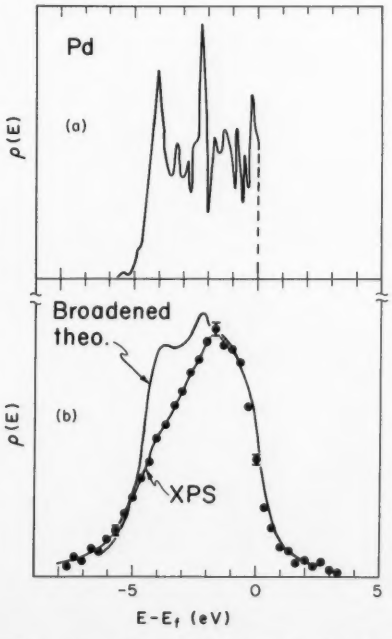

FIGURE 12. *Comparison of Pd XPS results with theory: (a) theoretical density-of-states function from reference 34, indicating the complexity of the one-electron* ρ(E), *(b) XPS results and a broadened theoretical curve.*

The $3d_{3/2}$ and $3d_{5/2}$ levels of Ag are also very narrow (see table 1), indicating no spurious linewidth contributions from instrumental or contamination effects. There is also strong evidence for a weaker component at $\sim E_f - 6.6$ eV. This two-component structure has also been verified by Siegbahn and co-workers in uncorrected XPS spectra [7,31]. Very similar structure appears in the *d* bands of several 5*d* metals and we discuss the possible significance of this below (sec. 3.5).

Silver has also been studied by means of UPS [5,29,35], using radiation up to 21.2 eV [29] in energy. The results of these studies (in particular those attained at 21.2 eV) are in essential agreement with our own, in that they show a peak of ~3 eV FWHM at $E_f - 5.0$ eV.

No theoretical $\rho(E)$ predictions for Ag are available at the present time.

e. Cadmium (as $CdCl_2$)

A corrected XPS-spectrum for $CdCl_2$ is shown in figure 13. The 4*d* peak appears at $\sim E_f - 14.5$ eV and the valence bands fall between roughly 5 and 10 eV below E_f. The 4*d* peak is very narrow (a FWHM of 1.7 eV, compared to 3.5 eV for Ag). As these *d* levels are quite strongly bound, we expect them to behave as core states, and perhaps to exhibit spin-orbit splitting (into $d_{3/2}$ and $d_{5/2}$ components). There is no evidence for splitting of this peak, but its shape is consistent with a theoretical free-atom prediction of only a 0.8 eV spin-orbit splitting [36]. The analogous 5*d*-series levels in HgO do exhibit resolvable spin-orbit splitting, however (sec. 3.4.e).

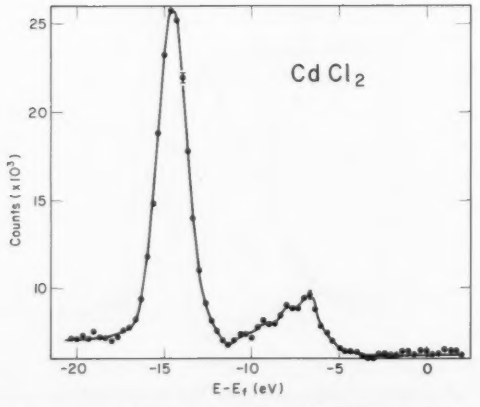

FIGURE 13. *Corrected XPS spectrum for $CdCl_2$. The filled 4d states appear at $E\text{-}E_f \approx -14.5$ eV. The broader peak at $E\text{-}E_f \approx -7$ eV represents valence bands.*

3.4. The 5*d* Series: Os, Ir, Pt, Au, and Hg

The corrected XPS spectra for the metals Os, Ir, Pt, and Au are shown in figure 14.

a. Osmium (hcp)

Hexagonal Os gives a valence band spectrum similar to that of hexagonal Ru. As in the Ru case, the Os peak rises sharply near E_f to a plateau beginning at $E_f - 1.7$ eV. The flat region of the Os peak extends over approximately 3 eV, and is broader than that for Ru. No comparisons with theory or other experiments are possible as yet.

The low energy tail of the Os peak does not fall to the base line primarily because of spurious photoelectron intensity in the valence band region due to the proximity of the very intense Os4*f* levels in energy (see table 1). These core levels appear to interact with very weak Mg x rays whose energies are as high as ~1300 eV, giving rise to photoelectrons in the same kinetic energy region as valence bands interacting with the 1250 eV Mg$K\alpha_{1,2}$ x rays. Similar problems were encountered with Ir, but they do not affect our conclusions as to peak shapes and structure. An additional problem was encountered in correcting for the Mg$K\alpha_{3,4}$ x rays in both Os and Ir, as the low intensity $5p_{1/2}$ and $5p_{3/2}$ photoelectron peaks overlap the $\alpha_{3,4}$ regions of the reference 4*f* peaks. For example, this effect appears as a slight deviation of the data from the fitted function near a kinetic energy of 1202 eV in figure 1. However, the $\alpha_{3,4}$ correction is a small one and could nonetheless be made with sufficient accuracy not to affect our fundamental conclusions.

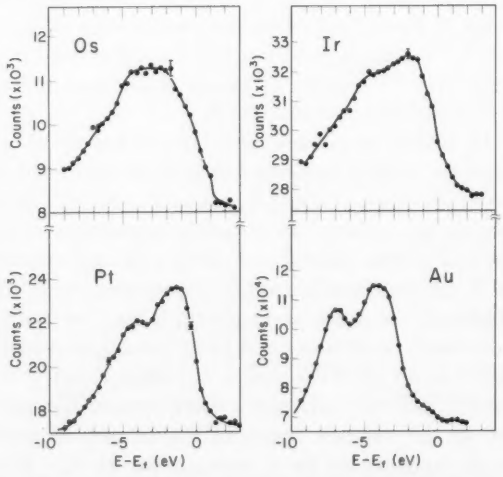

FIGURE 14. *Corrected XPS spectra for the 5d metals Os, Ir, Pt, and Au.*

b. Iridium (fcc)

The corrected XPS results for iridium are similar to those of Os in overall shape and width, but give evidence for two peaks, at approximately $E_f-1.5$ eV and $E_f-4.5$ eV. This two-peak structure is even clearer in the uncorrected XPS spectrum for Ir shown in figure 15. The higher-energy peak appears to be narrower, and, with allowance for this, we estimate the two peaks to be of roughly equal intensity.

c. Platinum (fcc)

Our corrected XPS results for Pt exhibit two partially-resolved peaks at $E_f-1.6$ eV and $E_f-4.0$ eV, with the more intense component lying nearer E_f. The steep slopes of our spectra for both Ir and Pt near E_f are consistent with the Fermi surface cutting through the d bands in a region of very high $\rho(E)$. The separations of the two components observed in the d bands are thus very nearly equal for Ir and Pt, but the relative intensities are different.

Theoretical results are available for Pt. The band-structure calculations of Mueller et al. [37] are shown in figure 16, together with our data. The theoretical $\rho(E)$ is also shown after broadening, to facilitate comparison. We note that both theory and experiment show roughly two major peaks but that the relative intensities are in poor agreement. The disagreement as to shape is the same as that observed for Pd in figure 12. (Relative intensities are arbitrary in both of these figures.) In addition, the band-structure calculations give a total width at half height of 8 eV, while the XPS data show a width of only 6 eV. Thus the overall agreement is only fair.

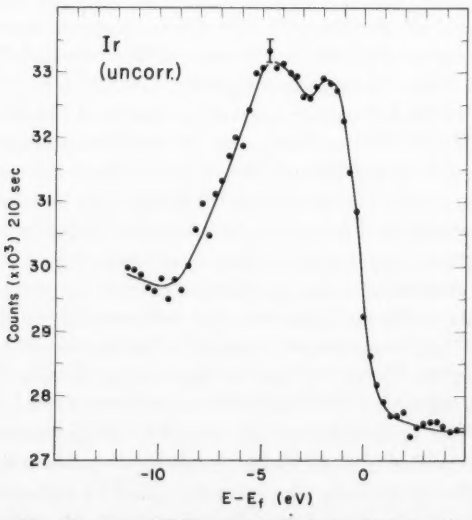

FIGURE 15. *Uncorrected XPS spectrum for Ir, in which the two-peak structure is clearly shown.*

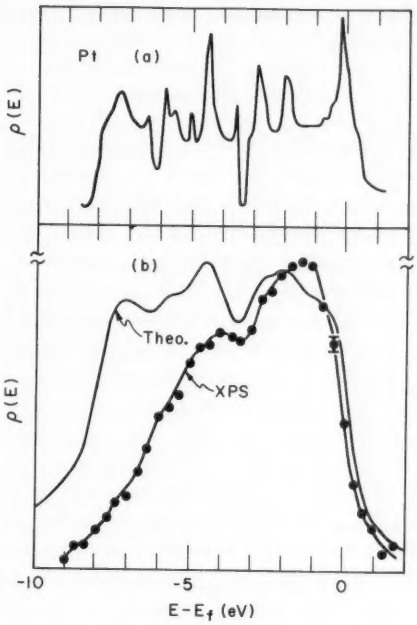

FIGURE 16. *Comparison of Pt XPS results with theory: (a) the theoretical density-of-states function of reference 37, (b) the broadened theoretical curve is compared to our XPS results.*

d. Gold (fcc)

The d bands of gold are filled and should lie several eV below E_f, as our results in figure 14 indicate. Two peaks are again evident in the corrected XPS results for gold, and these have been verified in uncorrected XPS spectra obtained by Siegbahn and co-workers [7,31]. The statistical accuracy of our data is quite good, and we can say that the lower intensity peak at $E_f-6.8$ eV is narrower than the higher intensity peak at $E_f-4.1$ eV. Apart from this, the shape of the d-band peak for Au is very similar to that for Pt.

Gold has also been studied by means of UPS [29,38]. In experiments at photon energies up to 21.2 eV [38], a two-peak structure is found, with components at $E_f-3.4$ eV and $E_f-6.1$ eV. The component at -3.4 eV is also observed to be split into a doublet [38], perhaps accounting for its extra width in the XPS results. Furthermore, a spectrum obtained with $h\nu = 26.9$ eV [29] (but not corrected for inelastic scattering) looks very much like our XPS results, again indicating that with increase in photon energy, UPS results converge rather quickly to those of XPS.

There are no theoretical $\rho(E)$ estimates at present available for Au.

e. Mercury (as HgO)

In HgO, the filled 5*d* levels should be tightly-bound and core-like. Figure 17 shows a corrected XPS spectrum for HgO, in which the 5*d* levels appear as a doublet whose components lie 13.6 and 12.0 eV below E_f. Valence bands overlap the high energy edge of the *d* peaks and extend to $E_f - 5$ eV. The intensity ratio of the two 5*d* peaks, as derived by least-squares fitting of Lorentzian curves to our data, is 1.4:1.0. The separation and intensity ratio are consistent with a $d_{3/2} - d_{5/2}$ spin-orbit doublet, as the free-atom theoretical prediction is for a 2.1 eV separation [36] and the intensity ratio should be given by the level multiplicities (*i.e.*, 6:4 = 1.5:1.0). (We have verified that the intensity ratios for the $3d_{3/2} - 3d_{5/2}$ core levels of the 4*d* metals in table 1 follow this rule to within experimental accuracy (± 0.1).) Thus the 5*d* levels of HgO appear to be very core-like. Furthermore, the relative intensity of the two components in the doublet is similar to those observed in Pt and Au. We discuss the possible implications of this similarity in the next section.

3.5. Discussion of Results

The XPS results for all 15 cases studied are presented in figure 18. In table 1 are given the binding energies and widths of the reference core levels used for correcting valence band spectra, as well as the width of the peak due to the *d* bands and (where observed) the separation of the two primary components in this peak.

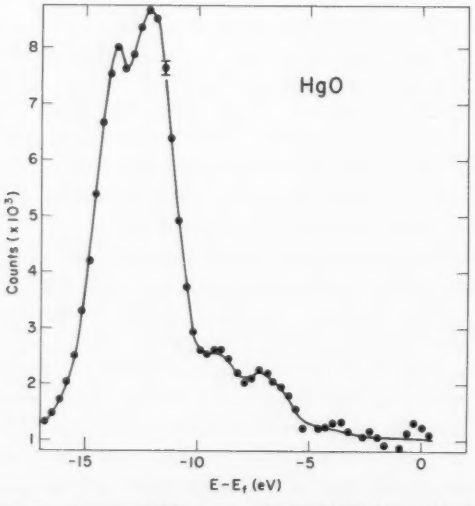

FIGURE 17. *Corrected XPS spectrum for HgO. The intense doublet at* $E\text{-}E_f \approx -12$ *eV is due to the core-like* $5d_{3/2}$ *and* $5d_{5/2}$ *states.*

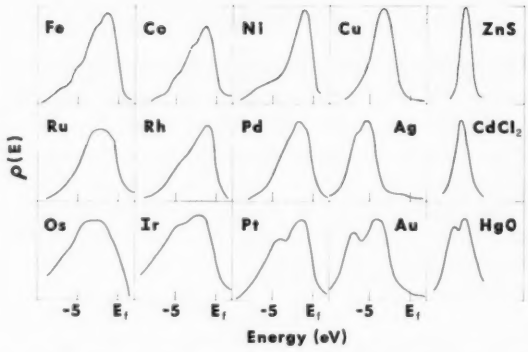

FIGURE 18. *Summary of the XPS results for the fifteen solids studied (cf. table 1). The peaks for ZnS,* $CdCl_2$*, and HgO lie at* $E\text{-}E_f \approx -13$ *eV,* -14 *eV, and* -12 *eV, respectively.*

Within a 3*d*, 4*d*, or 5d series, the XPS results show systematic variation, giving somewhat wider *d* bands for Fe, Ru, and Os than for Cu, Ag, and Au, respectively, and even narrower core-like states ~10 eV below E_f for ZnS, $CdCl_2$, and HgO. Much of this variation is no doubt connected with a one-electron $\rho(E)$, but we note also that experimental spectra obtained from metals with partially filled *d* bands might be broadened by the coupling of a localized hole to localized *d* electrons [17] (see fig. 3c and sec. 2). The 4*d* bands studied are only slightly wider than their 3*d* counterparts; the 5*d* bands are considerably wider and show gross structure.

Within two isomorphous series—Rh, Pd, Ag and Ir, Pt, Au, all members of which are face-centered cubic—there is sufficient similarity of the shapes of the *d*-band peaks to suggest a rigid-band model for $\rho(E)$. If $\rho(E)$ of Ag(Au) can be used to generate $\rho(E)$ of Rh and Pd (Ir and Pt) simply by lowering the Fermi energy to allow for partial filling of the *d* bands, then this model would apply. The peaks for Rh and Pd are too wide to be represented by a Ag $\rho(E)$, but the shapes of both could be very roughly approximated in this manner. The similarity of the two-peak structure for the three metals Ir, Pt, and Au gives more evidence for the utility of a rigid band model, especially as the uncorrected results for Ir (fig. 15) show a narrower peak near E_f (as though it were a broader peak cut off by the Fermi energy). The application of this model to the prediction of the experimental $\rho(E)$'s for Ir and Pt is shown in figure 19. The predictions are reasonably good. In our opinion, this limited success for Ir, Pt and Au probably indicates some similarity in the *d* bands in these metals, but we

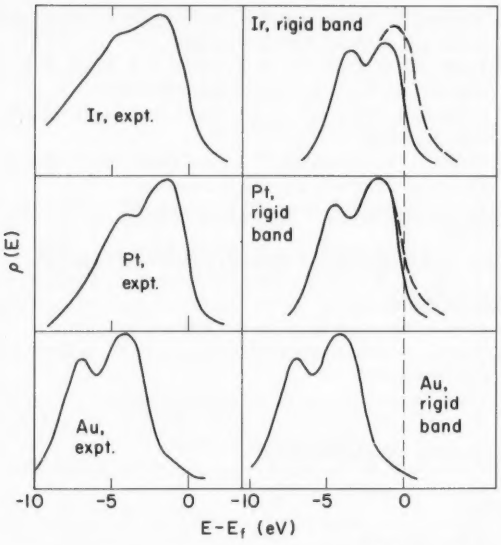

FIGURE 19. *An attempt to reproduce the shapes of the experimental XPS spectra for the 5d metals Ir, Pt, and Au from a Au-like rigid band density of states. Vertical scales are arbitrary. Note that the Ir experimental curve does not fall to as low a value as Pt or Au at low energy due to spurious sources of photoelectron intensity (see text).*

do not take it as a verification of the rigid band model *per se*.

The two-component structure observed in the *d*-band peaks of Pt and Au is very similar to the unresolved structure found in Ag. That is, a more intense component appears nearer E_f. To estimate the intensity ratios of these components more accurately, we have least-squares fitted two Gaussian peaks of equal width to our data for these three metals. The ratios and separations so derived are: Ag—1.51:1.00, 1.8 eV; Pt—1.60:1.00, 3.3 eV; and Au—1.48:1.00, 3.1 eV. As our accuracy in determining these ratios is $\sim \pm 0.1$, they could all be represented by a value of 1.50:1.00. A possible significance of this value is that it is the expected (and observed) intensity ratio for a spin-orbit split *d* level (e.g., the 5*d* levels of HgO). Thus, one might argue that as the 4*d* and 5*d* shells move nearer to the Fermi surface with decreasing Z, they must go continuously from core states to valence states, perhaps retaining some degree of simple spin-orbit character in the process. The observed separations are 1.5—2.5 times larger than free-atom theoretical spin-orbit splittings [36], but the various perturbations of the lattice might be responsible for this. Speaking against such a simple interpretation, however, is our observation (verified in UPS results [29,38]) that for Au the component nearer E_f is broader. In fact, the UPS results for $h\nu \leq 21.2$ eV show this component split into two peaks [29,32]. In view of this, our intensity ratio estimates based on two peaks of equal width may not have fundamental significance, and the agreement of these ratios, particularly between Ag and Pt or Au could be somewhat accidental. Nonetheless, the similarity in shape of our results for the *d* levels of Ag, Pt, Au, and Hg is rather striking.

We have noted that for Cu, Ag, and Au, the recent UPS work of Eastman [29] at higher photon energies (21.2 to 26.9 eV) is in much better agreement with XPS results than previous studies using a range of lower photon energies [28,35,38]. It thus appears that *as the photon energy is increased in a UPS experiment, the form of the energy distributions can be expected to approach rather quickly that observed in XPS work. We feel that photoelectron spectra for which XPS and UPS show agreement ought to be much more closely related to* $\rho(E)$. Further UPS experiments at greater than 20 eV photon energies would thus be most interesting.

4. Concluding Remarks

We have discussed the use of x-ray photoelectron spectroscopy (XPS) in the determination of densities of states. The application of this technique to the *d* bands of 12 metals and 3 nonmetallic solids seems to indicate that reliable information about the overall shape of $\rho(E)$ can be obtained. The results show systematic behavior with changes in Z and crystal structure and agree qualitatively and in some cases quantitatively with theoretical predictions for both unfilled valence *d* levels and filled core-like *d* levels.

Throughout our discussion, we have placed special emphasis on comparison of XPS with the closely related ultraviolet photoelectron spectroscopy (UPS). It appears that UPS at the present time has an advantage in resolution, but that XPS results can be more easily corrected for inelastic scattering, are not significantly affected by final state density, and are less susceptible to the effects of surface contaminants. UPS results at photon energies ≥ 20 eV appear to be more reliable indicators of $\rho(E)$ in the sense that they agree better with the rough outline predicted by XPS. The need for further work at higher resolution and at all photon energies (including those in the relatively untouched range from 20 to 1250 eV) is evident.

5. Acknowledgments

The authors wish to thank W. E. Spicer, D. E. Eastman, S. Doniach, F. M. Mueller, A. J. Freeman and F. Herman for fruitful discussions relating to this work.

383-876 O - 70 - 7

6. References

[1] We shall use the term "valence bands" for those occupied electronic states that are derived principally from atomic valence shell orbitals.

[2] Cuthill, J. R., McAlister, A. J., Williams, M. L., and Watson, R. E., Phys. Rev. **164,** 1006 (1967).

[3] Hanzely, S., and Liefeld, R., this Symposium.

[4] Hagstrum, H. D., Phys. Rev. **150,** 495 (1966); Hagstrum, H. D., and Becker, G. E., Phys. Rev. **159,** 572 (1967); and Hagstrum, H. D., this Symposium.

[5] Berglund, C. N., and Spicer, W. E., Phys. Rev. **136,** A1030 and A1044 (1964); and Spicer, W. E., this Symposium.

[6] Fadley, C. S., and Shirley, D. A., Phys. Rev. Letters **21,** 980 (1968); and Fadley, C. S., and Shirley, D. A., J. Appl. Phys. **40,** 1395 (1969).

[7] Siegbahn, K. *et al.*, Electron Spectroscopy for Chemical Analysis, (Almqvist and Wiksells AB, Stockholm, Sweden, 1967).

[8] Spicer, W. E., Phys. Rev. **154,** 385 (1967).

[9] Siegbahn, K., Nordling, C., and Hollander, J. M., Lawrence Radiation Laboratory Report **UCRL-10023** (1962).

[10] Fadley, C. S., Ph. D. dissertation, University of California, Berkeley, 1970 (Lawrence Radiation Laboratory Report **UCRL-19535** (1970)).

[11] We note that such level-specific effects as two-electron transitions (see ref. 21) and core-electron binding energy splittings (see ref. 17) may render invalid the assumption that the tail behind a core level photoelectron peak is due entirely to inelastic scattering. However, if such effects are significant, they will generally result in noticeable peaks in the tail. The only peaks observed for the cases studied here were weak and can be explained as inelastic plasma losses. Therefore, we expect level-specific effects to have negligible influence on the results under discussion. They should be noted as a possible source of error in this correction procedure, however.

[12] Eastman, D. E., and Krolikowski, W. F., Phys. Rev. Letters **21,** 623 (1968); and Eastman, D. E., J. Appl. Phys. **40,** 1387 (1969).

[13] Baer, Y., Physik der Kondensierten Materie **9,** 367 (1969).

[14] Hodges, L., Ehrenreich, H., and Lang, N. D., Phys. Rev. **152,** 505 (1966).

[15] Callaway, J., Energy Band Theory (Academic Press Inc., New York, 1964), p. 117.

[16] Herman, F., Ortenburger, I. B., and Van Dyke, J. P., to appear in Intern. J. of Quant. Chem., **Vol. IIIS.**

[17] Fadley, C. S., Shirley, D. A., Freeman, A. J., Bagus, P. S., and Mallow, J. V., Phys. Rev. Letters **23,** 1397 (1969).

[18] Doniach, S., and Sunjić, to appear in J. Phys., and Doniach, S., to be published.

[19] Hedin, A. L., Lundqvist, B. I., and Lundqvist, S., Sol. State Comm. **5,** 237 (1967) and this Symposium.

[20] Nesbet, R. K., and Grant, P. M., Phys. Rev. Letters **19,** 222 (1967).

[21] Carlson, T. A., Phys. Rev. **156,** 142 (1967).

[22] Turner, D. W., Ch. 3 in Physical Methods in Advanced Inorganic Chemistry, M. A. O. Hill and D. Day, Editors, (Interscience Publishers, Inc., London, 1968).

[23] Broden, G., Heden, P. O., Hagström, S. B. M., and Norris, C., this Symposium.

[24] Chan. D., and Shirley, D. A., this Symposium.

[25] Fadley, C. S., Hagström, S. B. M., Klein, M. P., and Shirley, D. A., J. Chem. Phys. **48,** 3779 (1968).

[26] Connolly, J. W. D., this Symposium. (These results have also been presented in ref. 12.)

[27] Wong, K. C., Wohlfarth, E. P., and Hum, D. M., Phys. Letters **29A,** 452 (1969).

[28] Krolikowski, W. F., and Spicer, W. E., Phys. Rev. **185,** 882 (1969).

[29] Eastman, D. E., private communication, to be published.

[30] Snow, E. C., Phys. Rev. **171,** 785 (1968).

[31] Siegbahn, K., private communication.

[32] Yu, A. Y-C., and Spicer, W. E., Phys. Rev. **169,** 497 (1968).

[33] Janak, J. F., Eastman, D. E., and Williams, A. R., this Symposium.

[34] Freeman, A. J., Dimmock, J. O., and Furdyna, A. M., J. Appl. Phys. **37,** 1256 (1966) and private communication.

[35] Krolikowski, W. F., and Spicer, W. E., unpublished results.

[36] Herman, F., and Skillman, S., Atomic Structure Calculations (Prentice-Hall Inc., Engelwood Cliffs, New Jersey, 1963).

[37] Mueller, F. M., Garland, J. W., Cohen, M. H., and Benneman, K. H., to be published; and Mueller, F. M., this Symposium.

[38] Krolikowski, W. F., and Spicer, W. E., to be published.

(Paper 74A4–621)

JOURNAL OF RESEARCH of the National Bureau of Standards—A. Physics and Chemistry
Vol. 74A, No. 4, July-August 1970

Tunneling Measurements of Superconducting Quasi-Particle Density of States and Calculation of Phonon Spectra*

J. M. Rowell

Bell Telephone Laboratories, Inc., Murray Hill, New Jersey

(October 10, 1969)

It is an unfortunate fact that the tunneling technique, which has proved incredibly successful in the study of superconductivity, has given little information about the normal state properties of metals and semiconductors. It will be shown that, in the determination of the superconducting quasi-particle density of states, it is the change in density induced by the onset of superconductivity which is measured rather than the total density.

Returning to the problem of normal materials, a review of the limited achievements and failures of tunneling will be presented. This will include the influence of band edges on tunneling in *p-n* diodes and metal-semiconductor contacts, the structures observed in tunneling into bismuth and the negative results obtained in nickel and palladium. The dominant effect of the change in barrier shape in most of these tunneling characteristics will be illustrated.

Key words: Density of states; phonons; semiconductors; superconductivity; tunneling.

Many of the talks heard this week have outlined experimental techniques which determine the density of electron states in metals and semiconductors over energy ranges which are typically 1-10 volts. I would like to discuss a technique which is much happier in the range of 1-10 millivolts, is the only method which can measure the change in density of electron states induced by superconductivity, but which to date must be classed as a failure in the determination of band properties of normal metals. For semiconductors and semimetals, because of smaller energies and larger fractional changes in electron density at band edges, the situation is a little better. Even in these materials, however, we can only say that density-of-states effects are observed and cannot generally deduce a density measurement from the experimental results.

After those opening remarks, it will be obvious that most of you attending this conference should not be familiar with the tunneling technique so I will briefly review the experimental method. Two structures are commonly used, the metal-insulator-metal (M-I-M) junction, which relies on the oxide of the first metal to form the insulator, and the metal-semiconductor (M-S) contact which uses the depletion layer (Schottky barrier) at the surface of the semiconductor. In the M-I-M case it is generally hard to prepare sufficiently smooth clean surfaces of bulk metal that oxidize in a controlled way so films have been used in all but a few cases. After evaporation of the first metal film (Al, Pb, Sn, Mg, for example), oxidation takes place by exposure to air, oxygen, or a glow discharge in oxygen, and the second film is then cross evaporated to complete the junction. Typical oxide thicknesses are 15–20 Å. To make the M-S contact a semiconductor is cleaved in vacuum and covered with the metal very rapidly. The barrier is lower and ~ 100 Å thick. In some materials, where a suitable Schottky barrier does not form at the surface (*e.g.* InAs), a M-I-S structure can be made by oxidizing the semiconductor before evaporation of the metal.

These three tunneling structures are shown in figure 1, with the circuit used to measure the current-voltage characteristic or, if greater detail is required, the

*An invited paper presented at the 3d Materials Research Symposium, *Electronic Density of States*, November 3–6, 1969, Gaithersburg, Md.

dynamic resistance $(dV)/(dI)$ versus voltage. The figure also shows schematically the potential barrier (with typical energies indicated) which separates the electrodes.

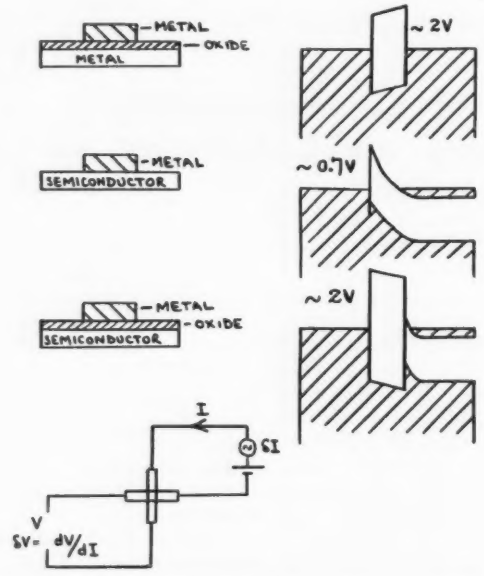

FIGURE 1. *Schematics of three widely studied tunneling structures and the circuit used to measure their I-V characteristics.*

Considering the M-I-M junction as the most favorable case for studying metals, I would like to make a number of points regarding the theoretical possibilities of observing band structure effects and the probable experimental difficulties.

The tunneling current through a barrier of the type shown in figure 2 is given by [1],

$$j=\frac{4\pi e}{\hbar}\sum_{k_t}\int_{-\infty}^{\infty} dE_x \rho_a(E)\rho_b(E)\,P(E_x)\,[f(E) - f(E-eV)], \quad (1)$$

where $\rho_a(E)$ and $\rho_b(E)$ are the density of states for a given transverse momentum k_t and total energy E, $f(E)$

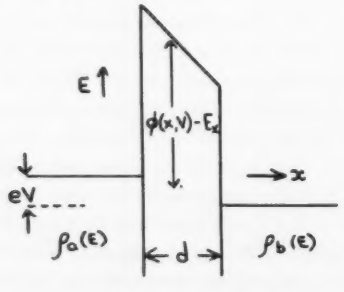

FIGURE 2. *The potential in an ideal trapezoidal barrier between metal electrodes.*

is the usual Fermi distribution and E_x the total electron energy perpendicular to the barrier. The tunneling probability $P(E_x)$ has the form

$$P(E_x)=A\exp\left\{-\frac{2}{\hbar}\int_0^d [2m(\phi(x,V)-E_x)]^{1/2}dx\right\} \quad (2)$$

where d is the barrier thickness and $[\phi(x,V)-E_x]$ is the barrier potential at position x when a voltage V is applied. The pre-exponential factor A describes the frequency with which an electron arrives at the barrier interface and its exact form determines whether one expects to observe density of states effects at all. In the W.K.B. approximation, which makes the metal-barrier interface properties vary slowly compared to the electron wavelength [1], A is proportional to $1/[\rho_a(E)\rho_b(E)]$ so that the current in (1) is independent of electron density of states. The other extreme limit, with the metal-barrier interface absolutely sharp, gives a complicated prefactor A which does not exactly cancel the density terms in eq (1) [1,2] so some density of states effect in tunneling might be expected. However, as the interface properties can never be known in this detail, a serious interpretation of any such observation would be impossible. Rather than looking for results of the slow energy variation of $\rho(E)$ within a band, a more likely experiment is to look for effects of band edges, where the number of final available states for the tunneling electron changes more abruptly. It is generally felt that band edges can be observed in tunneling as long as an appreciable fractional change in total electron density is produced by the new band. As we will see later, this usually happens at convenient energies only in semiconductors. Duke [3] has also pointed out that an increased tunneling probability into the new band will enhance the magnitude of the current onset near the band edge.

Apart from the theoretical question of the exact nature of the metal-insulator interface and its role in producing density of states effects, there are a number of serious experimental problems which lead me to question whether these effects could be observed in metals. These problems can be illustrated by reference to figure 3. First, typical barrier heights in oxides are ~ 2 volts, which is a small energy compared to interesting band structure in most metals. For an applied bias $> \phi_R$, electrons from the Fermi level (at A for example) tunnel into the conduction band of the insulator rather than into the second electrode. Second, the tunneling probability is much greater for electrons at B than for those at C, which enter the second metal just above the Fermi level. In figure 3b, for example, where

we assume $\phi_R = \phi_L = 2V$, the transmission probability at B is $\sim 10^{-9}$, whereas at C it is $\sim 10^{-16}$. Thus the chance of probing band edges far below the Fermi level in the left metal seems remote, as practically none of the

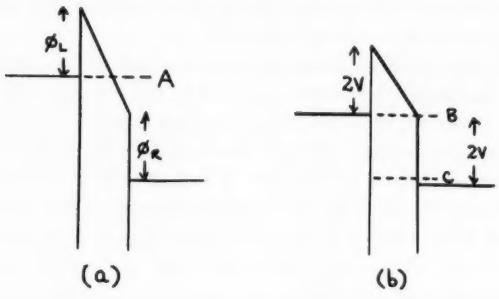

FIGURE 3. *Figure (a) shows the possible injection of electrons into the conduction band of the insulator (Fowler Nordheim tunneling). Figure (b) shows two possible tunneling paths into the second electrode.*

current, flows from these levels. The possibility of probing band edges above the Fermi level (at B in the right metal for example) raises the third problem, namely that the current-voltage characteristic of the junction is dominated very strongly by the changes in barrier shape. Typical results obtained by Fisher and Giaever [4] are shown in figure 4. At low voltages the junctions are ohmic (small deviations are observable only in detailed conductance plots) but from 0.2 to 1.4 V the current depends almost exponentially on voltage. This strong current dependence is purely the result of the barrier becoming lower (for electrons leaving the Fermi level) as the voltage increases. Thus any small changes in current (or conductance) due to band edges, superimposed on this exponential behavior, will be extremely hard to observe. There are also other difficulties which one has to consider in many tunneling experiments. If evaporated metal films are used it is unusual for these to have the properties of single crystals or even clean polycrystals. Even more critical are the surface properties of the films, as tunneling between normal metals is sensitive to the material only within a screening length of the surface. As this surface is in contact with (or diffused into) the insulating oxide the chance of it having bulk properties seems remote.

After this very pessimistic survey of why tunneling is not the right technique for the study of density of states effect in metals, let me review a number of experiments where band edges at least are observed, or affect the tunneling characteristic noticeably.

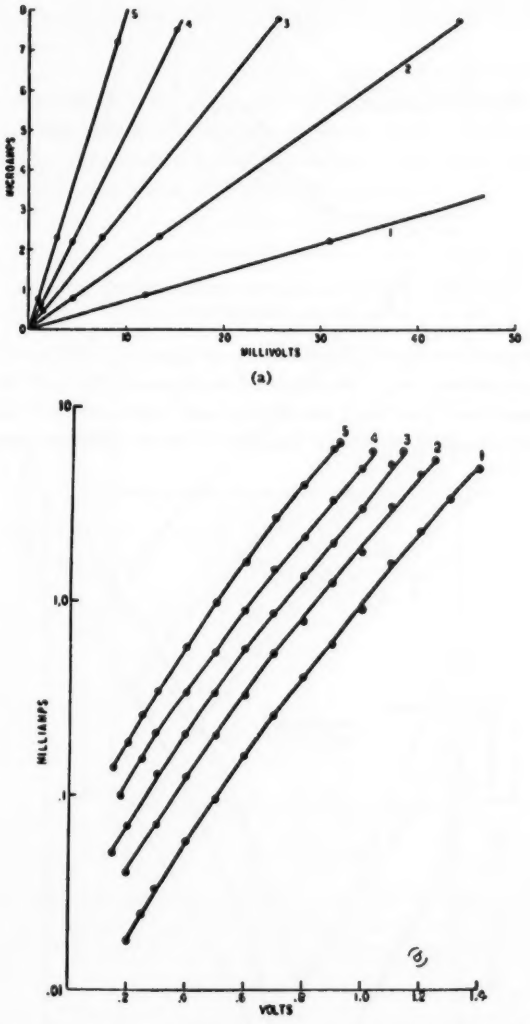

FIGURE 4. *I-V characteristics reported by Fisher and Giaever [4]. (a) At low voltages, the current through thin oxide films is proportional to voltage and to film area. Curves shown are for five films with areas in the proportions 5:4:3:2:1 as indicated. (b) At higher voltages, the current increases exponentially with voltage.*

1. Metal-Semiconductor Contacts

In a heavily doped n-type semiconductor the Fermi energy is relatively small (< 100 mV) and the depletion layer formed at the surface is thin enough to permit tunneling. Unfortunately the barrier height is rather low and barrier thickness varies with bias, leading to a strong dependence of conductance on voltage. Nevertheless, the calculation of Conley *et al.* [5] predicts that the minimum conductance occurs when the bottom of the band crosses the Fermi level of the metal (fig. 5). This has been observed in the experiments of

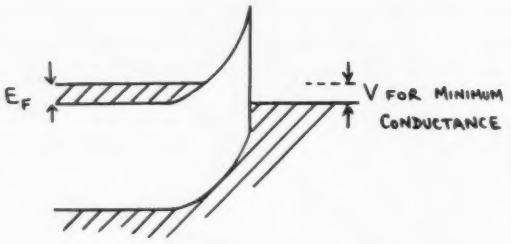

FIGURE 5. *Metal-semiconductor contact with bais applied to produce a minimum in conductance.*

Steinrisser *et al.* [6], as shown in figure 6. The barrier parameters were determined independently and the agreement between calculated and experimental conductances is orders of magnitude better than in most tunneling systems. The density of states in the semiconductor band was assumed constant in this calculation. The general aim of this type of experiment has been to obtain such a satisfactory agreement with the calculated conductance rather than to determine a density of states variation. Uncertainty in the energy dependence of the barrier parameters would make such a determination exceedingly difficult.

A second band structure effect, observed in Au-Ge surface barrier contacts by Conley and Tieman [7], is the onset of tunneling into the k=0 conduction band minimum, roughly 150 mV above the Fermi level. The influence of the band edge is rather dramatic in this case, as shown in figure 7, and a decrease of resistance by at least a factor of 10 is observed within ~ 10 mV of the edge. Note that the band edge is marked by a decrease in resistance, or increase in conductance.

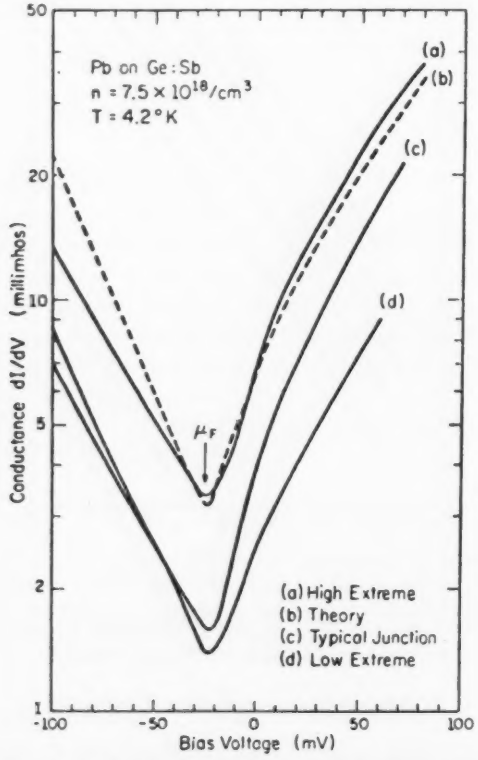

FIGURE 6. *Calculation and measurement of conductance in M-S contacts by Steinrisser et al.* [6]. *Comparison between three experimentally measured conductance curves on* $n = 7.5 \times 10^{18}/cm^3$ *Sb-doped Ge [solid lines (a), (c), and (d)] at 4.2 K and the calculated conductance [dashed line (b)] for a barrier height* $V_b = 0.63$ *eV obtained from capacitance measurements. The most commonly observed conductance curves were similar to (c), whereas (a) and (d) represent the high- and the low-conductance extremes. The contact metal is Pb and the contact area is* $2.5 \pm 0.5 \times 10^{-4}$ cm^2. *Structure associated with the superconducting energy gap has been omitted. The Fermi degeneracy* $\mu_F = 25$ *mV has been indicated.*

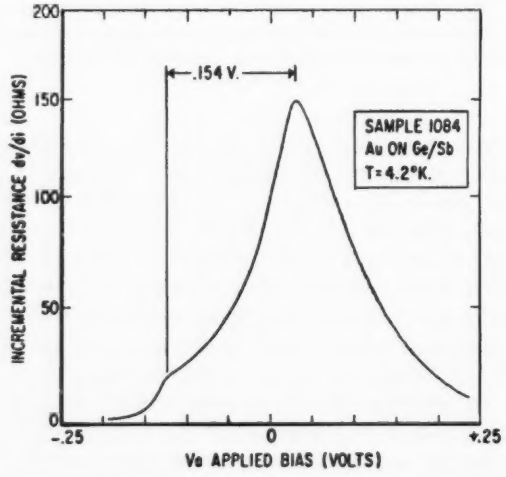

FIGURE 7. *Tunneling resistance of a Au-Ge surface barrier contact, measured by Conley and Tiemann* [7]. *The onset of transitions to the zone-centered* (Γ_2') *conduction band in Ge observed in the incremental resistance* dv/di *at an applied bias* $V_a = -0.124$ *V. Note that that threshold is* 0.154 *V from the maximum, a value which corresponds to the interband* $L - \Gamma_2'$ *separation.*

2. Metal-Insulator-Semiconductor Junctions

In order to investigate tunneling into semiconductors to higher voltages, or study those materials which do not form surface barrier contacts, an oxide can be grown on the surface before evaporation of the metal. Alternatively, for semiconductors which can be evaporated, junctions of the type aluminum-aluminum oxide-semiconductor have been fabricated. The current calculated by Chang *et al.* [8] for such a structure, on a degenerate *p*-type semiconductor, is shown in figure 8. The current is a maximum at the top of the valence

band and a minimum at the bottom of the conduction band. At higher voltages it is interesting to see that properties of the insulator, namely the increased tunneling probability at voltages corresponding to the heights ϕ_R and ϕ_L, dominate the characteristic. Experiments on a number of different III-V and II-VI semiconductors have confirmed this type of behavior except that the current minimum is not so sharp as the calculated one, as shown in figure 8 for SnTe.

The observation of interface states and impurity bands has also been reported from tunneling studies. The left-hand plots of figure 9 show the conductance results, obtained by Gray [9], for two M-I-S structures with different boron doping levels in silicon.

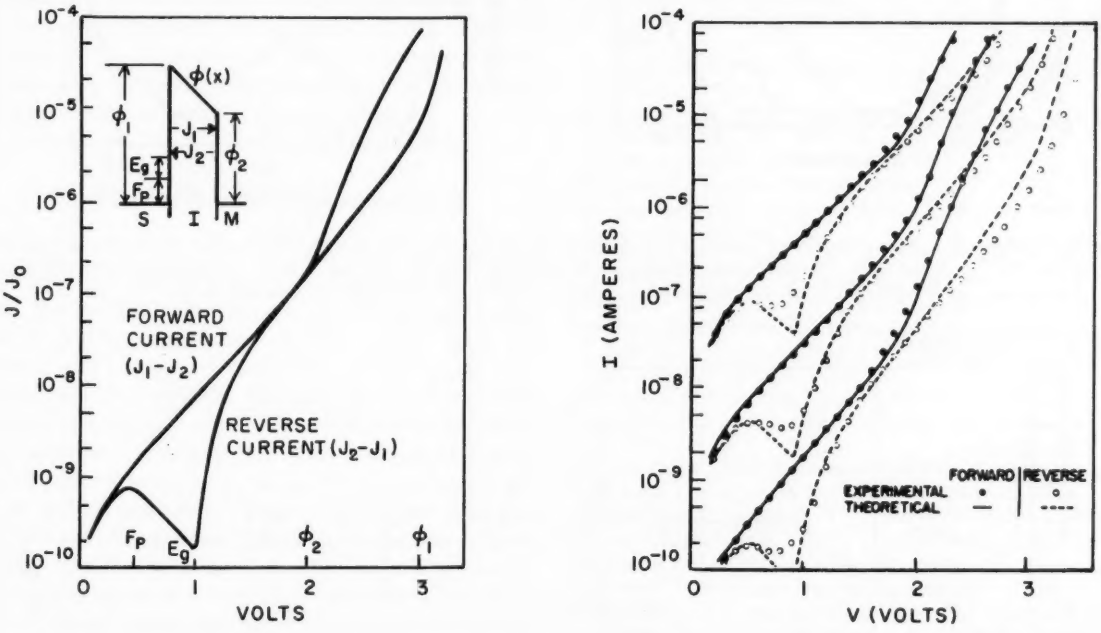

FIGURE 8. *Calculation and measurement of current in metal-insulator-semiconductor junctions by Chang et al. [8]. (a) Theoretical current-voltage characteristics for a M-I-S junction. The semiconductor is degenerate p type and the conduction band of the insulator provides the tunneling barrier. (b) Current-voltage characteristics for Al-Al_2O_3-SnTe junctions at 4.2 K. Three sets of curves are shown corresponding to samples with various oxide thickness.*

3. p-n Diodes

The I-V characteristic of the Esaki diode [10] is a clear observation of the influence of band edges on tunneling but recently this system has received little attention, probably because the barrier profile is difficult to measure. It is also difficult in this case to decide how much of the junction current is due to tunneling.

An interesting effect which has been observed in p-n diodes is the influence of Landau levels on the tunneling conductance. This was first reported by Chynoweth *et al.* [11] for InSb diodes and extensive studies of Ge diodes have been made by Bernard *et al.* [12]. Recently Landau levels in InAs have been measured by Tsui [13] in an M-I-S structure. Because only one electrode is a semiconductor the latter results are simpler to interpret.

4. Metal-Insulator-Metal Junctions

This type of tunneling structure is usually comprised of aluminum-aluminum oxide-second electrode of semimetal or metal. Considerable effort by various groups has gone into trying to observe the band edges in bismuth. Tunneling structures at low energies (<50 mV) have been reported by Esaki *et al.* [14] but these results have not been reproduced elsewhere [15]. At higher voltages the characteristics for polycrystalline films were first reported by Hauser and Testardi [16]. In figure 10 we show the good agreement between their results and those of Sawatari and Arai [17]. However, the exact position of the bands which give rise to this structure is difficult to determine from the tunneling characteristic.

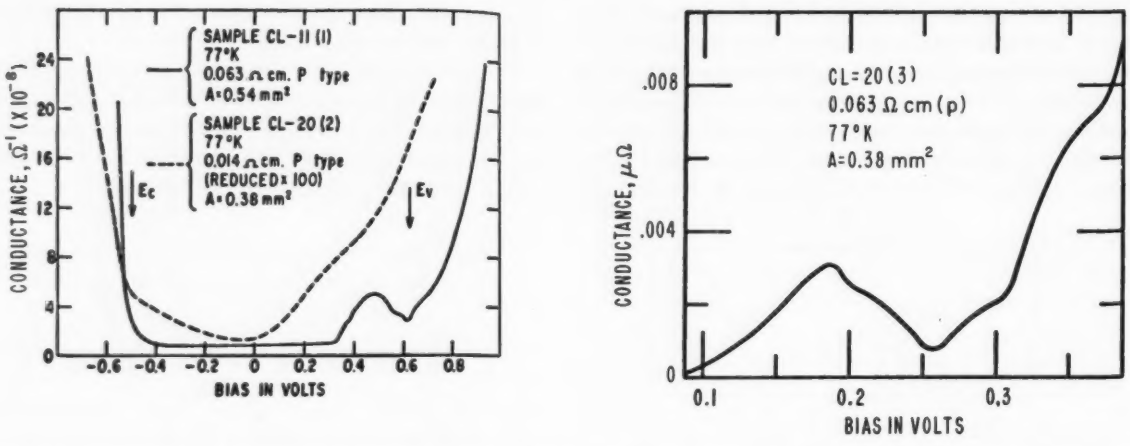

FIGURE 9. *Observation of impurity levels in tunneling by Gray* [9]. (*a*) dc *conductance versus bias showing the effect of a boron-impurity band at two different doping levels. The conductance of the more heavily doped sample is reduced* ×100 *for comparison.* (*b*) *Detailed* dc *conductance near an impurity band* (0.19 *V*). *This sample was cleaved in air before mounting in the vacuum jar.*

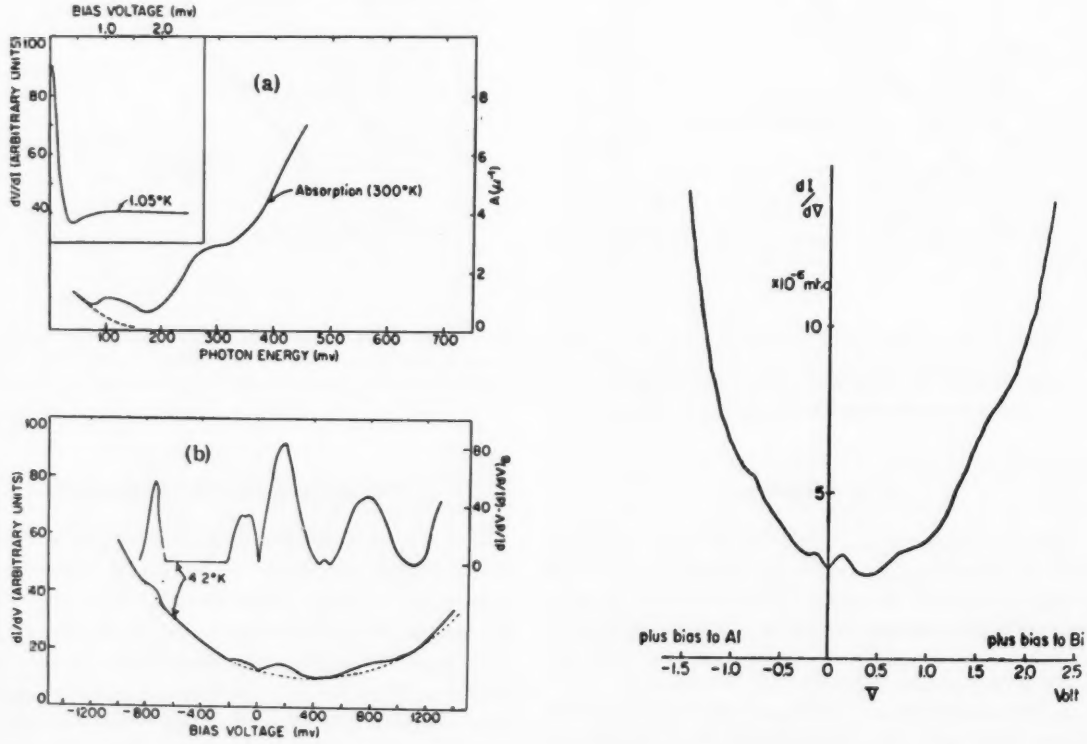

FIGURE 10. *Tunneling conductance for Al-I-polycrystalline Bi, as determined by Hauser and Testardi* [16] *(left figure) and Sawatari and Arai* [17] *(right figure). (a) Insert:* dV/dI *vs* V *for an Al-*Al_2O_3*-Bi junction. Bottom curve, adsorption as a function of energy. The dashed line shows the contribution from free carriers. (b)* dI/dV *vs* V *(solid line) and background curve (dashed line); curve of* (dI/dV) $(dI/dV)_{bkg}$ *vs* V. (+V *corresponds to Bi positive.) (c) Conductance-voltage curve in the voltage range* $-1.4 \sim +2.3$ *V at 77 K. The sample is different from that of (a) and (b).*

The conductance characteristics of M-I-M junctions generally show considerable structure at voltages <1 volt, most of which is due to excitation processes in the insulator (oxide). These excitation interactions of the tunneling electron are with organic impurities in the oxide [18], phonons of the oxide [18,19] or phonons of the surfaces of the metal electrodes [19]. In a number of junctions, (Al-I-Ni, Al-I-NiPd alloys [20] and single crystal Cr-I-Pb [21]) there are additional effects which are not yet understood. However, it would be unwise to ascribe these to density of states variations without much more detailed experimental work as the barrier properties are, as usual, practically unknown.

5. Metal-Insulator-Superconductor

There are two main reasons why tunneling into superconductors has been so successful. First, the important parameter is the normalized density of states, which is the conductance versus voltage with the second electrode superconducting divided by the conductance with it normal. Thus it is not necessary to be able to calculate, or even understand, the normal state characteristic, as long as it is entirely due to tunneling. The barrier parameters, which are exceptionally difficult to determine, can remain as unknowns as long as they do not change when the electrode becomes superconducting. As far as we know, the only change might be in the position of the excitation processes, but these are fortunately weak compared with the superconducting effects. The second advantage of the superconducting measurement is that we can determine essentially bulk properties of the superconductor, whereas all normal state measurements probe the interface and surface properties of the normal electrode. As this technique has been discussed in numerous publications [22], no more detail will be given in this text.

6. References

[1] Harrison, W. A., Phys. Rev. **123,** 85 (1961).

[2] Davydov, A. S., "Quantum Mechanics," Fizmatgiz, Moscow 1963, English trans. Neo Press, Ann Arbor, 1966.

[3] Duke, C. B., "Tunneling in Solids," Academic Press, New York, 1969, page 55.

[4] Fisher, J. C., and Giaever, I., J. Appl. Phys. **32,** 172 (1961).

[5] Conley, J. W., Duke, C. B., Mahan, G. D., and Tiemann, J. J., Phys. Rev. **150,** 466 (1966).

[6] Stinrisser, F., Davis, L. C., and Duke, C. B., Phys. Rev. **176,** (1967).

[7] Conley, J. W., and Tiemann, J. J., J. Appl. Phys. **38,** 2880 (1967).

[8] Chang, L. L., Stiles, P. J., and Esaki, L., J. Appl. Phys. **38,** 4440 (1967).

[9] Gray, P. V., Phys. Rev. **140,** A179 (1965).

[10] Esaki, L., Phys. Rev. **109,** 603 (1958).

[11] Chynoweth, A. G., Logan, R. A., and Wolff, P. A., Phys. Rev. Letters **5,** 548 (1960).

[12] Bernard, W., Goldstein, S., Roth, H., Straub, W. D., and Mulhern, J. E., Jr., Phys. Rev. **166,** 785 (1968).

[13] Tsui, D. C., Phys. Rev. Letters **24,** 303 (1970).

[14] Esaki, L., and Stiles, P. J., Phys. Rev. Letters **14,** 902 (1965); Esaki, L., Chang, L. L., Stiles, P. J., O'Kane, D. F., and Wiser, N., Phys. Rev. **167,** 637 (1968).

[15] Giaever, I., Solid State Comm. **5,** X (1967) unpublished.

[16] Hauser, J. J., and Testardi, L. R., Phys. Rev. Letters **20,** 12 (1968).

[17] Sawatari, Y., Arai, M., Japan J. Appl. Phys. **7,** 791 (1968).

[18] Lambe, J., and Jaklevic, R. C., Phys. Rev. **165,** 821 (1968).

[19] Rowell, J. M., McMillan, W. L., and Feldmann, W. L., Phys. Rev. **180,** 658 (1969).

[20] Rowell, J. M., J. Appl. Phys. **40,** 1211 (1969).

[21] Shen, L. Y. L., J. Appl. Phys. (to be published).

[22] McMillan, W. L., and Rowell, J. M., Phys. Rev. Letters **14,** 108 (1965); Chapter 11 of "Superconductivity," R. Parks, Editor, Marcel Dekker, New York, 1969.; Rowell, J. M., "Tunneling Phenomena in Solids," S. Lundqvist and E. Burstein, Editors, Plenum Press, New York, 1969.

(Paper 74A4–622)

JOURNAL OF RESEARCH of the National Bureau of Standards — A. Physics and Chemistry
Vol. 74A, No. 4, July-August 1970

Pauli Paramagnetism in Metals with High Densities of States*[1]

S. Foner

Francis Bitter National Magnet Laboratory, Massachusetts Institute of Technology, Cambridge, Massachusetts 02139

(October 10, 1969)

Because the Pauli paramagnetic susceptibility of a free electron gas, χ_p^0 is proportional to the density of states $N(0)$ at the Fermi energy, it is expected that measurements of χ_p^0 of metals and alloys can yield a reasonable measure of $N(0)$. If χ_p^0 can be measured directly, then $N(0)$ can be determined with high accuracy. The major obstacle to this procedure is that the measured static susceptibility $\chi_p = \chi_p^0/(1-N(0)V) = \chi_p^0 D$ (for the Stoner model) where V is a measure of the electron-electron interaction potential. Unfortunately, V is not easily determined experimentally, or theoretically, so that measurements of χ_p do not yield accurate measures of $N(0)$. More detailed (realistic) models involve additional parameters which are also not accurately determined. Thus direct measurements of χ_p can yield a measure of $N(0)$, but these values of $N(0)$ are subject to the uncertainties of various parameters in the theories. In this talk we discuss the present status of experiments and theories of χ_p in metals and alloys with low $N(0)$ where D is generally near unity, and high $N(0)$ where D is expected to be large. Comparisons with independent low-temperature electronic specific heat measurements are discussed and attempts to derive $N(0)$ from both susceptibility and specific heat are reviewed.

Many recent investigations of metals and alloys with high densities of states have been of great interest because such systems start to approach ferromagnetic order. The properties of Pd have been investigated extensively and very detailed band calculations now exist. The large exchange enhancements in this metal and its alloys have permitted considerable progress to be made. The properties of these systems are reviewed and estimates of $N(0)$ and V are examined. Here qualitative and quantitative comparisons of various experiments can be made. The possibilities of applying large magnetic fields and thereby independently measuring $N(0)$ and small changes of $N(0)$ near the Fermi energy by such studies are discussed. Recent theories which examine the changes of χ_p with alloying are also compared with experimental results.

A few useful references for relevant recent papers concerning the susceptibility of nearly ferromagnetic metals and alloys are tabulated in references 1 to 4. Recent detailed band calculations in Pd have been reported in references 5 to 8. Several papers at this conference also deal with high densities of states materials.

1. References

[1] Foner, S., Freeman, A. J., Blum, N., Frankel, R. B., McNiff, E. J., Jr., and Praddaude, H., Phys. Rev. **181**, 863 (1969).
[2] Foner, S., and McNiff, E. J., Jr., Phys. Rev. Letters **19**, 1438 (1967).
[3] Foner, S., and McNiff, E. J., Jr., Phys. Letters **29A**, 28 (1969).
[4] Doclo, R., Foner, S., and Narath, A., J. Appl. Phys. **40**, 1206 (1969).
[5] Mueller, F. M., Freeman, A. J., Dimmock, J. O., and Furdyna, A. (to be published).
[6] Hodges, L., Ehrenreich, H., and Lang, N. D., Phys. Rev. **152**, 505 (1966).
[7] Anderson, O. K., and Mackintosh, A. R., Solid State Comm. **6**, 285 (1968).
[8] Misetich, A. A., and Watson, R. E., J. Appl. Phys. **40**, 1211 (1969).

*An invited paper presented at the 3d Materials Research Symposium, *Electronic Density of States*, November 3-6, 1969, Gaithersburg, Md.

[1] Supported by the U.S. Air Force Office of Scientific Research.

(Paper 74A4-623)

JOURNAL OF RESEARCH of the National Bureau of Standards — A. Physics and Chemistry
Vol. 74A, No. 4, July-August 1970

Relevance of Knight Shift Measurements to the Electronic Density of States*

L. H. Bennett

Institute for Materials Research, National Bureau of Standards, Washington, D.C. 20234

R. E. Watson[1]

Brookhaven National Laboratory[2], Upton, New York 11973

G. C. Carter

Institute for Materials Research, National Bureau of Standards, Washington, D.C. 20234

The Knight shift, $\mathcal{K}$, measures the magnetic hyperfine field at the nucleus produced by the conduction electrons which are polarized in a magnetic field. Knight shifts are often dominated by the Pauli term and, in its most simple form, can be written as $\mathcal{K} = \langle a \rangle \chi_p$. Here χ_p is the conduction electron Pauli spin susceptibility which depends on the density of states at the Fermi level, $N(E_F)$, and $\langle a \rangle$ is an average magnetic hyperfine coupling constant associated with the wave function character at the nucleus, $|\psi_F(0)|^2$, for conduction electrons at the Fermi surface.

The Knight shift therefore provides, through $\langle a \rangle$, insight into the wave-function character associated with $N(E_F)$. Calculations of $\langle a \rangle$ involving an averaging over k-space have been attempted for a few simple metals up to the present time. For alloys and intermetallic compounds, rather different $\langle a \rangle$'s are experimentally observed for different local environments, indicating that $\mathcal{K}$ samples the variation in *local* wave-function character, or a variation in *local* density of states. There is no unique way of separating the local variation of $N(E_F)$ from $|\psi_F|(0)|^2$.

In this article the methods developed for relating $\mathcal{K}$ to the electronic properties for most of the types of cases encountered in the literature are reviewed. We discuss "simple" metals including problems of orbital magnetism and changes in $\mathcal{K}$ caused by electronic transitions such as melting. Knight shifts and their temperature dependence in metals and intermetallic compounds involving unfilled d shells, are discussed. We give estimates of atomic hyperfine fields due to single electrons, appropriate to those cases where problems due to electronic configurations do not make deductions from experiment too ambiguous. A density of states curve calculated for Cu is given, showing the relative importance of s-p, and d character for that metal. In a qualitative sense this Cu curve implies such information for other transition metals. We discuss alloy solid solutions for the cases where a "rigid" band model might be used to explain the results, and for cases where local effects have to be taken into account. The charge oscillation and RKKY approaches and their limitations are reviewed for cases of dilute nonmagnetic and d- or f-type impurities.

Key words: Electronic density of states; hyperfine fields; Knight shift; nuclear magnetic resonance; susceptibility; wave functions.

1. Introduction

Twenty years ago W. D. Knight [1][3] discovered that the nuclear magnetic resonance (NMR) of ^{63}Cu occurs at about a quarter percent higher frequency in metallic copper than in a salt, CuCl. Since then, there have been over 500 papers reported on the theory and observation of this effect, the "Knight shift," in a wide

*An invited paper presented at the 3d Materials Research Symposium, *Electronic Density of States*, November 3-6, 1969, Gaithersburg, Md.

[1] Also Consultant, National Bureau of Standards.

[2] Work supported by the U.S. Atomic Energy Commission.

[3] Figures in brackets indicate the literature references at the end of this paper.

variety of metals and alloys. The first observation of the Knight shift is shown in figure 1. This paramagnetic shift of the resonance between the diamagnetic salt, CuCl, and the diamagnetic metal, Cu, was attributed

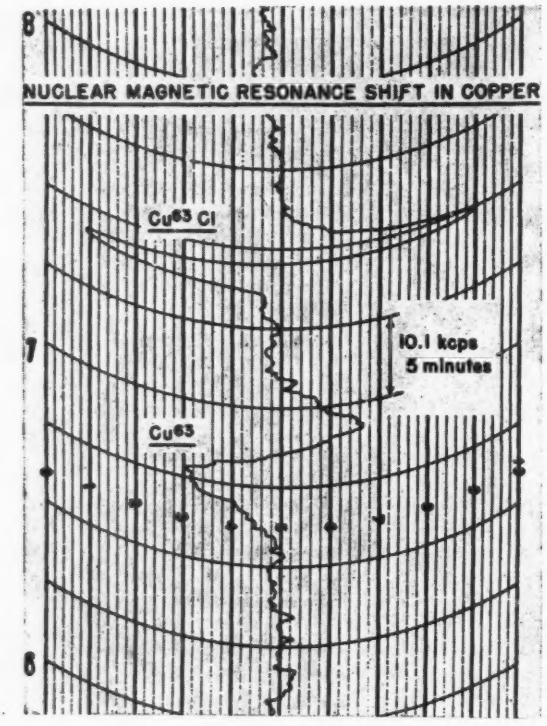

FIGURE 1. *The ^{63}Cu resonance in CuCl (upper resonance) and metallic copper (lower resonance), illustrating the Knight shift* [1].

[2] to the Pauli paramagnetism of the conduction electrons. The shift is much larger than could be explained by the average susceptibility of the conduction electrons. It was proposed [2] that the nuclei sampled a concentrated local susceptibility, arising from the fact that the conduction electrons in a metal have a very large probability density at the nucleus. In its simplest form, the Knight shift ($\mathcal{K}$) may be written

$$\mathcal{K} = \langle a \rangle \chi_p, \tag{1}$$

where $\langle a \rangle$ is an appropriate sampling of the hyperfine interaction of the conduction electrons at the Fermi surface.

For noninteracting electrons, χ_p is proportional to $N(E_F)$, the electronic density of states at the Fermi level,

$$\chi_p = \mu_B{}^2 N(E_F) \tag{2}$$

where μ_B is the Bohr magneton. Thus in this simple approximation, the Knight shift samples, via $\langle a \rangle$, local behavior of the density of states (at the Fermi level) at a particular atomic site.

In this article we will inspect in detail this relationship of $\mathcal{K}$ with the density of states, thereby omitting several important topics on other aspects of NMR in metals. Good review articles have appeared earlier on this broader topic [3-5].

Unfortunately, as with most of the methods for studying the electronic density of states discussed at this symposium, untangling the factors folded in with the density of states is not an easy task. Very often, the experimental Knight shift is used to measure the factor $\langle a \rangle$, χ_p having been obtained from other experiments such as electronic specific heat or bulk magnetic susceptibility. The Knight shift provides a particularly complicated weighted sampling of electronic character but with these complications comes the possibility of obtaining unique information which is otherwise experimentally inaccessible.

A more complete expression for the Knight shift would include other terms,

$$\mathcal{K} = \mathcal{K}_{\text{Pauli}} + \mathcal{K}_{\text{dia}} + \mathcal{K}_{\text{orb}} + \text{higher order terms}. \tag{3}$$

$\mathcal{K}_{\text{Pauli}}$, given by eq (1), includes isotropic and anisotropic effects, directly by contact and spin dipolar interactions, and indirectly via core polarization and polarization of conduction band electrons below the Fermi level. The orbital paramagnetic and diamagnetic terms, $\mathcal{K}_{\text{orb}}$ and $\mathcal{K}_{\text{dia}}$, are important at times. We will review in this paper the various contributions to $\mathcal{K}$, as summarized in eq (3), in the light of experimental observations, together with theoretical methods for relating these results to the electronic structure of metals.

2. General Observations

In NMR one looks at transitions of a nucleus (with spin states $m = I, I-1, I-2, \ldots 1-I, -I$) from spin state m to $m \pm 1$, by measuring the frequency, ν, of the photons involved in these transitions. The energy difference between the two states, $\Delta E_{m \to m-1} = h\nu$, is directly proportional to the applied magnetic field, H_{appl}. However, even for a given isotope, the proportionality constant is different for different solids because the electrons in the solid respond differently to H_{appl} (paramagnetically or diamagnetically) causing an additional (positive or negative) field at the resonating nucleus. This magnetization field, as seen by the nucleus, is often referred to as the "internal field," H_{int}.

The Knight shift, $\mathcal{K}$, measures the internal field at the nucleus produced by those electrons in metals which respond linearly (with one exception, noted in sec. 6) to an applied field. Thus $\mathcal{K} \equiv H_{\text{int}}/H_{\text{appl}}$. Specifically, this definition excludes materials with spontaneous magnetization.

For simple metals, the conduction electrons cover a broad band of energy states. Those electrons at the Fermi surface are aligned paramagnetically by an external applied magnetic field. The resulting polarization of these electrons causes large internal fields, via the Fermi contact interaction hamiltonian, $\mathcal{H}_F$,

$$\mathcal{H}_F = \frac{16\pi}{3}\mu_B\gamma\hbar\mathbf{I}\cdot\mathbf{S}(\mathbf{r})\delta(\mathbf{r}), \tag{4}$$

where γ is the nuclear gyromagnetic ratio, and $\mathbf{S}(\mathbf{r})$ is the electron spin as a function of its position vector $\mathbf{r}$ from the nucleus. The contact (or δ-function) interaction samples the probability density $|\psi_A(0)|^2 \equiv P_A$ at the nucleus, for an electron in the atom. It is related to the atomic hyperfine coupling constant, $a(s)$, by

$$a(s) = \frac{16\pi}{3}\gamma\hbar\mu_B P_A. \tag{5}$$

The $\delta(\mathbf{r})$ thus restricts this effect to s-electrons and to the minor components of relativistic p-electrons. The s-effects are large, while the p-terms are almost invariably small and will henceforth be neglected. This large hyperfine term is generally absent in nonmetallic materials, because for each s-electron of spin-up, there is an s-electron of spin-down, and these are not decoupled by the usual applied magnetic fields.

For monovalent metals, $a(s)$ is obtained with high accuracy from atomic beam experiments. Values of $a(s)$ for the alkali metals are shown in table 1. The quantity more important to Knight shift considerations, P_A, is also shown. Note that P_A increases monotonically with atomic number for a given group, whereas $a(s)$ is dominated by the nuclear moment and appears random. Except for a possible small hyperfine structure anomaly, P_A is the same for all isotopes of a given element, whereas $a(s)$ depends on the given isotope.

TABLE 1. *Comparison of different ways of expressing the hyperfine coupling of a single s-electron, for the alkali metals.*

	$a(s)$ (cm^{-1})	P_A(cm^{-3})	$H_{\text{eff}}^{\text{atom}}$ (kOe)
^{7}Li.....	0.0134	15.7×10^{23}	122
^{23}Na.....	.0296	50.2×10^{23}	390
^{39}K.....	.00770	74.6×10^{23}	580
^{87}Rb.....	.114	154×10^{23}	1200
^{133}Cs.....	.0766	257×10^{23}	2000

The data for $a(s)$ were derived from data given by P. Kusch and H. Taub. Phys. Rev. **75**, 1477 (1949); the other columns were calculated from these using eqs (5) and (12).

In a metal the appropriate probability density P_F is obtained by taking a suitable average over the Fermi surface, $P_F = \langle\psi(0)^2\rangle_{E_F}$. The Knight shift, eq (1), has shown [2] to be

$$\mathcal{K} = \frac{8\pi}{3}\chi_p P_F, \tag{6}$$

where χ_p is the Pauli spin susceptibility per atom. Sometimes an explicit volume or mass factor appears in the expression for $\mathcal{K}$, but this depends on the appropriate normalization of $\langle\psi^2(0)\rangle_{E_F}$ and on whether a mass, volume, atomic or molar susceptibility is used.

If we define

$$\langle a\rangle \equiv \frac{8\pi}{3}\langle\psi(0)^2\rangle_{E_F} = \frac{8\pi}{3}P_F, \tag{7}$$

then we obtain eq (1).

Alternately it is convenient to introduce the effective hyperfine field H_{eff}, which is the field measured directly in ferromagnetic materials by, for example, ferromagnetic NMR or by Mössbauer spectroscopy. Then

$$H_{\text{eff}} \equiv \mu_B\langle a\rangle = \frac{8\pi}{3}\mu_B P_F. \tag{8}$$

Hence

$$\mathcal{K} = \frac{1}{\mu_B}\chi_p H_{\text{eff}}. \tag{9}$$

It has been found useful to define a factor ξ, sometimes called Knight's ξ factor [3], as

$$\xi \equiv \frac{P_F}{P_A} \equiv \frac{H_{\text{eff}}^{\text{metal}}}{H_{\text{eff}}^{\text{atom}}}. \tag{10}$$

In the simplest cases, ξ has been said to express the fraction of s-character at the nucleus in the metal at E_F, but as we shall see, ξ is more complex in its meaning for less simple cases. The Knight shift then becomes

$$\mathcal{K} = \frac{1}{\mu_B}\chi_p\xi H_{\text{eff}}^{\text{atom}}, \tag{11}$$

where

$$H_{\text{eff}}^{\text{atom}} = 19650\ a(s)\frac{I}{\mu_I}. \tag{12}$$

Here $a(s)$ is in cm^{-1}, $H_{\text{eff}}^{\text{atom}}$ in kOe, and μ_I is in nuclear magnetons. Values of $H_{\text{eff}}^{\text{atom}}$ are listed in table 1 for the alkali metals and in table 2 for some B-subgroup metals. The values for the monovalent metals are derived from atomic beam measurements. For polyvalent metals, Knight [3] has used measurements

on *excited ionic* states and then corrected for the degree of ionization. Knight estimated his resulting values of $a(s)$ to be accurate to perhaps 50 percent. Rowland and Borsa [6] avoided the problem of corrections by using measurements on *excited neutral* atom states. The values for the polyvalent metals in table 2 do not depend on *excited* state measurements, but instead were determined by scaling, based on atomic calculations, from the known monovalent values [7].

TABLE 2. H_{eff}^{atom} *values obtained by scaling from monovalent values* [7].

Group	*Atom*	H_{eff}^{atom} (kOe)
I	Cu	2,600
	Ag	5,000
	Au	20,600
II	Cd	7,000
	Hg	25,800
III	B	1,000
	Al	1,900
	Ga	6,200
	In	10,100
	Tl	34,000
IV	Sn	12,800
	Pb	41,400
V	N	3,300
	P	4,700
	As	8,900
	Sb	14,500
	Bi	49,000
VI	Te	17,200
X	Pt	20,000

The ξ factor accounts for any deviation in hyperfine coupling from free atom behavior. It may deviate from a value of one for a variety of reasons. For example, the average conduction electron density in a metal is greater than that in the free atom (*i.e.*, P_ψ is normalized to a Wigner-Seitz cell in the metal whereas the free atom P_ϕ extends over a significantly larger volume). If no other factors were present, ξ would then be greater than unity. A Fermi surface orbital, ψ_F, has only partial *s*-character and this causes a reduction in ξ. In a "free electron metal," ψ_F is a plane wave ϕ_F (suitably orthogonalized to atomic core states) or a linear combination of plane waves. With increasing number of electrons in the bands the *s*-character of ψ_F decreases [8]. In a metal such as Tl, Pb, or liquid Bi, this reduction is quite substantial. In metals with one "free" conduction electron (*e.g.*, the alkali and noble metals), $\mathbf{k}_F$ is relatively small, and the reduction could be expected to be slight. Here, other orthogonalized plane waves, $\phi_{\mathbf{k}_F+\mathbf{Q}}$ (where $\mathbf{Q}$ is a reciprocal lattice vector) are mixed into ϕ_F and the normal *sign* of the mixing is such that interference causes $|\psi_F(0)|^2$ to be less than that predicted by $|\phi_F(0)|^2$ alone. This, as well as *d*-band hybridization and core-polarization factors which will be considered shortly, tend to predominate over the normalization effect reducing ξ to values typically between 0.1 and 0.8 in "simple" metals.

Experimental values for $\mathcal{K}$ are given in figures 2a and 2b. Using these measured values of $\mathcal{K}$, and obtaining χ_p as explained in the next section, the systematic trends for ξ seen in figure 3 are obtained.[4] In each period the largest ξ values are found for the monovalent metals, with ξ falling smoothly to lower values as the group valence increases, as would be expected from the wave function behavior just discussed. It is interesting that these results are obtained despite the changing crystal structures. About one-half the observed drop in ξ is expected from simple estimates [8] of the reduction in *s*-character with increasing $\mathbf{k}_F$; the increasing atomic volumes of the polyvalent over the monovalent metals further enhances the trend.

The induced conduction electron Pauli spin density may also contribute to the hyperfine coupling constant, $\langle a \rangle$, via the spin dipolar interaction

$$\mathcal{H}_{SD} = -2\mu_B \gamma N \hbar \mathbf{I} \cdot \left(\frac{\mathbf{S}}{r^3} - \frac{3\mathbf{r}(\mathbf{S}\cdot\mathbf{r})}{r^5} \right), \qquad (13)$$

where $\mathbf{r}$ is the vector from the nucleus to the electron. This interaction is anisotropic and contributes an orientation dependent Knight shift term, $\mathcal{K}_{anis}$, for nuclei at noncubic sites, and occasionally at cubic sites if spin-orbit coupling is present. In powders, this term results in structure and broadening of the NMR line.

The induced Pauli spin density interacts *directly* with the nucleus only via the contact and spin dipolar interactions but it may act *indirectly* as well. The spin density has a spin dependent exchange interaction associated with it, which arises from the Pauli exclusion principle. This may polarize the closed shells of an ion core and the paired electrons in the conduction bands *below* E_F, producing spin densities which will then interact with the nucleus via the contact (and for noncu-

[4] From figure 3, a ξ value for Zn between that of Cd and Hg can be extrapolated. From this $\mathcal{K}$ for Zn is predicted to be 0.20 percent. This is not far from the value 0.26 percent predicted [9] from quite different considerations.

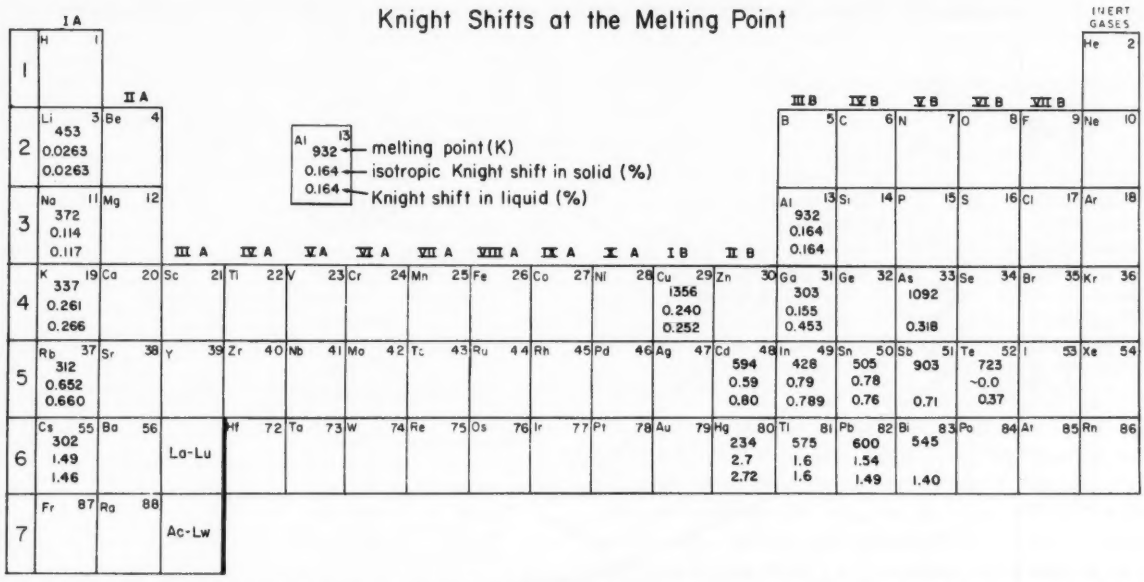

FIGURE 2a. *Knight shifts in metals as compiled at the Alloy Data Center (NBS). Note: Literature references available on request. (a) Knight shifts in the solid and liquid state at the melting point.*

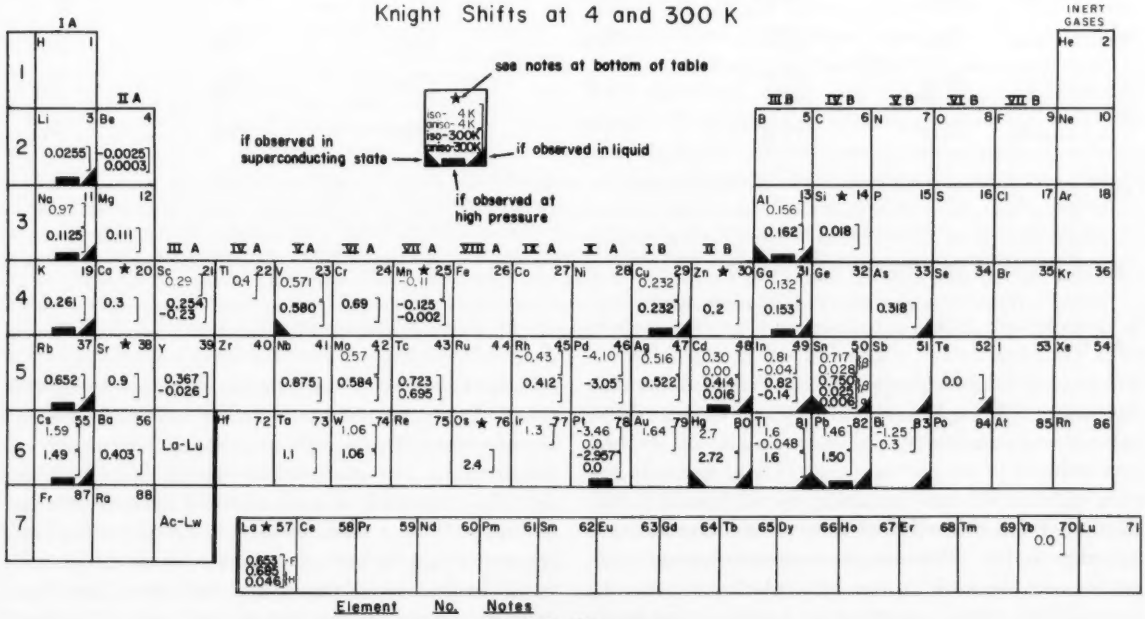

Element	No.	Notes
Si	14	Chemical shift
Ca	20	Predicted value (1956)
Mn	25	All data are for β phase
Zn	30	Predicted value
Ga	31	Anisotropic shifts: $K(X) = 0.015(4)\%$; $K(Y) = -0.001(4)\%$; $K(Z) = -0.014(4)\%$; all independent of T to 4K
Sr	38	Predicted value (1956)
La	57	F = FCC; H = HCP
Os	76	Predicted value (1956)

FIGURE 2b. *Knight shifts in metals as compiled at the Alloy Data Center (NBS). Note: Literature references available on request. (b) Isotropic and anisotropic Knight shifts at room and liquid helium temperatures.*

383-876 O - 70 - 8

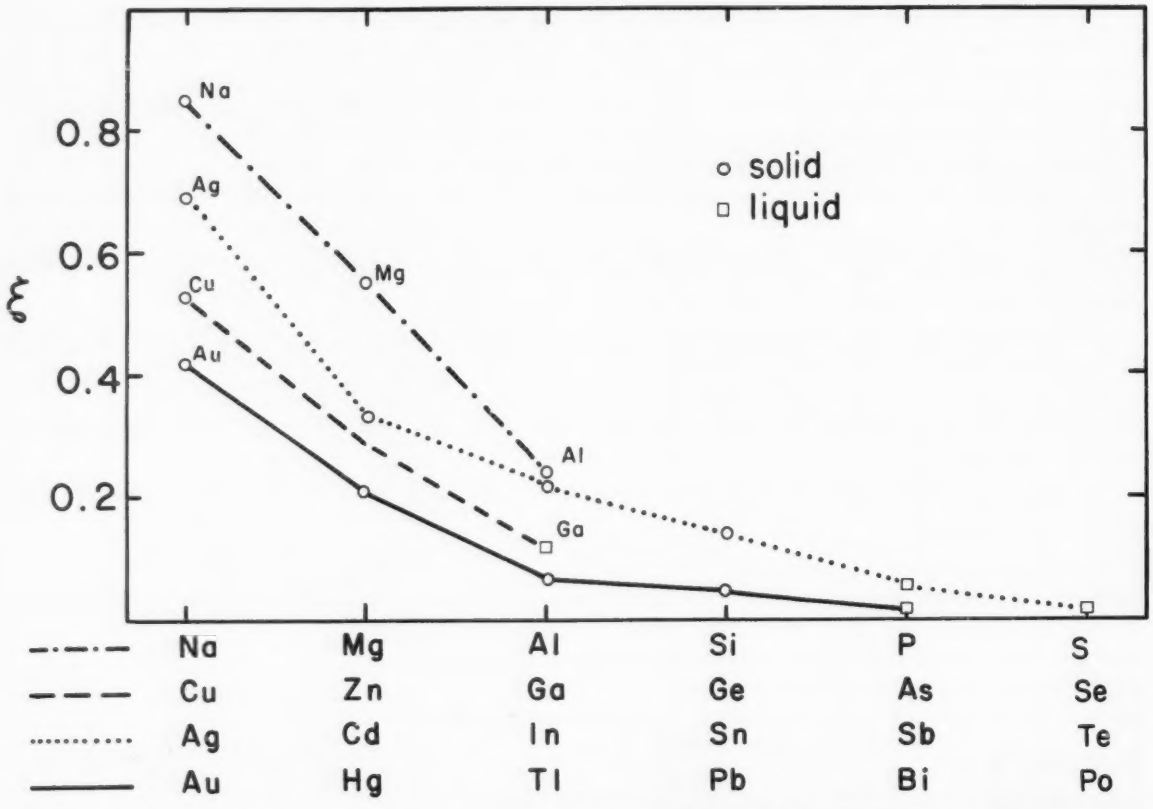

FIGURE 3. *Behavior of Knight's ξ values for metallic elements as a function of their position in the periodic table. The points for each row in the table are connected using the sumbols for lines as shown outside the left lower corner of the plot. Those points shown as circles are for the metals in the solid state and those shown as squares were calculated for the metals in the liquid phase. For the former points χ_p was calculated using γ_{el} values [37]; for the liquid metals χ_p was taken to be $3/2(\chi_{expt}-\chi_{dia}^{core})$ using χ_{expt} from the Landolt-Börnstein Tables and χ_{dia}^{core} from Hurd and Coodin [33]. The absolute values of ξ are affected by uncertainties in the estimates of χ_p and H_{eff} but the relative behavior (from element to element) along each row is probably realistic. Points for solid Ga and liquid As are omitted for lack of accurate values for $\mathcal{K}_{iso}$ and $\chi_p(liq)$, respectively. The plot provides an estimate for the Knight shift of Zn which has yet to be observed.*

bic sites, spin dipolar) interaction(s). These interactions arise from *differences* induced in the spatial behavior of spin up and spin down pairs of electrons with *zero net spin* induced in the electron pairs. Their existence has been established experimentally by the fact that half filled shell (p^3, d^5, and f^7) *S*-state atoms have nonzero hyperfine fields. While the exchange interaction is believed to be the origin of this spin polarization, correlation effects should, in principle, be important to its quantitative behavior. These interactions have been discussed extensively elsewhere [10].

For the moment we will limit our considerations to intra-atomic contributions to the contact interaction. This necessarily involves the spin polarization of closed *s*-shells of the core and of the *s*-character in the conduction bands below E_F, since only these will interact directly with the nucleus. Estimates of these core polarization effects from valence electrons in the various shells are summarized in table 3. These are based on experimental data and on exchange polarization calculations (*i.e.*, no correlation effects). Listed are the sign and magnitude characteristic of the core polarization response to a single unpaired *s*-, *p*-, *d*-, or *f*-valence electron characteristic of various rows of the periodic table. (In the case of the open *p*-shell atoms, the listed response includes that associated with the closed valence *s*-shell.) For comparison, the direct contact interaction appropriate to an unpaired atomic *s*-valence electron is shown in table 4, for the *d*- and *f*-shell atoms. The core polarization is negative for *d*- and *f*-shells, and for *np*-shells, where *n*, the principal quantum number, is 4 or greater. The negative sign implies a core spin density at the nucleus, whose orientation is *antiparallel* to the unpaired spin responsible for the

TABLE 3. *Rounded value for hyperfine fields due to the core polarization response to a single unpaired open valence shell electron.*

Open valence shell	Core polarization hyperfine field, H_{eff}, per unpaired valence electron, *kOe*	Comments on source(s) of core polarization values. (For further comments and details of most of the data see Ref. 10).
$2p$.....	+30	Experiment, appropriate to neutral N alone.
$3p$.....	+15	Experiment, appropriate to neutral P alone.
$4p$.....	−50	Experiment, (neutral As $4s^24p^3$ ^4S).
$5p$.....	−150	Experiment (neutral Sb $5s^25p^3$ ^4S).
$6p$.....	−300	Experiment (neutral Bi $6s^26p^3$ ^4S).
$3d$.....	−125	Calculation and experiment for $3d^n4s^0$ ions.
$4d$.....	−350	Calculation and limited experiment for $4d^n$ $5s^0$ ions.
$5d$.....	−750	Calculation (J. V. Mallow, A. J. Freeman and P.S. Bagus, J. Appl. Phys., to be published).
	−600	Inferred from hyperfine anomaly, [G. J. Perlow, W. Henning, D. Olson and G. L. Goodman, Phys. Rev. Letters **23**, 680 (1969)].
$4f$.....	0 to −50	Calculation and limited experimental data.
ns.....	>0	Estimated by calculation to make a 10–50% enhancement of a ns shell's direct contact interaction.

TABLE 4. *Direct plus associated core polarization contact hyperfine fields due to a single unpaired valence s-electron for various rows in the periodic table.*

s shell	Atoms	*s*-contact hyperfine field, H_{eff}, kOe
$2s$.....	$2p^1$–$2p^3$ elements	1,000– 4,000
$3s$.....	$3p^1$–$3p^3$ elements	2,000– 5,000
$4s$.....	$3d$ transition metals	2,000– 3,000
$4s$.....	$4p^1$–$4p^3$ elements	4,000–10,000
$5s$.....	$4d$ transition metals	4,000– 5,000
$5s$.....	$5p^1$–$5p^3$ elements	7,000–15,000
$6s$.....	rare earths	9,000–15,000
$6s$.....	$5d$ transition metals	15,000–20,000
$6s$.....	$6p^1$–$6p^3$ elements	25,000–50,000

polarization. The core polarization response to an unpaired *s*-valence electron is positive and simply serves to enhance the contact interaction associated with the valence electron. [When using experimental atomic hyperfine data to evaluate P_A, this effect is already included.] The $3d$, and $4d$ (little is known yet for the $5d$) core polarization values appear to be quite stable for their respective rows in the periodic table. The quoted values hold to within twenty percent for any member of a row and it is believed that these values are appropriate to the core polarization response to a *d*-moment in a metal.

The situation is less certain and more complicated for the *p*-shell elements. Experimental data for which there are no competing orbital and spin dipolar terms exist only for the p^3 *S*-state atoms. It should be noted that these experimental values include the contribution coming from the polarization of the closed *valence s*-shells. In a metal this term is associated with the conduction band and not the core states. There is some uncertainity as to the sign and magnitude of this core plus valence *s* polarization term as one goes across the $2p$ and $3p$ rows. Recent spin polarized Hartree-Fock calculations of Bagus *et al.* [11] for these rows suggest that both the core and valence contributions are significant with the total becoming less positive (or more negative) as one goes to the lighter elements in the row. As with earlier efforts [10], these calculations do not satisfactorily reproduce the experimental data and must be used with caution, (*e.g.*, the wrong sign is predicted for atomic P). Bagus *et al.* also obtained results for the $4p$ row. Again the total becomes more negative by a factor of, say, two for the lighter elements but now the valence term dominates. This latter fact suggests that such atomic hyperfine constants will be of little quantitative utility when inspecting *p*-electron metals until one understands the polarization response of *s*-electron character deep in a conduction band. An example in the literature of the use of a *p*-core polarization term larger than that shown in table 3, is Ga in $AuGa_2$ [12], where a *p*-term of an order of magnitude larger than that of As (table 3) was used to explain the observed negative Knight shift.

One complication associated with extracting wave function and density of states information from Knight shift measurements is suggested by the numbers in table 3. Consider the $3d$- and $4d$-transition metals. As discussed in section 7, the Pauli Knight shift term almost invariably has the opposite sign of temperature dependence as the Pauli susceptibility [13]. This is consistent with having *d*-bands at E_F, with negative hyperfine constants of the sort seen in the table. Now, the *s*-contact densities are an order of magnitude larger than the corresponding *d*-core polarization hyperfine constants. Thus a few percent admixture of *s*-character into the Fermi surface *d*-states can violently affect $\langle a \rangle$.

While complicating matters, such interband hybridization is of considerable interest in itself and one can attempt to use Knight shift data to ascertain its nature and extent [14,15].

Relatively little is known of the intra-atomic hyperfine contribution arising from the exchange polarization of conduction band states below E_F, except that it probably makes a positive contribution to $\langle a \rangle$ for transition metals. Some measure of the effect can be obtained for the 3*d* metals by inspection of the spin polarization of the $4s^2$ shell in the neutral $3d^n4s^2$ atoms. Experiment and exchange polarized calculations indicate [10,16] a $4s^2$ hyperfine field of $\sim +100$ kOe per unpaired *d*-electron, a contribution which almost cancels the $1s^2 + 2s^2 + 3s^2$ core polarization. One expects a smaller effect in a metal since there are typically one, not two, electrons worth of "*s*" character below E_F. One might expect a further reduction, in view of the fact that ξ values defined for Fermi level states always lie below 1. Paired Block states near the bottom and throughout an occupied "conduction" band contribute to the exchange polarization. These states have stronger hyperfine coupling than those at E_F which contribute to the Knight shift, as is evidenced by internal conversion experiments [17]. It is probable that there is little or no reduction in this polarization term due to band effects.

There may be *inter*-atomic as well as *intra*-atomic contributions to $\langle a \rangle$, since an applied magnetic field induces spin moments on the neighboring atoms as well as the atom in question. The two contributions are indistinguishable for the pure monatomic metals, but there is indirect evidence, from alloying, that the interatomic term is quantitatively important in some transition metals. *Inter*-atomic contributions will be seen to be important in transition metal alloys and intermetallics. As with the concept of a *local* density of states, there will frequently be ambiguity when attempting to divide $\mathcal{K}$ into inter- and intra-atomic terms.

In addition to these contributions to the Knight shift coming from the Pauli paramagnetism of the conduction electrons, there is an important contribution, especially in transition metals, from the orbital magnetic moment of the conduction electrons induced by the applied magnetic field. We can write, in analogy with eq (1)

$$\mathcal{K}_{\text{orb}} = \langle b \rangle \chi_{\text{orb}} \tag{14}$$

where $\langle b \rangle$ is an appropriate orbital hyperfine coupling constant. In contrast to the Pauli contribution to the Knight shift, the orbital Knight shift is not proportional to $N(E_F)$.

The orbital Knight shift [18-20] involves the orbital moment induced in occupied conduction electron states by an applied magnetic field, **H**. It is a second order term of the form

$$\mathcal{K}_{\text{orb}} = \frac{2\mu_B^2}{IH} \sum_{E_i < E_F} \sum_{E_f > E_F} \frac{\langle i|\mathbf{H}\cdot\vec{\ell}|f\rangle \left\langle f \left| \frac{2\vec{\ell}\cdot\mathbf{I}}{r^3} \right| i \right\rangle \delta(\mathbf{k}_f - \mathbf{k}_i)}{E_i - E_f}$$

$$\equiv \langle b \rangle \chi_{\text{orb}} \equiv 2\chi_{\text{orb}} \langle r^{-3} \rangle. \tag{15}$$

Here the matrix elements are evaluated over a Wigner-Seitz cell. The occupied and unoccupied Bloch states, *i* and *f*, are admixed by the application of the field. The resulting admixture produces a moment which interacts with the nucleus. Except for pathological cases, where there are a substantial number of strongly admixed states within kT or E_F, there is little or no temperature dependence in this term, as is the case in the analogous Van Vleck temperature-independent paramagnetism in ionic salts. A rough estimate of the strength of the orbital Knight shift is given by [17].

$$\mathcal{K}_{\text{orb}} \approx \frac{n_i n_f \left\langle \frac{1}{r^3} \right\rangle}{\Delta}, \tag{16}$$

where n_i and n_f are the numbers of occupied and unoccupied Bloch states respectively and Δ is the conduction electron bandwidth. This equation suggests that particularly strong orbital effects are expected in roughly half-filled *d*-band transition metals. In half-filled bands the product $n_i n_f$ is a maximum, and in transition metals, Δ is small. Strong effects have indeed been found in W [21], Nb [20], V [19,20,22], Cr [23] and CrV alloys [24].

Although we have treated the Pauli and orbital hyperfine parameters, *a* and *b*, as multiplicative factors of the appropriate susceptibilities, it should be emphasized that $\langle a \rangle$ and $\langle b \rangle$ are not the simple averages customarily employed, but are more correctly the weighted averages

$$\langle a \rangle \equiv \frac{\langle a\chi_p \rangle}{\chi_p} \tag{17}$$

and, as is clear from eqs (14) and (15),

$$\langle b \rangle \equiv \frac{\langle b\chi_{\text{orb}} \rangle}{\chi_{\text{orb}}}. \tag{18}$$

The $\langle\,\rangle$ denote an average over all bands. For the Pauli term, the average is over segments of Fermi surface where the contribution of a segment to χ_p is multiplied

by the hyperfine constant, a, appropriate to that segment (*i.e.*, to its electron character). Equation 15 defines the average for the orbital term, where the induced orbital moments associated with initial and final states, i and f, are weighted by their hyperfine coupling constants. With this, the general expression for the Knight shift, eq (3), becomes

$$\mathcal{K} = \langle a\chi_p \rangle + \mathcal{K}_{\text{dia}} + \langle b\chi_{\text{orb}} \rangle + \text{higher order terms.} \quad (19)$$

The Knight shift provides samplings of wave function and, in some senses, density of states character different from that obtainable in other experiments. The Pauli term can in principle, and does occasionally in practice, yield considerable insight into the Fermi surface states contribution to $N(E_F)$. A particular case is that of alloys and intermetallic compounds with different $\langle a \rangle$'s at different atomic sites. This involves the variation in wave function character from site to site and, if you will, the variation in a *local* density of states. There is some arbitrariness as to whether one wishes to describe this in terms of $\langle a \rangle$ or a local χ_p.

A particularly clear example of this local nature is that of α-Mn. For this structure there are four crystallographically inequivalent sites. Above the Néel temperature of 95 K, four distinct resonances were observed [25,26]. Two of these had large negative shifts of -5.2 and -2.6 percent at room temperature [26], and were temperature dependent [25], with the former value increasing to -5.85 percent at 120 K, where χ shows a maximum. The nuclei at the other two crystallographically inequivalent sites showed much smaller, and temperature independent, Knight shifts (-0.45 and -0.15%).

A number of complications have been indicated in this section. There is more than one term in the Knight shift; also the hyperfine constants $\langle a \rangle$ and $\langle b \rangle$ are significantly affected by band character and hybridization. There will in general be *inter-* and *intra*-site contributions to $\langle a \rangle$. As will be seen, two important "tools" are available to aid in the identification of the different contributions to $\mathcal{K}$: the Korringa relation [27] relating Knight shifts to nuclear spin-lattice relaxation times, and the temperature dependence of both $\mathcal{K}$ and χ [13]. Finally one can sample Knight shift behavior at sites involving different atoms in an alloy or intermetallic compound. Matters such as these, while complicating Knight shift interpretations in terms of density of states, can supply insight into the electronic structure and local wave function character which cannot generally be obtained from other experiments.

3. Pauli Spin Susceptibility

The Knight shift samples the density of states via the Pauli spin susceptibility, χ_p. However, in pure metals, the density of states has usually been obtained in other ways and the Knight shift then used to explore the associated wave-function character. In this section, we will review some of these methods of obtaining χ_p, and their implications to our understanding of Knight shift behavior.

First let us note that the expression relating the Pauli susceptibility to the density of states given in eq (2) neglects correlation and exchange effects between conduction electrons. Electron gas estimates are frequently applied to "free" electron metals [28,29], and exchange enhancement theories to transition metals [30-32]. With a conduction-electron conduction-electron exchange interaction parameter $\mathcal{J}_{\text{eff}}$ defined in reciprocal space and taken to be constant, the random phase approximation yields [30-32] an exchange enhanced susceptibility

$$\chi_p = \frac{\chi_p^0}{1 - \mathcal{J}_{\text{eff}}\chi_p^0}, \quad (20)$$

where χ_p^0 is the unenhanced susceptibility of eq (2). The induced spin sets up an exchange field encouraging further polarization hence an enhanced χ_p. Similar looking expressions, with $N(E_F)$ appearing in numerator and denominator are obtained from correlated electron gas theory. These as well as interband effects obviously complicate the averages taken in eq (17). In general one is forced to neglect them in $\langle a \rangle$ and assume their presence in χ_p alone. Even with this simplification, there is no simple linear relation between an observed Knight shift and the density of states at the Fermi surface. As remarked earlier, this shortcoming is shared with the experimental data obtained by many of the other techniques reviewed in this symposium.

It might appear that an adequate value of χ_p could be obtained from direct measurements of magnetic susceptibilities, χ_{exp}, especially since these would already have the exchange enhancement included. We will return to the case of transition metals later, but in simple metals it turns out that bulk susceptibility results usually do not give reliable values of χ_p. Consider, for instance, the noble metals. The bulk susceptibilities (χ_{exp}) are each negative, *i.e.*, the metals are diamagnetic. The ion core diamagnetism ($\chi_{\text{dia}}^{\text{core}}$) plus conduction electron diamagnetism ($\chi_{\text{dia}}^{\text{cond}}$) is larger than χ_p. Hartree-Fock [7] and Hartree-Fock-Slater [33] calculations for $\chi_{\text{dia}}^{\text{core}}$ agree to within two percent. However these calculations are for singly ionized valence states

which is not a totally satisfactory description in the metal. This, and interband mixing effects, raise the probable error in χ_{dia}^{core} considerably. By the same token, χ_{dia}^{cond} is poorly known due to electron-electron interactions. The net result is that χ_p obtained from χ_{exp} is probably good to no better than twenty percent for the noble metals. Various ξ values for the noble metals obtained by use of various schemes are shown in table 5. It can be seen that ξ values employing the traditionally quoted values for χ_{dia}^{core} are not consistent with those using more modern Hartree-Fock or Hartree-Fock-Slater estimates. The situation in the case of the alkali metals is not as bad for two reasons. First the theoretical evaluation of both the core- and conduction-electron diamagnetism is on firmer ground, especially for the free electron-like metal, Na. Secondly, χ_p has been obtained directly (*i.e.*, without the need for the troublesome diamagnetic corrections) using conduction electron spin resonance (CESR) for the alkali metals and for Be. Combined CESR-NMR has also been used in Na and Li [34-36] to obtain χ_p.

For many metals it has been customary to use electronic specific heat, γ, measurements for information about χ_p^0 using the one-electron relationship

$$\chi_p^0 = 3\left(\frac{\mu_B}{\pi k}\right)^2 \gamma, \tag{21}$$

where k is the Boltzmann constant. There are two difficulties here. One is that there may be many-body contributions to γ (such as electron-phonon or paramagnon enhancement). The other is that the exchange enhancement part of χ_p is missing here [see eq (20)]. The ξ values derived from γ, given in table 5, were obtained from eq (21) and experimental γ values [37], and therefore neglect these corrections for enhancement effects. It may be that in some cases these two factors approximately cancel one another. The ξ values plotted for the elements in figure 3 were obtained by use of uncorrected γ values [37]. The final set of ξ values in table 5 utilizes a set [38] of band theory predictions for χ_p^0. Cancellations of various enhancement factors do not occur. The resultant ξ values are therefore larger.

TABLE 5. *ξ values for Cu, Ag and Au using various available data for χ_p (see text for details).*

	Cu	Ag	Au
From $3/2(\chi_{exp} - \chi_{dia}^{core})$ Hartree-Fock core	.37	.50	.32
From $\chi_{exp} - \chi_{dia}^{core} - \chi_{dia}^{cond}$ Hartree-Fock core	.45	.45	.36
From $3/2(\chi_{exp} - \chi_{dia}^{core})$ Hartree-Fock-Slater core	.38	.52	.36
From $3/2\ (\chi_{exp} - \chi_{dia}^{core})$ traditional core	.45	.16	.08
From uncorrected electronic specific heat, γ	.53	.69	.42
From band calculations presented at this Symposium, χ_p^{bare} [38]	.57	.68	.56

It is instructive [39] to compare the value of χ_p^0 (obtained from γ) to the value of $\xi\chi_p$ obtained by dividing $\mathcal{K}$ by atomic H_{eff} values (tables 1 and 2). This is done in figure 4. The trend in our plot differs from that of Ziman [39] primarily due to our choice of atomic, rather than mass, units. The lightest alkali, Li, displays significantly less *s*-character than the other alkali metals [40-47]. The ξ values for the *B*-subgroup metals are all considerably lower, especially for the polyvalent elements; this might be expected, since the Fermi level lies higher in conduction bands, implying less *s*-character at E_F and hence a smaller contact term. The associated increase in *p*- and *d*-character will generally make a negative (core-polarization) contribution to $\mathcal{K}$, also lowering ξ.

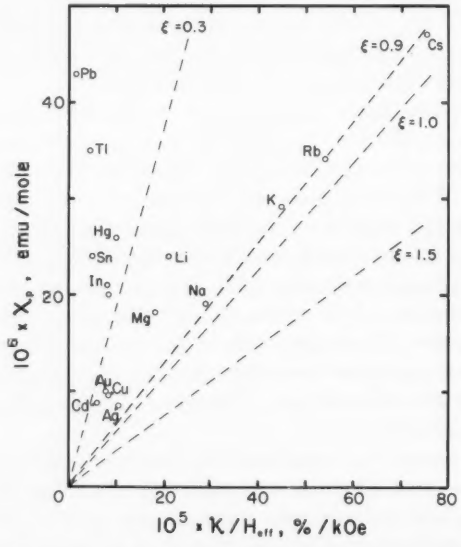

FIGURE 4. *χ_p versus $\mathcal{K}/H_{eff}$ for pure metals in customary units. Lines of constant ξ (dashed) are shown. Due to the small ξ values for the heavier metals most of the data points are bunched at the left hand side of the plot. The χ_p values were obtained from electronic specific heat data [37]. In the case of potassium a large uncertainty in the specific heat gives rise to an error of nearly half the size of the vertical dimension. The point shown for potassium represents the listed [37] γ value.*

We note an interesting correlation in figure 4 in that the alkali metals, except for Li, fall on a straight line near $\xi = 0.9$. That is to say, the *s*-density of states apparently increases proportionately to the total density of states at the Fermi level for Na, K, Rb and Cs. The

increase in χ_p from Na to Cs is attributable primarily to the large volume increase in this series. The constancy of ξ might seem to be surprising, since simple volume renormalization should effect ξ as well as χ_p. It is to be recalled, that volume renormalization of ξ depends on the atomic volume in the metal *relative* to that of the free ion. It would thus appear that the alkali metal lattice constants faithfully reflect the sizes of the free ions, and hence ξ is roughly constant implying that the amount of *s*-character is essentially constant for the alkali metals Na to Cs. This constancy was already noted by Pauling [47]. His calculations of *s-p* hybridization of bond orbitals indicated fractional *s*-characters of 0.72 to 0.74 for Na to Cs and a lower value (0.59) for Li, similar to the trend of figure 4.

Knight shift experiments on the pressure dependence, as well as alloying, show that the contact density in metals is not simply an inverse function of volume [7]. This is also illustrated by recent pressure dependence calculations [48] on monovalent metals. The wave function effects which depress ξ values below 1, suppress the dependence of ξ on volume.

In this section, we have seen the difficulty in obtaining a reliable value of χ_p for use in obtaining ξ values for simple metals. Nonetheless, even in these cases, the Knight shift provides a rather unique measure of the *s*-contribution to the density of states in "simple" metals.

4. "Simple" Metals

It is an interesting challenge to obtain the absolute value of the Knight shift, or its change with temperature or pressure, from band-theoretical calculations. A number of near *a priori* calculations have been made with varying degrees of semiquantitative success. For example, Das and coworkers, using the orthogonalized plane wave (OPW) method, have calculated wave functions and densities-of-state at various points on the Fermi surface for Al [49], Be [50-53] and In [54]. A few of these papers are of particular interest in that they represent efforts to use the weighted average form of $\langle a \rangle$ as given in eq (17). In the case of the divalent metals Be, Mg and Cd, the spin susceptibility has been extracted from Knight shift measurements by use of such estimates of $\langle a \rangle$ [55]. Comparison with theoretical values of their bare χ_p [*i.e.*, eq (2)] permitted estimates of the exchange enhancement to be made. This process resulted in a reduction in χ_p for Be; the authors concluded that this arose from inadequacies in the energy band estimate of χ_p^0 and $\langle a \rangle$.

The alkali metals, particularly Li and Na, have traditionally attracted theoretical attention, often giving relatively close agreement with experiment [40-42]. Even in these simplest "free electron" metals, corrections to the hyperfine coupling constant due to non-free electron-like band structure effects, can amount to 25 percent or more [45,56,57].

It should be stressed that for the heavier simple metals (*i.e.*, potassium and above) *d*-hybridization associated with *d*-bands above or below the conduction band affects the Knight shift and other properties at (and off) the Fermi level (see, for example, Kmetko [46]). In the case of Cu and Au these *d*-hybridization effects are large. Such effects do not arise in the Li row, but there may be abnormal "2*p*" effects due to the near degeneracy of atomic 2*s*- and 2*p*-levels [58-61]. In these "simple" metals, the change in Knight shift at the melting point [62] (fig. 2a) is usually not large, and its temperature dependence in the solid, slight (fig. 2b). As an example, consider Al. At the melting point, $\mathcal{K}$ has the same value for both liquid and solid. The temperature dependence in the solid is illustrated by the data of Feldman [63] (fig. 5). The change in Knight shift of Al is less than 2 percent of $\mathcal{K}$ over a temperature range from 4 to 300 K. The solid line in figure 5 represents a simple volume renormalization theory based on the thermal lattice expansion, which fits quite well at temperatures above the Debye temperature. No satisfactory explanation has been given for the deviation from this theory at low temperatures. Similar effects were observed in Na and Pb [63].

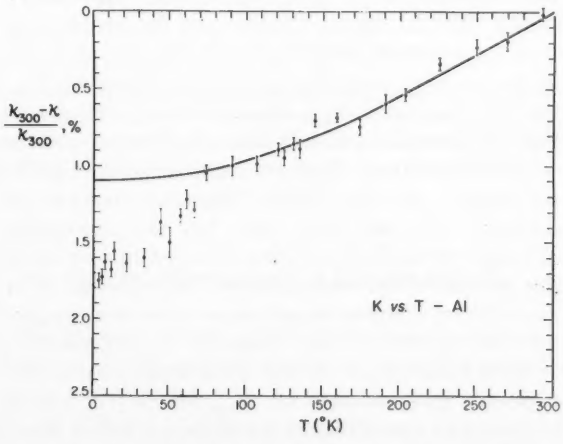

FIGURE 5. *Change in the aluminum Knight shift with temperature, as taken from Feldman [63]. The solid line is theoretical.*

A more unusual case is that of cadmium [64-70]. In the solid the Knight shift varies considerably. $\mathcal{K}$ increases ten times more rapidly in Cd than in Al, over the same temperature range (4-300 K). At 600 K, $\mathcal{K}$ in

Cd is about 70 percent larger than its value at 4 K. This change is seen in figure 6. An additional increase in $\mathcal{K}$ ($\sim 33\%$ of $\mathcal{K}$) is observed upon melting (see sec. 5). The anisotropic Knight shift, $\mathcal{K}_{anis}$, [see eq (13)] also increases with temperature. Cd exhibits a large change

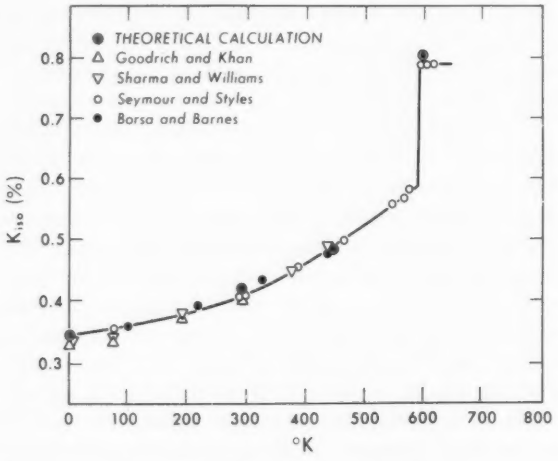

FIGURE 6. *Change in the cadmium Knight shift with temperature, as taken from Kasowski and Falicov [68].*

in the shape (c/a ratio) and volume of the unit cell with temperature and it had been suspected that the changes with temperature of $\mathcal{K}_{iso}$ and $\mathcal{K}_{anis}$ could somehow be correlated with these cell dimensions. Kasowski and Falicov [68] have explained the behavior with a different scheme: in the solid the lattice vibrations cause an increase in both χ_p and in the s-character as the temperature is raised, thereby increasing $\mathcal{K}_{iso}$. On the other hand, $\mathcal{K}_{anis}$ arises from the non-s part of the wave-function, which of course is decreasing as the s-part is increasing. However, again invoking eq (17), we require not the average hyperfine coupling associated with the non-s part, but the appropriate average over the Fermi surface. Cancellation occurs in this average at low temperatures. The reduction in the cancellation at higher temperatures more than compensates for the increase in s-character, thereby providing an increase in $\mathcal{K}_{anis}$. On the other hand, pressure dependence measurements of $\mathcal{K}_{anis}$ for Sn [71] was interpreted as due to charge redistribution rather than a change in the s-p character of the wave-function.

Other data further indicate the complexity of the behavior of the Knight shift in solid Cd. Borsa and Barnes [65] note that alloying Mg (in quantities of $\sim 1\%$) with Cd will cause substantial changes in cell size and shape without affecting the Knight shift. Kushida and Rimai [72] have separated the implicit and explicit contributions to the temperature dependence of $\mathcal{K}$ by their measurements of the pressure dependence in Cd. Volume renormalization was found inadequate to explain the observed pressure dependence [72].[5]

5. Sudden Changes in $\mathcal{K}$

The abrupt change in $\mathcal{K}$ of Cd upon melting was presumed by Ziman [39] to indicate an abrupt change in $N(E_F)$ associated with solid and liquid Cd. This conclusion was examined in two different calculations, each employing nonlocal pseudopotentials [68,70], resulting in opposite conclusions. Shaw's calculated [70] values for $N(E)$ per unit volume for solid and liquid Cd are shown in figure 7. $N(E_F)$ is found to be 0.7 percent *lower* in the liquid than in the solid. Shaw concludes that "Ziman's assertion that the strong change in the Knight shift of cadmium is a density-of-states effect is not borne out by our detailed calculations." In contrast Kasowski and Falicov [68] assume that Cd is free-electron-like in the liquid and finds that most of the change in $\mathcal{K}$(Cd) upon melting is due to an increase in $N(E_F)$. They note that "this agrees with Ziman's hypothesis and confirms it quantitatively." Although these two calculations [68,70] resulted in opposite conclusions, in part due to choice of different model-potentials, there is an abrupt increase in $N(E_F)$ in Shaw's calculations if solid Cd is compared with the free electron value, as indicated in figure 7.

An interesting example of an even more abrupt increase in $\mathcal{K}$ upon melting is found in the behavior of the III-V compound InSb [73]. In the semiconducting solid the Knight shift of either the In or Sb in InSb is zero, but in the metallic liquid state, the Knight shifts have normal metallic magnitudes. Another example is Bi [62], in which $\mathcal{K}$ has the opposite sign in the liquid from the solid.

There are various cases besides melting where a sudden change in $\mathcal{K}$ occurs. In an alloy system, $\mathcal{K}$ usually changes smoothly with composition within a particular phase, but shows a jump across a phase boundary. An example of this is shown for the AgCd system in figure 8, taken from Drain [74]. By correlating $\mathcal{K}$ and γ across a phase boundary, Drain showed that in this case the abrupt change is associated in part with changes in densities of states.

[5] There are other examples of an observation concerning the volume dependence of $\mathcal{K}$. As noted earlier, in our discussion of figure 4, simple volume renormalization is not often useful in explaining Knight shift results. See also [7] for a discussion of this point.

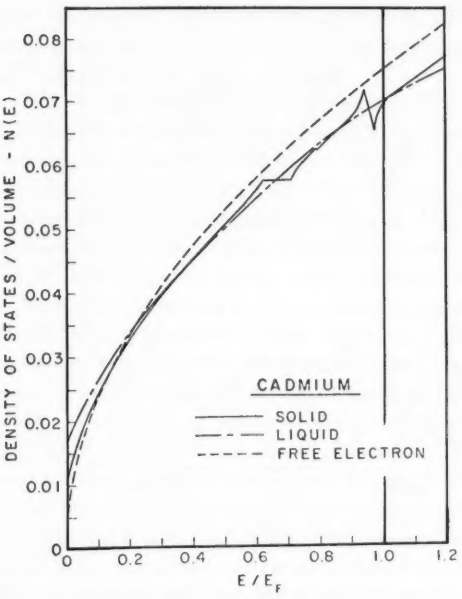

FIGURE 7. *Calculated values of* N(E) *for Cd, as taken from Shaw and Smith* [70].

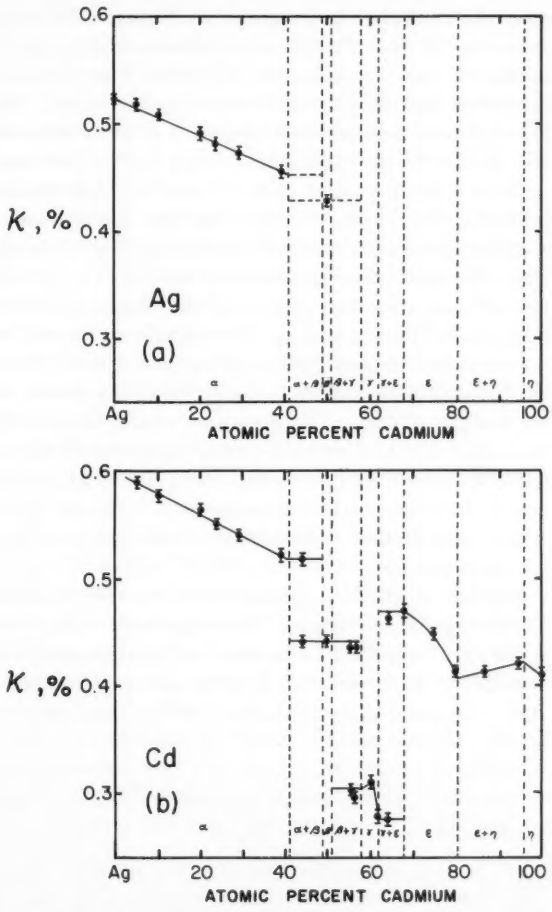

FIGURE 8. *Knight shifts in AgCd for (a) the Ag resonance and (b) the Cd resonance, as taken from Drain* [74]. *In the two phase regions, Cd resonances for both phases are simultaneously seen, due to the rather different $\mathcal{K}$'s for the different phases. For ranges of solid solubility $\mathcal{K}$ changes smoothly.*

The semiconductor-(or insulator-) to-metal transition, whether or not a Mott transition, offers a number of examples in which the Knight shift changes more or less suddenly. For example, when tin changes from its metallic to its semiconducting phase, $\mathcal{K}$ changes from 0.75 percent to near zero (see fig. 2b). Also consider VO_2 which is metallic above and semiconducting below a crystal structure change occurring at $T_c = 68$ °C [75,76]. The Knight shift is ~ -0.4 percent at 100 °C and $\sim +0.2$ percent below. The negative shift above T_c is attributed to a metallic d-band.

A case where there is an electronic transition without further structural changes is that of phosphorous-doped silicon [77-79]. At donor concentrations (n_d) greater than 2×10^{19} cm^{-3}, the material appears to be a metal, the Knight shift is proportional to $n_d^{1/3}$, and the Korringa relation holds. Below this critical concentration, $\mathcal{K}$ drops sharply. In the transition range, $3 \times 10^{18} < n_d < 2 \times 10^{19}$, there is a measurable $\mathcal{K}$, but the Korringa relation no longer holds. The electrons are "delocalized" in some type of impurity "band."

Other systems exhibiting nonmetal-to-metal transitions are the alkali-ammonia solutions. As the metal to ammonia ratio is increased, the liquid becomes gradually metallic, and the conductivity as well as the Knight shift increases substantially [80-83].

6. Orbital Magnetism in Simple Metals

The Bardeen, Cooper and Schrieffer theory of superconductivity [84] predicts that, as a result of spin pairing, χ_p vanishes at $T = 0$. Hence it was expected [85] that $\mathcal{K} \to 0$ as $T \to 0$ for superconductors. This expectation often is not borne out. It seems certain that the residual Knight shift is predominantly of orbital origin for transition metals such as V and Nb [22]. Ferrell [86] and Anderson [87] proposed that spin-reversal scattering due to spin-orbit coupling is another possible mechanism for obtaining a residual Knight shift. This mechanism requires that $\mathcal{K}$ be a function of mean free path, *i.e.*, particle size and impurity scattering. This

spin-orbit term has been shown by Wright [88] to be important in Sn. Wright also reviews earlier experiments on other metals. He concludes that although spin-orbit coupling is dominant in some cases, two types of orbital magnetism cannot be ruled out in simple metals. These are the Van Vleck orbital paramagnetism [18-22] and a higher order mechanism introduced by Appel [89]. Similar higher order mechanisms were discussed earlier by Clogston *et al.* [20]. We have already discussed the Van Vleck term and will note its importance in the transition metals and alloys to be discussed later. The Appel mechanism involves spin-orbit and $\vec{\ell}\cdot\vec{\mathbf{H}}$ coupling to an intermediate excited conduction electron state, which contributes to the Knight shift through the contact interaction. It is of the order of $\lambda/\Delta E$ times the contact Knight shift, where λ is the spin-orbit interaction energy, and ΔE is the energy between states connected by λ. The sign of the Appel contribution to the Knight shift may be either positive or negative.

Another important orbital effect is the Landau-Peierls diamagnetism [90]. The magnitude of this term is not easy to predict. In the simplest (and greatly oversimplified) free electron approximation the Knight shift, $\mathcal{K}_{dia}$ arising from Landau-Peierls diamagnetism, is

$$\mathcal{K}_{\text{dia}} = -\frac{8\pi}{3}\left(\frac{1}{3}\chi_p\right)\left\langle\frac{m}{m^*}\right\rangle^2, \qquad (22)$$

where m^* is an appropriate electron effective mass. This term has been proposed to explain a number of negative, or near zero, Knight shifts in nontransition metals. In transition metals, *d*-core polarization (see table 3) gives an important negative contribution to $\mathcal{K}$, through the Pauli paramagnetism of the *d*-band. In nontransition elements *p*-core polarization has often been proposed as an alternate to $\mathcal{K}_{\text{dia}}$ as a negative contribution to $\mathcal{K}$ (see table 3). For example Das and Sondheimer [90] first suggested the importance of the Landau term to the negative Knight shift in Be. In later papers, Das and coworkers [50-52] performed detailed calculations for the contact and the *p*-core polarization terms in this metal. A reluctance to believe that the diamagnetic shift is as large as was originally suggested [90] is evident from these papers [50-52]. Although they do not give further quantitative estimates for $\mathcal{K}_{\text{dia}}$ in this later work, in each case they are forced [52] to the same conclusion that the remaining negative shift is of diamagnetic origin. Using eq (22), available m^* values can, in fact, give a $\mathcal{K}_{\text{dia}}$ of -0.003% [52,53].

Yafet [91] considered the importance of $\mathcal{K}_{\text{dia}}$ for Bi, but Williams and Hewitt [92] proposed *p*-core polarization as the origin of the quite substantial negative Knight shift in Bi of -1.25%. It is interesting to note that if χ_p is estimated from the electronic specific heat [37], using eq (21), and if there is no *s* contact contribution to $\mathcal{K}$, the *p*-core polarization necessary to explain a shift of -1.25% is 800 times larger than the experimental value [93] for atomic Bi (table 3). The presence of an *s* term will increase this estimate of 800. Note that the experimental atomic "core" polarization term includes the polarization of the 6*s-valence* electrons which are part of the conduction bands in the metal. This atomic value therefore provides an estimate of the *s* polarization in the core *and* throughout the occupied conduction band: the applicability of this value to the metal depends on the distribution of *s*-character in the occupied bands (as compared with the free atom). Granted the uncertainty in χ_p and the question of relevance of the atomic hyperfine constant to this metal it would still appear that *p*-core polarization is at least one hundred times too small to account for the experimental Knight shift. On the other hand, Bi has m/m^* ratios which, using eq (22), are large enough to suggest a Landau diamagnetic shift that can approach magnitudes of the order of the observed $\mathcal{K}$ value.

Other examples of negative shifts in diamagnetic, non-*d* materials are Tl in NaTl [9,94-96] and In in BiIn at 77 K [97]. For these cases the situation is much less clear due to the lack of data for χ_p, m^*, and γ. In addition we do not have free atom experimental values for *p*-core polarization for Tl and In. Using some upper estimates for the unknown quantities, it is evident that either *p*-core polarization or Landau diamagnetism is hard pressed to reproduce the observed shifts. A discussion of diamagnetic Knight shifts and *p*-core polarization effects in these materials will be given elsewhere [98].

Das and Sondheimer [90] also indicated that oscillations would be present in the diamagnetic term. These would be periodic in $1/H$, similar to de Haas-van Alphen oscillations. However, when this effect was first observed by Reynolds *et al.* [99,100], the amplitude of the oscillations was considerably larger than that expected from the diamagnetic term [101-106]. Glasser [107] explained this by proposing that the Fermi surface wave functions also change with $1/H$, and that this introduces oscillations into the Pauli term which dominate over the diamagnetic oscillations. Goodrich *et al.* also observed Knight shift oscillations in Cd [108]. Their data are shown in figure 9.

The importance of observing oscillations in $\mathcal{K}$ is that it is possible to obtain the Knight shift over a segment of the Fermi surface. Thus the Knight shift has become

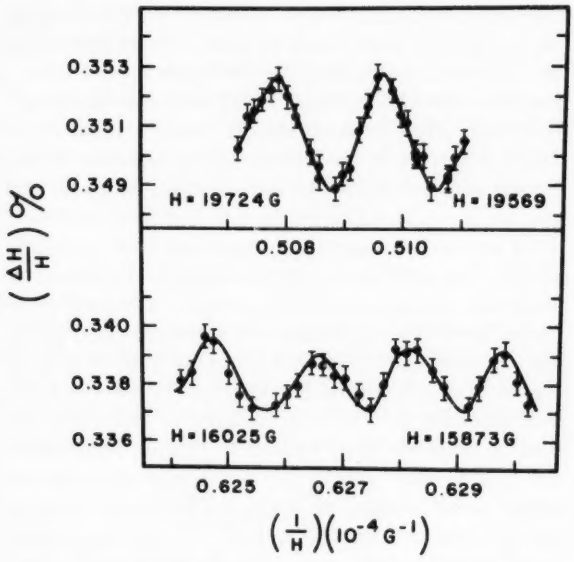

FIGURE 9. *Knight shift in Cd, illustrating oscillations in $\mathcal{K}$ with* 1/H, *as taken from Goodrich, Khan and Reynolds* [*108*].

a potentially important tool for examining the wavefunction character associated with $N(E_F)$ not only in the average sense of eq (19), but also in finer detail over Fermi surface segments.

7. Transition Metals

The simple metals considered in the preceding sections display, in the main, only weak orbital Knight shifts and temperature independent, usually positive, Pauli terms. Transition and noble metals with their *d*-bands tend to have a negative Pauli term arising from *d*-core polarization (see table 3). Narrow *d*-bands, with many states close in energy to E_F, often have substantial orbital effects [see eq (15)]. Structure and curvature in $N(E_F)$ contribute a temperature dependence to the Pauli term. Given the presence of *d*- and non-*d*, or "conduction" band character, it has been normal to describe the paramagnetic transition metals in terms of a "two band" model involving discrete "*s*" and "*d*" bands. We follow common nomenclature in designating the conduction band as an *s*-band. (The *d*-bands, of course, also contribute to conduction.) The orbital Knight shift is associated with the *d*-band; the average taken in the Pauli term is rewritten

$$\langle a\rangle\chi_p = \langle a_s\rangle\chi_p^s + \langle a_d\rangle\chi_p^d(T), \qquad (23)$$

where the "*s*" or conduction band is assumed to contribute a positive, temperature independent term, and the *d*-bands, a negative temperature dependent term. The latter dominates since $N(E_F)^d$, hence χ_p^d, is much larger than its *s*-band counterpart. It is assumed in eq (23) that the temperature dependence of $\mathcal{K}$ is entirely associated with the susceptibility and not with any variation in the hyperfine coupling constants [13]. The fact that the slope, $d\mathcal{K}/d\chi$, is a constant for these metals offers some experimental justification for this assumption. An example of this is seen [109] in figure 10, where $\mathcal{K}$ is plotted versus χ_{tot}, with temperature the implicit variable, for Pd. In this case $\chi(T)$ goes through an extremum with increasing T, but is faithfully tracked by $\mathcal{K}(T)$. Pd displays the largest temperature variation in χ among the paramagnetic metallic elements. As is discussed in Mott and Jones [110], such a temperature dependence arises from sampling by the Fermi function of structure and curvature in the density of states in the vicinity of E_F.

While the two band model has proven most useful when discussing Knight shifts and other experimental data, there is, in fact, strong hybridization of *s*- and *d*-band character and a transition metal is not constituted of discrete *d* and "*s*" bands. Some measure of this is given in figure 11, which displays the density of states obtained[6] for fcc Cu.

The results can be taken as characteristic of all transition metals. The density of states behavior is similar to that reported by Mueller for Fe [115], and to that obtained by Goodings and Harris [116], and by Cuthill *et al.* [117] in their estimates of soft x-ray spectra for Cu. The density of states has been plotted separately for the first, second and sixth bands while that for the third, fourth and fifth has been added together for the sake of legibility. In figure 11, the Cu Fermi energy is designated by E_F and that appropriate to Ni by E(Ni). The high density of states peak, intersected by E(Ni), is due to the fifth band. Details of this band and of its Fermi surface are essential to the differ-

[6] These results [111] involve a sampling of $\sim 1.5\times10^6$ points in 1/48th of the Brillouin zone. The sampling employed a quadratic fit to a set of pseudopotential bands by Ehrenreich *et al.* [112, 113] involving a mesh of 28 intervals from Γ-X in the zone. The pseudopotential bands were obtained from an adjusted analytic fit of some new APW calculations for Cu [114]. Spin-orbit coupling effects, though slight, have been included. The Fermi surface is in better agreement with experiment than is usual for calculations. Details of the density of states and grosser features of the wavefunction analysis are, of course, dependent on the use of a pseudopotential band description (which assumes tight binding *d*-bands and a set of four orthogonalized plane waves for the non-*d* part). These results can be considered analogous to the OPW results, obtained by Das and coworkers [49-52, 55] for the Knight shift in various "simple" metals.

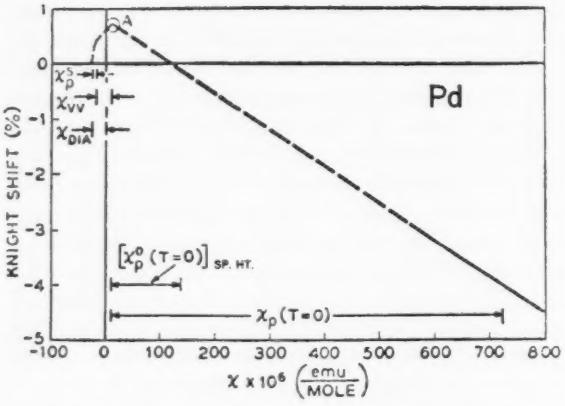

FIGURE 10. *$\mathcal{K}$(T) versus χ(T) plot for Pd, as taken from Seitchik, Gossard and Jaccarino [109].*

ing magnetic behavior of Ni, Pd, and Pt. The Cu Fermi level intersects the sixth band, often named the "free electron" band, which lies above the five "*d*" bands.

The density of states associated with non-*d* electron character; $N(E)_{\text{non-}d}$, is also shown in figure 11. It must be emphasized that details of these results depend on the scheme used to describe the bands (in this case a pseudopotential description [111] with tight binding *d*-functions). Hybridization effects cause a build up of non-*d* character at the bottom and a depletion in the middle and just above the bulk of the *d*-bands (*i.e.*, in the range $-0.35 \leq E \leq -0.15$ Ry). The peak seen at ~ -0.4 Ry can be important to optical and soft x-ray properties. The sixth band is predominantly of *d*-character at the bottom and remains almost thirty percent *d* at the Fermi level. This particular set of results [111] yields 9.8 electrons worth of *d*-character out of a total of eleven electrons, in the bands below E_F. [A free electron parabola, holding the remaining 1.2 electrons, and with an effective mass chosen so that its Fermi level matches E_F, has been drawn for comparison with the actual non-*d* density of states.] The lowest band is strongly free-electron like up to $E \sim -0.45$ Ry and 0.61 of the two electrons residing in the band are of non-*d* character. Roughly 0.35 of the remaining 0.6 non-*d*-

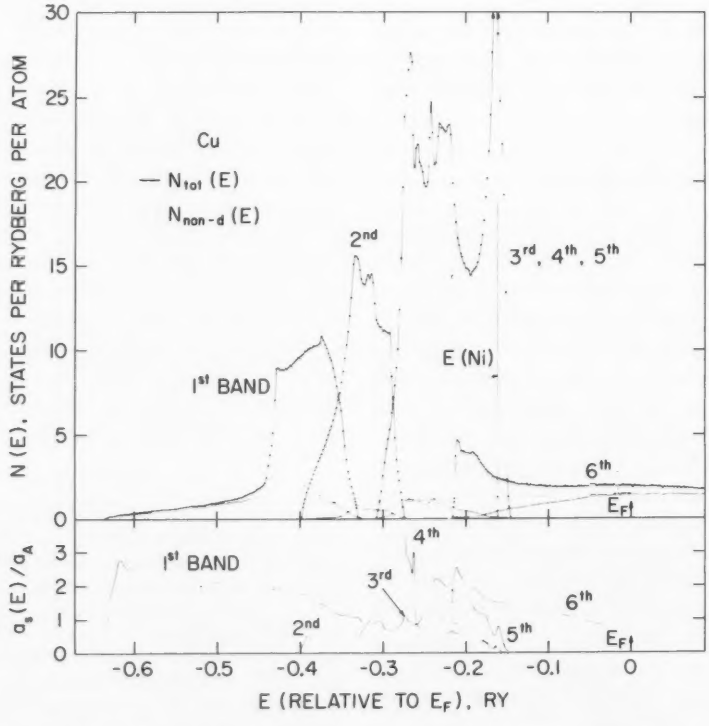

FIGURE 11. *(a) Total density of states and non-d density of states for the 1st, 2nd and 6th bands of Cu separately, and for the 3rd, 4th and 5th summed. The smooth, flat band is the free electron parabola containing 1.21 "conduction" electrons, as discussed in the text. This is shown for comparison with the $N_{\text{non-}d}(E)$ results. (b) Ratio of band to atomic hyperfine constants as defined by eqs (24a) and (24b).*

electron character is associated with the one electron in the sixth band.

The 3*d*-electron character can be expected to interact with the nucleus via a core polarization term of ~ -125 kOe per μ_B throughout the bands. The non-*d* character is expected to interact predominantly via the direct contact term. Its behavior is shown at the bottom of figure 11 in the form of the ratio

$$\frac{a_s(E)}{a_A} \equiv \frac{\langle a(E) N_{\mathrm{TOT}}(E) \rangle}{a_A N_{\text{non-}d}(E)} \tag{24a}$$

with respect to the non-*d* electron density of states at E, *i.e.*, the contact interaction normalized with respect to the non-*d* electron density at E, and to an atomic 4*s* hyperfine constant.[7] Omitting all core polarization contributions to $\mathcal{K}$, this ratio is then related to ξ by

$$\frac{a_s(E)}{a_A} = \xi(E) \frac{N_{\mathrm{TOT}}(E)}{N_{\text{non-}d}(E)}. \tag{24b}$$

A ratio of 2 to 2.5 occurs at the bottom of the bands reflecting the volume normalization enhancement of ξ discussed previously in connection with figure 4. Values closer to one are appropriate to the non-*d* character hybridized into the second, third, fourth and top of the first bands. This suggests that an $a_s(E)$ set equal to a_A can be used as a first approximation when estimating the effect of hybridization on reducing a *d*-band a_d from a pure *d*-core polarization value. The ratio is higher in the fifth band but here hybridization is almost zero. The ratio tends to fall with increasing E, as is seen in the lower part of the first and in the sixth bands. This is associated with the decrease in *s*-character in OPW's of increasing $\mathbf{k}$. The ratio has dropped to a value of 0.78 at the Cu Fermi level. Here $\xi(E_F)$, defined in the manner of eq (24b), has the value of 0.57. If one adds the negative core-polarization contribution which can be attributed to the twenty-eight percent *d*-character in the bands at E_F, $\xi(E_F)$ becomes 0.55.

The above $\xi(E_F)$ values agree with the upper end of the range estimated as the experimental ξ for Cu in table 5. Davis [118] has obtained[8] $\xi(E_F) = 0.67$ employing the method of Korringa-Kohn-Rostoker. Comparison with the experimental data may not be meaningful because core polarization terms, arising from "conduction band" spin character, have been omitted in the $\xi(E_F)$ estimates while being present in the quantities of tables 2 and 5. It is thus proper to make the comparison only if core polarization affects the numerator and denominator so as to leave the ratio constant. This seems unlikely since *s and p* character terms will contribute to the conduction electron core polarization.

These two band calculations yield $N(E_F)$ values which are in good numerical agreement with the electronic specific heat for Cu. Both calculations suggest that *d*-hybridization is a significant factor in reducing ξ. This is one reason for the tendency noted earlier for Ag to have a larger ξ than Cu or Au. The *d* bands are twice as far below E_F in Ag, and weaker *d* hybridization ($\sim 10\%$) occurs at the Fermi level of Ag.

Noting that the atomic *s*-contact interaction is typically ten times larger than, and opposite in sign to, *d*-core polarization, figure 11 suggests that hybridization is important throughout the transition metals. Consider the case of Ni. The Fermi level intersects the high peak of the fifth band. This band has almost no hybridization, as is shown in figure 11, which was obtained with Cu bands. The sixth band has an $N(E_F)$ value which is better than an order of magnitude smaller than the fifth band at E(Ni). However the sixth band has twenty percent *s*-admixture at E(Ni) causing a large, positive a_d, which compensates for this. Neglecting exchange enhancement of the susceptibility, the sixth band contribution can then cancel approximately one third of the Knight shift term, a_d, associated with the fifth band alone. Exchange enhancement is important and an estimate of the exact role of the sixth band requires opinions of interband exchange effects. Scanning the lower energy parts of the plot, it appears that hybridization may affect the a_d values for the lighter transition metals more severely. This hybridization trend should hold although changes occur in the crystal structures.

Despite the complexities just discussed, the two band model of the Knight shift has frequently proven fruitful, with hybridization absorbed in the a_d term. The various Knight shift contributions are normally disentangled in two ways. First, comparisons can be made between the relaxation time, T_1, and Knight shift results which weight the various terms differently. The Korringa relation [27] provides a test for the *s*-contact contribution. Secondly, one can employ the graphical technique of figure 10. This scheme, applied to Pt [20]

[7] An a_A of 1600 kOe/μ_B, omitting core polarization contributions, was used, since core polarization effects were omitted in the evaluation of $\langle a(E) N_{TOT}(E) \rangle$. With core polarization, correlation and relativistic effects present, the (experimental) a_A is ~ 2600 kOe/μ_B. For discussion of this see [7].

[8] Actually Davis [118] chose to quote a ξ-ratio by dividing his computed hyperfine term *without* core polarization by an atomic a_A *with* core polarization. This yields a smaller numerical value than we quote here.

appears in figure 12. The experimental data are plotted for $\mathcal{K}$ versus χ_{tot} with temperature the implicit parameter and, following eq (23), it is assumed that

$$\chi_{tot} = \chi_{dia} + \chi_{orb} + \chi_s^\beta + \chi_p^\beta \tag{25a}$$

and

$$\mathcal{K} = \langle b \rangle \chi_{orb} + \langle a_s \rangle \chi_s^\beta + \langle a_d \rangle \chi_p^\beta(T). \tag{25b}$$

The slope of the experimental data yields an empirical value for $\langle a_d \rangle$. The diamagnetic susceptibility is estimated and subtracted out, shifting the origin of the plot to point A. An estimate is then made of $\chi_p{}^s$ (usually with the free electron approximation) and of a_s and the s-band contributions are subtracted out shifting the origin, with respect to orbital and d-band Pauli terms, to point B. Finally, $\langle b \rangle$ is estimated, defining the slope of $\mathcal{K}_{orb}$ versus the χ_{orb} line, which is drawn until it intercepts the experimental $\mathcal{K}$ versus χ_{tot} curve (at point C). The intercept defines the relative roles of orbital and d-band Pauli terms. In this case, the d-band Pauli term dominates.

A value for the *unenhanced* $\chi_p{}^0$, estimated from specific heat data is shown in figure 12. The larger value, deduced from the Knight shift, provides a measure of the effect of exchange enhancement. While quantitative results depend on the detailed choice of χ_{dia}, $\chi_p{}^s$, $\langle a_s \rangle$ and $\langle b \rangle$, the qualitative conclusion does not. Changing the hyperfine constants by reasonable amounts or omitting the s band term altogether does not change the basic result. Analyses which compare T_1 and $\mathcal{K}$ data also rely on estimates of hyperfine constants. Results indicate that the d-band term also dominates in Pd (see fig. 10) and Rh [119]. Note that figures 10 and 12 indicate a greater exchange enhancement in Pd (5 to 6) than in Pt (~ 2). The enhancement in Pt is as expected, whereas the factor of 5 to 6 for Pd is somewhat smaller than is currently fashionable to believe. The orbital term dominates in V [19,20,22], Cr-rich Cr-V alloys [24], W [21] and Nb [22]. This is not surprising since these metals have roughly half-filled d-bands, encouraging orbital effects, whereas Pt, Pd, and Rh have almost filled d-bands. Equation (16) predicts the difference in magnitude of ortibal effects for these two groups of metals to within the uncertainty in the appropriate band occupation (n) factors appearing in that equation.

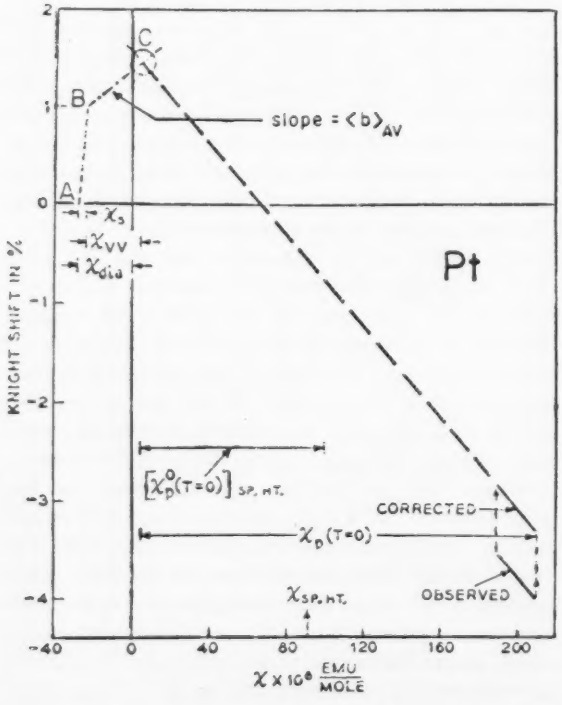

FIGURE 12. $\mathcal{K}$(T) *versus* χ(T) *for Pt, as taken from Clogston, Jaccarino and Yafet* [20].

The slopes of the $\mathcal{K}$ versus χ plots for Pd, Rh and Pt yield a_d values of -345, -162 and -1180 kOe/μ_B respectively. The Pd result is in good agreement with the 4d-core polarization value quoted in table 3 while that for Rh is half that value. It is believed [10] that core polarization is almost constant across the 4d-row, implying that the variation in a_d arises from other sources. Two suggest themselves. First, different amounts of s character may be hybridized into the d bands at the Fermi surface: increased s-d hybridization in Rh would produce a less negative a_d. Figure 11 suggests that there is a distinct probability that this occurs. Secondly, there may be different *intersite* contributions to a_d. The Pauli term spin density induced on neighboring sites will, after all, make some contribution to the hyperfine coupling constants. These two contributions are expected to be present in Pt as well, and may contribute to the fact that the experimental a_d is not in numerical agreement with table 3. (Some uncertainty must be attached to the theoretical estimate quoted there.)

Intersite effects, s-hybridization and d-core polarization cannot be separated by inspection of a_d for a pure metal alone, but some insight can be gained by studying alloys. NMR results have been obtained for Cu in the Cu-Pd system [120] and Ag in AgPd [121]. The data for dilute Cu or Ag in Pd suggest that these atoms go in the lattice with filled d shells and with relatively little perturbation on the surrounding Pd matrix. Negative solute Knight shifts are obtained, in contrast with the positive ones appropriate to pure Cu and Ag. Using Ag

site T_1 data to estimate an $a_s\chi_p^s$ term, Narath obtained [121] an intersite hyperfine field of -140 kOe/μ_B for dilute Ag in Pd. (The susceptibility is essentially that of the host, measured in μ_B units.) He noted that this term is approximately twice the value obtained for dilute Cu in Pd, *i.e.*, that

$$\mathcal{H}^{\text{solute}}_{\text{intersite}} \propto \chi_p^{\text{host}}\, a_{\text{solute}} \tag{26}$$

where a_{solute} is the atomic valence *s*-electron hyperfine coupling constant appropriate to the solute (see table 4). Now the intersite term sampled by Pd in Pd can be quite different from that sampled by either Ag or Cu which are charge impurities but the above results suggest that approximately one third of the a_d value in Pd arises from intersite effects and that the numerical agreement with the 4*d* core polarization value was fortuitous. The presence of an intersite contribution of between -100 and -150 kOe/μ_B then implies an equal but positive contribution from *s* hybridization, or from polarization of the paired *s* character in the occupied conduction bands (*e.g.*, see sec. 2). A two or three percent admixture of *s* character in the *d* bands at E_F would produce such an effect (see table 4). The variation in a_d between Pd and Rh is within the realm of reasonable change in hybridization, though intersite effects can be expected to vary.

Negative shifts of the Cu resonance are also observed [122] for dilute Cu in Pt. Inspection of the results is again troubled by the question of perturbations on the host lattice (which are thought to be slight) and second order quadrupole shifts (which are estimated). The result is [122] an intersite term of somewhat less than -100 kOe/μ_B in agreement with Cu-Pd. There also exist results for the Pt Knight shift in Cu-Pt[122] and Au-Pt[123] alloys. A similar tendency, of negative shifts in pure Pt and positive shifts in the noble metal-rich alloys, arises. This is in qualitative agreement with the above observations concerning a negative intersite term in Pt. Questions concerning the perturbation on the solvent's local susceptibility, due to the presence of an atom such as Pt (or Pd) in a noble metal, makes quantitative estimates of an intersite hyperfine constant from the dilute Pt data less plausible.

Experience with solute hyperfine fields [124,125] for impurities in Fe, Co and Ni, and the above observations for noble metal alloys, suggest that substantial intersite effects arise in the heavy 3*d*, 4*d* and 5*d* metals. These are expected to be of the order of -100 kOe/μ_B (the moment being that characteristic of the solvent susceptibility). There is some suggestion of weaker intersite effects in the lighter elements of the various transition metal rows. The changes in crystal structure from fcc to bcc, and the associated decrease in the number of nearest neighbors to any one site may be a factor contributing to this.

8. Alloys and Local Effects

The introduction of a foreign atom in a pure metal has several effects. First, if the atom has a different number of valence electrons than the host, its insertion will change the number of conduction electrons per atom (the e/a ratio) in the metal. Neglecting other effects of the insertion, this acts to shift the Fermi level in the bands. The bands will, of course, be perturbed by the addition of impurities. If the perturbation is gradual, and relatively weak, it is often useful to scan alloy data as if the Fermi level shifts (as a function of e/a) over a set of "rigid" bands. This is a rigid band picture which may (or may not) bear some resemblance to the host metal conduction bands off their Fermi energy [126], but this picture properly describes the alloy system at E_F. Such a rigid band scheme has little or no relevance to some alloy systems (*e.g.*, Cu-Pd) while displaying striking trends between alloys of common e/a (*e.g.*, $Cr_{1-x}V_x$ versus $TiFe_yCo_{1-y}$) elsewhere. Some examples will be considered in the next section.

Any impurity in a metal will produce a charge disturbance. Atomic size and electronegativity effects cause this to be true, to a limited extent, even in the case when the valence of the host and that of the impurity is identical. The conduction electrons act to screen the charge difference associated with the impurity as is indicated schematically in figure 13. There will be a build up (as in fig. 13) or dilation in the total conduction electron charge in the vicinity of the impurity, depending on the sign of the difference[9]. There is a highly local "main peak" with the familiar Friedel oscillations to the outside. These arise from the presence of a conduction electron Fermi surface and have a period which is inversely proportional to $2k_F$, *i.e.*, the extremal caliper of the Fermi surface in the direction in question [127].

[9] The conduction electron distribution is distorted by the Coulomb perturbation in a very similar manner to the core polarization effects discussed earlier, the latter case being an exchange polarization and the spin difference resulting from it, the present case involving the sum of charge terms. Both may be viewed as involving the admixture of excited orbital character into the originally unperturbed occupied one-electron states.

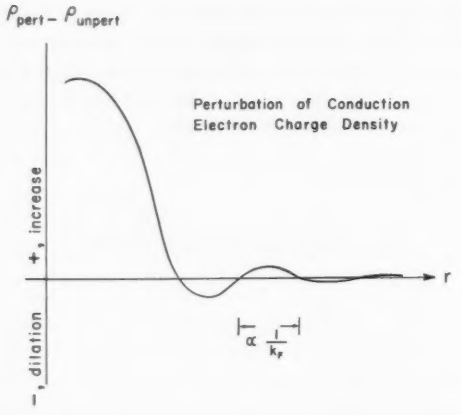

FIGURE 13. *Schematic illustration of conduction electron charge screening induced in a metal host by a single impurity at* R=0. *The half-period of the Friedel oscillations, which is proportional to* $1/k_F$, *is indicated.*

Solvent atoms can make various differently weighted samplings of this charge distribution, for example, by quadrupole interactions [128-133] and by isomer shifts.

The presence of an impurity also affects the solvent Knight shift. Only the perturbation of the Fermi surface electrons is important here, as it is these electrons which are involved in the Pauli term. The Fermi surface electrons undergo a redistribution [127,134] which is similar to the total charge screening in character and which can be sampled as a distribution through their $\langle a \rangle$ values appropriate to the different solvent sites in the lattice. This, and the bulk charge disturbance, are usually described in terms of free electron or simple OPW bands employing pseudopotential or phase shift scattering analyses of the perturbation. Due to the complex nature of the problem, neither scheme usually supplied quantitatively satisfying *a priori* predictions of experiment and, in the few cases where they have, there arise questions of the uniqueness of the result. In terms of the phase shift analysis, the change in Knight shift at a nucleus some distance R from the impurity is given [134] by

$$\frac{1}{\mathcal{K}}\frac{\Delta\mathcal{K}(R)}{\Delta c} = \sum_{\ell} \{\alpha_{\ell}(R) \sin^2 \eta_{\ell} + \beta_{\ell}(R) \sin 2\eta_{\ell}\}, \quad (27)$$

where

$$\alpha_{\ell}(R) \equiv (2\ell+1) \sum_{R} \{n_{\ell}^2(k_F R) - j_{\ell}^2(k_F R)\}, \quad (28)$$

and

$$\beta_{\ell}(R) \equiv -(2\ell+1) \sum_{R} j_{\ell}(k_F R) n_{\ell}(k_F R). \quad (29)$$

The ℓ^{th} term in the sum is associated with the ℓ^{th} partial wave, η_{ℓ} is the phase shift of the ℓ^{th} component, and j_{ℓ} and n_{ℓ} are spherical Bessel and Neumann functions respectively. To obtain the effect on a solvent metal Knight shift, the α_{ℓ} and β_{ℓ} must be suitably averaged over R. For "simple" solvent metals and "simple" solutes the effect is presumed to be dominated by s- and p-wave scattering. Changes in the relative roles of s- and p-wave scattering are important in rationalizing the variation in $\Delta\mathcal{K}/\mathcal{K}$ with varying valence of the solvent, or varying valence of a solute, relative to the solvent.

There is traditionally some question of how large an effect can be associated with pure s-screening. From a strictly atomic viewpoint, one might expect it to be limited to two electrons worth of charge. The recent investigations of Slichter *et al.* [135,136] conclude that higher ℓ scattering is very important to the screening when solute-solvent valence differences exceed two.

A local spin moment will produce a spin disturbance similar to that seen in figure 13. Such a spin disturbance is obviously important to magnetically ordered metals[10] but it also produces the dominant Knight shift term at some sites in certain paramagnetic alloys (see sec. 12). Consider the Knight shift of a nonmagnetic site in a paramagnetic rare-earth alloy. The principal term in the Pauli susceptibility, *i.e.*, in the spin induced by the magnetic field, is that of the open $4f$-shells, and this spin will contribute to the nonmagnetic site $\langle a \rangle$ behavior via conduction electron polarization. The susceptibility associated with the moment would obey a Curie-Weiss law. Examples of this are the above mentioned rare earths with their open $4f$-shells, and $3d$ alloys, such as Fe in Cu. Sometimes the moment may arise from band-paramagnetism involving localized d levels which are too weakly coupled by *intra-atomic* exchange to produce a true local paramagnetic moment. Curie-Weiss behavior is then not followed. The $3d$ elements as impurities in Ag, or dilute Ni in Cu are examples of such band paramagnetism.

Given an induced local spin monent of either of the above types, there will inevitably be a spin disturbance in the solvent conduction bands producing, in turn, a Knight shift term. There will be a variety of contributions to this. First, and most obviously, the exchange field due to the local moment will produce a spin dependent scattering of conduction electrons. As described

[10] We should note that in a magnetically aligned metal, cross terms will cause a magnetic imputiry to contribute a charge disturbance, and a charge impurity to contribute a magnetic disturbance (the charge impurity Knight shift contribution can be considered a special example of this).

by Ruderman, Kittel, Kasuya and Yosida (RKKY) [137-141], the Pauli response of the conduction electrons to the diagonal exchange term, $\mathcal{J}(k_F,k_F)$, contributes a net spin density which is then piled up in a screening distribution of the sort plotted in figure 13. Formally the theory is almost identical to the charge screening case. Exchange, rather than electrostatic Coulomb, terms are responsible for the disturbance, and details of the shape of the main peak and of the behavior of the phase and amplitude (relative to the main peak) of the Friedel oscillations should differ from the charge scattering distribution. The $\ell = 0$ and 1 partial waves will again tend to predominate. Details [141] of the intra-atomic term in the electrostatic exchange, $\mathcal{J}_{el}$, are such that if the local moment is of odd (or even) ℓ character, partial wave scattering of odd (or even) ℓ' is enhanced (*i.e.*, *s*-wave scattering is of increased importance with *d*-moments present while *p*-wave effects are amplified in 4*f*-moment scattering). Only *s*-wave spin density is nonzero at the solute's nucleus. In the scattering picture, it describes the intra-atomic conduction electron exchange polarization term discussed in section 2.

If the value of electrostatic exchange were somehow zero, the presence of a local spin moment would still cause a spin disturbance in the conduction bands [142-144]. Resonant scattering of spin-up and spin-down conduction electrons will occur at different energies as the result of the splitting of the local virtual (or real) bound state to form the local magnetic moment. One reason the scattering differs is the different occupation of spin up and spin down orbitals on the local moment site. Consider some partial wave component, with quantum members ℓ and m_ℓ of a scattered conduction electron at the local moment site. If the local moment had an occupied component of the same ℓ, m_ℓ and spin, the conduction electron component would be unaffected (except for any nonorthogonality effects which might arise); if there were a hole in that local moment orbital component, the orbital could be admixed into the conduction electron function to the extent it is energetically favorable. The existence of a net spin residing in the local moment implies a difference in hybridization (and orthogonalization) effects in conduction electron states of the same **k** and differing spin. This results in a spin density distribution similar to the core polarization effects discussed earlier. There is no net spin in the disturbance; instead there are regions of spin parallel and antiparallel to the local moment. In their original inspection of such hybridization effects, Anderson and Clogston concluded [142] that this disturbance would fall off as $1/r^4$; subsequent numerical estimates of their model [145] are consistent with this observation. It would seem that the effect is largely concentrated at the local moment site. An *effective* exchange interaction arises when the next order in hybridization effects is taken [142,143]. Consider the energy shift of a Fermi surface electron. The mixing of local moment *hole* components into the wave function will lower the state's energy whereas orthogonality with occupied components can only raise its energy. Hybridization thus stabilizes the energy of Bloch states with spin moment antiparallel to the local moment whereas those with spin moment parallel are less favored since they undergo orthogonalization and *decreased* hybridization. This produces [142-144] a *negative* interband exchange constant $\mathcal{J}_{ib}(k_F,k_F)$ in contrast with $\mathcal{J}_{el}(k_F,k_F)$ which is always positive.[11] A negative value implies a conduction electron Pauli spin density term of spin moment antiparallel to the local moment. Such situations occur experimentally, implying that "interband" hybridization (and higher order effects) do, on occasion, predominate over electrostatic exchange, which can only produce a net spin moment parallel to the local moments. (These effects are obviously intimately related to the Kondo effect.) The earliest evidence for negative exchange constants was obtained by nuclear magnetic resonance and electron paramagnetic resonance measurements for rare earths in several host metals [146-149] such as Pd. This has subsequently been borne out by magnetization and neutron diffraction studies.

Interband hybridization exchange also differs from electrostatic exchange in that hybridization will only be strong between band and local moment components of common ℓ. The summing over individual Bloch state contributions to the spin disturbance yields partial wave scattering only from those same ℓ components directly involved in the mixing. Thus, unlike electrostatic exchange, hybridization effects with their predominant *d*- or *f*-scattering, will not contribute an $\ell = 0$ contact spin density term to the hyperfine field at the scattering site, unless higher order (*i.e.*, double, triple, *etc.*) scattering processes are significant.

A disturbance of the type plotted in figure 13 produces a distribution in solvent site $\langle a \rangle$'s causing a broadening of the solvent Knight shift line. The distribution in $\langle a \rangle$ will not necessarily provide a detailed, accurate mapping of the bulk conduction electron disturbance. This is due to interference effects arising from orthogonalization of the conduction electron wave functions with the solvent site ion cores which are

[11] Schrieffer and Wolff [143] have explored the circumstances for which $\mathcal{J}_{ib}$ can be properly defined.

383-876 O - 70 - 9

penetrated. This interference is important in that it affects the apparent shape of the disturbance at sites near the impurity, while providing little more than scaling to the result for sites at asymptotically large R.

The sampling of the disturbance will inevitably cause the average solvent site $\langle a \rangle$ to increase or decrease with respect to the pure solvent value, thus causing a shift $\delta\mathcal{K}$, of the resonance line. Some sites will have values of $\langle a \rangle$ so different from the average that they will not contribute to the main resonance line, but satellites outside instead. This will cause a decrease in line intensity, *i.e.*, wipe-out, upon alloying. Blandin and Daniel's estimate [134] of one such distribution in $\langle a \rangle$ is seen in figure 14. The theoretical estimate is drawn to the same scale as an experimental [150] NMR derivative in Ag containing a small quantity of Sn. The

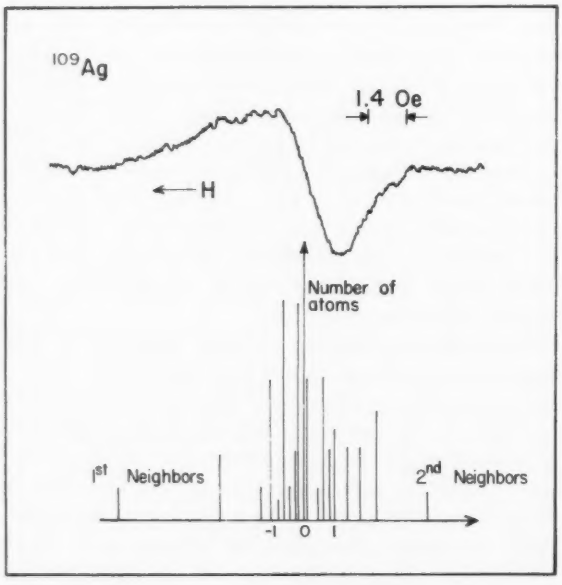

FIGURE 14. *(Above). Rowland's experimental [150] NMR absorption derivative curve in an alloy with 1 percent Sn in Ag. (Below). Blandin and Daniel's calculated [134] positions and relative contributions to silver Knight shifts at silver sites in near neighbor, next near neighbor, etc. . . positions with repsect to an Sn impurity in Ag. This is plotted on the same horizontal scale as the experimental curve.*

near and next near neighbor $\langle a \rangle$'s in Ag(Sn) may well be responsible for the partially resolved satellites. Another experimental example [151] of satellite structure is shown in figure 15 for Pt containing small quantities of Mo. Here three satellites are clearly resolved.

Details of the effect of alloying will depend on such

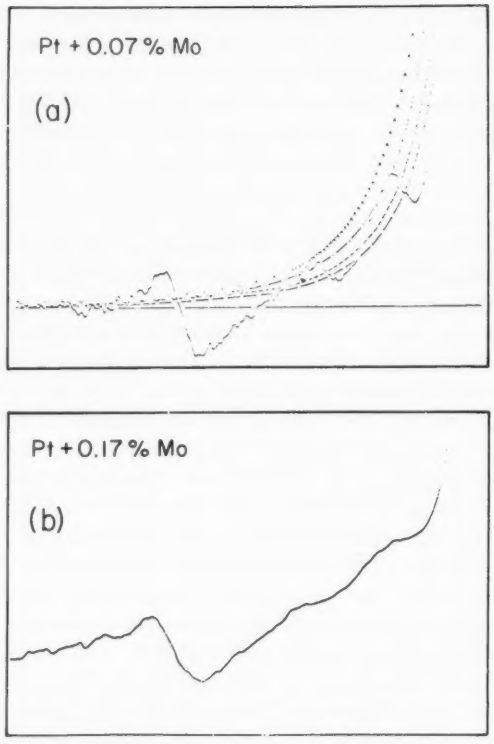

FIGURE 15. *Experimental NMR absorption derivative curve in Pt-Mo alloys as taken from Weisman and Knight [151]. The resonance in (a) shows several distinct satellites and that in (b) shows satellites in the same positions but those near the central resonance begin to merge with the central line, thus causing resonance broadening for increased alloy concentrations.*

factors as whether or not the main peak of the disturbance extends out and encompasses any neighboring nuclear sites. Little is known experimentally, and less from accurate calculation, concerning main peak behavior. (Most theoretical work makes the doubtful, but computationally necessary, use of asymptotic estimates for the entire disturbance.) It is generally thought that the main peak of the Coulomb screening is largely localized at the impurity site while the spin density peak is of longer range. For Fe in Pd the latter is known to cover many lattice sites. This is due to a large $1/2k_F$ value (which affects the main peak as well as the Friedel oscillations) and to the substantial conduction-electron conduction-electron enhancement of χ_p [152-154].

It has been seen that solvent data are largely limited to shifts of the main resonance line and this does not provide a unique test for any given detailed model of

alloy effects. Although such experiments are difficult, further observations of solvent satellite resonances in very dilute alloys would be invaluable for this purpose. Satellite lines would arise from near neighbor region $\langle a \rangle$'s and, providing they can be disentangled, would provide a severe test for any theory.

The interpretation of the alloy Knight shift data depends somewhat on the nature of the material in question. The change of $\mathcal{K}$, $\Delta\mathcal{K}$, upon introducing a second component into a metal, will cause a change in $\langle a \rangle \chi_p$. Whether one interprets $\Delta\mathcal{K}$ as a change in χ_p or in $\langle a \rangle$ [recall the latter is an average involving the product of a's and χ's, over all points of the Fermi surface; see eq (17)] depends upon one's preference for the particular case at hand.

In a simple form one may write, in analogy with eq (1),

$$\mathcal{K}_{\text{alloy}} = \langle a \rangle_{\text{alloy}} \chi_p^{\text{alloy}}. \tag{30}$$

Permitting both $\langle a \rangle$ and χ_p to vary, as in eq (30), is not as practical a viewpoint for scanning alloy data, as is holding one of the two quantities constant and attributing the trend in $\Delta\mathcal{K}$ to a variation in the other. For instance, in the case of the transition metal alloys such as the Ti-V-Cr series, the vanadium Knight shift change may be most conveniently discussed in terms of a change in density of states (*i.e.*, χ_p). We will discuss this case in more detail later and see that for this case such a description is a useful one. On the other hand, in dilute alloys, where the Friedel oscillation description may be used, the change in $\mathcal{K}$ is better described by considering the different $\langle a \rangle$ values as appropriate to the different environmental conditions of the host atoms, keeping χ_p constant.

A general version of eq (30), sampling the Knight shift behavior of the two types of atoms (*A*,*B*) in a binary alloy is

$$\chi_p = (1-c)\frac{\langle a\chi \rangle^A_{\text{alloy}}}{\langle a \rangle_{A \text{ in alloy}}} + \frac{c\langle a\chi \rangle^B_{\text{alloy}}}{\langle a \rangle_{B \text{ in alloy}}} \tag{31}$$

$$= (1-c)\frac{\mathcal{K}^A_{\text{alloy}}}{\langle a \rangle_{A \text{ in alloy}}} + \frac{c\mathcal{K}^B_{\text{alloy}}}{\langle a \rangle_{B \text{ in alloy}}}, \tag{32}$$

where $\mathcal{K}^A$ and $\langle a \rangle_A$, are the shift and averaged hyperfine constant of atom A in the alloy. χ_p is defined as the susceptibility per atom and c the concentration of B type atoms. Making the nontrivial assumptions that $\langle a \rangle_{\text{alloy}}$ is equal to its value in the pure metal (*A* or *B*), and that there is no significant exchange enhancement of χ, this equation may be rewritten (using eq 17) in the form given by Drain [74],

$$N(E_F)_{\text{alloy}} = (1-c)N_A(E_F)\frac{\mathcal{K}^A_{\text{alloy}}}{\mathcal{K}^A_{\text{metal}}} + cN_B(E_F)\frac{\mathcal{K}^B_{\text{alloy}}}{\mathcal{K}^B_{\text{metal}}}. \tag{33}$$

Thus

$$N(E_F)_{\text{alloy}} \equiv (1-c)N_A(E_F)^{\text{alloy}} + cN_B(E_F)^{\text{alloy}}, \tag{34}$$

which defines *local* densities of states $N_A(E_F)^{\text{alloy}}$ and $N_B(E_F)^{\text{alloy}}$. The assumption of setting $\langle a \rangle$ in the alloy equal to $\langle a \rangle$ in the metal forces the whole effect of alloying to be described in terms of these local densities of states. At times this proves useful. Drain [74] has used eq (33) and the data of figure 8 to scan the AgCd alloy system. The results are in agreement with general trends seen within and between phases obtained in a "rigid band" scan of electronic specific heat data. However, using eq (33), such a scan should not *rigorously* reflect the variation in the density of states of Ag at and above E_F for a number of reasons. These include charge screening (for discussion see ref. 8) and the fact that the hyperfine constants are held fixed.

Local effects in covalent compounds, such as chalcogenides and SiC can also be examined using eq (31). Consideration of these materials is aided by the fact that the energy bands are often more well-known in these than in intermetallic compounds. An example is n-doped silicon carbide [78,155]. The ^{29}Si Knight shift is near zero whereas a substantial Knight shift is measured for ^{13}C. This information, together with T_1 data for both sites, permitted Alexander and Holcomb [78,155] to infer important wave function symmetries. It was concluded that a zero Knight shift implied a zero wave function density at Si but that symmetry allowed a substantial shift at the carbon site.

Lead telluride is another case where local effects are important and where a significant amount of experimental and theoretical information is available on the energy band structure. Although the results are affected by sample preparation, for the better samples the ^{207}Pb Knight shift in n-type PbTe was found [156] to be temperature independent, and relatively small and positive with respect to undoped PbTe. On the other hand in p-type, PbTe $\mathcal{K}$(Pb) was found to be large, negative and temperature dependent. This was interpreted [156] in terms of a band structure model in which the valence band possesses substantial *s*-

character with respect to the Pb atoms, whereas the conduction band lacks *s*-character at Pb. The small positive shifts in *n*-type material were assumed to be of orbital origin. The negative contact interaction is ascribed to a negative *g*-value for the *L*-point valence band states. The same band model was used to explain the ^{125}Te Knight shift results in these materials.

9. Correlations of $\mathcal{K}$, χ and γ with Electron Concentration in Transition Metal Alloys

There are many cases in the literature where the Knight shift has been observed to vary smoothly with composition in alloy systems. Where γ values are available from specific heat data, or other $N(E_F)$ information is known, a direct correlation between these quantities and $\mathcal{K}$ can sometimes be found. Usually the complex nature of $\mathcal{K}$ (eq 19) causes the correlation to be somewhat obscured, and the fact that $\mathcal{K}$ does not follow the $N(E_F)$ curve is not necessarily an indication of nonrigid band behavior. Examples are shown in figure 16a. Looking first at the 3*d*-alloys, there is a gradual increase in $\mathcal{K}$ with *e*/*a*, with a peak at about 5.6 electrons per atom. Between $e/a = 5.6$ to 6, there is a gradual decrease in $\mathcal{K}$. This decrease is steepest for V-Fe alloys. The vanadium hydride results follow those of V-Cr extremely closely, as if the electron of the hydrogen is absorbed in the common conduction band, filling the band in the same manner that Cr does. Recent data by Rohy and Cotts [169,170] on V-Cr hydrides (not shown) fall on the same line. The other data, including those for the 4*d* alloys, all are similar to the V-Cr curve in that they show a peak in $\mathcal{K}$ at about $e/a = 5.6$. The Nb-Tc alloy data shown in figure 16a deviate from the general trend. The reason for discrepancy in the case of $\mathcal{K}$ measurements may be a result of a difference in $N(E_F)$, but again may be due to local effects so that no direct conclusion can be drawn from the $\mathcal{K}$ versus *e*/*a* results alone.

To give a further picture of the shape of the density of states curves for these alloys we show the total susceptibility data in figure 16b. Both for the 3*d* and 4*d* series, there is a possible cusp at $e/a = 5$. Both χ curves have quite similar behavior. The V-Tc(3*d*-4*d*) alloy system also follows this trend. From this picture we get a different impression of the density of states curve than from the curves obtained from γ data as shown in figure 16c. Here there is no cusp at $e/a = 5$ and a major peak occurs between $e/a = 4$ and 5. Thus there is a discrepancy between the γ curves on one hand, and the χ curves on the other. Depending on which curves are used, the Knight shift data may be interpreted in a

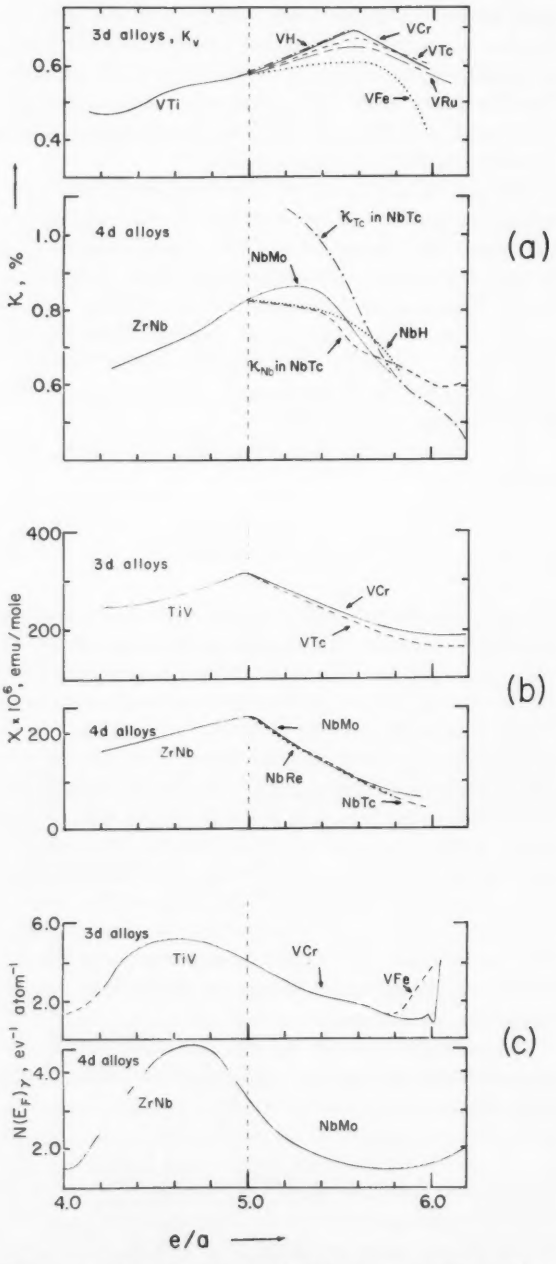

FIGURE 16. *Variation of (a) Knight shift, (b) susceptibility and (c) density of states as measured by electronic specific heat, with e/a ratio for the b.c.c. transition metals of the 3d, and 4d rows. While for $\mathcal{K}$ and χ there are substantial ranges where χ and $\mathcal{K}$ track one another, the $N(E_F)\gamma$ curves show less similarity. The data were taken from the following sources: (a) Ti-V [157], V-Cr [157,158], V-Tc [157], V-Fe [159], V-Ru [160], V-H [161], Nb-H [162], Nb-Tc [163], Zr-Nb and Nb-Mo [164]. (b) Ti-V [165], V-Cr [157,165], V-Tc [157], Zr-Nb [164], Nb-Mo [163,164], Nb-Re and Nb-Tc [163]. (c) Ti-V and V-Cr [164,166,167], V-Fe [164], Zr-Nb and Nb-Mo [168].*

quite different manner. In either case there is no direct correlation between $\mathcal{K}$ and the other data, and there must be an interplay of several terms as a function of e/a. A number of attempts have been made using γ, χ, $\mathcal{K}$, as well as T_1 data and the Korringa relation [27], to derive the various contributions to $\mathcal{K}$. For example, the results of figure 16 have been rationalized [24,163,164] by using a two-band model for the Pauli term, as in eq (23), and estimates of the Van Vleck orbital effects. Although these do explain the results, the description is not unique. An alternative explanation in terms of varying *s-d* admixture in a single band has been offered [171, 172] to explain the maximum in $\mathcal{K}$ at $e/a \approx 5.6$. In the region above 5.6 both γ and χ are decreasing. Within this model, the decrease in $\mathcal{K}$ arises from a Pauli contribution which becomes less negative, and, in fact, positive with increasing e/a. Only 10 to 15 percent *s*-character in the *d*-band is required to balance or overtake the negative *d*-core polarization term. Changes in *s*-character of only a few percent can produce the observed variations in $\mathcal{K}$. As noted earlier for Cu (see fig. 10), admixture and variations of admixture of this magnitude are not unreasonable. This model is more obviously appropriate to the $TiFe_{1-x}Co_x$ alloys, with e/a from 6 to 6.5 [172], where the slope of the $\mathcal{K}(^{59}Co)$ versus χ plot reverses sign across the alloy sequence. If the hybridization model is proven valid, the Knight shift can provide a useful probe of the variation of the density of *s*-states in "*d*"-bands.

An example of a different type of application of a rigid band model is the proposed band structure in the lanthanum-hydrogen system by Bos and Gutowsky [173]. Lanthanum is a metal and upon adding hydrogen up to 67 percent (LaH_2) the material remains metallic. At LaH_3, however, the material becomes an insulator. This, together with $\mathcal{K}$ and χ information, was then used [173] to propose the density of states shown in figure 17. These measurements lead to the conclusion that adding hydrogen means *lowering* the e/a ratio, which can be considered equivalent to the hydrogen absorbing an electron. This is in contrast to the other model in which hydrogen in the alloy gives up an electron to the conduction band and remains in the lattice as a proton. This latter model has been used, for example, to describe the V-H and Nb-H results shown in figure 16a, and for the compounds ScH_2 and YH_2 [174]. An interstitial proton is expected to be a larger perturbation in the La matrix and it may bind two 1*s* electron states to it (as in fig. 17) whereas such electrons might not be bound in the other systems where the perturbation is weaker. Such behavior can be anticipated from *s*-wave impurity scattering theory.

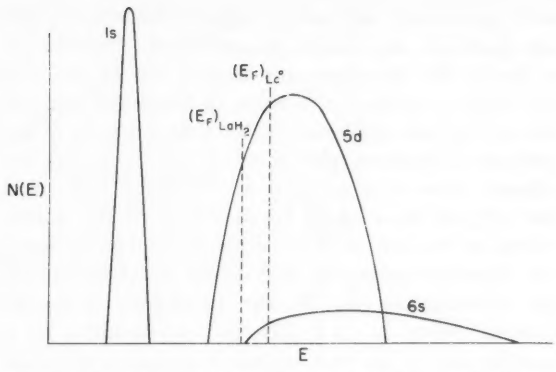

FIGURE 17. *Proposed band structure for lanthanum dihydride [173]. For each hydrogen atom entering the metallic lattice, two electrons are assumed to be transferred to localized hydrogen 1s orbitals. Formation of LaH_3 would correspond to complete emptying of the conduction band.*

10. Solvent Knight Shifts

Confidence that the Friedel oscillations (fig. 13) can be observed was given by Rowland's quadrupole wipeout data in Cu alloys [129], and reinforced by his solvent Knight shift results [150]. Rowland measured the change of the Knight shift upon alloying, $\Delta\mathcal{K}$, for a large number of *B*-subgroup solutes in Ag. From these, he obtained values for Γ ($\Gamma \equiv \mathcal{K}^{-1}\Delta\mathcal{K}/\Delta c$, where c is the fractional impurity concentration). These Γ data are plotted in figure 18. While there is a general tendency

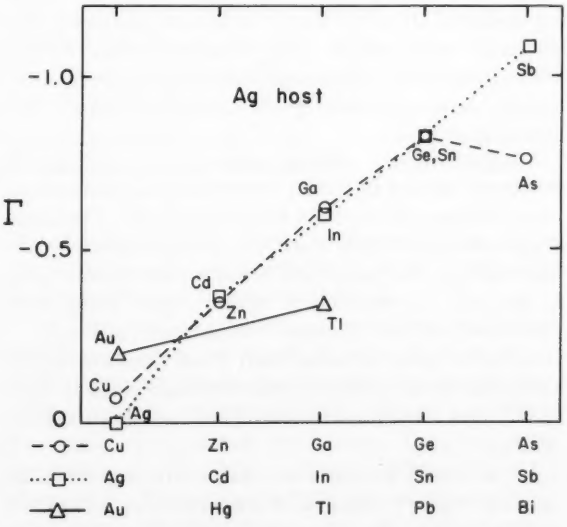

FIGURE 18. *$\Gamma = 1/\mathcal{K} \cdot \Delta\mathcal{K}/\Delta c$ values for impurities in a Ag host versus position of the impurity in the periodic table. The dashed, dotted and solid lines connect points for impurities occurring in the Cu, Ag and Au rows, respectively. These data are taken from Rowland [150], from his table 1. As pointed out by Rowland, the Γ values are dependent on the range of data employed.*

for Γ to increase with solute valence, there is a slight turn back (*i.e.*, decrease in magnitude) of Γ from Ag-Ge to Ag-As. For the silver row (namely Cd, In, Sn, and Sb), there is no such turn back. In figure 19a we have chosen two sets of Rowland's $\Delta\mathcal{K}$ data, for pairs of impurities of common valence, which clearly display the valence effect seen in figure 18. Rowland [150] noted that curved lines could be drawn to fit the datum points, as we have done for some of the data in figure 19b. Rowland points out that due to lineshape effects (for example, see fig. 14), the uncertainty of the individual points is such that his representation by a straight line is all that is quantitatively reasonable. Granted this uncertainty, the possibility of nonlinearity in these plots of $\mathcal{K}$ versus c may be real, as was noted by Rowland. Using Rowland's raw data, a Γ defined for low concentrations is smaller than that defined by fitting out to larger concentrations. This fact was used by Alfred and Van Ostenburg [175] in *their* version of the Γ plot which differs from figure 18, for the Sb in Ag point. By using low concentration data, this Γ point was reduced from the value given by Rowland, bringing it into line with their [175] predicted turn back. If the same treatment over the same concentration range is used for *all* of Rowland's datum points, then all the Γ points in figure 18 will tend to be somewhat lower but the general picture will remain as shown in our figure 18. Alfred and Van Ostenburg neither used Rowland's choice for Γ, nor treated the data for all the alloys equivalently. If all of the Γ values are obtained consistently, their phase shift analysis yields neither better, nor worse, agreement with experiment than the earlier phase shift estimates of Kohn and Vosko [176], and of Blatt [177].

Similar valence effects have been seen for *B*-subgroup solutes in liquid copper alloys [178] and, as seen in figure 20a, in solid lead alloys [179]. The liquid copper results of Odle and Flynn [178] also display the high valence turn back. This result is more evident than in the solid Ag case, the $\mathcal{K}$ versus c plots being more linear and the turn back in Γ being larger, although errors for the points of most interest are somewhat large. Odle and Flynn [178], utilized the phase shifts of Blatt [176] and Kohn and Vosko [177] to discuss their results.

In the solid Pb case, the Γ values are largest for the smallest valence (Hg), but a reduced effect of valence difference (*i.e.*, the beginning of a turn back) is also evident. The raw data in figure 20a also reveal curvature in $\mathcal{K}$(Pb) versus concentration for solid PbTl [179], similar to the Ag data in figure 19b. This curvature is not evident for the other Pb alloys. In liquid lead alloys, as seen in figure 20b, taken from Heighway and

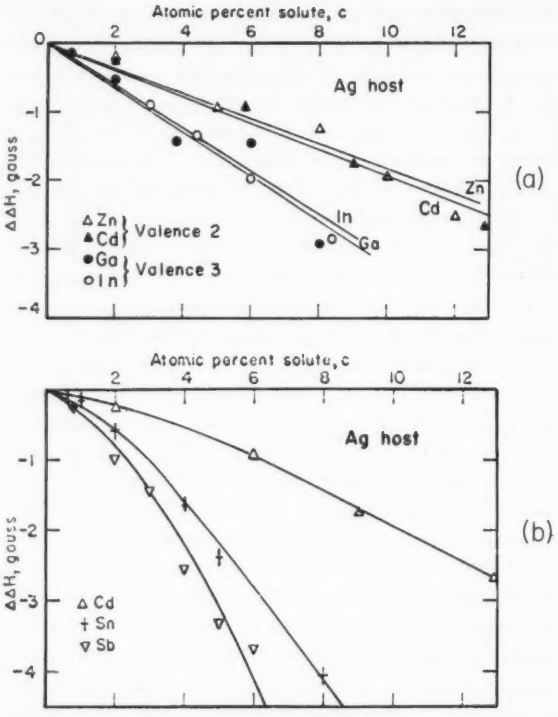

FIGURE 19. *(a) Silver solvent Knight shift datum points with straight lines, as chosen by Rowland [150]. (b) Silver solvent Knight shift datum points [150], indicating smooth curves through these points, without the assumption of linearity.*

Seymour [180], there are some cases of linearity and others of nonlinearity. A very interesting fact here is that, in the solid, Γ has the opposite sign to Γ in the liquid for many of these alloys. This result was verified [180] by following the resonance in Pb-Bi from the liquid to the solid state.

In figure 21a and *c*, $\mathcal{K}$ versus c plots for solid InPb and InSn alloys [123] are shown. These are examples where there is a tremendous dip in $\mathcal{K}$ versus c, before a more linear behavior is achieved. This dip falls within a 1% impurity concentration in one case, and 2% in the other. The magnitude of these dips is up to 10% of the total Knight shift. For comparison, data for these alloys in the liquid state [181] are shown in figure 21b and d on the same vertical scale as the solid data [182]. Dips may also exist in the liquid state, but, if so, were missed due to the coarse grain scans over the dilute range of alloying. On the other hand the dip may be peculiar to these alloys in the solid state only.

The linearity of $\mathcal{K}$, bearing in mind the coarse composition mesh studied, is striking for the liquid alloys displayed in figure 21 b and d. This linearity is characteristic of many, though by no means all alloy systems.

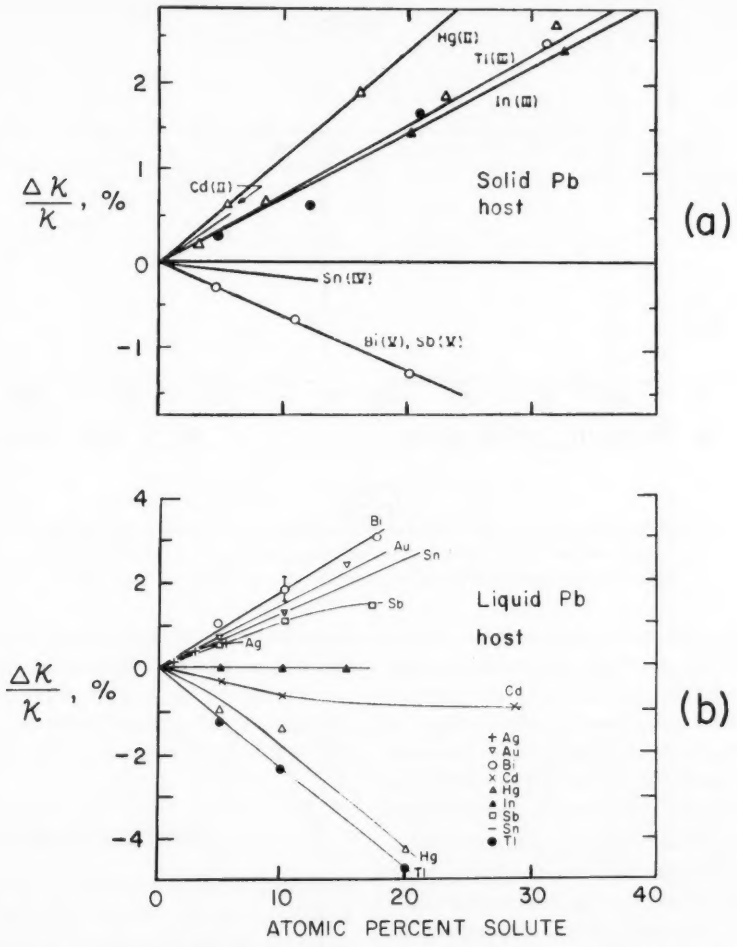

FIGURE 20. *(a) Pb solvent Knight shifts upon alloying in solid alloys, as taken from Snodgrass and Bennett [179]. (b) Pb solvent Knight shifts upon alloying in liquid alloys, as taken from Heighway and Seymour [180].*

Several other examples of linear behavior have been observed [183-188]. In these papers some cases of nonlinear behavior are also encountered. The linearity, even at higher concentrations, may be relevant to some suitable phase shift description. However, it should be recalled that in its formulation the traditional phase shift analysis was developed for infinite dilution only.

A dip in $\mathcal{K}$ versus c is also suggested by the solid Cd-In data [189] shown in figure 22. In this case we have drawn a straight line through the higher concentration data points merely to show a very general trend for the alloys. Although the scatter is large, it is again clear that the data are not best represented by a single straight line from the origin.

The complexity of the various terms contributing to $\mathcal{K}$, and the local nature of $\mathcal{K}$, is such that the observation of nonlinearities should not be surprising. These nonlinearities are not amenable to simple phase shift analyses, although the turn back in Γ is.

For the liquid alkali alloys a form of the single scattering model was employed by van Hemmen *et al.* [190]. Agreement with experiment was obtained by including volume renormalization, without considering the details of the charge oscillations. The phase shift description used by Odle and Flynn [178] for liquid Cu alloys, and similar attempts by Rigney and Flynn [191] using newly derived phase shifts, as well as pseudopotential methods as employed by Moulson and Seymour [192] have been partially successful in describing $\mathcal{K}$ versus c behavior in liquid alloys.

The observed behavior of $\mathcal{K}$ upon alloying should be described by a "nondilute" scattering model coupled

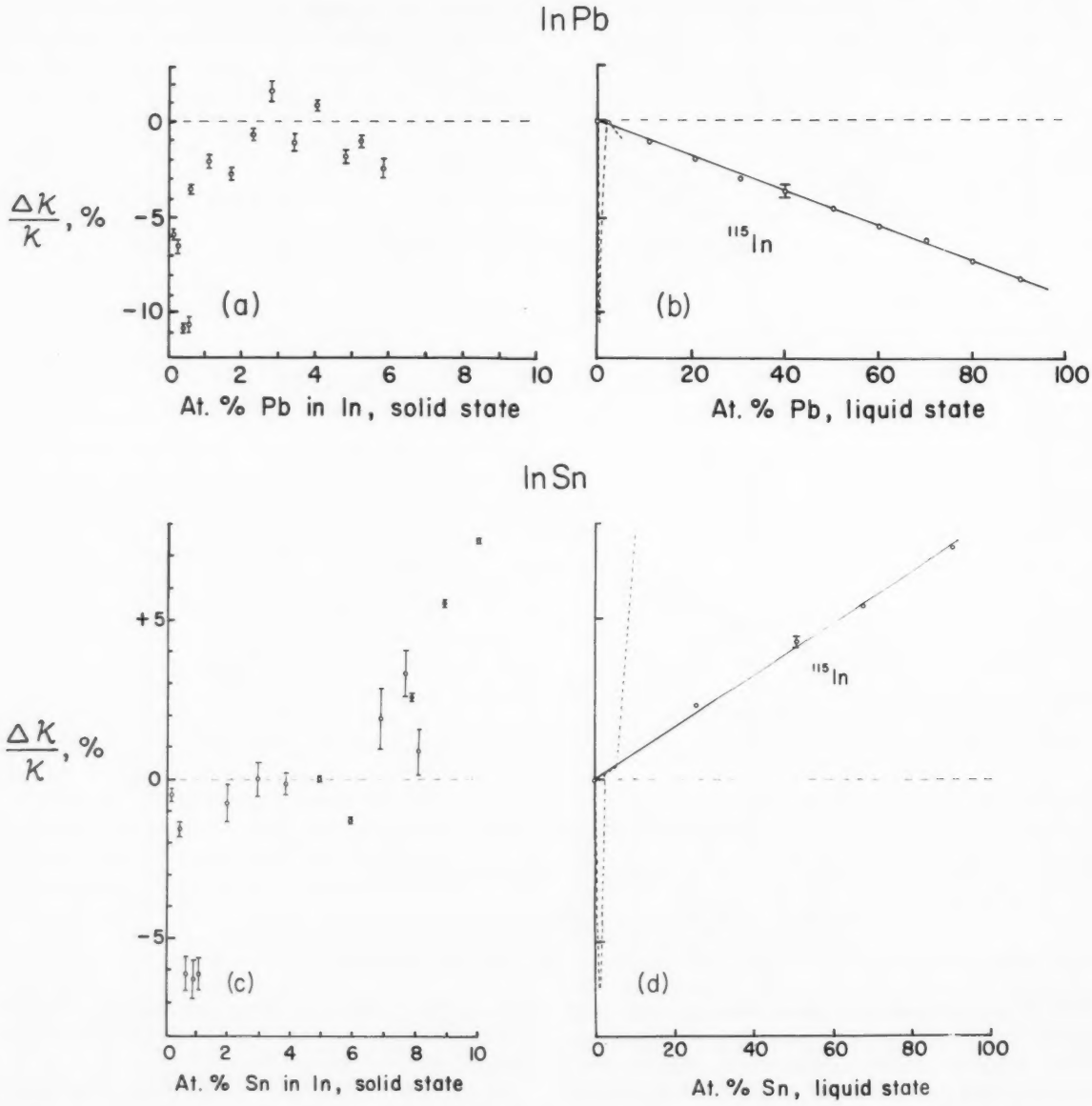

FIGURE 21. *Solvent Knight shifts for two alloy systems in the solid and the liquid state. The indium shift is shown for InPb alloys in (a) and (b), and for InSn alloys, in (c) and (d). In the left hand picture, (a) and (c), data are shown for solid alloys of up to ten percent impurity taken from Anderson, Thatcher and Hewitt [182]. On the right, (b) and (d), data for these same alloys in the liquid state by Seymour and Styles [181] are shown on the same vertical scale over the full range of alloy composition. All the reported alloy datum points are shown. (Note that there is no overlap of the data in the dilute region. We have merely transferred the solid data as dashed lines, onto the liquid curves for ease of comparison.) Lacking data there may or may not be strong structure in these liquid alloys in the dilute region.*

with some accounting of "rigid band" effects [8], in addition to other possible mechanics. Such a combined theory is not yet available.

{**Note added in proof:** An interesting proposal to explain the low composition dip was given by R. A. Craig. (We thank the author for sending us a preprint of his manuscript, to be published in the Journal of Physics and Chemistry of Solids.) Anisotropic many-body effects were found to give a contribution to $\mathcal{K}$ in a pure metal. According to Craig, the contribution

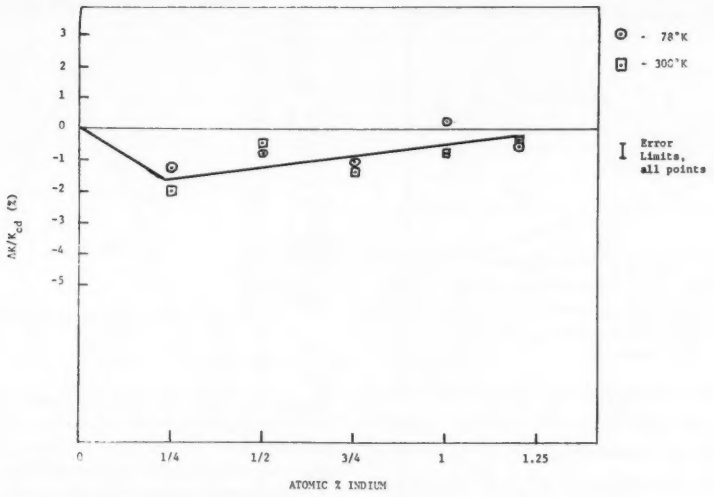

FIGURE 22. *Change of the cadmium Knight shift in CdIn alloys, as taken from Slocum [189]. The indicated straight line through these points has been drawn to demonstrate that these points are clearly nonlinear with respect to the origin.*

is expected to become unimportant upon introducing impurities and at high temperatures (e.g. absent in the liquid), because impurity scattering of the quasiparticles will cause a loss of memory of the angular correlations between the quasiparticle-quasiparticle collisions.}

11. Solute Knight Shifts

When a foreign atom is substituted in a lattice, it causes a certain amount of screening about it, and long range charge oscillations, as discussed in previous paragraphs. Let us now look at what this impurity atom sees as situated in a foreign host. The Knight shift will respond to such a situation in the same way noted above, namely by an $\langle a \rangle$ of the impurity (be it altered somewhat by its environment) and a χ_p of the host, which may also be changed by the introduced impurity. Again it is a matter of how Knight's ξ factor is used as to whether we use χ_p to mean the measured average derived from χ_{expt}, or whether to ascribe a local χ nature to the immediate environment as the impurity sees it. To make this situation more clear we rewrite eq (11) for the Knight shift of an impurity, B, in a given host, A, as

$$\mathcal{K}_{B \text{ in } A} = \frac{1}{\mu_B} \chi_p^A \xi H_{\text{eff}}^B. \tag{35}$$

This definition then uses ξ to absorb solute site changes in both $\langle a \rangle$ and χ_p from the free atom and pure solvent behavior, respectively.

It is useful to explore eq (35) for a sequence of alloys, varying either impurity or host. One might follow the quantity $\mathcal{K}_{B \text{ in } A}$, or $\mathcal{K}_{B \text{ in } A}/\chi_p^A$, for a specific impurity through a series of host metals. For example, we have done this for charge impurities in the sequence Cu, Ag, Au. A similar type of scan is often done for Mössbauer hyperfine data across rows in the periodic table.

Alternatively, one can dissolve a series of impurities in a particular host. The observed trends are less difficult to interpret as we have the advantage of remaining within one crystal structure. Such solute studies have been done for example for Cu and Ag [6], for lead [193], and for Au [7,194] based alloys. Taking these data, we have plotted the quantity $\mathcal{K}_{B \text{ in } A}/H_{\text{eff}}^B$ in figures 23 and 24. We have connected points of impurities belonging in the same row of the periodic table, and dissolved in the same host metal. We see a general downward trend as we go to higher valence for three of the four host materials, but for gold there is a definite reversal of trend. If we now assume an experimental χ_p^A of the pure host material, A, then this behavior reflects directly the nature of ξ, or $\langle a \rangle$, in Au versus that in Cu, Ag and Pb. In other words, the gold host causes the details of the wave function at the impurity site to change quite differently from the other three hosts. This could, of course, involve local density of states effects as well. We believe [7] that strong *s-d* hybridization, arising from the proximity of the *d* band to the Fermi level, is important to the Au behavior. Unfortunately, auxiliary specific heat, susceptibility, and other experimental data which might help resolve this

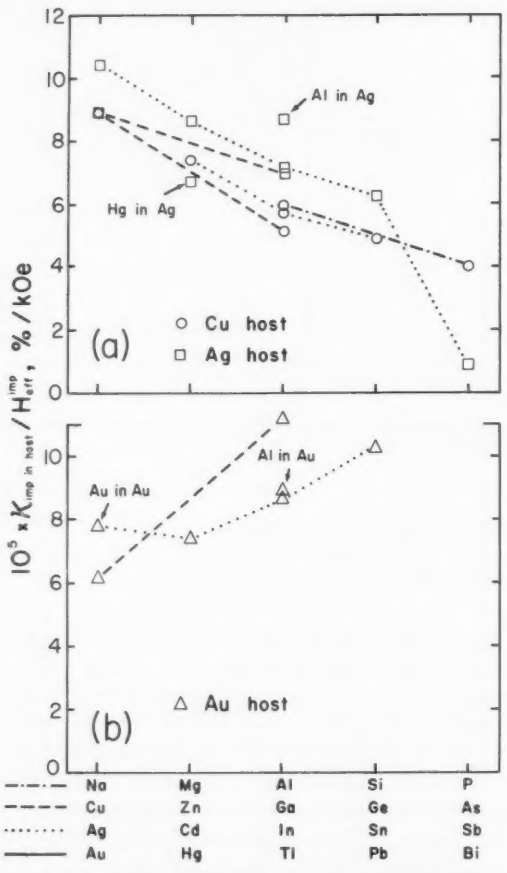

FIGURE 23. *Impurity Knight shifts in Cu, Ag and Au hosts. Atomic effects due to the hyperfine coupling constants are divided out, using our* H_{eff} *values for the impurities, listed in table 2. The resulting trends are opposite for a gold host than for copper and silver hosts. (Data for boron in gold [195] of* 15×10^{-5}% *per kOe agrees with the upward trend for the gold host. The uncertainty in this value is greater than that of the points given in the plot.) Points for impurities occurring in the same row of the periodic table are connected with the line symbols indicated in the lower left hand corner (e.g., the dotted line connecting the square datum points is for Ag, Cd, In, Sn, and Sb in a silver host). The Cu and Ag data were taken primarily from Rowland and Borsa [6]; the Au data from Bennett* et al. *[7]. This latter paper gives in its table 1 further references to the literature for several of the shown points. The Sb in Ag point was taken from Matzkanin* et al. *[194].*

matter is not readily available for the Au alloys. More data of this type would be worth obtaining.

12. Magnetic Disturbances

The effects of a charge impurity in a metal have been described above (sections 8, 10, 11). When a *magnetic* impurity is introduced into the metal, a similar response occurs: spin density oscillations (rather than, or in addition to, charge oscillations) are set up around the impurity, as discussed in section 8. The behavior is similar to the oscillations shown in figure 13. The unbalanced spin at a neighboring site interacts with that nucleus via a spin-dependent interaction. Generally this interaction is rather strong compared to charge effects causing correspondingly larger variations in the Knight shift and thus larger values of Γ.

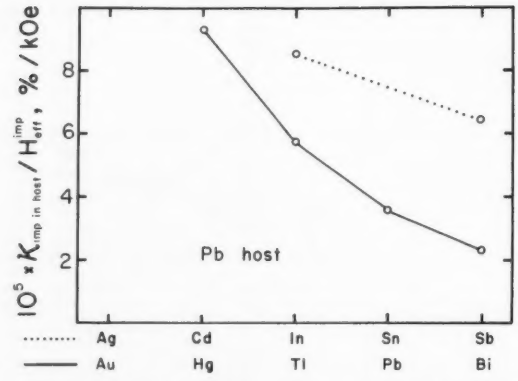

FIGURE 24. *Impurity (B) Knight shifts in a lead host divided by the impurity hyperfine fields,* H_{eff}^{B}. *Data taken from Bennett* et al. *[193]. The dotted line connects points for impurity atoms belonging to the Ag row of the periodic table and the solid line connects those for impurity atoms belonging to the Au row. The trend is similar to that for Cu and Ag hosts and opposite that for an Au host.*

Gardner and Flynn [196] have reported susceptibility and solvent Knight shift results for transition element (3*d*) impurities in liquid Cu. The dominant Knight shift term in these cases is associated with the 3*d*-magnetic moment aligned at impurity sites by the magnetic field. The susceptibilities of alloys with Cr, Mn, Fe, and Co as impurities obey the Curie-Weiss law implying the existence of local paramagnetic *d*-moments at impurity sites. The moment values, μ, inferred from the susceptibilities are plotted in figure 25. Sc, Ti and Ni alloys do not follow a Curie-Weiss law, suggesting that local virtual *d*-level *band* paramagnetism dominates.[12] The Mn, Fe, and Co moments plotted in figure 25 are of some interest if one assumes that they are entirely associated with impurity site *d*-character, *i.e.*, little or no moment either residing on the host lattice, or in conduction band character at an impurity site. The moments then equal the number of holes in the *d*-bands and the quantity (10-μ) provides an estimate of the number of *d*-electrons at a local site.

[12] The detailed susceptibility behavior of the Cr, Mn, Fe and Co alloys suggests the presence of a small term, of perhaps this sort, in addition to local moment paramagnetism.

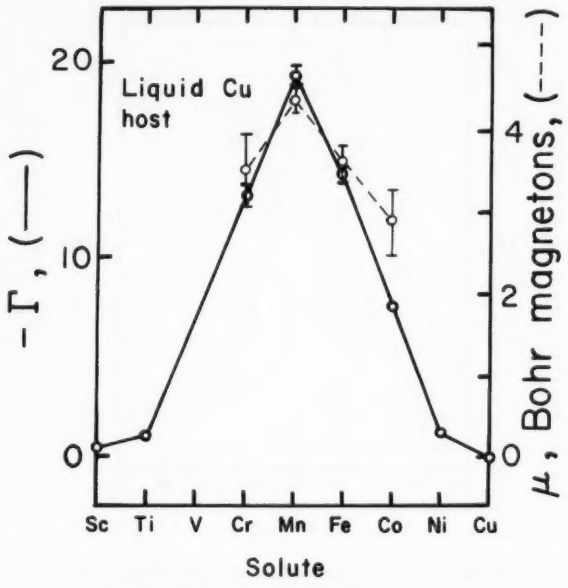

FIGURE 25. *$\Gamma = 1/\mathcal{K} \cdot \Delta\mathcal{K}/\Delta c$ values for 3d transition metal impurities in liquid copper (solid line) and effective magnetic moment, μ, (dashed line) plotted versus position in the periodic table. Both sets of data are taken from Gardner and Flynn [196]. The vertical scale of the μ plot was arbitrarily chosen so that the height of the Γ and μ peaks are nearly equal.*

Gardner and Flynn [196] obtained values of 7.1, 6.4, and 5 for the number of Co, Fe and Mn respectively. These numbers are 0.5 to 1.0 electrons smaller than the *d*-electron counts believed appropriate to the pure solute transition metals and, if real, this trend offers valuable evidence as to the electronic character of these impurities. The estimate, of course, relies strongly on the assumption that the moments are entirely of impurity site *d*-character with no hybridization with the conduction bands. Electron count estimates for lighter 3*d*-element impurities, such as Cr, are further hampered by the question of whether or not there is any occupied *d*-character of spin antiparallel to the net spin of the moment. The density of states with and without such behavior is shown schematically in figure 26. It is probably reasonable to assume that a strong paramagnetic moment such as Cr in Cu has little or no *d*-spin moment component antiparallel to the net local moment.

The Γ values appropriate to the various 3*d*-Cu alloys are also plotted in figure 25. These roughly follow the moment behavior, are negative, and are large when compared with the charge perturbation Γ's of, for example, figure 17. They are large because a local 3*d*-susceptibility, and its associated spin density disturbance, contributes a larger Knight shift effect

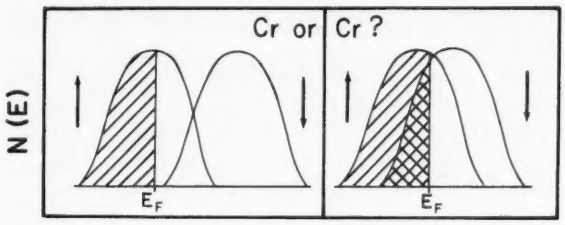

FIGURE 26. *Schematic density of states as a function of energy for Cr metal. In the first case the spin up (↑) band and spin down (↓) band do not overlap at the Fermi surface; in the second case both spin up, and spin down bands are partially filled.*

than the weak perturbation of charge impurities. Charge effects are undoubtedly also present in the vicinity of 3*d*-impurity sites, but these appear to be insignificant if a local paramagnetic moment is formed. The strength of the magnetic term, relative to other effects, is a prime reason for the observed linearity in $\mathcal{K}$ versus impurity concentration. (This assumes that the magnetic term above tends to be linear.) The negative sign of the Γ's might imply that the main peak of the conduction electron spin disturbance (see fig. 13) has its moment antiparallel to the local moment. This negative sign is reminiscent of charge impurity effects and might instead indicate, as in the charge case, that the main peak either fails to overlap solvent nuclear sites or, if it does overlap, contributes satellite lines which are shifted out of the main resonance (*e.g.*, see fig. 14). While the latter would be consistent with charge impurity experience, most workers believe that the main peak is sampled by the main resonance line, and that a negative Γ indicates spin moment antiparallel to the local moment. This in turn implies that hybridization and higher order effects predominate over electrostatic exchange scattering. Combined hybridization and electrostatic exchange terms will provide an *effective* exchange coupling which is *not* constant as one traverses the 3*d*-elements. One thus expects a crude but *by no means linear* relation between Γ and μ. This is seen to be the case in figure 25. Gardner and Flynn showed that a partial wave description involving *d*-wave scattering crudely reproduces the trend and magnitude of the Γ's.

Flynn and coworkers have also obtained [197] results for 3*d*-impurities in liquid Al and these are summarized in figure 27. Since band, rather than local moment, paramagnetism prevails for all impurities, the added susceptibilities per mole of solute have been plotted (rather than local moment μ values). The Γ values, except for Sc and Ti, are smaller than those obtained in the Cu alloys. This is largely accounted for by

the smaller susceptibilities (per added solute atom) in the Al alloys.

The Cu and Al hyperfine fields, per effective spin moment induced on solute sites, are of the order of −100 kOe for impurities in the middle of the 3*d*-series. The hyperfine fields obtained (and the ξ's derived from them) for the Cu alloys are plotted in figure 28. (A similar plot for 3*d*-impurities in liquid Al alloys results in much larger uncertainties.) One might expect a somewhat smaller value of H_{eff} for Al relative to that of Cu, since the free atom *s*-contact interaction of Al is approximately half that of Cu. The fact that it has a similar value suggests that the magnetic response in the Al matrix, due to a given moment on the impurities, is slightly larger[13] than in Cu.

If one attributes H_{eff} on an average solvent site to an *s*-moment, with its associated atomic $\langle a \rangle$, the results correspond to antiparallel spin moments of 0.05 to 0.08 μ_B for Al and up to 0.05 μ_B for Cu for every Bohr magneton of moment aligned at solute sites and in the solvent matrix. The moment at any given solvent site is small but the total moment residing in the solvent lattice can become a significant fraction of that residing on the solutes thus affecting the arithmetic average of *d*-electron population estimates from susceptibility data.

A comparison of the Γ behavior and the susceptibilities for the Al alloys (fig. 27) shows Γ tracking χ more poorly than was the case in the Cu alloys (fig. 25). When making such a comparison it should be noted that the Γ for Sc, Co, Ni and Cu are of the order of charge impurity Γ's. Thus, charge as well as magnetic effects, may be contributing to Γ. As we have discussed, the negative sign of the Γ's in figures 25 and 27 would seem to indicate that hybridization exchange scattering predominates over direct exchange effects (see sec. 8). There is no reason why such hybridization effects should be constant across the 3*d* row and the deviation in Γ from the χ curve in figure 27 is of a magnitude appropriate to such a variation in hybridization effects. Flynn and coworkers explain the trend with a particular version of such higher order effects, in which the exchange enhancement of the virtual *d*-level susceptibility (see eq. 20) plays an important role. The fact that Γ lies higher for the lighter 3*d* impurities could be due to charge effects but it would seem to imply that hybridization effects are stronger (and/or coulomb exchange weaker) for the lighter elements in Al. The peaking of Γ at Cr or Mn seen in figures 25 and 27 is characteristic of the 3*d* elements. Quite different behavior is seen for the rare earths (*e.g.*, see fig. 29).

As already noted, the variation in Knight shift with impurity concentration is strikingly linear in both the Al and Cu alloys over the ranges of concentration studied.

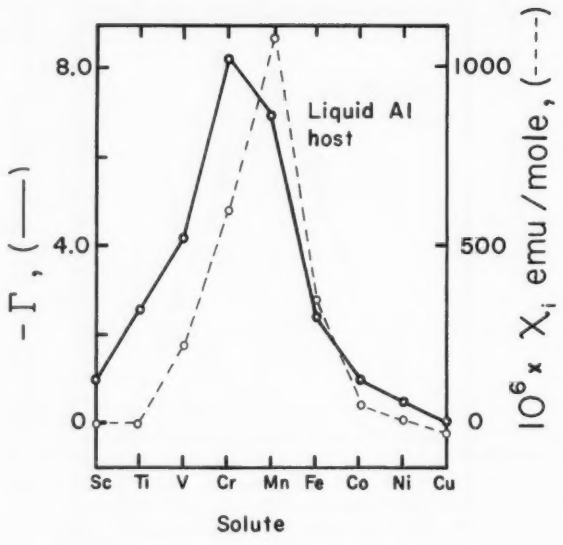

FIGURE 27. *$\Gamma = 1/\mathcal{K}\,\Delta\mathcal{K}/\Delta c$ values for 3d transition metal impurities in liquid aluminum (solid line) and χ_i, the susceptibilities per mole of solute plotted versus position in the periodic table. Both sets of data are taken from Flynn* et al. *[197].*

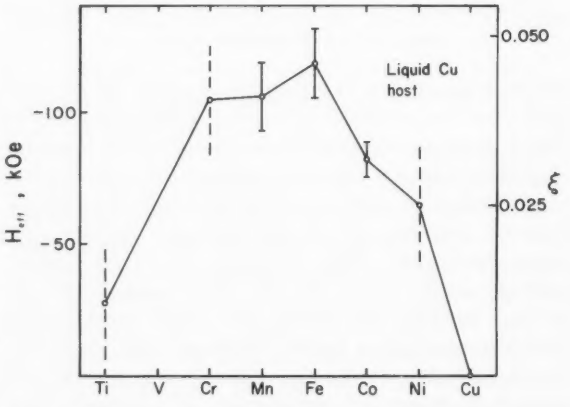

FIGURE 28. *Hyperfine fields and effective ξ values for liquid copper sampling the effects produced by liquid transition metal impurities. Unlike the normal definition of such quantities these are defined with respect to the impurity susceptibility. This is accomplished by using composition, rather than temperature, as the implicit parameter in a $\mathcal{K}$ versus χ plot.*

[13] One might be tempted to attribute this to band effects associated with the band paramagetism of the impurities in Al versus the local moment paramagnetism of Cr, Mn, Fe and Co in Cu, but note the small effective fields for the band paramagnetic impurities of V and Ni in Cu.

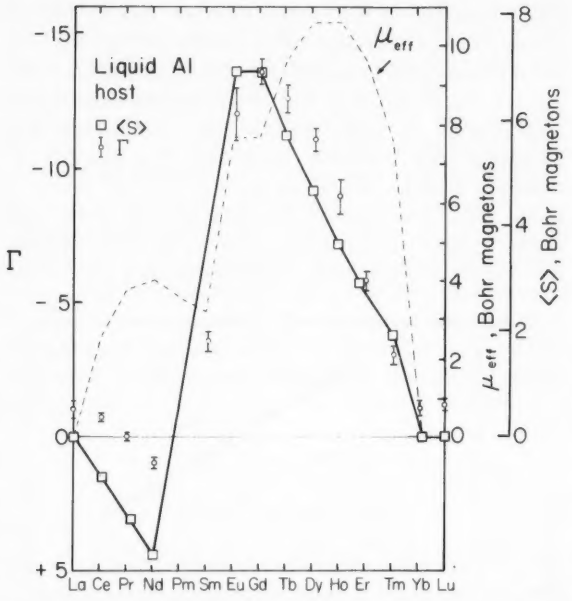

FIGURE 29. *$\Gamma = 1/\mathcal{K} \cdot \Delta\mathcal{K}/\Delta c$ for rare earth metal impurities in liquid aluminum (circles with error bars) and μ_{eff}, the effective total magnetic moment (dashed line) plotted versus position in the periodic table. Both sets of data are taken from Stupian and Flynn [200]. Also plotted is the effective spin moment ⟨S⟩, as discussed in the text (solid lines with squares).*

In some cases these extended up to five and six percent. These are concentrations at which one magnetic impurity would have another magnetic impurity as a near neighbor roughly half the time. At such concentrations it is doubtful that a Friedel or RKKY type of theory should be expected to work, for they assume noninteracting impurities which are dilute enough that there are no saturation effects in the solvent. Any effective local-moment local-moment exchange coupling is reduced due to the fact that the experiments were done at high temperature (above 1000 K). This may serve to reduce apparent nonadditive effects. It may be that averaged multimoment effects are contributing to the Γ's. Extremely dilute alloys were not examined; with one exception the lower ranges of alloy concentrations were one-half to one percent.

Knight shift data in alloys have also been obtained by γ-γ, perturbed angular correlation experiments [198]. In such an experiment, a nucleus is observed which has emitted a gamma ray in some particular direction. Thus defining the nuclear orientation, one then observes that nucleus as it emits a second gamma ray in some characteristic multipole distribution. Application of an applied magnetic field produces a Larmor precession of the nucleus between the emission of the first and second gamma ray. The precession rate, with its associated Knight shift term, can be deduced from its effect on the second gamma ray distribution. Rao *et al.* [198] have recently used the technique to obtain the Knight shift of very dilute Rh in Pd over a temperature range of 4.2 to 1053 K. They then used existing susceptibility data, extrapolated to infinite Rh dilution, to obtain a $\mathcal{K}$ versus impurity site χ plot, which was not linear. The $\mathcal{K}$ versus χ slope appropriate to particular temperature regimes are uncertain due to questions concerning scatter in the Knight shift data and the purity of the samples used in two different sets of susceptibility measurements. (These are strongly paramagnetic alloys and any magnetic impurities will strongly perturb the magnetic response.) The results yield a large negative $\mathcal{K}$ versus χ slope at high temperatures, which is of the order of 4*d*-core polarization effects, but a much smaller slope at low temperatures. This is consistent with a picture where the impurity contribution to the susceptibility at high temperatures is almost entirely associated with Rh sites, but, due to exchange enhancement effects involves the entire Rh-Pd matrix at low temperatures. The low temperature $\mathcal{K}$ versus χ slope is consistent with an effective magnetic moment of $\sim 10\mu_B$ residing largely on the solvent matrix. Such a moment was *independently* deduced [199] from Curie-Weiss fits for these alloys at low temperatures.

Stupian and Flynn [200] studied the effect of adding rare earth impurities to liquid Al. The susceptibilities were consistent with local moments as predicted by Van Vleck [201]. With the exception of $Sm(4f)^5$ where there is strong multiplet mixing, the moments are approximately

$$\mu_{eff} = [J(J+1)]^{1/2} g\mu_B \equiv \frac{\mathbf{L}\cdot\mathbf{J} + 2\mathbf{S}\cdot\mathbf{J}}{[J(J+1)]^{1/2}}\mu_B, \quad (36)$$

where the Landé *g*-factor has been written out. Very substantial orbital terms contribute to μ and therefore the Γ's should not, and do not, track μ. The Γ's are compared with $\langle S\rangle$ in figure 29 where $\langle S\rangle$ is the spin component along **J**, *i.e.*

$$\langle S\rangle \equiv \frac{2\mathbf{S}\cdot\mathbf{J}}{[J(J+1)]^{1/2}} = \mu_{eff}\left(\frac{2\mathbf{S}\cdot\mathbf{J}}{\mathbf{L}\cdot\mathbf{J} + 2\mathbf{S}\cdot\mathbf{J}}\right) = 2\mu_{eff}\left(\frac{g_J - 1}{g_J}\right) \quad (37)$$

is a measure of the spin component (in μ_B) parallel to the aligned **J**. This provides a crude first order measure of effective exchange perturbations. **S** is antiparallel to **J** in the first half of the rare earth row and parallel in the second, hence the sign reversal in $\langle S\rangle$. The Γ's dis-

play a weaker reversal which is, in part, associated with uncertainties such as the *natural* zero line for magnetic contributions to Γ. [Note that La, Yb and Lu impurities have zero-valued magnetic moments yet their Γ's lie above the zero line.] The differences between Γ and $\langle S \rangle$ are on a similar scale to the effects seen in figure 27. Otherwise there are fundamental differences in Γ behavior as one transverses the rare earths in contrast to the 3*d*'s. Negative Γ's prevail suggesting a tendency for the conduction electron spin disturbance to be antiparallel to the spin of the rare earth moment. This is consistent with almost all experience with rare earth elements in alloys or intermetallics. This sign was also observed for rare earths as impurities in Pd [202-204], at Al sites in $REAl_2$ intermetallic compounds [205], and for ^{31}P, ^{75}As and ^{121}Sb in PrP, PrAs, TmP, TmAs and TmSb[14] [206]. There is general agreement that hybridization effects are responsible for these results.[15]

The situation with magnetic alloys is seen to be similar to the charge impurity case. Both can be described with models of the perturbations which reproduce the experimental behavior, usually crudely, although occasionally in detail. The magnetic alloy problem is complicated by the presence of several scattering mechanisms and by the fact that a magnetic impurity is also a charge impurity. Solvent Knight shift experiments provide unique data for testing alloy models in both magnetic and charge difference systems, but as yet they have provided little *unique* insight into alloy behavior. Further studies of very dilute systems and of satellite lines outside the main resonance peak should prove invaluable for this purpose.

13. Intermetallic Compounds

Relating the Knight shift to the electronic density of states in ordered alloys or intermetallic compounds presents some problems which we have tacitly ignored when considering disordered systems. Let us review the analysis of the Knight shift results [22,208,209] for the technologically important V_3X compounds [X = As, Au, Ga, Ge, Pt, Sb, Si or Sn]. It was in their now classic investigation of these intermetallic compounds that Jaccarino and Clogston developed the graphic $\mathcal{K}$ versus χ analysis described earlier [13]. $\mathcal{K}$ versus χ plots (with temperature an implicit parameter) are shown in figure 30 for V and Ga in V_3Ga. The temperature variation in χ is huge. The variation in χ *per* V atom

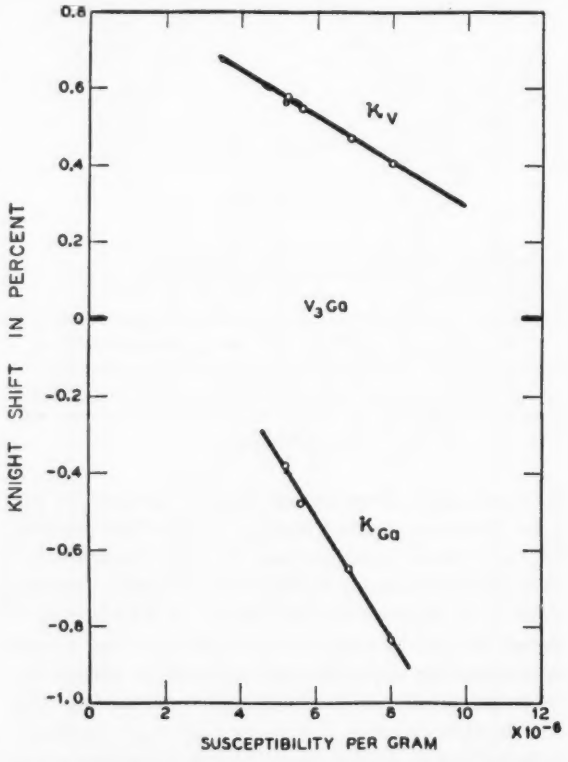

FIGURE 30. *Knight shift versus susceptibility for V and Ga in V_3Ga, as taken from Clogston and Jaccarino [13].*

as a function of temperature in V_3Ga is somewhat larger than that per Pd atom in Pd metal. This strong variation requires significant structure in the density of states (*e.g.*, see [110]) within kT of the Fermi energy. To investigate possible sources of density of states structure, Weger [210] considered the role of the linear chains of V atoms which occur on the cube faces in the V_3X structure. These chains impose anisotropic electronic properties which, in turn, could produce strong structure in $N(E)$ near E_F. Gossard [211] has studied Knight shift and quadrupole effect changes in V_3Si across the low temperature cubic-to-tetragonal phase

[14] Jones [207] also succeeded in observing the ^{141}Pr and ^{169}Tm Knight shifts in these paramagnetic compounds. Shifts as large as 8,900 percent were observed. Jones showed that this is consistent with theory and is due to large orbital hyperfine effects associated with the 4*f*-moments. He also noted that the temperature dependence of the rare earth and of the nonmagnetic site Knight shifts tracked each other quite faithfully.

[15] But other effects may also play a role. For example, direct electrostatic exchange scattering was not added to hybridization effects in Stupian and Flynn's consideration of the rare earth-Al alloys. Reasonable estimates of the appropriate exchange integrals suggest contributions to Γ of the order of (and opposite sign to) the observed Γ behavior. Inclusion of the effect would have overburdened the model with too many disposable parameters.

transition. He interpreted the transformation in terms of such a linear chain model. Labbé and Friedel [212] presented an alternative linear chain model which also is in accord with the experimental situation.

Strong negative $\mathcal{K}$ versus χ slopes are seen in figure 30. The slope for Ga is twice as steep as that for V. The χ=0 intercepts of $\mathcal{K}$ are positive and were attributed to a temperature independent Pauli term arising from a broad conduction band with *s*-like wave function character at both Ga and V sites. (There is probably also a significant orbital Knight shift term contributing to the V site intercept.) The temperature dependent Knight shift was attributed to a narrow V 3*d*-band into which Ga 4*p*-character is hybridized, contributing shifts of the form

$$\mathcal{K}_V(T) = w_V \langle a \rangle_V \chi_p$$
$$\mathcal{K}_{Ga}(T) = w_{Ga} \langle a \rangle_{Ga} \chi_p \qquad (38)$$

where χ_p is the *d*-band Pauli susceptibility per formula unit. The w_i are weights *per atom* of V and Ga character in a formula unit in the band. They *also* account for any deviation in the hyperfine constants from the chosen values. With correct $\langle a \rangle$'s chosen, then the w_i are simply weights and subject to the normalization requirement[16]

$$3\, w_V + w_{Ga} = 1. \qquad (39)$$

The $\langle a \rangle$'s were assumed to arise from V 3*d* and Ga 4*p* core polarization. The free atom values of -117 and -44 kOe/μ_B (consistent with table 3) were used, respectively. Given these $\langle a \rangle$'s, the slopes of the $\mathcal{K}$ versus χ plots yield $w_V = 0.13$, and $w_{Ga} = 0.92$. The greater w_{Ga} value is in large part due to the steeper slope of the Ga plot. Testing the normalization condition yields

$$3\, w_V + w_{Ga} = 1.31, \qquad (40)$$

a sum remarkably close to one. This might suggest that the *w*'s are essentially measures of wave function weight. Clogston and Jaccarino observed trends in Knight shift behavior of various V_3X compounds which further suggest this. If the *w*'s are real weights, their values are surprising, for they would indicate that Ga *p*-character, rather than transition metal *d*-character, dominates at the Fermi surface. Subsequent band calculations by Mattheiss [213], yield $2 \leq w_V/w_{Ga} \leq 3$ unlike a value of 1/7 obtained from $\mathcal{K}$ versus χ plots. The V_3X compounds have large $N(E_F)$'s and their susceptibilities are strongly temperature dependent. Such behavior is characteristic of a *d*-band metal. This would suggest that the ratio obtained by Mattheiss is reasonable, and thus, that the w_i's obtained from the Knight shifts are largely a measure of hyperfine field behavior. Assuming a value for the weight ratio, the Knight shift slopes can be used to estimate experimental $\langle a \rangle$ values for this compound. A ratio of 2 yields values of -53 and -283 kOe/μ_B for V and Ga respectively. The reduced $\langle a \rangle_V$ could be caused by interatomic effects, by intrasite *s*-band polarization, or by *s*-*d* hybridization. Three percent *s*-character admixture into the *d*-band at E_F will account for the reduction. Large negative intra-atomic effects, over and above the core polarization term, are unknown. The value for the core polarization term, shown in table 3, includes the polarization of the closed valence *s*-shell. Wave function changes on going from a neutral atom to the metal might effect this core polarization term by a factor of two or three but not likely by an order of magnitude. Thus the enhanced $\langle a \rangle_{Ga}$ is most likely due to interatomic effects [$\langle a \rangle_{Ga}$ goes to -400 kOe/μ_B if w_V/w_{Ga} is taken equal to 3]. A similar situation occurs in V_3Si. The $\langle a \rangle_{Si}$ is observed to be negative yet the core polarization hyperfine field appropriate to atomic P, and thus presumably Si, is positive. The P atomic behavior might be irrelevant to Si but the result again suggests the presence of substantial negative interatomic terms at X sites in the V_3X compounds. An X-site in these compounds has twelve nearest V neighbors. This implies the presence of a nearest neighbor spin moment which is 20 to 40 times that induced at the X site itself by the magnetic field. Conduction electron polarization effects of the order of those encountered for transition metals in either liquid Cu or Al can, given such a large neighboring moment, account for the value of $\langle a \rangle_{Ga}$ as well as the apparent sign reversal in $\langle a \rangle_{Si}$. With such a large *near neighbor* moment, it is also possible that there is a substantial contribution to $\langle a \rangle$ via direct exchange polarization of the X-site ion core. Knight shift data [214,215] suggest that similar effects occur at Sn sites in the isostructural system Nb_3Sn.

Subsequent investigations of rare earth and transition metal intermetallic compounds have often relied on $\mathcal{K}$ versus χ plots to disentangle terms. Most of the data are associated with nonmagnetic atomic sites and band hybridization. Interatomic effects are featured heavily when rationalizing the behavior of the hyperfine constants. Interatomic effects are normally interpreted

[16] Noting that the molar susceptibility appears in eq (38) and an atomic χ_p in eqs (31) and (32), eqs (38) and (39) are equivalent to, and can be used to derive, eqs (31) and (32).

in terms of an RKKY type of spin distribution induced by the aligned spin moments on the magnetic ion sites. A variant of the two-band description of the nonmagnetic site Pauli shift has frequently proved useful, namely

$$\mathcal{K}(T)=\mathcal{K}_0+\mathcal{K}_{loc}(T), \tag{41}$$

where $\mathcal{K}_0$ is the Knight shift associated with the conduction band Pauli term and $\mathcal{K}_{loc}$ is the shift arising from the interatomic response to the aligned spin moment on the magnetic atom site. $\mathcal{K}_{loc}$, which is presumably responsible for the temperature dependence of $\mathcal{K}$, has the form

$$\mathcal{K}_{loc}(T)=\frac{2(g_J-1)}{g_J}H'_{eff}\chi_{loc}(T)/N\mu_B. \tag{42}$$

Here χ_{loc} is the Pauli susceptibility of either the local moment or band type associated with the moment induced on the local moment site. The $2(g_J-1)/g_J$ factor is included in anticipation of the rare earths, so that H'_{eff} is the hyperfine field at the nonmagnetic site per local *spin* moment (per molecule) at the magnetic site. The details of the conduction electron distribution arise in the sampling

$$H'_{eff}\sim\sum_R\rho(R), \tag{43}$$

where we have assumed that H'_{eff} arises from the contact interaction and the sum spans all interatomic radii, R, connecting all magnetic sites with a nonmagnetic atom. Efforts [216,217] have been made to relate such a sum to $\mathcal{K}$ values. These have been hampered by inadequate knowledge of $\rho(R)$. Asymptotic RKKY distributions were of necessity used, although it is the near R (nonasymptotic) region which is most important to H'_{eff}. More often the alternate approach of assuming that H'_{eff} effectively samples the *average* ρ, *i.e.*, the Pauli or Zener response to the local moment exchange field is used. Then

$$H'_{eff}=\mathcal{K}_\alpha\mathcal{J}/2\mu_B, \tag{44}$$

where $\mathcal{J}/2\mu_B$ is the exchange coupling per unit local moment between the local moment and the Fermi surface conduction electrons. $\mathcal{K}_\alpha$ is the Pauli response of the conduction electrons to this exchange field. If one assumes that the *average* hyperfine coupling in the RKKY disturbance equals that associated with Fermi surface states alone, then $\mathcal{K}_\alpha=\mathcal{K}_0$ and

$$\mathcal{K}(T)=\mathcal{K}_0[1+(g_J-1)\mathcal{J}\chi_{loc}(T)/g_JN\mu_B^2]. \tag{45}$$

Knowing $\mathcal{K}_0$ from an isostructural nonmagnetic compound, $\mathcal{J}$ can be estimated. Physically reasonable numbers for the exchange constants normally result. Even assuming that the average spin moment sampled is equal to the Pauli term in the RKKY response, it is not inevitable that $\mathcal{K}_\alpha$ should equal $\mathcal{K}_0$. The spin response involves states off E_F and the hyperfine coupling for these states can vary radically from that at E_F, as is indicated for the case of Cu in figure 11. Another possible shortcoming of the scheme is that the entire resonant scattering disturbance is not necessarily describable in terms of an effective exchange scattering. Although $\mathcal{J}$ can be numerically affected by factors other than exchange coupling, tabulation of shift results in this form can prove useful when comparing results in a sequence of intermetallic compounds. For example, Jones [206] has tabulated the nonmagnetic site Knight shift results of rare earth intermetallic compounds in terms of $\mathcal{J}$. The same results [205,218-230] are plotted in a different form in figure 31, namely in terms of $\xi\equiv H'_{eff}/H^{Al}_{eff}$. Atomic hyperfine behavior is thus normalized out, providing a crude estimate, in μ_B, of the spin moment residing at a nonmagnetic site due to the local moment disturbance. The resulting ξ's are an order of magnitude smaller than those appropriate to the transition metal alloys (compare with figure 28) implying much weaker magnetic perturbations in rare earth compounds.[17] The ξ's appear to be in three distinct groups; the Al compounds, the P, As and Sb compounds, and those involving elements in the 6*s*-6*p*-5*d* row of the periodic table. (Data also exist for two hexaborides yielding ξ's of ~ -0.005.) We presume the grouping is associated with band and wave function character specific to the various sets of compounds. More interesting than the grouping is the variation in ξ across the rare earth row; ξ is largest at the Ce end, falling and becoming relatively constant for the heavy rare earths. The trend is very different than that seen for 3*d*-moments in figure 28 and appears characteristic of rare earth 4*f*-moment effects. This trend was first observed in electron spin and nuclear resonance of the $REAl_2$ compounds [202,205] and subsequently in ESR of rare earth impurities in Pd [203]. The negative sign of ξ suggests that hybridization polarization effects dominate. One contributing factor to the large ξ at the Ce end is the well-known tendency for the occupied 4*f* levels to be close to E_F. The resulting small energy

[17] This comparison underestimates the drop in polarization because the ξ values natural to ordered intermetallic compounds are intrinsically larger than those in alloys by the nature of the differing definition of these two ξ factors. For example, the ξ appropriate to the intermetallic compounds $REAl_2$ and $REAl_3$ (see fig. 31) are larger than those for the RE-Al alloys.

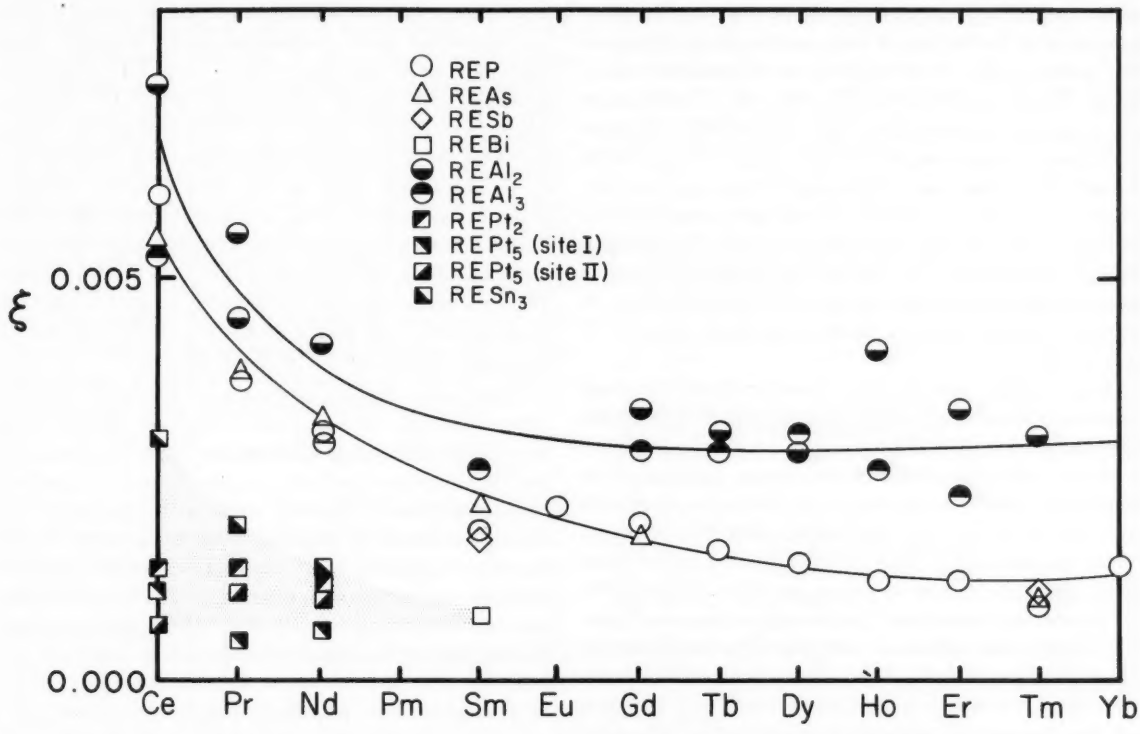

FIGURE 31. *Behavior of Knight's ξ factor as defined in the text, for the light metal site in rare earth intermetallic compounds. The data are from a number of sources [205, 218-230], as collected in tabular form by Jones [206].*

denominators tend to enhance hybridization, and hence ξ. An example of this 4*f* behavior is that a phase transition occurs in metallic Ce, one phase involving no 4*f* electrons, and the other, one.

Positive, strongly temperature dependent $\mathcal{K}$'s have been observed for nonmagnetic sites in UAl_2 [216] and USn_3 [231]. The susceptibility behavior suggests the presence of 5*f* band paramagnetism, rather than local moment paramagnetism. The resulting ξ's (~ 0.1 to 0.3) for the two compounds are opposite in sign and substantially larger than the values appropriate to the isostructural rare earth compounds (fig. 31). The authors [216,231] pointed out that the results could arise from several percent Al (or Sn) valence *s*-orbital hybridization into the 5*f* bands at E_F and/or from RKKY polarization with quite reasonable $\mathcal{J}$ values. The positive sign of the ξ's implies that electrostatic exchange then dominates. The $\mathcal{K}$ versus χ plots for the two compounds also indicated the presence of a strong χ_{orb} term associated with 5*f* character at the U sites, which makes no contribution to the Al (or Sn) site $\mathcal{K}$.

Abundant data exist for a variety of transition metal compounds. In some of the more magnetic systems the results are strongly dependent on metallurgical details of the samples. For example, NiAl, CoAl and FeAl have been studied by West [232,233] and by Seitchik and Walmsley [217,234] at and off stoichiometry. West found that the Co susceptibility results in CoAl are very sensitive to the thermal history. These results suggested nonequilibrium magnetic clustering. The effects of thermal history on the Knight shift are less important, because the number of atoms near clusters is small and do not contribute sensibly to the observed resonance. Despite these difficulties there are several distinct features of the results which give insight into the character of these compounds. First, the Al shift in FeAl is negative and temperature dependent, suggesting the existence of intersite effects of the sort encountered in the Al alloys and the V_3X compounds. Second, while the Co shift can be strongly temperature dependent (depending on Co concentration), the Al shift in CoAl is small and is effectively independent of temperature (not depending on Co concentration). From this it was concluded that there is little Al *s*-character in the Fermi surface states of CoAl. The slope of a $\mathcal{K}$(Co) versus χ plot, using composition as the intrinsic parameter, is negative at room temperature and positive at low temperature. Thus there are at least two par-

383-876 O - 70 - 10

tially cancelling temperature dependent mechanisms operative at the Co site in this system. West attributed the positive slope to a temperature dependent orbital term. Finally in NiAl, the Al shift, the Al relaxation time, and the susceptibility are characteristic of an *s*-band metal, suggesting that Al electrons "fill" the Ni 3*d* band. This does not imply that there are ten 3*d*-electrons at a Ni site in NiAl, just as there aren't at a Cu site in pure Cu (see discussion of fig. 11). Instead, charge effects have so affected the bands that there is no substantial *d*-band character at or within kT of E_F. A similar situation appears to occur in dilute alloys of Ni in Cu [235].

Knight shift results have been obtained for both transition metal sites and nonmagnetic sites in itinerant ferromagnets [236,237,14] such as $ZrZn_2$. These systems are characterized by having ferromagnetic saturation moments, q_s, which are small compared with *effective* moments, q_c, associated with the paramagnetic susceptibility. This implies a band rather than local Heisenberg type of ferromagnetism. A plot of the q_c/q_s ratio for a variety of compounds is shown in figure 32. These were obtained with the Rhodes-Wohlfarth "intermediate model" [238]. There has been some uncertainty as to whether magnetic impurities drive some of the "itinerant" systems ferromagnetic. In cases,

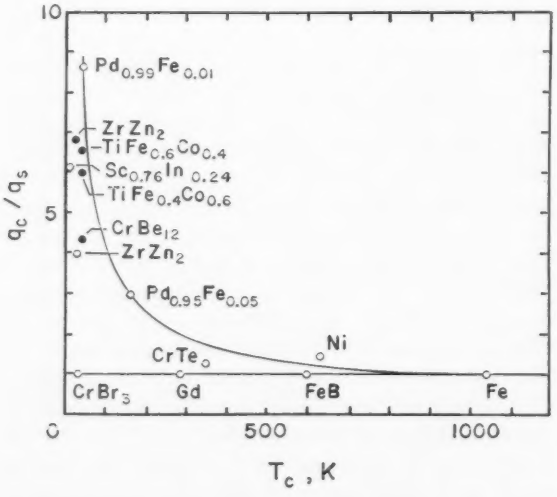

FIGURE 32. *The ratio q_c/q_s of the number of magnetic carriers deduced from the paramagnetic Curie-Weiss constant to the number deduced from the saturation magnetization. Datum points are identified by Rhodes and Wohlfarth [238] and Swartz* et al. *[15].*

such as $CrBe_{12}$ [237], the NMR lines are sharp and the hyperfine fields track the magnetization, indicating that the ferromagnetism is a bulk effect, whether or not triggered by impurities. The slopes of the $\mathcal{K}$ versus χ plots for hyperfine fields associated with magnetic atom sites, such as Zr in $ZrZn_2$, or Fe or Co in $TiFe_xCo_{1-x}$, are generally small, ranging between 0 and ± 100 kOe/μ_B. Similar small fields occur for Ti in paramagnetic $TiBe_2$, and V in the V_3X compounds, suggesting the presence of band effects such as *s-d* hybridization. Weaker hyperfine constants occur at nontransition metal sites in the itinerant ferromagnets, implying that only weak intersite effects are present in this class of compounds. This contrasts with the X site behavior of the localized paramagnetic V_3X systems which we believe is due, in large part, to substantial intersite effects.

There are a number of examples where $\mathcal{K}$ versus χ plots, with $\langle a \rangle$ assumed constant, have proven to be very useful. This is not always the case. For example, the Ga resonance in $AuGa_2$ is temperature dependent [12] and while $\mathcal{K}$ follows χ quite faithfully, T_1 data indicate a substantial variation with temperature in the contact *s* contribution to $\langle a \rangle$. This has led to a model of thermal population of an *s* band [239], which, however, does not explain the susceptibility behavior. As of yet, this system is not completely understood.

14. Summary

In this paper, we have dealt with the Knight shift and its interpretation in terms of various models of the electronic behavior in metals, emphasizing recent developments. It is apparent that the relation of the Knight shift to the density of states is complicated, but there are compensations in that a large amount of closely related and more intricate information may be deduced from Knight shift studies in metals, compounds and alloy systems. Information may be obtained concerning the wave functions of the electrons at the Fermi surface as probed at the resonating nuclei. Contributions to $\mathcal{K}$ can be separated into terms arising from *s*-electron and *d*-electron character, and in some instances there are indications of contributions due to *p*-character. In addition, orbital and diamagnetic contributions can be deduced at times. We have discussed most of the methods with which one obtains wavefunction insight from Knight shifts. This wavefunction information is related directly to $N(E)$ and is needed in the evaluation of $\langle a \rangle$. The relations between $\mathcal{K}$, $\langle a \rangle$, and the density of states are shown quantitatively in several equations throughout the text.

These same equations display the unique relation of $\mathcal{K}$ with a *local* density of states due to the weighted averaging associated with $\langle a \rangle$. This becomes useful particularly in the case of intermetallic compounds and

less so for alloys where atoms occupy positions with a random arrangement. Often it is preferable to absorb this randomness into $\langle a \rangle$. In intermetallic compounds, the Knight shift behavior definitely suggests a description in terms of wavefunctions *and* densities of states that are different for inequivalent sites. In such a situation the magnetic response of one site to another is of concern. In other words now there are *inter-* as well as *intra*-atomic effects. In the case of pure metals this complication also arises but is hidden in $\langle a \rangle$.

In this Symposium, a number of advanced theoretical and experimental techniques for studying the electron density of states have been discussed. It is to be hoped that fruitful correlations between these methods and Knight shifts will be obtained in the future.

15. Acknowledgments

Valuable assistance with the bibliographical aspects and preparation of the Knight shift tables, by D. J. Kahan of the Alloy Data Center (part of the National Standard Reference Data System) is gratefully acknowledged. Useful suggestions and comments by T. J. Rowland, M. N. Alexander, A. T. Fromhold and I. D. Weisman have aided in preparation of this manuscript. We wish to thank J. A. Hofmann for making a draft of his work [156] available to us prior to publication.

16. References

[1] Knight, W. D., Phys. Rev. **76,** 1259 (1949).
[2] Townes, C. H., Herring, C., and Knight, W. D., Phys. Rev. **77,** 852 (1950).
[3] Knight, W. D., Solid State Phys. **2,** 93 (1956).
[4] Rowland, T. J., Prog. Materials Sci. **9,** 1 (1961).
[5] Drain, L. E., Metallurgical Rev. **119,** 195 (1967).
[6] Rowland, T. J., and Borsa, R., Phys. Rev. **134,** A743 (1964).
[7] Bennett, L. H., Mebs, R. W., and Watson, R. E., Phys. Rev. **171,** 611 (1968).
[8] Watson, R. E., Bennett, L. H., and Freeman, A. J., Phys. Rev. Letters **20,** 653 (1968); ibid. **20,** 1221 (1968); Phys. Rev. **179,** 590 (1969).
[9] Bennett, L. H., Phys. Rev. **150,** 418 (1966).
[10] Watson, R. E., and Freeman, A. J., in Hyperfine Interactions, A. J. Freeman and R. B. Frankel, Editors (Academic Press, N.Y. 1967) p. 53.
[11] Bagus, P. S., Liu, B., and Schaefer, H. F., III, Phys. Rev. **A** (to be published Sept. 1970).
[12] Jaccarino, V., Weger, M., Wernick, J. H., and Menth, A., Phys. Rev. Letters **21,** 1811 (1968).
[13] Clogston, A. M., and Jaccarino, V., Phys. Rev. **121,** 1357 (1961).
[14] Bennett, L. H., Swartzendruber, L. J., and Watson, R. E., Phys. Rev. **165,** 500 (1968).
[15] Swartz, J. C., Bennett, L. H., Swartzendruber, L. J., and Watson, R. E., Phys. Rev. **B1,** 146 (1970).
[16] Winkler, R., Phys. Letters **23,** 301 (1966).
[17] Pleiter, F., (private communication).
[18] Kubo, R., and Obata, Y., J. Phys. Soc. Japan **11,** 547 (1956).
[19] Orgel, L. E., J. Phys. Chem. Solids **21,** 123 (1961).
[20] Clogston, A. M., Jaccarino, V., and Yafet, Y., Phys. Rev. **134,** A650 (1964); Clogston, A. M., Gossard, A. C., Jaccarino, V., and Yafet, Y., Phys. Rev. Letters **9,** 262 (1962); Jaccarino, V., Proc. Col. Ampère **13,** 22 (1964).
[21] Narath, A., and Fromhold, A. T., Jr., Phys. Rev. **139,** A794 (1965).
[22] Clogston, A. M., Gossard, A. C., Jaccarino, V., and Yafet, Y., Rev. Mod. Phys. **36,** 170 (1964).
[23] Barnes, R. G., and Graham, T. P., Phys. Rev. Letters **8,** 248 (1962); Denbigh, J. S., and Lomer, W. M., Proc. Phys. Soc. (London) **82,** 156 (1963).
[24] Butterworth, J., Proc. Phys. Soc. (London) **83,** 71 (1964); Erratum, *ibid.* **83,** 893 (1964).
[25] Seitchik, J., Jaccarino, V., and Wernick, J. H., Bull. Am. Phys. Soc. **10,** 317 (1965).
[26] Andersson, L. O., Phys. Letters **26A,** 279 (1968).
[27] Korringa, J., Physica **16,** 601 (1950).
[28] Herring, C., in Magnetism, G. T. Rado and H. Suhl, Editors (Academic Press, N.Y. 1966) **Vol. IV,** Section III.
[29] Silverstein, S. D., Phys. Rev. **128,** 631 (1962); and Silverstein, S. D., Phys. Rev. **130,** 912 (1963).
[30] Wolff, P. A., Phys. Rev. **120,** 814 (1960).
[31] Wolff, P. A., Phys. Rev. **129,** 84 (1963).
[32] Herring, C., in Magnetism, G. T. Rado and H. Suhl, Editors (Academic Press, N.Y. 1966) **Vol. IV,** Sections X and XII.
[33] Hurd, C. M., and Coodin, P., J. Phys. Chem. Solids 28, 523 (1967).
[34] Schumacher, R. T., and Slichter, C. P., Phys. Rev. **101,** 58 (1956).
[35] Schumacher, R. T., and Vehse, W. E., J. Phys. Chem. Solids **24,** 297 (1963).
[36] Schumacher, R. T., and Vander Ven, N. S., Phys. Rev. **144,** 357 (1966).
[37] Hultgren, R. R., Orr, R. L., Anderson, P. D., and Kelley, K. K., Selected Values of Thermodynamic Properties of Metals and Alloys (John Wiley & Sons, Inc., N.Y. 1963) and Addenda (unpublished).
[38] O'Sullivan, W. J., Switendick, A. C., and Schirber, J. E., this Symposium.
[39] Ziman, J. M., Advances in Phys. **16,** 421 (1967).
[40] Kohn, W., Phys. Rev. **96,** 590 (1954).
[41] Kjeldaas, T., Jr., and Kohn, W., Phys. Rev. **101,** 66 (1956).
[42] Cohen, M. H., Goodings, D. A., and Heine, V., Proc. Phys. Soc. (London) **73,** 811 (1959).
[43] Jones, H., and Schiff, B., Proc. Phys. Soc. (London) **67A,** 217 (1954).
[44] Holland, B. W., Phys. Stat. Solidi **28,** 121 (1968).
[45] Micah, E. T., Stocks, G. M., and Young, W. H., J. Phys. C (Solid St. Phys.) **2,** 1653 (1969); Meyer, A., Stocks, G. M., and Young, W. H., this Symposium.
[46] Kmetko, E. A., this Symposium.
[47] Pauling, L., Proc. Roy. Soc. **196A,** 343 (1949).
[48] Micah, E. T., Stocks, G. M., and Young, W. H., J. Phys. C (Solid St. Phys.) **2,** 1661 (1969).
[49] Shyu, Wei-Mei, Das, T. P., and Gaspari, G. D., Phys. Rev. **152,** 270 (1966).
[50] Pomerantz, M. and Das, T. P., Phys. Rev. **119,** 70 (1960).
[51] Shyu, Wei-Mei, Gaspari, G. D., and Das, T. P., Phys. Rev. **141,** 603 (1966).
[52] Jena, P., Mahanti, S. D., and Das, T. P., Phys. Rev. Letters **20,** 544 (1968); ibid. **20,** 977 (1968).

[53] Gerstner, J., and Cutler, P. H., Phys. Letters **30A,** 368 (1969), and this Symposium.
[54] Gaspari, G. D., and Das, T. P., Phys. Rev. **167,** 660 (1968).
[55] Jena, P., Das, T. P., Mahanti, S. D., and Gaspari, G. D., this Symposium.
[56] Moore, R. A., and Vosko, S. H., Canadian J. Phys. **46,** 1425 (1968).
[57] Moore, R. A., and Vosko, S. H., Canadian J. Phys. **47,** 1331 (1969).
[58] Hartree, D. R., Hartree, W., and Swirles, B., Phil. Trans. Royal Soc. (London) **A238,** 229 (1939).
[59] Kabartas, Z. V., Kavetskis, V. I., and Yutsis, A. P., JETP **2,** 481 (1956).
[60] Linderberg, J., and Shull, H., J. Mol. Spectros. **5,** 1 (1960).
[61] Watson, R. E., Ann. Phys. **13,** 250 (1961).
[62] Knight, W. D., Berger, A. G., and Heine, V., Ann. Phys. (N.Y.) **8,** 173 (1959).
[63] Feldman, D., Ph. D. Thesis, University of California, Berkeley, (1959).
[64] Seymour, E. F. W., and Styles, G. A., Phys. Letters **10,** 269 (1964).
[65] Borsa, F., and Barnes, R. G., J. Phys. Chem. Solids **27,** 567 (1966).
[66] Sharma, S. N., and Williams, D. L., Colloque Ampère **XIV,** 480 (1967).
[67] Dickson, E. M., Phys. Rev. **184,** 294 (1969).
[68] Kasowski, R. V., and Falicov, L. M., Phys. Rev. Letters **22,** 1001 (1969).
[69] Schone, H. E., Phys. Rev. Letters **13,** 12 (1964).
[70] Shaw, R. W., and Smith, N. V., Phys. Rev. **178,** 985 (1969).
[71] Matzkanin, G. A., and Scott, T. A., Phys. Rev. **151,** 360 (1966).
[72] Kushida, T., and Rimai, L., Phys. Rev. **143,** 157 (1966).
[73] Allen, P. S., and Seymour, E. F. W., Proc. Phys. Soc. (London) **85,** 509 (1965); Warren, W. W., Jr., and Clark, W. G., Phys. Rev. **177,** 600 (1969).
[74] Drain, L. E., Phil. Mag. **4,** 484 (1959).
[75] Umeda, J., Kusumoto, H., Narita, K., and Yamada, E., J. Chem. Phys. **42,** 1458 (1965).
[76] Adler, D., Solid State Physics **21,** 1 (1968).
[77] Sundfors, R. K., and Holcomb, D. F., Phys. Rev. **136,** A810 (1964).
[78] Alexander, M. N., and Holcomb, D. F., Revs. Mod. Phys. **40,** 815 (1968).
[79] Alexander, M. N., and Holcomb, D. F., Solid State Communications **6,** 355 (1968).
[80] O'Reilly, D. E., J. Chem. Phys. **41,** 3729 (1964).
[81] Acrivos, J. V., and Pitzer, K. S., J. Phys. Chem. **66,** 1693 (1962).
[82] McConnell, H. M., and Holm, C. H., J. Chem. Phys. **26,** 1517 (1957).
[83] Hughes, T. R., Jr., J. Chem. Phys. **38,** 202 (1963).
[84] Bardeen, J., Cooper, L. J., and Schrieffer, J. R., Phys. Rev. **106,** 162 (1951); **108,** 1175 (1957).
[85] Yosida, K., Phys. Rev. **110,** 769 (1958).
[86] Ferrell, R. A., Phys. Rev. Letters **3,** 262 (1959).
[87] Anderson, P. W., Phys. Rev. Letters **3,** 325 (1959).
[88] Wright, F., Jr., Phys. Rev. **163,** 420 (1967).
[89] Appel, J., Phys. Rev. **139,** A1536 (1965).
[90] Das, T. P., and Sondheimer, E. H., Phil. Mag. **5,** 529 (1960).
[91] Yafet, Y., J. Phys. Chem. Solids **21,** 99 (1961).
[92] Williams, B. F., and Hewitt, R. R., Phys. Rev. **146,** 286 (1966).
[93] Christensen, R. L., Hamilton, D. R., Bennewitz, H. G., Reynolds, J. B., and Stroke, H. H., Phys. Rev. **122,** 1302 (1961).
[94] Bloembergen, N., and Rowland, T. J., Acta. Met. **1,** 731 (1953).
[95] Schone, H. E., and Knight, W. D., Acta. Met. **11,** 179 (1963).
[96] Bennett, L. H., Acta Met. **14,** 997 (1966).
[97] Setty, D. L. Radhakrishna, and Mungurwadi, B. D., Phys. Rev. **183,** 387 (1969).
[98] Watson, R. E., Bennett, L. H., Weisman, I. D., and Carter, G. C. (to be published).
[99] Reynolds, J. M., Goodrich, R. G., and Khan, S. A., Phys. Rev. Letters **16,** 609 (1966).
[100] Khan, S. A., Reynolds, J. M., and Goodrich, R. G., Phys. Rev. **163,** 579 (1967).
[101] Kaplan, J. I., J. Phys. Chem. Solids **23,** 826 (1962).
[102] Stephen, M., Phys. Rev. **123,** 126 (1961).
[103] Dolgopolov, D. G., and Bystrik, P. S., Sov. Phys. JETP **19,** 404 (1964).
[104] Dolgopolov, D. G., Phys. Metal Metaloved **22(3),** 6 (1967).
[105] Hebborn, J. E., Proc. Phys. Soc. (London) **80,** 1237 (1962).
[106] Hebborn, J. E., and Stephen, M. J., Proc. Phys. Soc. (London) **80,** 991 (1962).
[107] Glasser, M. L., Phys. Rev. **150,** 234 (1966).
[108] Goodrich, R. G., Khan, S. A., and Reynolds, J. M., Phys. Rev. Letters **23,** 767 (1969).
[109] Seitchik, J. A., Gossard, A. C., and Jaccarino, V., Phys. Rev. **136,** A1119 (1964).
[110] Mott, N. F., and Jones, H., The Theory of the Properties of Metals and Alloys, (Clarendon Press, N.Y. 1936).
[111] Misetich, A., Hodges, L., and Watson, R. E. (unpublished).
[112] Hodges, L., Ehrenreich, H., and Lang, N. D., Phys. Rev. **152,** 505 (1966).
[113] Ehrenreich, H., and Hodges, L., Methods in Comp. Physics **8,** 149 (1968).
[114] Watson, R. E., Ehrenreich, H., and Hodges, L., Phys. Rev. Letters **24,** 829 (1970).
[115] Mueller, F. M., this Symposium.
[116] Goodings, D. A., and Harris, R., Phys. Rev. **178,** 1189 (1969), and J. Phys. C. **2,** 1808 (1969).
[117] Dobbyn, R. C., Williams, M. W., Cuthill, J. R., and McAlister, A. J., Phys. Rev. **2B** (to be published).
[118] Davis, H., Phys. Letters **28A,** 85 (1968).
[119] Seitchik, J., Jaccarino, V., and Wernick, J. H., Phys. Rev. **138,** A148 (1965).
[120] Kobayashi, S., Asayama, K., and Itoh, J., J. Phys. Soc. (Japan) **18,** 1735 (1963).
[121] Narath, A., J. Appl. Phys. **39,** 553 (1968).
[122] Itoh, J., Asayama, K., and Kobayashi, S., Proc. Col. Ampère **13,** 162 (1964).
[123] Froidevaux, C., Gautier, F., and Weisman, I., Proc. Col. Ampère **13,** 114 (1964).
[124] Balabanov, A., and Delyagin, N., Soviet Phys. JETP 27, 752 (1968).
[125] Shirley, D. A., and Westenbarger, G. A., Phys. Rev. **138,** A170 (1965).
[126] Stern, E. A., Phys. Rev. **157,** 544 (1967) and in Energy Bands in Metals and Alloys, L. H. Bennett and J. T. Waber, Editors (Gordon and Breach, 1968) p. 151.
[127] Watson, R. E., in Hyperfine Interactions, A. J. Freeman and R. B. Frankel, Editors (Academic Press, N.Y., 1967) p. 413.
[128] Kohn, W., and Vosko, S. H., Phys. Rev. **119,** 912 (1960).
[129] Rowland, T. J., Phys. Rev. **119,** 900 (1960).
[130] Drain, L. E., J. Phys. C. **1,** 1690 (1968).

[131] Redfield, A. G., Phys. Rev. **130,** 589 (1963).
[132] Fernelius, N. C., Thesis, University of Illinois (1966); Proc. Colloque Ampère **14,** 497 (1967); ibid. **15,** 347 (1968).
[133] Minier, M., Phys. Letters **26A,** 548 (1968); Minier, M., and Berthier, Cl., Proc. Colloque Ampère **15,** 368 (1968); Minier, M., Phys. Rev. **182,** 437 (1969).
[134] Blandin, A., and Daniel, E., J. Phys. Chem. Solids **10,** 126 (1959).
[135] Asik, J. R., Ball, M. A., and Slichter, C. P., Phys. Rev. **181,** 645 (1969).
[136] Ball, M. A., Asik, J. R., and Slichter, C. P., Phys. Rev. **181,** 662 (1969).
[137] Vonsovski, S., JETP **16,** 981 (1946); ibid. **24,** 419 (1953).
[138] Ruderman, M. A., and Kittel, C., Phys. Rev. **96,** 99 (1954); Mitchell, A. H., Phys. Rev. **105,** 1439 (1957).
[139] Kasuya, T., Prog. Theoret. Phys. **16,** 45 (1956).
[140] Yosida, K., Phys. Rev. **106,** 893 (1957).
[141] Condon, E. U., and Shortley, G. H., The Theory of Atomic Spectra (University Press, Cambridge, 1964).
[142] Anderson, P. W., and Clogston, A. M., Bull. Am. Phys. Soc. **6,** 124 (1961).
[143] Schrieffer, J. R., and Wolff, P. A., Phys. Rev. **149,** 491 (1966).
[144] Watson, R. E., Koide, S., Peter, M., and Freeman, A. J., Phys. Rev. **139,** A167 (1965).
[145] Watson, R. E., and Freeman, A. J., J. Appl. Phys. **37,** 1444 (1966).
[146] Jaccarino, V., Matthias, B. T., Peter, M., Suhl, H., and Wernick, J. H., Phys. Rev. Letters **5,** 251 (1960).
[147] Peter, M., J. Appl. Phys. **32,** 338S (1961).
[148] Peter, M. Shaltiel, D., Wernick, J. H., Williams, H. J., Mock, J. B., and Sherwood, R. C., Phys. Rev. **126,** 1395 (1962).
[149] Shaltiel, D., Wernick, J. H., Williams, H. J., and Peter, M., Phys. Rev. **135,** A1346 (1964).
[150] Rowland, T. J., Phys. Rev. **125,** 459 (1962).
[151] Weisman, I. D., and Knight, W. D., Phys. Rev. **169,** 373 (1968).
[152] Wolff, P. A., Phys. Rev. **120,** 814 (1960).
[153] Wolff, P. A., Phys. Rev. **129,** 84 (1963).
[154] Giovannini, B., Peter, M., Schrieffer, J. R., Phys. Rev. Letters **12,** 736 (1964).
[155] Alexander, M. N., Phys. Rev. **172,** 331 (1968).
[156] Senturia, S. D., Smith, A. C., Hewes, C. R., Hofmann, J. A., and Sagalyn, P. L., Phys. Rev. B, **Vol. 1,** 40–45 (1970).
[157] Van Ostenburg, D. O., Lam, D. J., Trapp, H. D., and MacLeod, D. E., Phys. Rev. **128,** 1550 (1962).
[158] Drain, L. E., J. Phys. Radium **23,** 745 (1962).
[159] Lam, D. J., Van Ostenburg, D. O., Nevitt, M. W., Trapp, H. D., and Pracht, D. W., Phys. Rev. **131,** 1428 (1963); ibid. **133I,** 1 (1964).
[160] Bernasson, M., Descouts, P., Donzé, P., and Treyvaud, A., J. Phys. Chem. Solids **30,** 2453 (1969).
[161] Betsuyaku, H., Takagi, Y., and Betsuyaku, Y., J. Phys. Soc. Japan **19,** 1089 (1964).
[162] Zamir, D., Phys. Rev. **140,** A271 (1965).
[163] Van Ostenburg, D. O., Lam, D. J., Shimizu, M., and Katsuki, A., J. Phys. Soc. Japan **18,** 1744 (1963).
[164] Masuda, Y., Nishioka, M., and Watanabe, J. Phys. Soc. Japan **22,** 238 (1967).
[165] Taniguchi, S., Tebble, R. S., and Williams, D. E. G., Proc. Roy. Soc. **265A,** 502 (1962).
[166] Cheng, C. H., Gupta, K. P., Van Reuth, E. C., and Beck, P. A., Phys. Rev. **126,** 2030 (1962).
[167] Gupta, K. P., Cheng, C. H., and Beck, P. A., Metallic Solid Solutions, J. Friedel and A. Guinier, Editors, (W. A. Benjamin, Inc., N.Y., 1963) chapter 25.
[168] Morin, F. J., and Maita, J. P., Phys. Rev. **129,** 1115 (1963).
[169] Rohy, D., and Cotts, R. M., Phys. Rev. **1B,** 2070 (1970).
[170] Rohy, D., and Cotts, R. M., Phys. Rev. **1B,** 2484 (1970).
[171] Swartz, J. C., Swartzendruber, L. J., Bennett, L. H., and Watson, R. E., Phys. Rev. **B1,** 146 (1970).
[172] Bennett, L. H., Swartzendruber, L. J., and Watson, R. E., Phys. Rev. **165,** 500 (1968).
[173] Bos, W. G., and Gutowsky, H. S., O.N.R. Tech. Rept. No. 93, (available as AD-640514) (1966).
[174] Schreiber, D. S., Phys. Rev. **137,** A860 (1965).
[175] Alfred, L. C. R., and Van Ostenburg, D. O., Phys. Rev. **161,** 569 (1967).
[176] Kohn, W., and Vosko, S. H., Phys. Rev. **119,** 912 (1960).
[177] Blatt, F. J., Phys. Rev. **108,** 285 (1957).
[178] Odle, R. L., and Flynn, C. P., Phil. Mag. **13,** 699 (1966).
[179] Snodgrass, R. J., and Bennett, L. H., Phys. Rev. **134,** A1294 (1964).
[180] Heighway, J., and Seymour, E. F. W., Phys. Letters **29A,** 282 (1969).
[181] Seymour, E. F. W., and Styles, G. A., Proc. Phys. Soc. (London) **87,** 473 (1966).
[182] Anderson, W. T., Jr., Thatcher, F. C., and Hewitt, R. R., Phys. Rev. **171,** 541 (1968).
[183] Kaeck, J. A., Ph. D. Thesis University of Cornell, N.Y. (1968).
[184] Van der Molen, S. B., Van der Lugt, W., Draisma, G. G., and Smit, W., Physica **38,** 275 (1968).
[185] Van der Molen, S. B., Van der Lugt, W., Draisma, G. G., and Smit, W., Physica **40,** 1 (1968).
[186] Van der Lugt, W., and Van der Molen, S. B., Phys. Stat. Solid **19,** 327 (1967).
[187] Seymour, E. F. W., Styles, G. A., and Taylor, B., Proc. Col. Ampère **11,** 612 (1962).
[188] Seymour, E. F. W., and Styles, G. A., Proc. Phys. Soc. (London) **87,** 473 (1966).
[189] Slocum, R. R., Ph. D. Thesis, College of William and Mary, Virginia (1969).
[190] Van Hemmen, J. L., Caspers, W. J., Van der Molen, S. B., Van der Lugt, W., and Van de Braak, H. P., Z Physik **222,** 253 (1969).
[191] Rigney, D. A., and Flynn, C. P., Phil. Mag. **15,** 1213 (1967).
[192] Moulson, D. J., and Seymour, E. F. W., Advan. Phys. **16,** 449 (1967).
[193] Bennett, L. H., Cotts, R. M., and Snodgrass, R. J., Proc. Colloque Ampère **13,** 171 (1965).
[194] Matzkanin, G. A., Spokas, J. J., Sowers, C. H., Van Ostenburg, D. O., and Hoeve, H. C., Phys. Rev. **181,** 559 (1969).
[195] Wells, J. C., Jr., Williams, R. L., Jr., Pfeiffer, L., and Madansky, L., Phys. Letters **27B,** 448 (1968).
[196] Gardner, J. A., and Flynn, C. P., Phil. Mag. **15,** 1233 (1967).
[197] Flynn, C. P., Rigney, D. A., and Gardner, J. A., Phil. Mag. **15,** 1255 (1967).
[198] Rao, G. N., Matthias, E., and Shirley, D. A., Phys. Rev. **184,** 325 (1969).
[199] Clogston, A. M., Matthias, B. T., Peter, M., Williams, H. J., Corenzwit, E., and Sherwood, R. C., Phys. Rev. **125,** 541 (1962).
[200] Stupian, G. W., and Flynn, C. P., Phil. Mag. **17,** 295 (1968).
[201] Van Vleck, J. H., Theory of Electric and Magnetic Susceptibilities, (Oxford University Press, 1932).

[202] Peter, M., Shaltiel, D., Wernick, J. H., Williams, H. J., Mock, J. B., and Sherwood, R. C., Phys. Rev. **126,** 1395 (1962).
[203] Shaltiel, D., Wernick, J. H., Williams, H. J., and Peter, M., Phys. Rev. **135,** A1346 (1964).
[204] Cragle, J., Phys. Rev. Letters **13,** 569 (1964).
[205] Jaccarino, V., Matthias, B. T., Peter, M., Suhl, H., and Wernick, J. H., Phys. Rev. Letters **5,** 251 (1960).
[206] Jones, E. D., Phys. Rev. **180,** 455 (1968).
[207] Jones, E. D., Phys. Rev. Letters **19,** 432 (1967).
[208] Shulman, R. G., Wyluda, B. J., and Matthias, B. T., Phys. Rev. Letters **1,** 278 (1958).
[209] Blumberg, W. E., Eisinger, J., Jaccarino, V., and Matthias, B. T., Phys. Rev. Letters **5,** 149 (1960).
[210] Weger, M., (to be published).
[211] Gossard, A. C., Phys. Rev. **149,** 246 (1966); Errata, ibid. **164,** 878 (1967) and **185,** 862 (1969).
[212] Labbé, J., and Friedel, J., J. Physique **27,** 153 (1966).
[213] Mattheiss, L. F., Phys. Rev. **138,** A112 (1965).
[214] Shulman, R. G., Wyluda, B. J., and Matthias, B. T., Phys. Rev. Letters **1,** 278 (1958).
[215] Lütgemeier, H., Z. Naturforsch. **20A,** 246 (1965).
[216] Gossard, A. C., Jaccarino, V., and Wernick, J. H., Phys. Rev. **128,** 1038 (1962).
[217] Seitchik, J. A., and Walmsley, R. H., Phys. Rev. **137,** A143 (1965).
[218] Cooper, B. R., Phys. Letters **22,** 244 (1966).
[219] Jaccarino, V., J. Appl. Phys. **32S,** 102 (1961).
[220] Jones, E. D., and Busick, J. I., J. Appl. Phys. **37,** 1250 (1966).
[221] Barnes, R. G., and Jones, E. D., Solid State Comm. **5,** 285 (1967).
[222] de Wijn, H. W., van Diepen, A. M., and Buschow, K. H. J., Phys. Rev. **161,** 253 (1967).
[223] van Diepen, A. M., de Wijn, H. W., and Buschow, K. H. J., J. Chem. Phys. **46,** 3489 (1967).
[224] Buschow, K. H. J., van Diepen, A. M., and de Wijn, H. W., Phys. Letters **24A,** 536 (1967).
[225] van Diepen, A. M., de Wijn, H. W., and Buschow, K. H. J., Phys. Letters **26A,** 340 (1968).
[226] Gossard, A. C., and Jaccarino, V., Proc. Phys. Soc. (London) **80,** 877 (1962).
[227] Vijayaraghavan, R., Malik, S. K., and Rao, V. U. S., Phys. Rev. Letters **20,** 106 (1968).
[228] Barnes, R. G., Borsa, F., and Peterson, D., J. Appl. Phys. **36,** 940 (1965).
[229] Rao, V. U. S., and Vijayaraghavan, R., Phys. Letters **19,** 168 (1965).
[230] Borsa, F., Barnes, R. G., and Reese, R. A., Phys. Status Solidi **19,** 359 (1967).
[231] Rao, V. U. S., and Vijayaraghavan, R., J. Phys. Chem. Sol. **29,** 123 (1968).
[232] West, G., Phil. Mag. **9,** 979 (1964).
[233] West, G., Phil. Mag. **15,** 855 (1967).
[234] Seitchik, J., and Walmsley, R. H., Phys. Rev. **131,** 1473 (1963).
[235] Asayama, K., J. Phys. Soc. Japan **18,** 1727 (1963).
[236] Yamadaya, T., and Asanuma, M., Phys. Rev. Letters **15,** 695 (1965).
[237] Wolcott, N. M., Falge, R. L., Jr., Bennett, L. H., and Watson, R. E., Phys. Rev. Letters **21,** 546 (1968).
[238] Rhodes, P., and Wohlfarth, E. P., Proc. Roy. Soc. (London) **273A,** 247 (1963).
[239] Switendick, A. C., and Narath, A., Phys. Rev. Letters **22,** 1423 (1969).

(Paper 74A4–624)

JOURNAL OF RESEARCH of the National Bureau of Standards—A. Physics and Chemistry
Vol. 74A, No. 4, July–August 1970

Publications of the National Bureau of Standards*

Selected Abstracts

Achenbach, P. R., Project Director and Coordinator, **Investigation of performance characteristics for sanitary plumbing fixtures,** *Nat. Bur. Stand. (U.S.), Bldg. Sci. Ser. 22, 72 pages (Jan. 1970), 70 cents, SD Catalog No. C13.29/2:22.*

Key words: Abrasion resistance; chemical resistance; cigarette-burn resistance; cleanability and soilability; concentrated static-load capacity; performance characteristics; performance level; sanitary plumbing fixtures; scratch resistance; stain resistance; surface-impact resistance; test methods.

This report gives findings and recommendations developed during an investigation of performance characteristics for sanitary plumbing fixtures, conducted at the request of the Building Research Advisory Board of the National Academy of Sciences—National Research Council. The report describes the test methods that are recommended for the evaluation of 16 performance characteristics, and the nature of further work required to complete the development of four or five additional test procedures.
The suitability of various existing test methods for evaluating the functional and performance characteristics of sanitary plumbing fixtures was investigated in the laboratory. In addition, new or modified tests for certain characteristics were developed. The laboratory work was performed only on bathtubs and flat specimens provided by industry through appropriate arrangements with the Building Research Advisory Board. Field inspection trips were made to provide the NBS project staff with up-to-date information on certain manufacturing processes and on installation and use problems. The complexities involved in the selection of valid performance levels are discussed, as well as the elements of judgment involved. A format that might be used in specifying performance is suggested for each test procedure, and the rationale underlying each suggested format is given.

Beatty, R. W., Editor, **Commission 1 progress in radio measurement methods and standards (Triennial report of progress),** *Radio Sci.* **4,** *No. 7, 579–590 (July 1969).*

Key words: International Scientific Radio Union report; measurement methods; radio measurements; radio standards; URSI XVIth general assembly.

A review of progress within the U.S.A. in Radio Standards and Measurement Methods, covering the period 1966–1968, inclusive, is presented. This review is a part of the Triennial Report of the U. S. National Committee of URSI (International Scientific Radio Union) to the XVIth General Assembly of URSI.
The following topics dealing with U.S.A. progress in Radio Standards and Measurement Methods are included: 1) Time and Frequency, 2) CW Power, 3) CW Voltage, 4) Noise, 5) Pulsed Voltage and Power, 6) Attenuation, Phase Shift, and Time Delay, 7) Impedance, 8) Antenna Characteristics, 9) Field Strength, 10) RF Properties of Materials, 11) Broadband Measurement Techniques, and 12) Laser Measurements.
The report does not include all the developments which have occurred in the U.S.A. in the period indicated, but rather has attempted to include the most significant developments in each field.

Bennett, H. S., **F center in ionic crystals. II. Polarizable-ion models,** *Phys. Rev.* **184,** *No. 3, 918–935 (Aug. 15, 1969).*

Key words: *F* center; *Huang-Rhys factor;* ionic crystals (NaCl, KCl, MgO, CaO, SrO, CaF_2, SrF_2, BaF_2); polarizable ion; zero phonon transition.

The states of the *F* center are considered on the basis of models which treat the movement of the nearest neighbors to the *F* center and the *F* electron in a self-consistent manner. The lattice is first described in terms of a classical ionic-crystal theory. The theory is then extended to treat the nearest neighbor ions in a quantum mechanical manner. The one defect electron (the *F* electron) is treated according to polarizable ion models. The absorption energy, the emission energy, the lifetime of the first excited state, the zero-phon transition energies, and the Huang-Rhys factors are evaluated for two models which differ in the rigor used to compute the ionic polarization of the nearest and next nearest neighbors. It is found that the model which contains the more rigorous evaluation of the ionic polarization agrees best with the experimental results of CaO and perhaps MgO. In addition, it is found that these models are least successful for *F* centers in NaCl and KCl. Not enough data exist to make judgements about the agreement for CaF_2, SrF_2, and BaF_2.

Bennett, H. S., **Frequency shifts of acoustic phonons in Heisenberg paramagnets. III,** *Phys. Rev.* **185,** *No. 2, 801–804 (1970).*

Key words: Acoustic phonons; antiferromagnet; attenuation; EuO; ferromagnet; magnetic insulators; MnF_2; phonon frequency shift; $RbMnF_3$.

The propagation of sound waves in ferromagnetic and antiferromagnetic insulators is studied within the framework of two models which describe the interaction between the spin system and the lattice. Expressions for the frequency shifts (phonon renormalization) at high temperatures and near the transition temperatures are obtained in terms of time dependent correlation functions. The frequency shifts for long wavelength phonons are found to be negative, to increase rapidly in the vicinity of the transition temperature, and to be less singular than the attenuation coefficients. The ratio of the frequency shift divided by the unperturbed phonon frequency is shown to be independent of the phonon frequency for long wavelengths. These results agree qualitatively with present experiments.

Bennett, L. H., Swartzendruber, L. J., Watson, R. E., **Magnetic clusters associated with isolated Fe atoms in paramagnetic Cu-Ni alloys,** *Phys. Rev. Letters* **23,** *No. 20, 1171–1174 (Nov. 17, 1969).*

Key words: Alloys; Cu; Fe; magnetism; moments; Mössbauer effect; Ni.

A small magnetic cluster is shown to exist around an isolated Fe atom in $Cu_{1-x}Ni_x$ alloys with a moment and saturation hyperfine

field depending on the number, n, of Ni near neighbors. This small cluster changes from moments of $2.85 + 0.6n\ \mu_B$ to large moments similar to those known to be present in the absence of Fe for Ni concentrations near the critical composition. The moment compensation (Kondo effect) known to be present for isolated Fe in Cu is found to persist in Cu-Ni for Ni concentrations up to at least 10 at. %.

Berger, M. J., Seltzer, S. M., **Calculation of energy and charge deposition and of the electron flux in a water medium bombarded with 20-MeV electrons,** *(Proc. Cong. High Energy Radiation Therapy Dosimetry under the auspices of the American Association of Physicists in Medicine, New York, N.Y., June 15–17, 1967), Ann. N.Y. Acad. Sci. 161, Art. 1, 8–23 (July 3, 1969).*

Key words: Charge deposition; electrons; energy deposition; flux; Monte Carlo; multiple scattering.

A combination of Monte Carlo and analytical techniques is used to compute the penetration of fast electrons in water, taking into account multiple elastic scattering by atoms, multiple inelastic scattering by atomic electrons, and the production of bremsstrahlung. Secondary electrons are also considered which result from electron-electron collisions, or from the absorption or scattering of bremsstrahlung. The calculation provides information about the spatial distribution of energy deposition, charge deposition and the electron flux (primary and secondary) down to a spectral energy of 400 eV. Representative results are presented, mainly for 20-MeV electrons incident perpendicularly on a semi-infinite water medium.

Blandford, J. M., **In-plant testing for wash-and-wear apparel performance and labeling,** *Third Annual Tech. Conf. The Apparel Research Foundation, Inc., Washington, D.C., Oct. 14–16, 1969, 12 pages (Oct. 14, 1969).*

Key words: Apparel; care instructions; labeling, apparel; performance, apparel; properties, apparel; testing textiles; wash-and-wear.

A distinction is made between washable garments, in general, and wash-and-wear apparel, in particular, with reference to the properties associated with appearance, performance, and ease of care. The testing equipment, testing procedures, and evaluation materials required by the apparel manufacturer in his assessment of these properties and formulation of ease-of-care instructions for labels and hang tags, are discussed. Tabulations and charts are included.

Braun, W., Carrington, T., **Line emission sources for concentration measurements and photochemistry,** *J. Quant. Spectr. Radiative Transfer* **9,** *1133–1143 (1969).*

Key words: Absorption; analysis; gas; photochemistry; spectroscopy; vacuum ultraviolet.

When a resonance line is absorbed in its own gas, measurements of this absorption can be used to derive a value of the product, nf, of concentration of the absorber and f value of the transition. This line absorption process is also important in the study of fluorescence and photochemistry, where it is possible to produce atoms or molecules in a single quantum state without otherwise disturbing the system. The interpretation and success of these applications of line absorption depend critically on the shape of the line emitted by the light source. This is strongly influenced by the optical depth in the emitting region, and by the inevitable presence of a reversing layer through which the light must travel on its way out of the lamp. This paper presents a simple model which can be used to estimate the effects of these properties of the light source on the threshold and sensitivity of measurements of nf, and on the power which can be delivered to absorbing atoms outside the lamp. Emphasis is on the general principles of lamp design and diagnosis, rather than on accurate description of a particular lamp.

Brenner, F. C., **Research for a uniform quality grading system for tires,** *Rubber Chem. Technol.* **42,** *No. 5, 1446–1449 (Dec. 1969).*

Key words: Bias ply; grading; passenger car; speed capability; tires.

The National Traffic and Motor Vehicle Safety Act of 1966 requires the establishment of a *uniform quality grading system.* This paper discusses the needs for the system and the complexity of the problem. The system proposed here will depend on five properties; tread wear, traction, impact resistance, endurance, and wheel speed capability.

Brenner, F. C., Barton, F. W., **Cuts and cut growth in tires,** *Rubber Chem. Technol.* **42,** *No. 1462–1465 (Dec. 1969).*

Key words: Cut growth; cutting; road test; tires.

Forty tires were subjected to severe road use on a course (approximately 3500 miles) that included Belgian block, over highways at turnpike speeds while overloaded. The course was repeated until the tires were worn smooth. At the end of each course, the number of new cuts and the length of all cuts in grooves was determined. Ten miles of Caliche (sharp stones) road was included between the first and second measuring period.
The tires experienced a total of 169 cuts. Forty seven (47) of these grew, 34 of which grew less than 0.11 inches. No cut grew continuously throughout the test. The cuts grew but not enough to cause tire failure except in one case where the cut exposed the fabric.

Brenner, F. C., Mandel, J., Simson, B. G., Research for a uniform quality grading system for tires. II. Wheel speed capability test, *Rubber Chem. Technol.* **42,** *No. 5, 1450–1461* (Dec. 1969).

Key words: Bias ply; grading; passenger car; radial; speed capability; tires; winter.

The wheel speed capability of a tire is defined by a test method which determines the speed at which the tire fails on a laboratory test wheel. Data are reported on over 100 different passenger car tires of all grades and types over a range of sizes.
A scaling system is devised for this property. It is found that the system produces consistent results for tires of given manufacturer's nominal grade across the size range tested and for samples produced several months apart.

Catanzaro, E. J., Champion, C. E., Garner, E. L., Marinenko, G., Sappenfield, K. M., Shields, W. R., **Standard reference materials: Boric acid; isotope and assay standard reference materials,** *Nat. Bur. Stand. (U.S.), Spec. Publ. 260–17, 70 pages (Feb. 1970), 65 cents, SD Catalog No. C13.10:260–17.*

Key words: Absolute ratios; assay standards; boron; coulometry; isotopic standards; mass spectrometry.

A precise coulometric titration method has been developed for the assay of boric acid. The method is capable of providing boric acid assays precise to within 0.0025 percent (1 sigma) which is an order of magnitude better than existing techniques. Using this method, a lot of high purity boric acid has been assayed and found to be virtually stoichiometric H_3BO_3. Its acidimetric assay value of 100.00 $\pm$ 0.01 percent characterizes this material as a primary chemical standard for boron determinations.
Multiple samples of boric acid were studied and characterized with respect to homogeneity and the effect of relative humidity on stoichiometry. Procedures for precise preparation, aliquoting and storage of boric acid solutions were devised.
A mass spectrometric technique for the precise measurement of boron isotope ratios was developed. Single-filament tantalum-ribbon sources are used, and $^{11}B/^{10}B$ ratios are determined by measuring the relative abundances of $Na_2{}^{11}BO_2^+$ and $Na_2{}^{10}BO_2^+$ ions, at masses 89 and 88, respectively. The effects of various parameters such as sample mounting procedure, filament material, sample size, total sample composition and sodium concentration were studied and alternative procedure were evaluated.
Absolute values were obtained for the isotopic abundance ratios of two boron isotopic standards, using surface emission mass spectrometry. Samples of known isotopic composition, prepared from nearly pure separated boron isotopes, were used to calibrate the mass spectrometers. The resulting absolute values are: SRM 951, Boric Acid, $^{11}B/^{10}B = 4.04362 \pm 0.00137$; and SRM 952, Boric Acid, $^{11}B/^{10}B = 0.053199 \pm 0.000032$. The indicated uncertainties are overall limits of error based on 95 percent confidence limits for the means and allowances for effects of known sources of possible systematic error.

Deslattes, R. D., **Optical and x-ray interferometry of a silicon lattice spacing,** *Appl. Phys. Letters* **15,** *No. 11, 386–388 (Dec. 1969).*

Key words: Interferometer; lattice parameter; x-ray.

A device permitting simultaneous x-ray and optical interferometry over traverses in excess of 20 μm is reported. Results obtained to date suggest that such devices will permit measurements of certain crystal lattice parameters with accuracies better than one part per million.

Deslattes, R. D., **Relative energy measurements in the K series of argon,** *Phys. Rev.* **186,** *No. 1, 1–4 (Oct. 5, 1969).*

Key words: Argon; energy relation; x-ray spectra.

The relative positions of the principal features of the emission and absorption spectra of argon in its K series have been measured. The results are discussed with particular emphasis on the non-equality of the Rydberg limit to Kβ interval with the optical ionization potential. The difficulty is suggested to arise from use of a constant quantum defect in assessing the Rydberg limit. Location of the limit via the experimental ionization potential leads to new values for the L_{II} and L_{III} terms from measurements of $K\alpha_2$ and $K\alpha_1$. These are in reasonable agreement with Hartree-Fock calculations and with recent grating measurements from other laboratories and preliminary single crystal measurements newly reported here.

Ernst, M. H., Dorfman, J. R., Hoegy, W. R., Van Leeuwen, J. M. J., **Hard sphere dynamics and binary collision operators,** *Physica* **45,** *127–146 (1969).*

Key words: Binary collision expansion; binary collision operator; hard sphere dynamics; N-body dynamics; overlap function W; overlapping configuration.

The dynamics of a classical hard sphere system has the peculiarities that the particles suffer instantaneous collisions and that certain ("overlapping") areas in phase space are not accessible to the particles. It is mainly the latter feature that prevents a straight forward application of the usual binary collision expansion, generating the particle trajectories. Depending on how the relevant streaming operators are extended to the overlapping area's binary collision expansions can be developed. The different expressions so far proposed are critically examined and the restrictions to their applicability are determined. The binary collision expansion for potentials consisting of a hard core and a soft tail is discussed briefly.

Farrar, T. C., Tsang, T., Johannesen, R. B., **Internal reorientations in K_2ReH_9 via wide-line and pulsed proton resonance studies,** *J. Chem. Phys.* **51,** *No. 8, 3595–3596 (Oct. 15, 1969).*

Key words: Internal reorientation; nuclear magnetic relaxation; potassium rhenium hydride; potential barrier; proton; second moment.

Proton spin-lattice relaxation times (T_1) and second moments (M_2) have been measured as a function of temperature for K_2ReH_9. The activation energies for internal reorientation of $ReH_9^{=}$ ions, and their rms errors, are 9.9 ± 0.4 and 25.0 ± 0.8 kilojoules per mole (2.4 ± 0.1 and 6.0 ± 0.2 kcal/mol) respectively for type *a* and *d* sites. Our results suggest that the barriers are determined by nearest neighbor $ReH_9^{=}$-$ReH_9^{=}$ interactions.

Fatiadi, A. J., **Novel aromatization of a trihydroxycyclohexanetrione (triketoinositol) to a dibenzo-*p*-dioxin derivative,** *Carbohydrate Res.* **12,** *130–132 (1970).*

Key words: Acetylation; aromatization; benzenehexol; carbonium ion; dibenzo-*p*-dioxin; hemiacetal; hydrogen shift; mass spectrometry; phosphoric acid; triketoinositol.

Novel aromatization of a triketoinositol on acetylation in the presence of acidic catalyst is described. Treatment of 4,6/5-trihydroxy-1,2,3-cyclohexanetrione (a triketoinositol) with acetic anhydride and 100% phosphoric acid yields octaacetoxy dibenzo-*p*-dioxin in 38–42% yield. It is believed that reaction proceeds by isomerization on a half of triketoinositol to benzenehexol followed by intramolecular cycloaddition with the formation of a bishemiacetal intermediate. Aromatization of a newly formed ring probably involves: (a) carbonium ion formation (b) hydrogen shift and (c) elimination of two molecules of water. The structure was proved by ultraviolet, infrared, nuclear magnetic resonance, and mass spectroscopy.

Freeman, D. H., Zielinski, W. L., Jr., Editors, **Separation and Purification Section: Summary of activities July 1968 to June 1969,** *Nat. Bur. Stand. (U.S.), Tech. Note 509, 73 pages (Feb. 1970), 70 cents, SD Catalog No. C13.46:509.*

Key words: Gas chromatography; infrared analysis; ion exchange; liquid chromatography; purification; separation; styrene/divinylbenzene; ultra-pure reagents.

This is the annual progress report on the Separation and Purification Section activities. The major task of developing a certified ion exchange microstandard as a Standard Reference Material is presented in terms of the preparative and characterizational work involved. Fundamental studies of ion exchange substrates includes the application of quantitative analytical infrared spectrophotometry to measure crosslinking in the copolymer network, and to determine the degree of sulfonation. Optical microscopy is applied to the study of swelling kinetics for single copolymer particles. Analytical gas chromatography is applied to the isomers of divinylbenzene. The recently acquired quadrupole mass spectrometer is described. Liquid chromatography at high pressures and with high resolution has been begun recently. The activities of a project dealing exclusively with ultrapure reagents is described including the problems of contamination free storage.

Hoegy, W. R., **Convergent generalization of the Boltzmann equation for a hard sphere lorentz gas,** *Phys. Rev.* **185,** *No. 1, 210–218 (Sept. 5, 1969).*

Key words: Binary collision expansion; generalized collision integrals; multiple scattering system; single scatter propagator; physical expansion.

The Lorentz-Boltzmann equation is generalized for a classical hard sphere Lorentz gas. The generalized equation appears in two forms: the product dynamical equation and the convolution dynamical equation. The product collision integral contains a sum of products of script streaming operators, $S(1 \ldots I) = S(1 \ldots t;\ t)S(-t)$, whereas the convolution collision integral is composed of products of binary propagators. The product form contains more collision events (reverse streaming events) than the convolution form. The cluster streaming operators are analyzed using a sequential trajectory decomposition. This method systematically decomposes configuration space and expresses the successive binary encounters of the decomposed regions with binary propagators. When the physically unrealizable trajectories are omitted from the binary collision expansion, it reduces to the form given by the sequential trajectory decomposition. A simple prescription is given for the generalized Lorentz-Boltzmann collision integral and for a generalized Stosszahlansatz both consequences of the Liouville equation.

Hust, J. G., **A compilation and historical review of temperature scale differences,** *Cryogenics* **9,** *No. 6, 443–455 (Dec. 1969).*

Key words: Temperature; temperature scales; thermometry.

A brief review is given of temperature, its definition, and measurement. Methods of practical temperature measurement are described. Differences between internationally accepted temperature scales are presented graphically and in tabular form; comparisons are also given for several national temperature scales. Emphasis has been placed on temperatures below 0°C, but some information on temperatures above 0°C has also been included. Suggested methods of conversion between different temperature scales are described.

Jones, M. C., Giarratano, P. J., Simpson, A. U., **Heat transfer to solid-vapor mixtures of cryogens below their triple points flowing through heated tubes,** *AIChE J.* **15,** *No. 5, 890–897 (Nov. 1969).*

Key words: Boundary layer; cryogenic; heat transfer; hydrogen; low pressure; nitrogen; particle-wall interaction; solid-vapor; tube; two-phase.

Data are presented for wall temperatures and heat transfer coefficients for solid-vapor mixtures of parahydrogen and nitrogen flowing in an electrically heated straight tube of length 40 times its diameter. These are interpreted by the application of flat plate, constant property boundary layer theory to models in which the solid particle geometrical distribution takes on simple limiting forms. The observed enhancement of the heat transfer coefficient over that for gas alone traveling at the same velocity is qualitatively predicted as a function of a dimensionless heat flux, the Sterman parameter $q_w/\rho_v U\lambda$. This parameter is also shown to be an index of particle-wall interaction and is used to correlate observed limiting wall heat fluxes above which free flow may be guaranteed.

Kamper, R. A., **The Josephson effect,** *IEEE Trans. Electron Devices* **ED16,** *No. 10, 840–844 (Oct. 1969).*

Key words: Electron tunneling; electronics; low temperature; superconducting devices.

This is a review of the Josephson effect in superconductors, with emphasis on the electrical properties of Josephson junctions and their application to devices and measurement techniques.

Kusuda, T., **Algorithms for psychrometric calculations (skeleton tables for the thermodynamic properties of moist air),** *Nat. Bur. Stand. (U.S.), Bldg. Sci. Ser. 21, 53 pages (Jan. 1970),* *55 cents, SD Catalog No. C13.29/2:21.*

Key words: Computer algorithm; psychrometrics; saturated and unsaturated moist air; thermodynamic properties.

Computer algorithms to obtain thermodynamic properties of saturated and unsaturated moist air are presented in this paper. The saturated moist air properties are calculated by the methodology developed by J. A. Goff and S. Gratch for their ASHRAE tables (1967 Book of Fundamentals, The American Society of Heating, Refrigerating and Air Conditioning Engineers). Sample calculations were performed using a computer program based upon the algorithms presented herein and the results are attached.

McClintock, M., Balling, L. C., **Atomic and molecular fluorescence from laser excited diatomic cesium and rubidium,** *J. Quant. Spectro. Radiative Transfer* **9,** *1209–1214 (1969).*

Key words: Atomic fluorescence; cesium rubidium; laser induced fluorescence; molecular fluorescence.

It has been found that several argon laser lines and the 6328 A helium-neon line cause excitation of diatomic rubidium and cesium in the vapor phase to excited electronic states. The excitation of only a few, well separated rotation levels in the upper state, and the resulting simple line fluorescence spectra will allow determination of molecular constants not available by other methods. Atomic fluorescence was also present. Twenty-seven atomic cesium lines were observed between 3611 and 8946 A under illumination at 4880 A. The intensities of several atomic lines were found to have a quadratic dependence upon laser intensity, and are therefore attributed to excitation processes involving two photons.

McDonald, D. G., Kose, V. E., Evenson, K. M., Wells, J. S., Cupp, J. D., **Harmonic generation and submillimeter wave mixing with the Josephson effect,** *Appl. Phys. Letters* **15,** *No. 4, 121–122 (Aug. 15, 1969).*

Key words: Infrared; Josephson effect; lasers; submillimeter waves; superconductivity.

By observing constant-voltage steps from Josephson junctions at voltages as high as 17 mV we deduce that junctions can generate harmonics up to frequencies as high as 8200 GHz. In consonance with this, submillimeter wave laser detection, harmonic generation and mixing are demonstrated. These results suggest a model for the upper frequency limit of the Josephson effect.

Margoshes, M., Rasberry, S. D., **Application of digital computers in spectrochemical analysis—computational methods in photographic microphotometry,** *Spectrochim. Acta* **24B,** *497–513 (1969).*

Key words: Computers; emulsion; microphotometry; photographic emulsion; photographic photometry; photometry programs; spectrochemical.

A new method is described for calibration of photographic emulsions and conversion of microphotometer readings to relative intensities on a digital computer with special application to spectrochemical analysis. The method for emulsion calibration replaces graphical procedures by a numerical method which is well suited for digital computations. The method of computation and its underlying assumptions are described, and results are given of tests of the procedure. It is recognized that the entire experimental arrangement is being calibrated, not merely the photographic emulsion, and it is shown how malfunctions of the microphotometer which affect the calibration can be recognized from the output of the computer. The program for conversion of microphotometer readings to relative intensities provides for several alternate calculations, including selection of the proper calibration parameters according to the wavelength of the line when these data are supplied for more than one wavelength region, as well as correction for step and background where required. The program is written to provide for automatic selection of the required alternative calculation, based on preliminary analysis of the input data.

Mies, F. H., **Resonant scattering theory of association reactions and unimolecular decomposition. II. Comparison of the collision theory and the absolute rate theory,** *J. Chem. Phys.* **51,** *No. 2, 798–807 (July 1969).*

Key words: Absolute Rate Theory; association; configuration interaction; recombination decomposition; resonance scattering; scattering theory; unimolecular kinetics; quantum mechanics.

The rate expressions derived in the preceding paper using a resonant scattering theory (RST) to describe recombination and unimolecular decomposition are compared to the Absolute Rate Theory (ART). A one to one correspondence exists between the resonance states in RST and the activated states in ART. The "states of the activated complex" are shown to be the channel states in RST, and using the adiabatic approximation to describe the continuum states it is shown that ART does give a proper *upper bound* to the rate even when non-adiabatic effects are included in RST, i.e., the mean transmission coefficient κ is equal to or less than one. The collision theory gives explicit expressions for $\kappa(kT, P)$ which is a function of temperature and includes the dependence on pressure. Specific expressions are given for the "tight complex" where the "activated complex" occurs at some distorted region in configuration space, and for the "loose complex" where the activated complex is the rotational barrier in the asymptotic channel states. Particular attention is given to the high pressure rate constant where the specific transmission coefficient can be simply related to the ratio of the mean widths to the mean spacings of the activated states. Criteria are given for the validity of ART, and it is shown that Light's statistical theory of reaction rates is simply a special microcanonical version of the ART for the "loose complex."

Mullen, L. O., **On efficient use of selective vacuum pumping modes,** *J. Environ. Sci.* **12,** *No. 5, 26–30 (Oct. 1969).*

Key words: Cryopumps; getters; ion pumps; pumping efficiency; sublimation pumps; vacuum pumps; vapor pressure.

Most vacuum pumps are selective in the sense that they pump different molecular species at different speeds. Some pumps, such as sublimation pumps and cryopumps, are extremely selective. Efficient use of selective pumps requires that they be chosen to match the gas load. We present experimental data on some commonly encountered gas loads and discuss the choice of compatible pumps.

Paulsen, P. J., Alvarez, R., Kelleher, D. E., **Determination of trace elements in zinc by isotope dilution spark source mass spectrometry,** *Spectrochim. Acta* **24B,** *535–544 (April 1969).*

Key words: Electrodeposition; isotope dilution; preconcentration; spark source mass spectrometry; trace elements; zinc.

The applicability of the isotope dilution technique in spark source mass spectrometry has been investigated for the determination of Pb, Cu, Cd, Ag, Tl, and Sn in zinc metal. In the procedure developed, a solution of the zinc is spiked with known amounts of stable isotopes of the elements to be determined, and the elements are electrodeposited onto gold wires that subsequently serve as electrodes for the mass spectrographic isotopic analysis. Chemical operations, including isothermal distillation of reagents, dissolution of the zinc, and the electrodeposition step are conducted in a closed system to minimize contamination. The results of the analysis of two NBS zinc standard reference materials show determination ranging from 11 ppm (11 μg/g) for Pb to as low as 0.02 ppm (20 ng/g) for Sn. It is concluded that this method is of general utility for simultaneous multi-element trace analysis and is especially applicable in providing much needed standardization in spark source mass spectrometry.

Rankin, K., Tan, J. L., **Component combination and frame-embedding in Chinese character grammars,** *Nat. Bur. Stand. (U.S.), Tech. Note 492, 36 pages (Feb. 1970), 40 cents, SD Catalog No. C13.46:492.*

Key words: Blocking; Chinese characters; component combination; frame embedding; generative grammar; grammar; linguistics.

Chinese characters can be almost completely described from the point of view that each character is composed of a number of components and that each component is composed of a number of strokes. This note offers a grammatical treatment of component combination. It is concerned with the three most productive processes of component arrangement. This grammar differs from previous grammars in that the constraints on recursion have been minimized and great lexical economy has been achieved.

Robbins, R. F., **Cryogenic properties of a polyurethane adhesive,** *J. Macromol. Sci.* **A3,** *No. 7, 1367–1380 (Nov. 1969).*

Key words: Adhesive; low temperature; mechanical properties; polymer; polyurethane; resilience; thermal properties.

Differential Thermal Analysis (DTA) Rebound Resilience, and Tensile Properties of a polyurethane adhesive were measured at cryogenic temperatures. The experimental methods are described, and test results which aid in evaluating the polyurethane for use at low temperatures are discussed. The DTA thermogram reveals that the glass transition temperature (T_g) is 235 K. The resilience profile indicates a resilience minimum (T_m) at 270 K and a frequency of 3800 Hz, which is consistent with the T_g measured by DTA. The low resilience below T_m, caused by secondary low temperature transitions, shows the high energy absorption capabilities of the polyurethane. Considerable plastic flow at 195 K (40 K below T_g) is evidenced in the results of the tensile tests. The results of the three tests indicate that the polyurethane adhesive will perform well at low temperatures. The test methods should also be useful for evaluating the low temperature performance of new experimental polymers.

Robinson, H. E., Editor, **Durability of insulating glass.** *Proceedings of a seminar held at the National Bureau of Standards, Gaithersburg, Maryland, November 14–15, 1968, Nat. Bur. Stand. (U.S.), Bldg. Sci. Ser. 20, 84 pages (Feb. 1970), 75 cents, SD Catalog No. C13.29/2:20.*

Key words: Accelerated laboratory tests; double-glazed window units; factory-sealed insulating glass units; field performance tests, correlation with laboratory tests; sealant performance; standardized testing; test methods.

A two-day seminar on the Durability of Insulating Glass was attended by some 130 persons on November 14 and 15, 1968. The seminar was held at the Gaithersburg, Maryland, facilities of the National Bureau of Standards and featured fourteen speakers who participated in panel discussions or delivered individual papers. Numerous agencies interested in design, manufacture, specification, purchase, installation or maintenance of windows were represented at the seminar.
Among the topics considered in the panel discussions were: (1) The need for reliability and durability of insulating glass; (2) manufacturers' test methods; (3) proposals for future action. The Canadian experience with an accelerated test method and acceptance program was presented and discussed, as were the Norwegian accelerated test methods and their correlation with field experience. A review of current practices leading to new test methods and standards was also presented, and a "round robin" program that would compare various test methods now employed in the industry was proposed. Affirmative interest in participating in the proposed round robin was expressed by about a score of manufacturers present at the seminar.

Silverman, S., **The National Measurement System—a concept to assist the private sector,** *Mater. Res. Std.* **9,** *No. 10, 11–14 (Oct. 1969).*

Key words: Measurement; National Bureau of Standards; National Measurement System; national standards; self-calibration; standards, national; systems concept.

The concept of a National Measurement System, involving the entire complex of measurement activities within the United States, is developed. The central element of this Measurement System is the National Bureau of Standards. The role of NBS and of other functional elements of the System, such as private laboratories, is discussed.

Smith, E. W., Cooper, J., Vidal, C. R., **A unified classical path treatment of stark broadening in plasmas,** *Phys. Rev.* **185,** *No. 1, 140–151 (Sept. 5, 1969).*

Key words: Classical path; spectral line broadening.

A theoretical treatment of spectral line broadening in plasmas is developed using classical path methods. This treatment unifies certain aspects of the familiar impact, one-electron and relaxation theories to produce results which are valid from the line center to the far line wings where the electrons may behave quasi-statically. Calculations of the Lyman-alpha line of hydrogen are used to illustrate the theory.

Smith, R. V., **The influence of surface characteristics on the boiling of cryogenic fluids,** *J. Eng. Ind.* **91,** *No. 4, 1217–1221 (Nov. 1969).*

Key words: Boiling; boiling hysteresis; boiling inception; boiling-site spreading; radiation.

This paper reviews the influence of the characteristics of the solid surface on the boiling of cryogenic fluids. Particular emphasis is placed on papers presented in the cryogenics section of the 1968 Annual ASME meeting.
Hysteresis, boiling-site spreading and the influence of radiation on the surfaces are discussed in detail.

Strohlein, J. N., Bagg, T. C., **A selective roll-to-roll printer for producing duplicate microfilm copies,** *Nat. Bur. Stand. (U.S.), Tech. Note 516, 9 pages (Feb. 1970), 25 cents, SD Catalog No. C13.46:516.*

Key words: Information retrieval device; microcopier; microfilm duplicator; reader-printer; selective copier.

The "Selectaframe" printer, a convenient device for copying onto roll film selected frames from other rolls of film for subsequent automatic enlargement printing is described in detail.

Vidal, C. R., Cooper, J., **Heat pipe oven: a new, well-defined metal vapor device for spectroscopic measurements,** *J. Appl. Phys.* **40,** *No. 8, 3370–3374 (July 1969).*

Key words: Absorption spectroscopy; heat pipe; metal vapor device; oven.

A new well defined metal vapor device called the heat pipe oven has been developed on the basis of the heat pipe, a heat conductive element designed by G. Grover and his co-workers in Los Alamos. It generates continuously homogeneous vapors of well defined temperature, pressure and optical path length. The vapor is confined

by inert gas boundaries which remove the window problem and allow a direct pressure measurement without relying on vapor pressure curves. Due to the continuous evaporation and condensation the vapor purifies itself during operation.

Walton, W. W., Cadoff, B. C., Editors, **Performance of buildings—concept and measurement.** *Proceeding of the 1st conference in a series of conferences on Man and His Shelter held at the National Bureau of Standards, Gaithersburg, Maryland, September 23–25, 1968, Nat. Bur. Stand. (U.S.), Bldg. Sci. Ser. 1, 132 pages (Jan. 1970), $2.75, SD Catalog No. C13.29/2:1.*

Key words: Building systems; performance of buildings; standards; test methods; urban planning; user needs.

The Conference entitled "Performance of Buildings—Concept and Measurement" was held at the National Bureau of Standards, Gaithersburg, Md. on September 23–25, 1968. This was the first in a planned series of conferences on "Man and His Shelter." The purpose of these conferences is to bring together those people from various disciplines who may contribute to improving the quality of man's shelter. At the present conference, papers were presented by nineteen authors representing government and industry in such diverse disciplines as architecture, engineering, science, urban planning, and standards. These papers emphasize the prime importance of considering user needs in the development of performance criteria, the necessity of test methods to determine whether the desired performance has been achieved, and the development of performance specifications and standards. Application of these ideas to building systems, and to the planning and design of entire communities, is also discussed.

Weber, L. A., **Saturation densities of oxygen in the critical region,** *Physics Letters* **30A,** *No. 7, 390–391 (Dec. 1, 1969).*

Key words: Critical density; critical point; critical temperature; oxygen; properties of fluids; P–V–T, saturation densities.

A description is given of an apparatus used to determine the detailed nature of the P–V–T surface of fluids in the critical region by means of dielectric measurements. Data are given for the saturation densities of oxygen within 3 percent of the critical temperature. Analysis of the data yields the following values of the critical parameters: $T_c = 154.575 \pm .010$K on the IPTS 1948 scale, $\rho_c = 0.4362 \pm .0005$ kg/l. The critical index $\beta = 0.352 \pm .005$.

Wiederhorn, S. M., **Crack propagation in polycrystalline ceramics** *(Proc. 15th Sagamore Army Materials Research Conf., Sagamore Conference Center, Raquette Lake, New York, Aug. 20–23, 1968), Chapter in Ultra-fine-Grain Ceramics* **15,** *317–338 (Syracuse University Press, Syracuse, N.Y., 1970).*

Key words: Ceramics; fracture; fracture surface energy; strength; thermal shock.

In this paper, the strength and shock resistance of ceramic materials will be related to microstructural details and the energy necessary to form fracture surfaces. The influence of grain size, grain orientation, crystal anisotropy and residual stresses on crack propagation will be discussed. It will be argued that the strength of ceramic materials is closely related to the grain boundary or single crystal fracture surface energy while shock resistance is related to the surface energy required to propagate large cracks through polycrystalline materials. The use of fracture surface energies as a research technique and as a design parameter will be discussed.

Wilson, W. K., **Reflections on the stability of paper,** *Restaurator* **1,** *No. 2, 79–86 (1969).*

Key words: Degradation; paper; preservation of records; records; stability.

Variables in the composition of paper are discussed in relation to stability, and new approaches to research on preservation of records are described.

Yakowitz, H., **The divergent beam x-ray technique,** *Chapter in Advances in Electronics and Electron Physics, Suppl. 6, Electron Probe Microanalysis;* A. J. Toksimis and L. L. Marton, ed., *pp. 361–431 (Academic Press Inc., New York, N.Y., 1969).*

Key words: Kossel method; x-ray microdiffraction.

This is a review paper discussing the technique of divergent beam (Kossel) x-ray diffraction. The Kossel method is studied with regard to line intensities, photographic contrast, data reduction, specimen preparation, and contribution to scientific research.

Other NBS Publications

J. Res. Nat. Bur. Stand. (U.S.), 74B (Math. Sci.), No. 2 (Apr.–June 1970), SD Catalog No. C13.22/sec. B:74/2.

Acoustic propagation and stability within an inviscid, heat-conducting fluid. J. E. McKinney and H. J. Oser.

On some indefinite integrals of confluent hypergeometric functions. E. W. Ng and M. Geller.

On complementary polar conical sets. C. Witzgall.

On contractive semigroups and uniform asymptotic stability. P. R. Meyers.

Normal subgroups of the modular group. L. Greenberg and M. Newman.

Jones, M. C., Far infrared absorption in liquid hydrogen, J. Chem. Phys. **51,** No. 9, 3833–3834 (Nov. 1, 1969).

Ku, H. H., Varner, R. N., Kullback, S., Analysis of multi-dimensional contingency tables (Proc. 14th Conf. Design of Experiments in Army Research Development and Testing, Edgewood Arsenal, Md., October 23, 1968), ARO–D Report 69–2, 141–180 (U.S. Army Research Office-Durham, Durham, North Carolina, Sept. 1969).

Meinke, W. W., The NBS standard reference materials program: Past, present, and future, Mater. Res. Std. **9,** No. 10, 15–18 (Oct. 1969).

Simpson, A. U., Timmerhaus, K. D., Kreith, F., Jones, M. C., Heat and mass transfer in dispersed, two-phase, single-component flow, Intern. J. Heat Mass Transfer **12,** No. 9, 1141–1155 (Sept. 1969).

Strobridge, T. R., Refrigeration techniques, U.S. Bureau Mines Info. Circ. No. 8417, pp. 39–56 (1969).

Wampler, R. H., An evaluation of linear least squares computer programs: A summary report (Proc. 14th Conf. Design of Experiments in Army Research Development and Testing, Edgewood Arsenal, Md., October 23, 1968), ARO–D Report 69–2, 103–126 (U.S. Army Research Office-Durham, Durham, North Carolina, Sept. 1969).

Wood, R. E., Hamer, W. J., Theoretical electromotive forces of metal-halogen cells: Some recalculations based on recent data, J. Electrochem. Soc. **117,** No. 1, 82–83 (Jan. 1970).

**Publications for which a price is indicated are available by purchase from the Superintendent of Documents, U.S. Government Printing Office, Washington, D.C. 20402 (foreign postage, one-fourth additional). The NBS non-periodical series are also available from the Clearinghouse for Federal Scientific and Technical Information, Springfield, Va. 22151. Reprints from outside journals and the NBS Journal of Research may often be obtained directly from the authors.*

U.S. GOVERNMENT PRINTING OFFICE : 1970 OL—383–876

UNITED STATES
GOVERNMENT PRINTING
DIVISION OF PUBLIC DOCUME
WASHINGTON, D.C. 204

OFFICIAL BUSINESS
PENALTY FOR PRIVATE USE, $300

A OCT 46129
UNIVERSITY MICROFILMS INC
ATTN SERIALS SECTION
300 NORTH ZEEB RD
ANN ARBOR MICH 48106

POSTAGE AND FEES PAID
U.S. GOVERNMENT PRINTING OFFICE

JOURNAL OF RESEARCH of the National Bureau of Standards
A. Physics and Chemistry

Vol. 74A, No. 4 July–Aug. 1970

Contents

Page

Solubility of $CaHPO_4 \cdot 2H_2O$ in the system $Ca(OH)_2 - H_3PO_4 - H_2O$ at 5, 15, 25, and 37.5 °C. Thomas M. Gregory, Edgard C. Moreno, and Walter E. Brown. 461

Effect of oxide additions on the polymorphism of tantalum pentoxide II. "Stabilization" of the high temperature structure type. R. S. Roth, J. L. Waring, and W. S. Brower. 477

Effect of oxide additions on the polymorphism of tantalum pentoxide III. "Stabilization" of the low temperature structure type. R. S. Roth and J. L. Waring. 485

The dissociation constant of *m*-nitroanilinium ion in water-tetrahydrofuran solvents at 25 °C. R. A. Robinson. 495

Specific heats of fluorine at coexistence. Robert D. Goodwin and Rolf Prydz. 499

A theoretical investigation of the configurations $(3d + 4s)^6$ $4p$ in neutral manganese (Mn I). C. Roth. 507

A literature survey of the chemistry of flame inhibition. E. C. Creitz. 521

The NBS Alloy Data Center: Description of index to the literature. G. C. Carter, D. J. Kahan, L. H. Bennett, J. R. Cuthill, and R. C. Dobbyn. 531

Papers presented at the Conference, Electronic Density of States, National Bureau of Standards, Gaithersburg, Maryland November 3–6, 1969

What is a quasi-particle? J. R. Schrieffer. 537

Electronic densities of states from x-ray photoelectron spectroscopy. C. S. Fadley and D. A. Shirley. 543

Tunneling measurements of superconducting quasi-particle density of states and calculation of phonon spectra. J. M. Rowell. 559

Pauli paramagnetism in metals with high densities of states. S. Foner. 567

Relevance of Knight shift measurements to the electronic density of states. L. H. Bennett, R. E. Watson, and G. C. Carter. 569

Publications of the National Bureau of Standards. 611

Library of Congress Catalog Card Number: 62–37059

For sale by the Superintendent of Documents, U.S. Government Printing Office, Washington, D.C. 20402. (Order by SD Catalog No. C 13.22/sec.A:74/4). Single copy price varies. This issue $2. Subscription price: $9.50 a year; $2.25 additional for foreign mailing.

UNITED STATES GOVERNMENT PRINTING OFFICE, WASHINGTON : 1970

XU